Photomultiplier Tubes for the XENON1T Dark Matter Experiment and Studies on the XENON100 Electromagnetic Background

Dissertation

zur
Erlangung der naturwissenschaftlichen Doktorwürde
(Dr. sc. nat.)

vorgelegt der
Mathematisch-naturwissenschaftlichen Fakultät
der
Universität Zürich

von

Daniel Mayani Parás

aus
Mexiko

Promotionskomitee:

Prof. Dr. Laura Baudis
Prof. Dr. Florencia Canelli
Dr. Teresa Marrodán Undagoitia

Zürich, 2016

Abstract

The amount of ordinary matter in the Universe is surpassed five-fold by a completely different kind of matter that manifests itself only through its gravitational effects on the former. This so-called Dark Matter does not absorb nor emit electromagnetic radiation of any kind—hence its name. Weakly Interacting Massive Particles, or WIMPs, are a leading candidate for Dark Matter and many experiments are currently in the pursuit of their direct detection. Amongst these are the XENON100 and XENON1T experiments—both dual-phase time projection chambers searching for WIMP interactions in liquid xenon. The latest results from XENON100, published in 2016, exclude WIMP-nucleon interactions for cross-sections above $1.1 \times 10^{-45}\,\mathrm{cm}^2$ for a WIMP mass of 50 GeV. Meanwhile, XENON1T aims to improve the sensitivity by two orders of magnitude, exploring cross-sections down to $1.6 \times 10^{-47}\,\mathrm{cm}^2$ at the same WIMP mass.

This thesis presents work on both XENON100 and XENON1T. Regarding the former, a study of the electromagnetic background has been performed, focusing specifically on the science run in the period between April 2013 and January 2014. This study is relevant for the understanding of the background sources in the experiment, including the radioactivity of the detector materials and the intrinsic contaminants in the liquid xenon. The effect of the signal saturation in the XENON100 photosensors on the event position reconstruction has been studied. A shift of the reconstructed positions towards inner radii has been observed, which increases the measured event rate within a given fiducial volume. The effect has been quantified—as a function of the event position and energy—and used to correct the Monte Carlo simulations to which the background spectrum is compared. An improved match between the simulated and measured XENON100 data has thus been achieved.

In the case of XENON1T, an in-depth study of the photomultiplier tubes (PMTs) used in the time projection chamber of the detector has been performed and is presented here. Prior to their installation in XENON1T, the Hamamatsu R11410-21 photomultipliers underwent an extensive testing campaign, during which their performance was evaluated both at room temperature and in cryogenic conditions, including liquid xenon. This thesis encompasses work performed at the University of Zurich, as well as a one-year fellowship at the Max-Planck-Institut für Kernphysik in Heidelberg, and a two-month internship at Hamamatsu Photonics—the Japanese company producing the phototubes.

After the evaluation and characterization of the PMTs in various experimental setups, a total of 248 were selected and installed in the XENON1T detector. An online database containing all PMT data and test results has been built for the use of the XENON collaboration. The analysis and methods developed during the testing phase of the PMTs are also used to evaluate their performance during operation in XENON1T. The experiment is currently taking data and the first scientific results are expected in 2017.

Zusammenfassung

Die Menge an gewöhnlicher Materie in unserem Universum wird fünffach übertroffen von einer völlig neuen Form von Materie, die sich bisher nur durch ihre Gravitation zeigt. Da diese Materie keine elektromagnetische Strahlung emittiert oder absorbiert, wird sie "Dunkle Materie" genannt. Einer der Haupt-Kandidaten für Dunkle Materie ist das "Weakly Interacting Massive Particle", WIMP, und verschiedene Experimente versuchen dieses Teilchen direkt nachzuweisen. Unter diesen Experimenten sind auch XENON100 und XENON1T, beide nutzen Zeit-Projektions Kammern um nach WIMP Stössen in flüssigem Xenon zu suchen. Die neuesten Resultate von XENON100, publiziert im Jahr 2016, schließen WIMP-Kern Wechselwirkungen für Wirkungsquerschnitte von mehr als $1.1 \times 10^{-45}\,\mathrm{cm}^2$ für WIMP-Massen von 50 GeV aus. Währenddessen versucht man mit XENON1T die Sensitivität um zwei Größenordnungen zu verbessern, was es ermöglicht nach Wirkungsquerschnitten von bis zu $1.6 \times 10^{-47}\,\mathrm{cm}^2$ bei WIMP-Massen von 50 GeV zu suchen.

In dieser Dissertation werden Ergebnisse von XENON100 sowie von XENON1T vorgestellt. Für XENON100 wurde der elektromagnetischen Untergrund untersucht, speziell für die Daten zwischen April 2013 und Januar 2014. Dieses Resultat ist relevant um den Untergrund des Experiments zu verstehen, der aus der Radioaktivität von verwendeten Detektormaterialien und intrinsischen Verunreinigung im flüssigen Xenon besteht. Die Auswirkung von saturierten Signalen auf die Positionsrekonstruktion der Interaktionspunkte wurde untersucht. Es wurde herausgefunden, dass eine Verschiebung der rekonstruierten Positionen in Richtung kleiner Radien existiert, die zu einer erhöhten gemessen Interaktionsrate in einem gewählten Volumen führt. Dieser Effekt wurde als Funktion der Position sowie Energie quantifiziert und in Monte Carlo Simulationen zur Berechnung der erwarteten Untergrundspektren implementiert. Dies führte zu einer verbesserten Übereinstimmung zwischen simulierten und gemessenen Daten.

Für XENON1T werden in dieser Dissertation detaillierte Studien zu den "photomultiplier tubes" (PMTs) vorgestellt, die in der Zeit-Projektions Kammer des Detektors verwendet werden. Vor der Installation in XENON1T wurde der R11410-21 PMT umfangreich auf die Funktionsweise bei Raumtemperatur sowie bei Tieftemperatur, einschließlich in flüssigem Xenon, getestet. Diese Dissertation umfasst Arbeiten an der Universität Zürich, am Max-Planck-Institut für Kernphysik in Heidelberg, während eines einjährigen Forschungsstipendiums,

sowie bei einem Praktikum bei Hamamatsu Photonics, dem japanischen Hersteller der PMTs. Nach der Auswertung von Tests und Charakterisierung der PMTs in verschiedenen Experimenten, wurden 248 PMTs ausgewählt und in das XENON1T Experiment eingebaut. Die erarbeiteten Ergebnisse und Methoden werden verwendet um die Leistung die PMTs im Detektor während des Betriebes zu evaluieren. XENON1T ist bereits in Betrieb und die ersten wissenschaftlichen Resultate werden 2017 erwartet.

Contents

Chapter 1

Dark Matter is Out There

All objects in everyday life, whatever can be moved, touched or seen—from the smallest particles to the largest stars—are all made of *matter*. But, what exactly *is* matter? For much of the history of natural philosophy and modern science, people have contemplated this fundamental question. Over the centuries, the definition of matter has evolved—and, along with it, so has mankind's understanding of the world and its constituents.

The ancient Greeks were among the first to speculate about the underlying nature of the visible world. In the 5th century BC, Empedocles reduced the composition of everything to four basic elements: earth, water, air, and fire. Meanwhile, atomism—the idea that matter is built of indivisible constituents called "atoms"—emerged during the same period with Leucippus and Democritus. Clusters of atoms with different shapes and sizes would give rise to the various macroscopic objects [1]. It wasn't until the 17th century that the concept of matter was reconsidered. René Descartes postulated that having length, breadth, and depth constituted the essence of all bodies. *Matter* is that which occupies space—being this its main property, aside from locomotion [2]. Isaac Newton inherited this mechanical conception of matter, listing its universal qualities as "extension, hardness, impenetrability, mobility and inertia", further including *mass* as one of its intrinsic properties [3]. Newton's law of universal gravitation comes as a consequence of mass, with gravity being a force exerted by bodies that works "at a distance"—extending beyond physical contact.

The 19th century saw the development of the periodic table and the modern atomic theory, being atoms the fundamental constituents of matter, forming molecules and compounds. A revolution began with the discovery of the electron in 1987 by Thomson [4] and the discovery of the atomic nucleus in 1911 by Rutherford [5]. At the turn of the century, rather than simply possessing mass and occupying space, matter was held to have chemical and electrical properties as well.

With the birth of particle physics came a massive expansion in the knowledge of matter and its building blocks. Today it is known that the atomic nucleus is made of protons and neutrons, being themselves comprised of other particles

called *quarks*. These, along with the electron and its family of leptons, are currently seen as the fundamental components of matter. However, such elementary particles are considered to have no size or volume themselves. In addition, they obtain mass only through their interaction with the Higgs boson—discovered in 2012 at CERN [6] [7]—being otherwise massless. Thus, it is through their interactions alone that quarks and leptons contribute to the volume and mass of the "ordinary matter" that they make up.

The Standard Model of particle physics encompasses the building blocks of matter—altogether called *fermions*—and the force carriers, called *gauge bosons*, which mediate the strong, weak, and electromagnetic interactions. The force carriers are the "glue" that holds matter together. Photons—the carriers of the electric force—possess energy but no mass, whereas the W and Z bosons—carriers of the weak force—do possess mass. Together, they also contribute to the total mass of other subatomic particles and atoms, as well as the more complex systems that contain them.

It is clear that the concept of matter has become more complex over the centuries. Einstein's famous $E = mc^2$ even states that matter and energy are one and the same. It is thus striking to realize that matter—the type that is made out of atoms and which has been studied from antiquity to this day—is but a small fraction of the entire Cosmos. Overwhelming evidence shows that more than 95 % of the content of the Universe is in the form of so-called Dark Matter and Dark Energy—both of which have yet to be detected in a laboratory. How is the existence of Dark Matter known? What exactly is it? How can it be detected? This is the subject of the following sections. Dark Energy, although briefly discussed, will not be further detailed here.

1.1 The Existence of Dark Matter

At the beginning of the 20th century, the hypothesis that there was more matter in the Universe than met the eye was suggested by several astronomers studying the motion of stars and galaxies [8] [9]. The first formal inference of the existence of such matter was made in 1933 by the Swiss astrophysicist Fritz Zwicky [10]. While studying the Coma galaxy cluster, Zwicky estimated the total gravitational mass based on the motion of the outer galaxies of the cluster. He then compared the result with an estimation of the luminous mass based on the total brightness and number of galaxies. The result showed that the cluster had about 400 times more gravitational mass than that which was visible. Zwicky baptized this unseen mass as *dunkle Materie* or "dark matter".

More robust indications of a non-unitary mass-to-light ratio came with the measurement of galaxy rotation curves by H. W. Babcock in 1939 [11] and by Vera Rubin and Kent Ford in the 1960s and '70s [12]. In a study of over twenty galaxies, Rubin found that most of them had to contain about six times more dark mass than visible [13]. By the 1980s, the need for dark matter was a widely

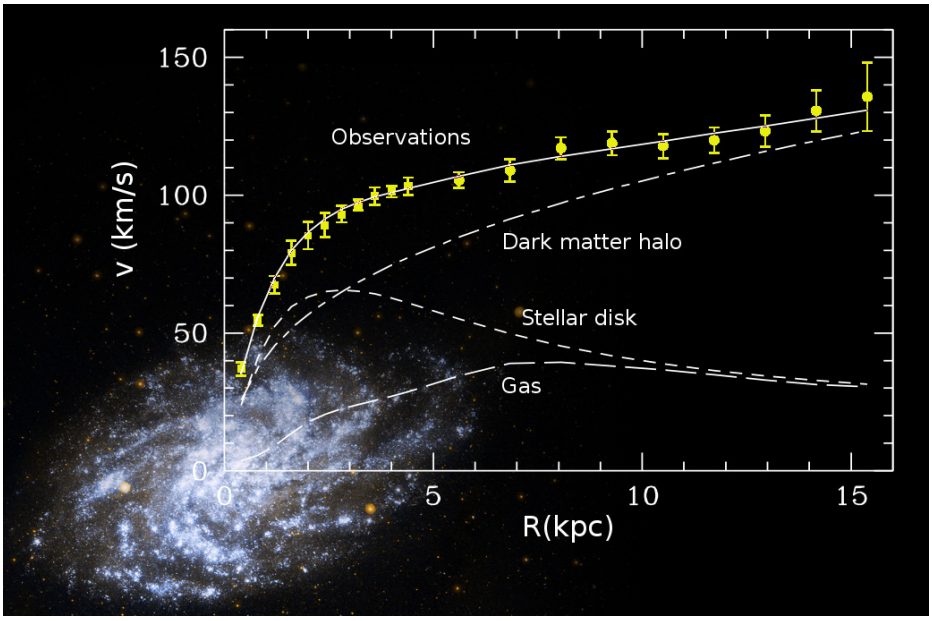

Figure 1.1: Rotation curve of the Triangulum Galaxy—a.k.a. M33 or NGC 598. The best fit model for the measured data (continuous line) is compared to the contributions from the stellar disk and hydrogen gas. The required contribution from the dark matter halo is also shown (dashed-dotted line). Graph taken from [14]. M33 galaxy image from GALEX [15].

accepted problem in astronomy. Additional independent observations, such as gravitational lensing and anisotropies of the cosmic microwave background, further support the existence of dark matter, as explained in the following sections.

1.1.1 Galaxy Rotation Curves

Abundant evidence for dark matter is found at the galactic scale. It has been observed that the orbital motion of stars within a galaxy does not follow the same pattern as that of other systems such as planets orbiting stars or moons orbiting planets, where most of the mass of the system is found at its center. In the latter cases, the velocity of planets and moons decreases with distance, as predicted by Newtonian dynamics:

$$v(r) = \sqrt{\frac{GM(r)}{r}}, \tag{1.1}$$

while in the case of galaxies, the orbital velocities of stars around the galactic center have been observed to remain constant or increase at larger distances.

The motion of stars and gas within a galaxy can thus be used to probe the underlying mass abundance influencing their motion. This is typically achieved by measuring the redshift of starlight in spiral galaxies, as well as the redshift

of the 21 cm hyperfine transition line of neutral hydrogen [16]. The hydrogen cloud in a galaxy extends farther than the visible disk and thus allows to probe rotational velocities at distances far beyond the stars. Such measurements allow to construct the rotation curve of galaxies, such as the one shown in figure 1.1, where the rotational velocities are plotted as a function of the distance from the galactic center. What is observed in spiral galaxies is a typically flat or even rising rotation curve at large radii, while the stellar density falls exponentially. Thus, the mass of stars and hydrogen alone cannot account for the observed rotational speeds. The measured data requires the existence of an additional mass component—a halo of dark matter.

The local properties of the dark matter halo around the Earth can be determined by observing the rotation curves of the Milky Way. Such measurements are difficult to perform from within the galaxy, which leads to uncertainties in the calculations. Furthermore, the rotation curves of the Sun and nearby stars provide a measurement of the total mass within the full solar orbit, thus requiring the density distributions of the galactic bulge and disk to accurately calculate the dark matter profile [17]. Different profile models of the Milky Way halo give results for the local dark matter density in the range $(0.2 \lesssim \rho_0 \lesssim 0.6)\,\mathrm{GeV/cm^3}$ [18] [19], with a preferred value of $\rho_0 = 0.3\,\mathrm{GeV/cm^3}$, an average velocity of 220 km/s [20] and escape velocity of $\sim$544 km/s [21]. These values are relevant for the prospects of dark matter detection, as will be discussed in section 1.2.

1.1.2 Galaxy Clusters and Gravitational Lensing

Galaxy clusters are of great importance for the study of dark matter given that their masses can be estimated in a variety of ways:

Orbital velocity distribution of galaxies within a cluster: Using the measured velocities of galaxies, the total mass of the system can be estimated by implementing the virial theorem, $2\langle T\rangle = -\langle V\rangle$, where T is the total kinetic energy and V the total gravitational potential energy. Thus:

$$M_{cl} \simeq \frac{2R_{cl} \cdot v^2}{G}, \tag{1.2}$$

where M_{cl} is the total mass of the cluster, R_{cl} is the system radius, v is the average velocity and G is the gravitational constant.

The mass-to-light ratio of the cluster, Υ_{cl}, is the quotient between M_{cl} and the total luminosity of the cluster L_{cl}. These ratios are generally reported in terms of the mass-to-light ratio of the Sun ($\Upsilon_\odot$)—equal to a solar mass divided by a solar luminosity ($M_\odot/L_\odot$). The Υ_{cl} of most galaxy clusters has been found to be up to several hundred times larger than $\Upsilon_\odot$ [22] [23]. This indicates that most of the matter does not reside within the stars and strongly hints to the presence of dark matter.

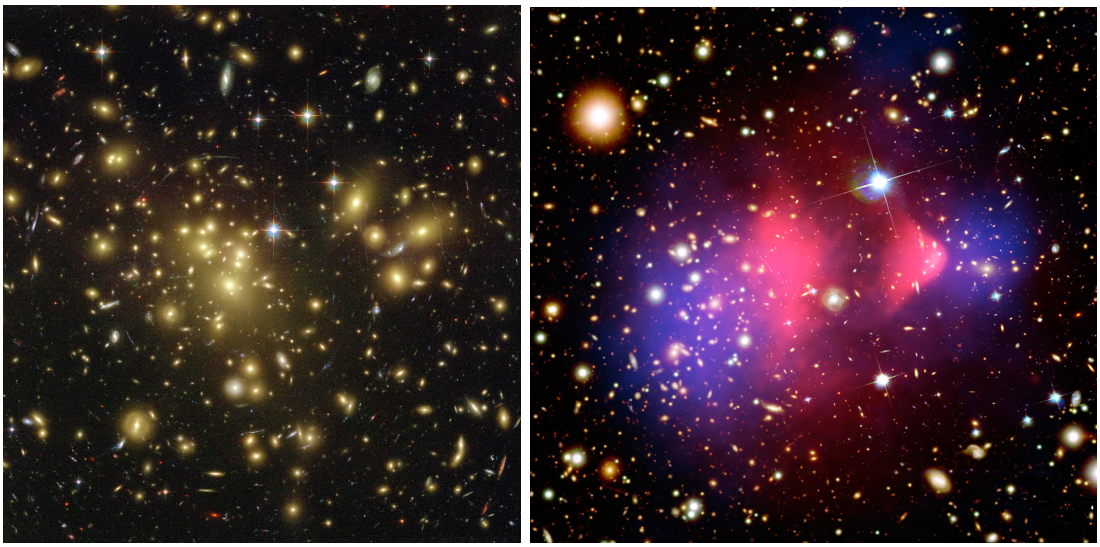

Figure 1.2: (Left) The stars and dark matter of the Abell 1689 cluster create a gravitational lens that distorts the images of background galaxies, seen as arcs of light. Source: Hubble Space Telescope [25]. (Right) Merger of two galaxy clusters known as the Bullet cluster. The collision has separated the luminous component (red)—observed through x-ray emission—from the dark matter (blue)–measured by gravitational lensing. Source: Chandra X-Ray Observatory [26].

X-rays emitted by hot plasma within a cluster: Galaxy clusters contain large quantities of plasma that is heated by the gravitational potential well of the cluster. The emission of *bremsstrahlung* x-rays is proportional to the plasma density squared. The mass of the cluster can thus be estimated through measurements with x-ray satellites, such as the Chandra X-ray Observatory, which generally indicate a greater dark matter abundance than that of the stellar and baryonic intracluster components [24].

Gravitational lensing: Large distributions of matter, such as galaxy clusters, are capable of bending the light from distant sources and changing its trajectory. This effect is one of the predictions of Einstein's theory of general relativity. The first observation of such a phenomenon took place in 1919 during a total solar eclipse [27]. The eclipse allowed the stars behind the Sun to be observed, demonstrating that the starlight passing close to the Sun was slightly bent. Fritz Zwicky posited in 1937 that the same effect could allow galaxy clusters to act as gravitational lenses [28]. It was not until 1979 that this effect was confirmed with the observation of the Twin QSO, a quasar that appears as two images from the gravitational lensing of the galaxy YGKOW G1 [29]. Figure 1.2 (left) shows an image of the Abell 1689 cluster in the constellation of Virgo. It is one of the biggest and most massive galaxy clusters known. Its massive nature has been

used for the study of dark matter through what is known as strong gravitational lensing [30]. The image distortion of galaxies behind the cluster results in one of the largest groups of gravitational light-arcs ever found. The degree at which the light is bent indicates the amount of gravitational mass found within the cluster.

1.1.3 Cluster Mergers

The most unambiguous evidence for the existence of dark matter comes from the collision of galaxy clusters. While, generally, dark and visible matter overlap in the same regions of space due to their gravitational attraction, cluster collisions have been observed to separate the two components. The electromagnetic interactions between baryonic particles causes the intracluster plasma to slow down and concentrate around the center of impact, while the galaxies, stars and dark matter pass through with negligible resistance. X-ray observations show that most of the luminous matter is concentrated in the center of the merger, given that the total intracluster plasma can exceed the stellar mass by a factor of ~ 6 [31]. On the other hand, lensing observations show that most of the gravitational mass (i.e. dark matter) resides in the outer regions of the merger. Unlike other pieces of evidence, such as galactic rotation curves, these observations are independent of the details of Newtonian gravity and unambiguously support the existence of dark matter.

The so-called "Bullet cluster", shown in figure 1.2 (right), is one of several examples of a cluster collision in which the luminous and dark matter components have been separated during the merger [32]. Other cases are those of MACS J0025.4-1222 [33], MACS J0717.5+3745 [34] and Abell 520 [35].

1.1.4 Cosmic Microwave Background and ΛCDM

The most precise determination of the abundance of dark matter in the Universe is obtained through measurements of the cosmic microwave background (CMB). This radiation is the left over heat from the Big Bang itself. The early Universe was in a hot and dense state which cooled and became transparent to photons at around 380,000 years after the Big Bang. At this time—known as the "time of last scattering"—the temperature of the Universe was about 3000 K and has since decreased due to the cosmological expansion. Results from the COBE satellite in the early '90s showed that the CMB is a nearly isotropic radiation field with a thermal black body spectrum at a temperature of 2.73 K [36]. Precision measurements by WMAP [37] and most recently by the Planck satellite [38] show the existance of temperature anisotropies in the CMB. As seen in the all-sky map of figure 1.3, the CMB fluctuations are extremely faint, only one part in 100,000 compared to the 2.73 K average temperature of the radiation field. These ripples are believed to be the product of quantum fluctuations in the surface of last scattering that gave way to the large scale structure of the Universe as seen today.

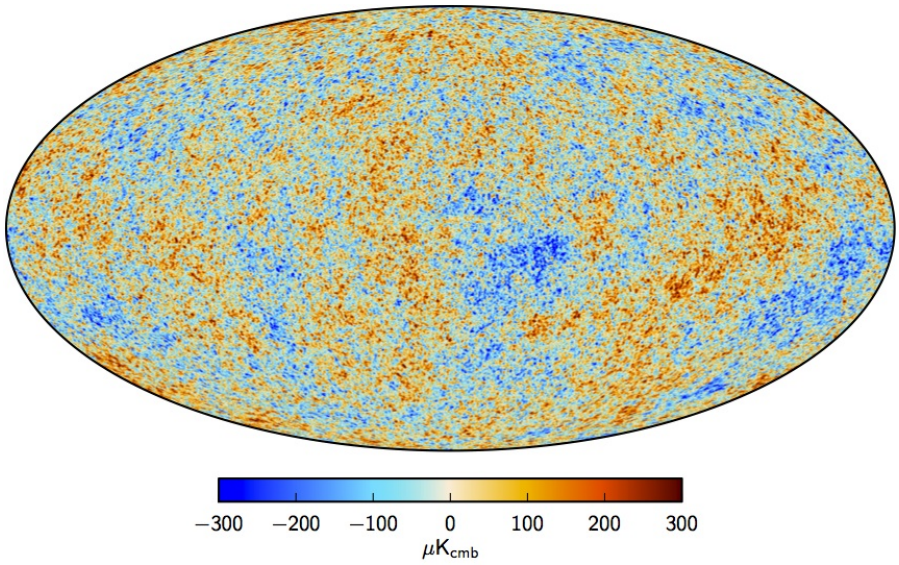

Figure 1.3: All-sky map of the CMB temperature anisotropies derived from the joint analysis of *Planck*, WMAP and 408 MHz observations. The inhomogeneities result from the expansion of quantum fluctuations in the early Universe. Image from Planck Collaboration I [38].

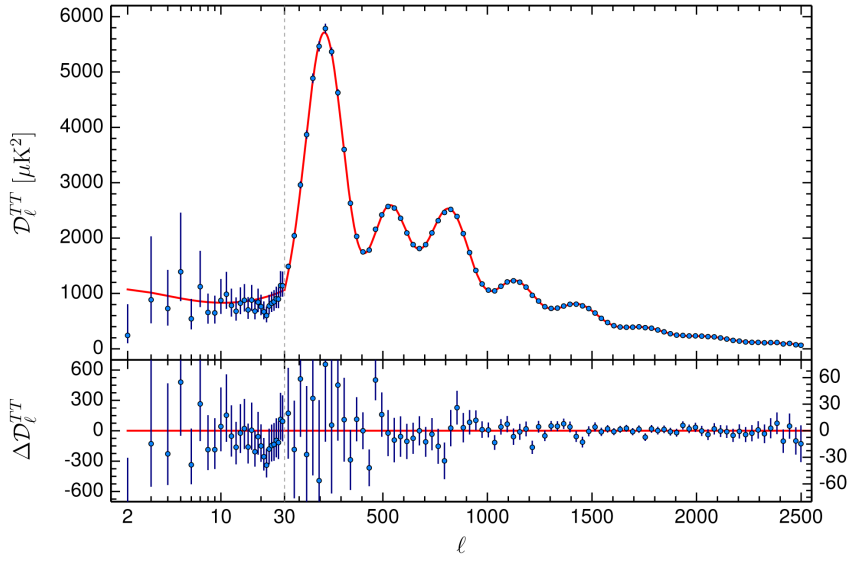

Figure 1.4: The *Planck* 2015 temperature power spectrum as a function of the multipole moment l. The first peak indicates primarily the density of baryonic (normal) matter, while the third peak relates mostly to the density of dark matter. The best-fit ΛCDM theoretical model (red curve) accurately describes the data. From these results, the content of the Universe is estimated to be 4.9 % baryonic matter, 26.5 % dark matter and 68.6 % dark energy. From Planck Collaboration XIII [39].

Cosmological information can be obtained from the CMB power spectrum—a plot of the temperature fluctuations as a function of the angular degrees in the sky. Figure 1.4 shows the 2015 Planck spectrum in terms of the multipole moment (l), related to the inverse of the angular scale. The position of the first peak, for example, is related to the curvature of the Universe and indicates that it is almost flat. The ratio between the heights of the first and subsequent peaks indicates how much matter in the Universe is baryonic and how much is dark. The latest estimates show that the density of baryonic matter (Ω_b) is 0.049, the density of dark matter (Ω_{DM}) is 0.265 and the density of dark energy (Ω_Λ) is 0.686 [39]. Dark energy and the cosmological constant Λ explain the current observations of an accelerated expansion of the Universe [40]. Without dark energy, a flat universe would expand forever, but at a continually decelerating rate—asymptotically approaching to zero.

The current standard model of cosmology, known as ΛCDM, is based on a spatially flat, expanding Universe dominated by cold (non-relativistic) dark matter and a cosmological constant. This model, based on six parameters (including the baryon density, dark matter density and the age of the Universe), fits the observational data with high accuracy, as seen in figure 1.4.

Several N-body simulations have been carried out to reproduce the formation of the current large scale structure of the Universe from the initial CMB anisotropies [41] [42]. The results require the inclusion of cold dark matter in order for the simulations to agree with the measurements from modern galactic surveys [43].

1.2 The Search for Dark Matter

The case for the existence of dark matter is undeniable. The question now is: what exactly *is* dark matter?

A first explanation for the observations detailed in section 1.1 could be a modification of the laws of gravitation—or what is known as Modified Newtonian Dynamics (MOND) [44]. While such models can successfully describe the galactic rotation curves, MOND cannot account for the large scale structure of the Cosmos or explain the details of the CMB, failing also to respect fundamental conservation laws [45]. Some of these problems are solved with the relativistic generalization of Tensor-Vector-Scalar gravity (TeVeS) [46]. While also being able to account for gravitational lensing, TeVeS fails to accommodate it simultaneously with galactic dynamics [47]. In addition, as mentioned earlier, the matter distributions resulting from the collisions of galaxy clusters are incompatible with any current theories of modified gravity.

The more straight-forward candidates have also been considered: black holes, neutron stars, brown dwarfs and other massive bodies composed of normal baryonic matter that emit little or no radiation. They are categorized as Massive Astrophysical Compact Halo Objects (MACHOs). However, searches for such

objects in the Milky Way—via gravitational microlensing—have ruled out the possibility of MACHOs accounting for the totality of dark matter in the Galaxy with a 95 % confidence level [48]. In addition, theoretical work on Big Bang nucleosynthesis shows that not enough baryons could have been produced in the early Universe to account for dark matter and still be consistent with the observed elemental abundances [49].

The most common hypothesis to date is that dark matter is composed of some type of neutral elementary particles. Of the known particles in the Standard Model, only the neutrino could be a possibility. However, due to their relativistic speeds in the early Universe (hence denoted as "hot dark matter"), neutrinos alone could not account for the totality of dark matter since the Universe would not have evolved into the large scale structures observed today [50]. The remaining possibility is that dark matter is composed of a yet undiscovered elementary particle—or several—not included in the Standard Model. The search for such a candidate is an on-going challenge in the frontier of physics [51] and constitutes the motivation for the experiments detailed in this work.

1.2.1 WIMPs and Other Candidates

The dark matter particle, as other particles in the early Universe, would have been in a constant state of creation and annihilation, i.e. thermal equilibrium, within the primordial plasma. As the Universe expanded and cooled, particles of a certain species ceased to be created as the temperature fell below their production energy. During expansion, the annihilation rate of a given particle is also suppressed as the interaction cross-section with its corresponding antiparticle drops to zero. At this point, the relic abundance of the particle in question is fixed. This process is known as *freeze-out*. The relic density for a particle χ after freeze-out is given by [52]:

$$\Omega_\chi h^2 \approx \frac{3 \times 10^{-27} \mathrm{cm}^3 \mathrm{s}^{-1}}{\langle \sigma v \rangle}, \tag{1.3}$$

where $\langle \sigma v \rangle$ is the thermally-averaged total annihilation cross section multiplied by the relative particle velocity. In the case of dark matter, in order for Ω_{DM} to be around the value observed today, its interaction cross-section must be in the order of the electroweak scale. Such a dark matter particle is thus given the name Weakly Interacting Massive Particle (WIMP). Its mass, which should be large in order to account for its gravitational effect, is hypothesized to be between 1 GeV and several TeV [53].

Further theoretical aspects support the candidacy of WIMPs. Supersymmetry (SUSY) is an extension of the Standard Model motivated independently from dark matter. It aims at unifying the electromagnetic, weak and strong fundamental forces at high energies. SUSY also manages to solve the so-called *hierarchy problem*, which is the question of why the observed discrepancy between the electroweak scale and the Planck scale is so large, in the order of 10^{16}.

The lightest supersymmetric particle, called the *neutralino*, is a stable particle in the Minimal Supersymmetric Standard Model (MSSM). The theory predicts that neutralinos would tend to have masses at the weak scale (100 GeV - 1 TeV) and couple to other particles with strengths characteristic of the weak force [54]. It is rather "miraculous" that its interactions and mass scale are consistent with the estimations from thermal relic abundance calculations for dark matter. This is the so-called "WIMP miracle", by which two independent aspects of physics beyond the Standard Model produce the same candidate for dark matter in the form of a WIMP.

What makes the WIMP hypothesis so attractive is that the detection of such particles is within the reach of high-energy colliders and other experiments attempting to directly detect dark matter [17]. This will be discussed in the following section.

There are other popular non-WIMP candidates. Superheavy particles with masses of $(10^{12} - 10^{16})$ GeV could have been produced non-thermally in the Universe and be a source of dark matter [55]. These so-called "WIMPzillas" could also be responsible for observed ultra high-energy cosmic rays [56]. Another candidate, the axion, arises as a solution to another long-standing problem in physics. The question of why quantum chromodynamics (QCD) does not seem to break the CP–symmetry is known as the "strong CP problem". According to QCD, the CP–symmetry could be violated in strong interactions. However, there is no experimental evidence of this to occur. Postulated as a pseudo-Nambu-Goldstone boson within the Peccei-Quinn theory to solve the strong CP problem [57], the axion—in case of existing—could also be the dark matter particle [58]. Although these are well-motivated candidates, the following work will mainly focus on the search for dark matter in the form of WIMPs.

1.2.2 Methods for WIMP Detection

If dark matter is to be detected, it must be through its interaction with ordinary matter. There are three main processes by which this may be achieved: its production at particle colliders, its indirect detection through self-annihilation products and its direct detection from scattering with ordinary particles. These different channels are depicted in figure 1.5.

The creation of dark matter could be achieved in a laboratory setting with high-energy particle accellerators. Experiments such as CMS and ATLAS, at the Large Hadron Collider (LHC), have been studying the creation of particles in proton-proton collisions at center-of-mass energies of 7 TeV and, since 2015, at 13 TeV. If dark matter particles were to be produced, their signature in a measured event would be that of missing energy. Thus, studies at the LHC focus on identifying events with energetic jets and an unbalanced transferred momentum. As of yet, no dark matter production has been confirmed at 13 TeV, since the current results are consistent with expectations from Standard Model physics [59] [60].

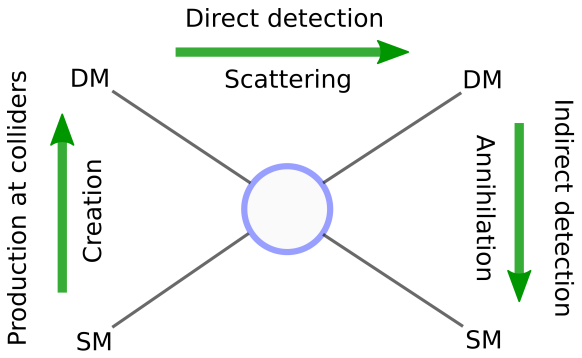

Figure 1.5: Dark matter detection channels involving the interaction between dark matter particles (DM) and Standard Model particles (SM).

Indirect detection of dark matter is attempted by searching for the products of its self-annihilation and decay. If WIMPs are Majorana particles (i.e. their own antiparticle) they could annihilate to produce gamma rays or Standard Model particle-antiparticle pairs. In addition, if WIMPs are unstable, they could also decay into Standard Model particles. Given their gravitational interaction, WIMPs can accumulate in large quantities within and around massive astrophysical objects. Due to their increased density in places like the Sun and the galactic center of the Milky Way, several experiments search for WIMP signatures from these sources [61].

Direct detection, in turn, is concerned with the identification of recoils in ordinary matter caused by the scattering of dark matter particles off a target material. This search mode is the basis of experiments like XENON100 and XENON1T. Given the low scattering cross-section of dark matter, the probability of multiple interactions within a detector is negligible. Because of this, its expected signature is a recoil spectrum of single scattering events, which in the case of a WIMP would consist of nuclear recoils [62]. The differential recoil spectrum can be written as follows [63]:

$$\frac{dR}{dE}(E,t) = \frac{\rho_0}{m_\chi \cdot m_A} \cdot \int v \cdot f(\mathbf{v},t) \cdot \frac{d\sigma}{dE}(E,v)\, \mathrm{d}^3 v, \tag{1.4}$$

where m_χ is the WIMP mass and $\frac{d\sigma}{dE}(E,v)$ is its differential scattering cross-section on nuclei. These are the two observables of a dark matter experiment. The mass of the target nucleus, a parameter of the detector, is m_A. The first of the astrophysical parameters, required to interpret the detection results, is the local dark matter density ρ_0. Different profile models of the Milky Way dark matter halo give results for ρ_0 in the range $(0.2 - 0.6)\,\mathrm{GeV/cm}^3$ [18] [19]. The current value used as a benchmark for direct searches by XENON100 is $\rho_0 = 0.3\,\mathrm{GeV/cm}^3$[64]. The second astrophysical parameter is the WIMP velocity distribution $f(\mathbf{v},t)$. An isotropic Maxwell-Boltzmann distribution is normally used for the dark matter velocity profile:

$$f(\mathbf{v}) = \frac{1}{\sqrt{2\pi\sigma}} \cdot \exp\left(-\frac{|\mathbf{v}|^2}{2\sigma^2}\right), \tag{1.5}$$

which is truncated at the escape velocity, $v_{esc} \approx 544$ km/s [21]. The dispersion velocity σ is a function of the circular velocity via $\sigma = \sqrt{3/2}\, v_c$. The average value for v_c in the Milky Way is around 220 km/s [20].

Additional particle and nuclear physics assumptions are required to interpret detection results. WIMP interactions can be either spin independent or spin dependent. The first case involves scalar interactions which make no distinction between neutrons and protons in the target nucleus. In the second case, only nuclei with a total non-zero spin are sensitive to WIMP interactions, meaning nuclei with an odd number of protons or neutrons. The differential WIMP-nucleus cross-section, $d\sigma/dE$ in equation 1.10, will depend on the case. In general, it can be written as:

$$\frac{d\sigma}{dE} = \frac{m_A}{2\mu_A^2 v^2}\sigma_0 F^2 \tag{1.6}$$

where μ_A is the WIMP-nucleus reduced mass, A is the number of target nucleons and F is a correction form-factor that accounts for a decrease in the scattering cross-section with increasing momentum transfer. The cross-section at zero transfered momentum corresponds to σ_0, which in the spin-independent case (SI) is given by:

$$\sigma_0^{\mathrm{SI}} = \frac{4\mu_A^2}{\pi} \cdot [Z \cdot f_p + (A - Z) \cdot f_n]^2 \approx \frac{4\mu_A^2}{\pi} A^2 f_p^2 \tag{1.7}$$

where $f_{p,n}$ are the contributions of protons and neutrons to the total coupling strength, approximated to be equal. Because the exact value of f_p is model dependent, the cross-section is usually normalized to the cross-section of a WIMP with a single proton $\sigma_p^{\mathrm{SI}} = \frac{4\mu_p^2}{\pi} f_p^2$, so:

$$\sigma_0^{\mathrm{SI}} \approx \frac{\mu_A^2}{\mu_p^2} A^2 \sigma_p^{\mathrm{SI}}, \tag{1.8}$$

where μ_p is the WIMP-nucleon reduced mass.

For spin-dependent (SD) interactions, the cross-section at zero transfered momentum is given by:

$$\sigma_0^{\mathrm{SD}} = \frac{32}{\pi}\mu_A^2 \cdot G_F^2 \cdot [a_p \cdot \langle S_p \rangle + a_n \cdot \langle S_n \rangle]^2 \cdot \frac{J+1}{J}, \tag{1.9}$$

where G_F^2 is the Fermi coupling constant, J is the total nuclear spin, $a_{p,n}$ is the effective proton (neutron) coupling, and $\langle S_{p,n} \rangle$ is the expectation value of the nuclear spin due to the proton (neutron) content. The form factor F in equation 1.6 for spin-dependent interactions is written in terms of the spin structure function and is highly dependent on the nuclear shell model [65].

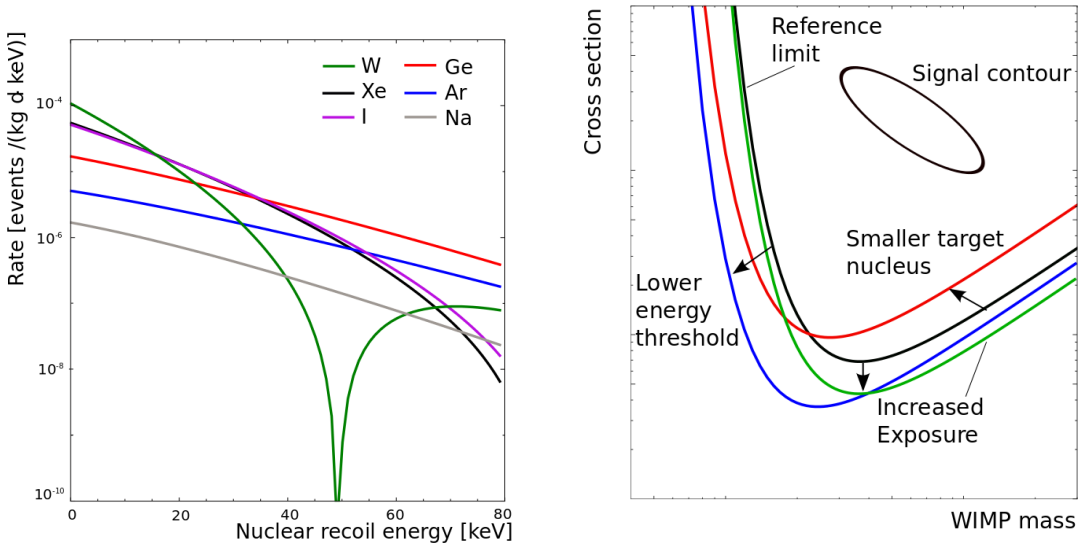

Figure 1.6: (Left) Differential event rate for interactions of a 100 GeV WIMP with a cross-section of 10^{-45}cm^2 in different target materials with decreasing mass number: tungsten (green), xenon (black), iodine (magenta), germanium (red), argon (blue) and sodium (grey). (Right) Sample cross-section limits for direct detection as a function of WIMP mass. The black curve indicates a reference limit, with the colored curves illustrating variations in the exclusion limit due to changes in the detector parameters. The closed contour indicates a possible detection at a certain confidence level. Figures taken from [67].

Returning to the spin-independent case, the combination of equations 1.8, 1.6 and 1.4 results in the following expression for the differential rate for spin-independent interactions:

$$\frac{dR}{dE}(E,t) = \frac{\rho_0}{m_\chi \cdot 2\mu_p^2} \cdot \sigma_p^{\text{SI}} \cdot A^2 \cdot F^2 \int_{v_{min}}^{v_{esc}} \frac{f(\mathbf{v},t)}{v}\, \mathrm{d}^3 v. \tag{1.10}$$

The form-factor F is commonly described through the Helm parameterization [66], given as:

$$F(q\,r_A) = 3\frac{j_1(q\,r_A)}{q\,r_A} e^{-(qs)^2/2}, \tag{1.11}$$

where q is the transfered momentum, r_A is the nuclear radius, $s \approx 1\,\text{fm}$, and $j_1(q\,r_A)$ is the first spherical Bessel function.

The effects of A and F on the event rate measured by a detector are illustrated in figure 1.6 (left). Heavier target elements show an increased rate at lower deposited energies, while the coherence loss caused by the form-factor decreases the rate at higher recoil energies.

Figure 1.6 (right) shows an example of direct detection limits in the form of an interaction cross-section as a function of WIMP mass. The shape of the limit is defined by the astrophysical parameters and the properties of the detector. The sensitivity towards low WIMP masses is dependent on the energy threshold of the detector. The position of the minimum value in the exclusion curve depends on the target nucleus and its scattering kinematics. As the event rate is proportional to A^2, a larger value of A increases the overall sensitivity. For large WIMP masses, the event rate is suppressed as a function of $1/m_\chi$. This follows from the fact that the local dark matter density is constant, so heavier particles imply a lower amount available for scattering in the detector. In addition, an increased exposure of the experiment will lower the overall exclusion limit. This may be achieved by a longer measurement time or a larger detector volume. See [67] for further details and an in-depth discussion.

In addition to measuring the energy dependence of WIMP interactions, another possible signature of dark matter is its "annual modulation". Since the Earth rotates around the Sun, which in turn moves along with the Galaxy, the speed of the Earth changes relative to the dark matter halo of the Milky Way on an annual basis. Because of this, the relative velocity of dark matter particles in the halo would be largest in June and lowest in December, with respect to the detectors on Earth [68]. As a consequence, the amount of nuclear recoils above the detection threshold is expected to modulate accordingly. This relative motion of WIMPs can also be exploited by measuring the direction of the nuclear recoils they generate. A detector able to determine the direction of WIMP interactions can better discriminate the signal from other backgrounds and enhance a potential discovery [69].

1.2.3 Direct Detection Experiments

Direct dark matter detectors implement different techniques for measuring the interaction of particles. The elastic scattering of WIMPs with masses between 10 GeV and 1 TeV is expected to produce an energy deposition through nuclear recoils in the order of $(1-100)$ keV [63]. This energy transfer can result in three different types of signals, which can be measured according to the technology used. Figure 1.7 illustrates the different outcomes of a WIMP interaction and lists some of the detectors designed to measure each type of signal, or a combination of signals.

The first signature of a possible WIMP interaction is the production of heat. This effect is measured as *phonons* in cryogenic bolometers or superheated fluids. Example detectors are the COUPP bubble chamber [70] and the PICASSO superheated droplet detector [71]. The merger of both groups resulted in the PICO collaboration, which operates the PICO-60 and PICO-2L bubble chambers [72] [73]. Discrimination of the electromagnetic background in these detectors is achieved by tuning their operational thermodynamic parameters, while alpha decays are rejected according to their acoustic signature [74].

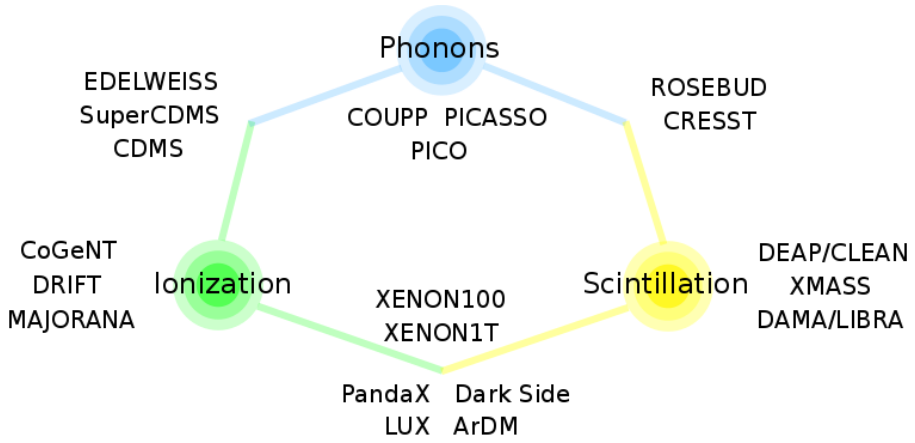

Figure 1.7: Measurable signals from particle interactions in different direct dark matter experiments. The XENON100 and XENON1T detectors measure both scintillation and ionization signals.

The second type of signal is scintillation light. A WIMP interaction may excite a target atom, which consequently forms an excited molecular state—or excimer. Upon de-excitation, photons are emitted as the components of the excimer dissociate and return to the ground state. Scintillating crystals and noble gases are used as detector materials. Examples of experiments in this group include the XMASS [75] and DEAP [76] detectors. These single phase detectors employ liquid xenon and liquid argon, respectively, with particle discrimination being achieved through pulse shape analysis. Another example is the DAMA experiment, which uses ultra low-radioactive NaI(Tl) crystals [77]. The combined data of DAMA and its successor DAMA/LIBRA show an annually-modulated signal rate consistent with the expected phase of dark matter interactions. The significance of the signal is of $9.3\,\sigma$ over 14 annual cycles [78] [251]. Since other experiments contradict the DAMA results, explanations other than dark matter are under consideration [79]. Several collaborations are aiming to test the DAMA results by employing similar high-purity NaI(Tl) crystals, such as SABRE [80], ANAIS [81] and KIMS [82].

The third possibility is to measure the charge resulting from ionization. In germanium detectors, the electrons stripped from ionized atoms are measured as a signal of a particle interaction. The CoGeNT experiment is an example using p-type point contact germanium detectors [83]. In 2014, the CoGeNT collaboration reported an annual modulation signal matching the expected WIMP phase at a $2.2\,\sigma$ level [84]. However, the amplitude of the signal is 4 to 7 times larger than expected and independent analyses of the released data have not found a significant signal when using different background models [85] [86].

Some experiments combine two of the three possible signals for the detection of dark matter. Cryogenic bolometers can achieve an excellent energy resolution

and a very low energy threshold by measuring the phonon signal in a crystal. When combined with the scintillation or ionization signals, discrimination between nuclear and electronic recoils can be achieved given the dependence of signal quenching with energy. The CRESST-II detector, for example, measures both the phonon signal and scintillation light emitted in $CaWO_4$ crystals. For WIMP masses above a few GeV, CRESST-II does not have a competitive sensitivity, due to its large number of background events. But it is in the sub-GeV region where the detector excels, being capable of exploring WIMP masses down to 0.5 GeV [87].

The CDMS and CDMS II experiments are cryogenic bolometers of germanium and silicon that combine the phonon and ionization charge signals to perform particle discrimination [88] [89]. An annual modulation study with data from October 2006 to September 2008 has been performed by CDMS II, showing no evidence for an event rate modulation [90]. This result directly contradicts the modulation claim by CoGeNT, since both use germanium detectors. The succeeding SuperCDMS and CDMSlite detectors have set the most sensitive exclusion limits at low WIMP masses to date [91] [92]. Focusing on the range below 30 GeV, the SuperCDMS results of 2014 determined an exclusion cross-section of $1.2 \times 10^{-42}\,\mathrm{cm}^2$ at an 8 GeV WIMP mass.

Finally, some detectors combine the scintillation and ionization signals in their search for dark matter. This is performed with time projection chambers (TPCs) operating with noble gases—such as argon and xenon—in both the gaseous and liquid phases [93]. The ratio between the prompt scintillation signal in the liquid and the delayed signal from the extracted ionization charge in the gas phase allows to discriminate between electronic and nuclear recoils. The XENON100 detector is a two-phase TPC implementing liquid xenon as the target material. In 2012, XENON100 published the lowest limits at the time for the cross-section of spin-independent WIMP-nucleon interactions: $2 \times 10^{-45}\,\mathrm{cm}^2$ at a 55 GeV WIMP mass [94]. The LUX experiment, employing the same detection principle, revealed in 2013 an even lower limit of $7.6 \times 10^{-46}\,\mathrm{cm}^2$ [95]. In 2016, several experiments released updated results. XENON100 performed a combined analysis of its three science runs—a total of 477 live days—for a minimum cross-section of $1.1 \times 10^{-45}\,\mathrm{cm}^2$ at 50 GeV and 90 % confidence level [96]. The PandaX experiment set its best upper limit at $2.5 \times 10^{-46}\,\mathrm{cm}^2$ at 40 GeV [97]. Meanwhile, the latest LUX results show a minimum of the scattering cross-section at $2.2 \times 10^{-46}\,\mathrm{cm}^2$ for a 50 GeV WIMP, which further reduces to $1.1 \times 10^{-46}\,\mathrm{cm}^2$ when combining the full LUX exposure [98]. Other detectors in this category of two-phase noble liquid detectors include DarkSide [99] [100] and ArDM [101].

Figure 1.8 shows an overview of the signal claims and exclusion limits for spin-independent WIMP-nucleon interactions set by various direct detection experiments.

XENON1T is the successor of XENON100 and aims to further improve the sensitivity for dark matter detection. Its construction has been finalized and, as

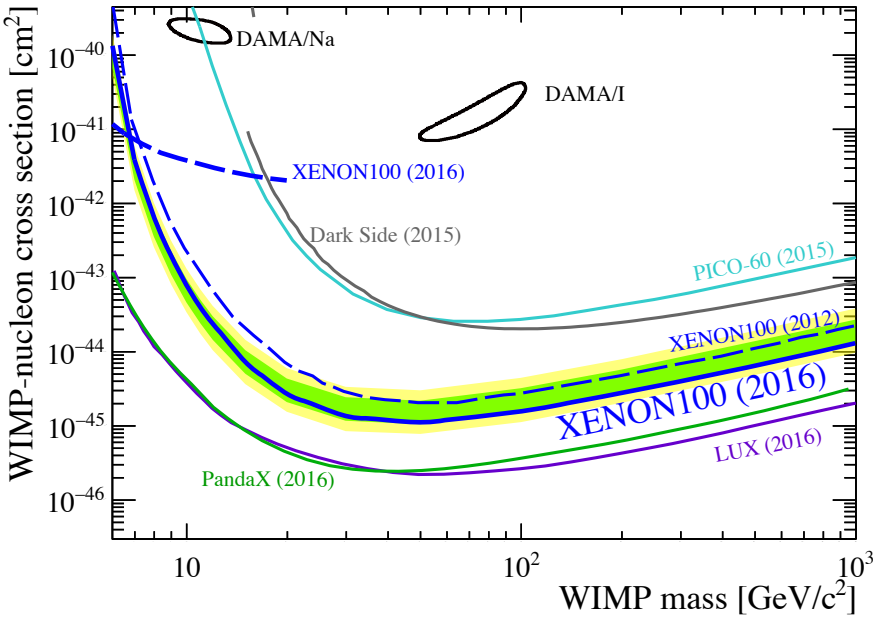

Figure 1.8: Exclusion limits and signal claims from various direct detection experiments for spin-independent WIMP-nucleon interactions. The result from the combined analysis of the three XENON100 science runs is shown by the blue limit (solid curve) and the $1\,\sigma$ (green band) and $2\,\sigma$ (yellow band) expected sensitivity regions at 90 % CL. A comparison is made with other experimental limits at 90 % CL, as well as detection claims of $2\,\sigma$. Figure from [96].

of 2016, the first results with the operational detector are underway. The goal of XENON1T is to provide the most sensitive measurement yet for WIMP interactions. After a 2 year measurement in a 1 ton fiducial volume, it is expected to reach a minimum cross-section of $1.6 \times 10^{-47}\,\mathrm{cm}^2$ at a 50 GeV WIMP mass [102]. XENON1T has been designed in such a way that an upgrade can be made towards a larger detector, known as XENONnT. The LUX collaboration, in turn, has joined with the ZEPLIN group to build yet another multi-ton detector named LZ [103]. Finally, DARWIN (DARk matter WImp search with liquid xenoN) is the most ambitious proposal yet on the road towards the ultimate dark matter detector [104].

Chapter 2

The XENON Detectors

The XENON collaboration has been constructing and operating dark matter detectors for over a decade. These experiments have been installed in the Laboratori Nazionali del Gran Sasso (LNGS), in Italy. Under the mountains of the Gran Sasso range, the LNGS laboratories provide an excellent location for rare event searches, such as dark matter and neutrinoless double beta decay.

The recently constructed XENON1T detector is the latest in a series of dual-phase TPCs using liquid xenon as detection medium, leading the way towards the next generation of multi-ton scale detectors. The first in the series was XENON10, installed at LNGS in 2006. The TPC contained 15 kg of LXe in a cylindrical volume of 20 cm diameter and 15 cm height. In 2008, XENON10 published its limits for dark matter detection with a WIMP-nucleus spin independent cross-section of $4.5 \times 10^{-44}\,\mathrm{cm}^2$ for a 30 GeV WIMP mass [105]. The next step was XENON100, with 65 kg of LXe in a TPC of 30 cm diameter and 30 cm height. Replacing XENON10 underground in 2008, XENON100 has continued to operate until 2016. Its 2012 spin independent cross section of $2 \times 10^{-45}\,\mathrm{cm}^2$ at a 55 GeV WIMP mass set the most stringent limit for dark matter interactions at the time [94]. Starting operations in 2016, XENON1T has gone one step further with 2 tons of LXe in a 1 m length TPC. It is expected to reach a minimum cross-section of $1.6 \times 10^{-47}\,\mathrm{cm}^2$ at a 50 GeV WIMP mass [102].

This chapter will describe the principles of dark matter detection with dual-phase time projection chambers using liquid xenon. The focus will be on the XENON100 and XENON1T detectors, setting the fundamentals for the topics in the chapters ahead.

2.1 Liquid Xenon as Detection Medium

As seen in section 1.2.3, liquid noble-gas detectors are in the forefront of spin-independent dark matter searches. Liquid argon (LAr) and liquid xenon (LXe) are the principal media in use, while some R&D is underway for the implementation of liquid neon [106]. Such detectors present a major advantage over other

technologies, that of *scalability*. The technical challenges of scaling a liquid tank by a certain factor are minimal compared to growing a scintillating crystal by the same amount, for example. There are two main advantages of scaling up a detector: First, that the expected WIMP interaction rate increases linearly with the target mass, reducing the run time required to achieve a certain sensitivity. Second, that a larger mass provides more shielding against external radiation, reducing the background rate in the effective detection volume. LXe is particularly efficient in both cases, given its high density of $3\,\mathrm{g/cm^3}$.

Both LAr and LXe produce scintillation in the ultraviolet regime—at wavelengths of 128 nm and 178 nm, respectively. Such scintillation photons can be detected directly if the photosensors used are equipped with windows transparent to such wavelengths. Since most window materials are only transparent to photons above 150 nm (except in the case of MgF_2 crystals), detectors using LAr often make use of wavelength shifters that re-emit the light at higher wavelengths, around 400 nm.

Since nearly half of the naturally occurring isotopes of Xe carry spin, LXe detectors profit from additional sensitivity to spin-dependent interactions [107]. Another advantage of Xe is that it has essentially no intrinsic radioactivity, which makes it ideal for rare event searches. It is the second element with most stable isotopes and has no long-lived radioisotopes, besides ^{136}Xe, which undergoes double beta decay with a half life of 2.17×10^{21} y [108]. The second longest-lived radioisotope is ^{127}Xe with a half-life of 36.3 days. Xenon is also the heaviest of the noble gases before the radioactive Rn. With a mass number $A = 131.29$, it presents an excellent target for spin-independent interactions, whose rate scales with A^2 (see equation 1.10). Given its large atomic number ($Z = 54$), LXe is also a good γ-ray absorber. This property is exploited in what is known as *self-shielding*, by which the outer regions of the LXe volume absorb much of the external γ radiation, leaving the inner volume with a highly reduced background.

Photons interact with matter through the processes of photoelectric absorption, Compton scattering and pair production. In LXe, photoelectric absorption is the dominant interaction below 300 keV, while Compton scattering dominates at higher energies [109]. The photon attenuation length in LXe at $2.86\,\mathrm{g/cm^3}$ density is $\sim$2 cm at 300 keV and $\sim$6 cm at 1 MeV. Thus, most of the external γ radiation will be stopped before reaching the central volume of a LXe detector, as mentioned before. The remaining electromagnetic background in the region of interest for dark matter searches will consist of low-energy single Compton scatters.

Neutrons will interact in LXe primarily through scattering with the Xe nuclei, producing nuclear recoils. At neutron energies below 100 keV, interactions consist mostly of elastic scattering, while inelastic scattering starts to play a role at MeV energies. The nuclear recoils from neutron elastic scattering constitute an undesirable background in dark matter searches since they are indistinguishable from a WIMP interaction. For this reason, precautions must be taken to reduce

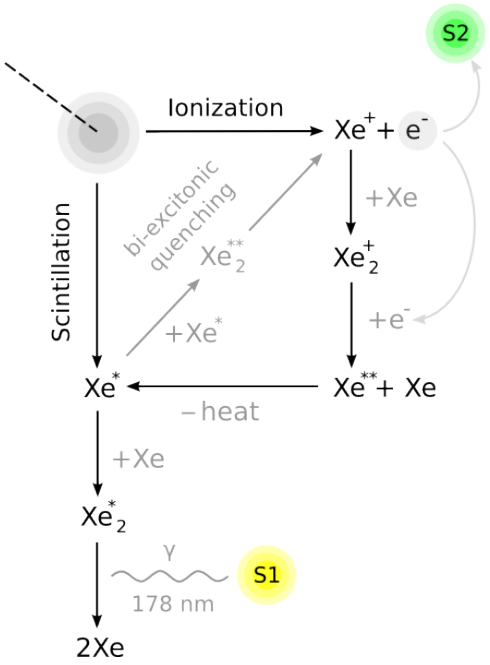

Figure 2.1: A particle interaction in LXe produces both excited and ionized xenon atoms, denoted by Xe^* and Xe^+, respectively. Both states can ultimately lead to the creation of excimers—Xe_2^*—whose de-excitation produces the scintillation signal S1. The free electrons from ionization can also be drifted through an electric field—avoiding their recombination—and extracted to subsequently produce the S2 signal by electroluminescence. Illustration based on the schematic in [110].

the neutron background as much as possible.

For a material to be an effective particle detector, it must be able to transform the absorbed energy into signals that can be measured. Xenon is also useful in that respect, since it produces both scintillation photons and ionization electrons in response to ionizing radiation. It is also transparent to its own scintillation light, which is of crucial importance.

2.1.1 Scintillation Signal (S1)

The scintillation process in LXe is illustrated in figure 2.1. A recoiling particle in LXe creates both excitons (excited atoms)—Xe^*, and electron-ion pairs—$Xe^+ + e^-$. Both cases subsequently give rise to excited molecular states, called excimers—Xe_2^*. In the first case, excimers are produced by the collision of excitons with neighboring Xe atoms: $Xe^* + Xe \rightarrow Xe_2^*$. In the second case, excimers arise from ionized atoms through a more elaborate process:

$$\begin{aligned} Xe^+ + Xe &\rightarrow Xe_2^+ \\ Xe_2^+ + e^- &\rightarrow Xe^{**} + Xe \\ Xe^{**} &\rightarrow Xe^* + \text{heat} \\ Xe^* + Xe &\rightarrow Xe_2^*. \end{aligned} \tag{2.1}$$

Once excimers have been created, these de-excite into the dissociative ground state, producing scintillation photons:

$$Xe_2^* \rightarrow 2Xe + h\nu. \tag{2.2}$$

The excimers have both a singlet and a triplet state, with de-excitation times of 2.2 ns and 27 ns, respectively [111]. The resulting photons have a wavelength of 178 nm, placing them in the vacuum-ultraviolet (VUV) range of the electromagnetic spectrum. The detection of these scintillation photons is known as the S1 signal.

Relative Scintillation Efficiency

The correlation between the number of measured scintillation photons and the actual energy deposited by an incident particle is not straight-forward. This is because energy can be lost through various processes. Electrons may escape or be extracted from the interaction region, reducing the amount available for exciton creation in equation 2.1. Bi-excitonic quenching can also occur, by which two excitons interact and produce an electron-ion pair, reducing by half the possible photon yield—$Xe^* + Xe^* \rightarrow Xe + Xe^+ + e^-$ [112]. In addition, impinging particles may lose energy through elastic collisions with the target atom. The energy is lost as heat, without any scintillation—a process known as Lindhard quenching [63].

The amount of energy lost in each of the quenching effects is dependent on the type of recoil—electronic or nuclear. The scintillation yield, defined as the number of photons produced per unit energy, is thus also dependent on the recoil type—as well as the interaction energy. In LXe detectors, the scintillation signal is commonly used as a measure of the particle energy. In order to have an equivalence between the electronic and nuclear light yields (L_y), the latter is converted in terms of the former through the *relative scintillation efficiency*—$\mathcal{L}_{eff}$. This quantity—which is itself a function of energy—is defined as the ratio between the scintillation yield for nuclear recoils and that of electronic recoils for the photo-absorption of γ-rays from a ^{57}Co source at zero electric field:

$$\mathcal{L}_{eff}(E_{nr}) = \frac{L_{y,nr}(E_{nr})}{L_{y,er}(E_{er} = 122\,\text{keV})}, \tag{2.3}$$

where the *er* and *nr* subscripts indicate electronic and nuclear recoils, respectively. The 122 keV γ-ray energy comes from the commonly used ^{57}Co calibration source. Different measurements of $\mathcal{L}_{eff}$ are presented in [113] [114] and references therein.

2.1.2 Ionization Signal (S2)

Complementary to the scintillation signal, a second signal can be obtained by means of the ionization electrons. The average energy required to produce an electron-ion pair in LXe is 15.6 eV—the largest ionization yield amongst all liquified noble gases. In order to measure the ionization signal, the recombination of electrons—seen in equation 2.1—must be prevented. This is achieved by applying an external electric field, which drifts the electrons to be extracted from the LXe volume.

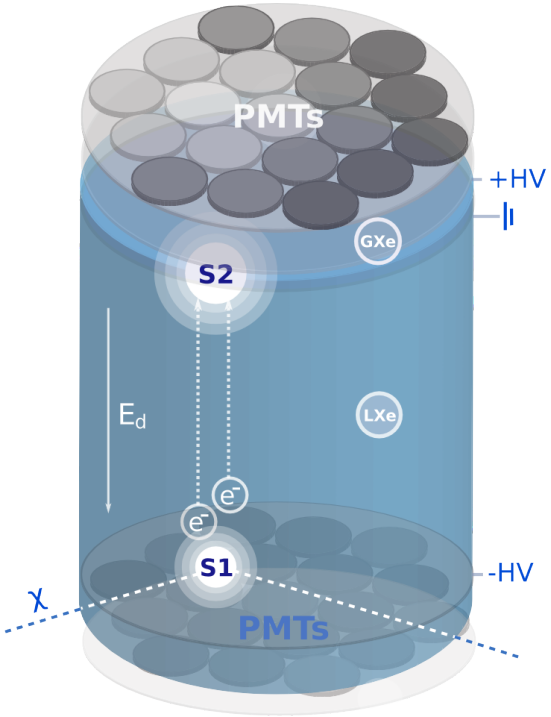

Figure 2.2: Operating principle of a dual-phase time projection chamber. A particle interaction in the LXe will produce both a prompt scintillation signal (S1) and free electrons from ionization. The electrons are drifted by an electric field (E_d) towards the GXe phase, where they are extracted by means of a second—stronger—electric field. Here, a proportional scintillation signal is produced by electroluminescence (S2). Photons from these signals are detected by PMT arrays located at both the top and the bottom of the TPC.

An important factor affecting the extraction of ionization electrons in LXe is the presence of electro-negative impurities—the most common of which is O_2. The electrons may attach to these impurities, reducing the measured output signal. The average time an electron remains free before attachment is known as the *electron lifetime*, which is maximized by purifying the LXe as best as possible.

In a dual-phase TPC, the ionization electrons are extracted from the liquid phase into a volume of gaseous xenon (GXe) by means of a strong electric field (in the order of 10 kV/cm). The extracted electrons acquire energies high enough to excite Xe atoms in their path. The subsequent de-excitation produces scintillation proportional to the extracted charge—an effect known as *electroluminescence*. The measurement of this proportional scintillation is known as the S2 signal.

2.2 The Detector Principle

The dual-phase time projection chamber (TPC) exploits both the prompt scintillation signal (S1) and the ionization signal in the form of proportional scintillation by electroluminescence (S2) for particle detection and discrimination. The photons from both signals are measured by photomultiplier tubes (PMTs) arranged in two separate arrays, located both at the top and at the bottom of the detector. Figure 2.2 illustrates the layout and operation principle of a dual-phase TPC. A particle—such as a WIMP—interacts with the LXe and produces scin-

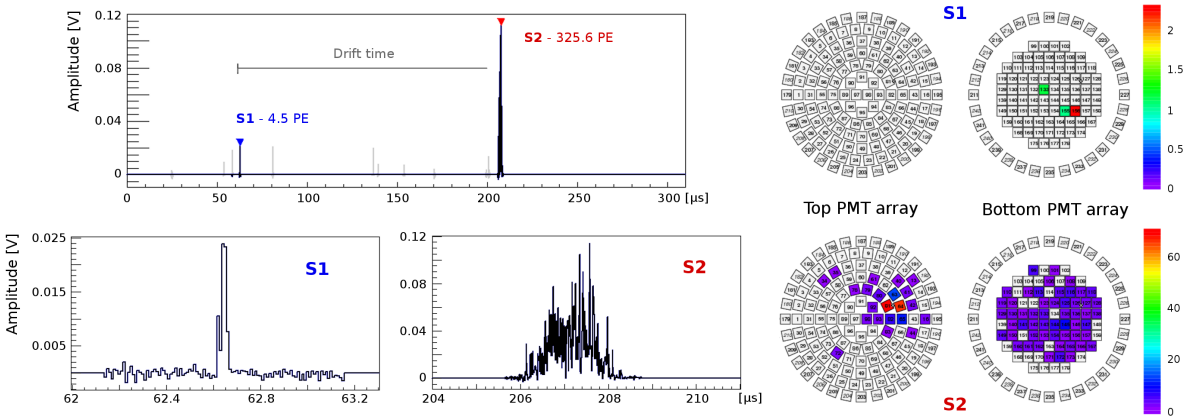

Figure 2.3: Example event in a dual-phase TPC (in this case, XENON100). The top panel shows the summed waveform from all PMTs in the TPC. The bottom left and right panels zoom into the S1 and S2 signals, respectively. The drift time between the two signals determines the z–coordinate of the interaction vertex. The hit patterns of the S1 and S2 signals, on both the top and bottom PMT arrays, are shown on the right side of the figure. The (x, y) position of the event is determined by the S2 pattern on the top array.

tillation and ionization. The prompt scintillation photons are collected mostly by the bottom PMT array, which is submerged in the LXe. This is due to the total reflection that occurs at the liquid-gas interface, which reduces the number of photons that enter the GXe volume, where the top PMT array is located. Meanwhile, the electrons produced by ionization are drifted by an electric field generated between the cathode mesh (−HV) and the gate grid (ground). The strength of the drift field is commonly around a few 100 V/cm. The electrons are then extracted into the gas phase by means of a stronger electric field, in the order of 10 kV/cm, between the gate grid and the anode mesh (+HV). The accelerated electrons subsequently emit photons via electroluminescence, which are measured by both PMT arrays.

The dual-phase TPC also allows to determine the vertex of a particle interaction. Figure 2.3 shows an example event as measured by XENON100. The time difference between the detected S1 and S2 signals, corresponding to the electron drift time, is used to determine the z–coordinate of the interaction. Meanwhile, the S2 hit pattern on the top PMT array is used to determine the (x, y) position. Combining this information gives a 3D reconstruction of the event vertex. This feature is very useful for two reasons: the first is that it allows to define a central fiducial volume that excludes events occurring in the outer part of the TPC, rejecting background radiation that is stopped by the LXe. The second is the possibility to identify single-scatter events. A WIMP—being a weakly interacting particle—is expected to produce only one recoil in the detector volume.

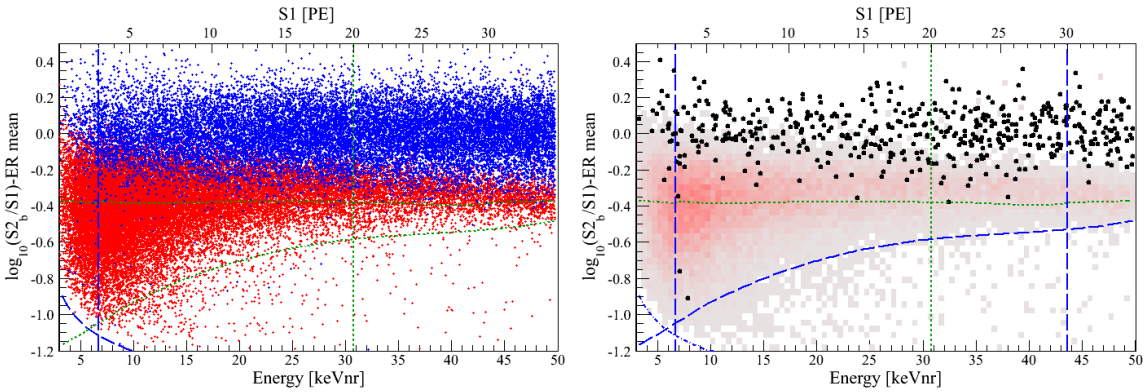

Figure 2.4: (Left) Distribution of electronic recoils (blue) and nuclear recoils (red) from XENON100 calibration data in the discrimination parameter space $\log_{10}(S2_b/S1)$. (Right) XENON100 results from 225 live days of dark matter search [94]. The benchmark WIMP search region is delimited on the y-axis by the 99.75 % ER rejection cut (horizontal green dotted line) and the border running along the 97 % NR quantile (inclined blue dashed curve). The delimiters on the x-axis indicate the lower analysis threshold of 6.6 keV_{nr} and the upper limit of 30.5 keV_{nr} (a range equivalent to 3 – 20 PE). Two events are found in the WIMP search region, where (1.0 ± 0.2) events are expected from background.

Hence, the discrimination of multi-scattering events further reduces the signal background.

As mentioned before, the S1 and S2 signals are complementary—to a larger S2 signal corresponds a smaller S1, and vice versa. Furthermore, the scintillation yield for electronic and nuclear recoils in LXe is different. Hence, the ratio between the two signals can be used as a discrimination tool for events measured in the detector. Electronic recoils (ER), produced by β and γ interactions, have a larger S2/S1 ratio than nuclear recoils (NR), generated by neutrons and WIMPS:

$$\left(\frac{\mathrm{S2}}{\mathrm{S1}}\right)_{ER} > \left(\frac{\mathrm{S2}}{\mathrm{S1}}\right)_{NR}$$

Figure 2.4 (left) shows the distribution of electronic and nuclear recoil events from XENON100 calibration data, represented in the discrimination parameter space $\log_{10}(S2_b/S1)$, where $S2_b$ corresponds to the signal in the bottom PMT array. While the ER events can be discriminated in this way, there is an unavoidable leakage of events into the NR space, where possible WIMP signals are expected to be located. Because of this, the ER background must be reduced as much as possible through detector shielding and material selection—a topic discussed in chapter 3.

The result of a dark matter search in XENON100 is exemplified in figure 2.4 (right). The plot shows the data from 225 live days published in July

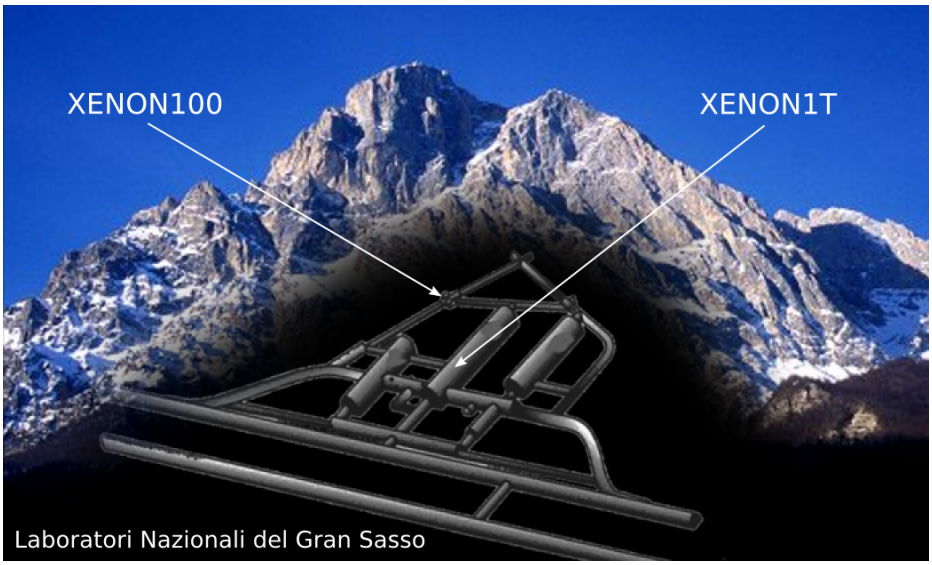

Figure 2.5: Location of the XENON100 and XENON1T dark matter experiments at the Laboratori Nazionali del Gran Sasso (LNGS). The underground facilities of the laboratory are situated below the Gran Sasso mountain in Italy, providing excellent low-background conditions for rare-event searches.

2012 [94]. After unblinding, two events were observed below the 99.75 % ER rejection line, corresponding to the benchmark WIMP search region. The number of events expected from background in the same area was 1.0 ± 0.2. The probability of the background fluctuating to 2 events in the benchmark region was 26.4 %, so no excess due to a possible dark matter signal was determined.

2.3 XENON100 and XENON1T

Both XENON100 and XENON1T are located at the INFN Laboratori Nazionali del Gran Sasso (LNGS) in Italy. The particle physics laboratory has extensive underground facilities beneath the Gran Sasso mountain where many low-background experiments operate. Figure 2.5 shows the locations of both XENON detectors in the underground laboratories.

XENON100 operated from 2008 until 2016, becoming a benchmark for following dual-phase TPC dark matter experiments. It has been succeeded by XENON1T, which was inaugurated in November 2015. During 2016, its multiple subsystems have been commissioned and first data has been obtained, allowing to assess the performance of the detector (see chapter 5).

The XENON100 detector consists of a cylindrical TPC with a height of 30.5 cm and a radius of 15.3 cm. The total amount of LXe in the experiment is 161 kg, with 62 kg contained in the inner TPC volume. The walls surrounding

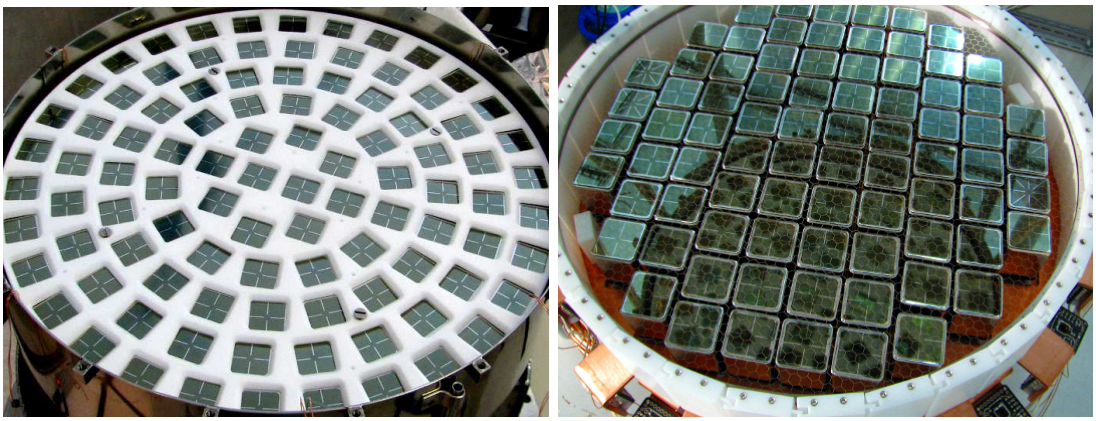

Figure 2.6: (Left) XENON100 top PMT array. The 98 Hamamatsu R8520-06-Al PMTs are arranged in concentric circles to improve the radial event position reconstruction. (Right) Bottom array with 80 PMTs arranged in a tight configuration to achieve a high light collection. Images from [116].

the TPC consist of 24 panels of 1/4 inch-thick polytetrafluorethylene (PTFE). This barrier separates the target volume from the surrounding LXe, which acts as an active veto shield. PTFE is chosen for both its insulating properties and its good reflectivity for VUV light [115].

The PMTs used in XENON100 are the Hamamatsu R8520-06-AL with 1-inch square windows. They have been selected for their low radioactivity and their capability to detect VUV photons. The top array consists of 98 PMTs located above the target volume in the gas phase. The array is arranged in concentric circles in order to improve the radial event position reconstruction—see figure 2.6 (left). The outermost ring extends beyond the TPC radius to improve the position reconstruction at the edges. The bottom PMT array—figure 2.6 (right)—is immersed in LXe and contains 80 PMTs arranged in such a way to provide an optimal area coverage for efficient S1 light collection (52 % overall and up to 61 % in the central area) [116]. The photoelectron collection efficiency from the photocathode to the first dynode of this PMT model is about 70 %, according to Hamamatsu.

Located 17 mm above the bottom PMT array, a cathode mesh is biased at a voltage of around −16 kV. A grounded screening mesh, placed 12 mm below the cathode, shields the PMTs from the high voltage. The cathode mesh, together with a grounded gate grid at the top of the TPC, produce an electric field of around 530 V/cm for drifting electrons. An anode mesh located 5 mm above the gate grid is biased at around 4.5 kV, producing a 12 kV/cm extraction field. Finally, a grounded screening mesh is placed between the anode and the top PMT array. A homogeneous electric field over the length of the TPC is obtained with 40 copper rings functioning as field-shaping electrodes. A cage structure is formed, generating the required field within the target volume.

Over the top PMT array, a stainless-steel diving bell is used to regulate the LXe level and keep it at a precise level just above the gate grid. Outside the bell, the liquid level can be increased arbitrarily, providing a full coverage of the TPC with a LXe veto.

The XENON1T detector is based on the successful design of XENON100, while improving over its predecessor in scale, materials and technology. The TPC is roughly 1 m in height and 1 m in diameter, containing 2 t of LXe out of the total 3.2 t in the full cryostat volume. The TPC is enclosed by 24 interlocking PTFE panels with a radius of 480 mm. The electric field in the TPC is generated by the same structure of cathode, gate grid and anode as in XENON100, along with screening meshes to protect the PMTs from the high voltages on the electrodes. A stack of 74 copper field-shaping rings surround the lateral PTFE panels and ensure the uniformity of the electric field. The design goal is to reach a drift field of ∼1 kV/cm and an extraction field in the order of 10 kV/cm [102].

The PMT of choice for XENON1T is the Hamamatsu R11410-21, with a circular window of 3 inches in diameter. It has been developed specifically for operation in LXe, with low-radioactivity materials and a high detection efficiency for VUV photons. The R11410-21 PMT—and its earlier iterations—are the focus topic of chapter 4, where all details on its characterization and performance are given.

The top PMT array is comprised of 127 units arranged in concentric rings for optimal radial position reconstruction. Meanwhile, the bottom array consists of 121 PMTs arranged in a compact hexagonal structure to maximize the light collection efficiency. While the bottom array fits completely within the TPC radius, the top array is ∼40 mm larger in order to increase the resolution of the position reconstruction at the edge of the TPC. Further details on the assembly and operation of the PMT arrays are given in chapter 5. As in XENON100, a diving bell covers the TPC on the top, allowing to adjust the level and uniformity of the LXe.

An important feature of the XENON1T detector is its enclosure in a water tank of ∼10 m height and diameter functioning as an active Cherenkov detector that allows to tag muons and muon-induced backgrounds. The tank is equipped with 8-inch PMTs and cladded by a reflective foil. The muon veto provides a high detection efficiency for muons ($> 99.5\%$) and showers of secondary particles from muon interactions in the rock ($> 70\%$). The background from muon-induced neutrons in XENON1T will thus be negligible [117].

A comparison between the XENON100 and XENON1T detectors is shown in figure 2.7, presenting a summary of their main features and the upgrades achieved in XENON1T.

Figure 2.7: (Left) TPC of the XENON100 detector. (Right) TPC of the XENON1T detector. The table summarizes the features of both experiments for a direct comparison between the two.

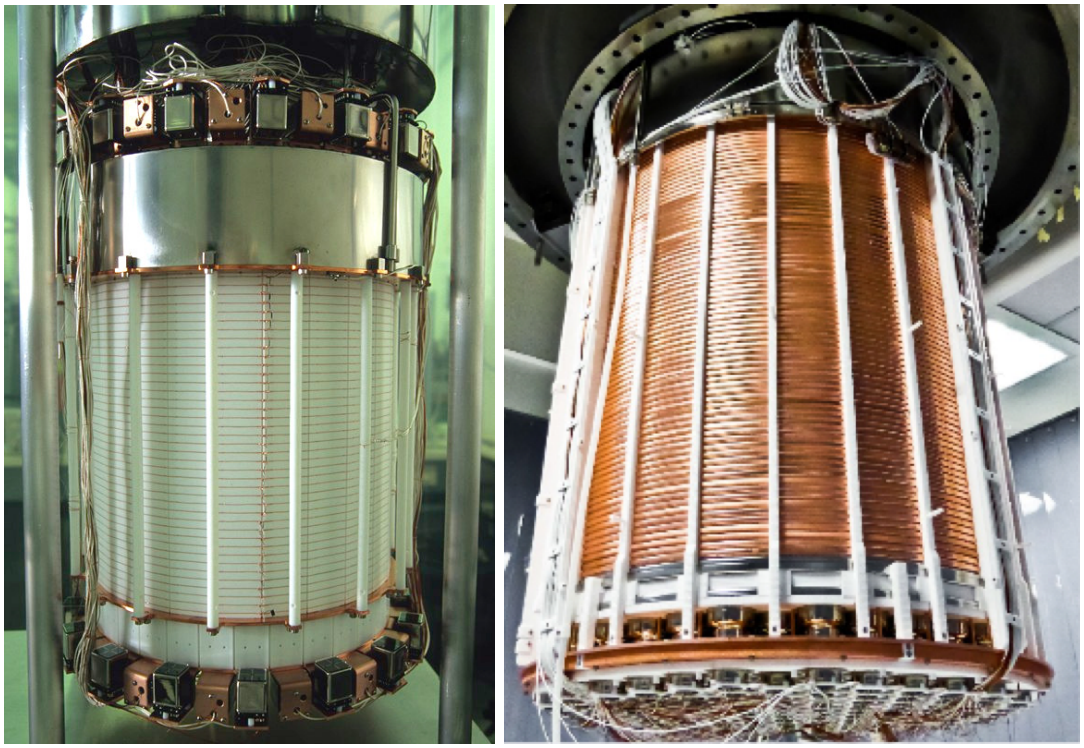

	XENON100	XENON1T
Years in operation	2007 – 2016	2016 —
TPC height [cm]	30.5	96.7
TPC diameter [cm]	30.6	96.0
Total LXe [kg]	161	3200
LXe in TPC [kg]	62	2000
Drift field [kV/cm]	0.53	∼1
Extraction field [kV/cm]	12	∼10
PMT model	R8520-06-AL	R11410-21
PMT window	Square, 1-inch	Circular, 3-inch
PMTs in top array	98	127
PMTs in bottom array	80	121
Sensitivity* [cm^2]	1.1×10^{-45} **	1.6×10^{-47} ***

* Spin-independent WIMP-nucleon cross-section
** 50 GeV WIMP—combination of 477 live-days [96], 2016
*** 50 GeV WIMP—expected sensitivity [102]

Chapter 3

Studies on the XENON100 Electromagnetic Background

In the search for rare WIMP interactions in a dark matter experiment, the suppression and discrimination of the surrounding radioactive backgrounds is of utmost importance. In the standard scenario, WIMPs interact with the LXe atoms through elastic scattering, producing nuclear recoils (NRs). Since neutrons also produce NRs, these are the most unwanted sources of background and must be suppressed effectively. Although γ and β radiation produce electronic recoils (ER) that can be rejected via the discrimination parameter S2/S1, as described in detail in section 2.2, a leakage of ER events inevitably contaminates the NR signal region for WIMP searches. Because of this, the ER background must be well understood and minimized.

A brief discussion on the NR and ER backgrounds in XENON100 follows—with some comments on the upgraded XENON1T. The subsequent analyses focus on the ER background of XENON100 and its sources, specifically in the period between April 2013 and January 2014, corresponding to Run 12.

3.1 Shielding of the Detector

The first layer of shielding for any experiment searching for rare events is the Earth itself. Dark matter detectors are typically installed underground, below mountains or deep down in mines, to reduce the flux of cosmic radiation. As mentioned before, the signature of a WIMP is a single NR via elastic scattering off the target nuclei. Unfortunately, neutrons also produce NRs which are indistinguishable from a WIMP on an event-by-event basis. Spallation processes from cosmic muon interactions, for example, are an undesirable source of neutrons.

Neutrons with energies of up to several GeV are generated by muons interacting with the rock and concrete surrounding the detector, or with the materials of the detector itself [118]. Such energetic neutrons can penetrate through the shields of the experiment and produce a single scatter in the active volume. In its

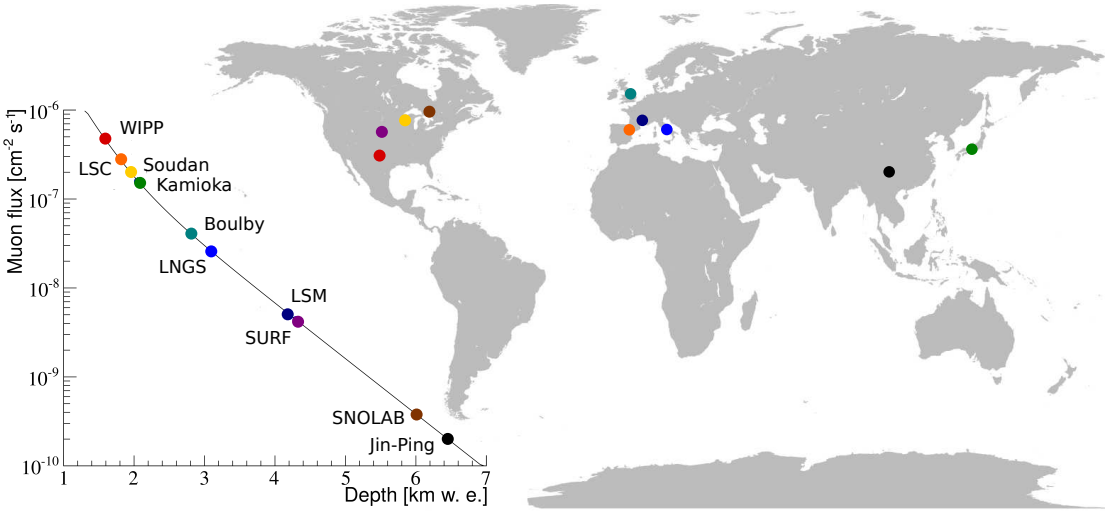

Key	Name	Location	Experiments
WIPP	Waste Isolation Pilot Plant	USA	DMTPC, EXO-200
LSC	Laboratorio Subterráneo de Canfranc	Spain	ArDM, ANAIS
Soudan	Soudan Underground Laboratory	USA	MINOS+, SuperCDMS, CoGeNT
Kamioka	Kamioka Observatory	Japan	Super Kamiokande, KamLAND, T2K, XMASS
Boulby	Boulby Underground Laboratory	UK	DRIFT-II
LNGS	Laboratori Nazionali del Gran Sasso	Italy	XENON100, XENON1T, GERDA, DAMA/LIBRA
LSM	Modane Underground Laboratory	France	NEMO, EDELWEISS
SURF	Sanford Ugnd. Research Facility	USA	LUX, LZ, MAJORANA
SNOLAB	Sudbury Neutrino Observatory	Canada	DAMIC, PICO, DEAP-3600, SuperCDMS
Jin-Ping	JinPing Underground Laboratory	China	PandaX, CDEX

Figure 3.1: Muon flux as a function of depth for different underground laboratorie. The depth in kilometers water equivalent is calculated in [118].

path through the different layers, the neutron energy is moderated to the order of MeV, which results in nuclear recoils in the energy range relevant for WIMP searches. Having the dark matter detector in an underground laboratory allows to minimize this muon-induced neutron background. An increase in depth of the underground location will consequently reduce the muon flux reaching the experiment.

The muon flux as a function of depth for different underground facilities is shown in figure 3.1. The data is taken from [118]. The Gran Sasso massif, under which the XENON100 and XENON1T detectors are installed, provides a 1.4 km overburden of rock, equal to 3.1 ± 0.2 km water equivalent. This reduces the muon flux by a factor 10^6 with respect to the surface. The total flux reported in [118] for the underground facilities at LNGS is $(2.58 \pm 0.3) \times 10^{-8}\,\mathrm{cm}^{-2}\mathrm{s}^{-1}$.

In order to further reduce the radioactive background—from the radioactivity in the laboratory environment, for example—the XENON100 detector is surrounded by a series of passive shields. The outermost shield consists of a 20 cm thick layer of water and polyethylene that absorbs incoming neutrons. The following layer is a 20 cm wall of lead, of which the innermost 5 cm contain

Figure 3.2: The XENON100 detector and its shield cavity. The detector is surrounded by the following layers of shielding (from inside to outside): copper walls for the absorption of γ radiation from outer shield layers; polyethylene for blocking neutrons; lead for γ absorption. An outermost layer of water and polyethylene (not seen in the picture) blocks neutrons from the radioactivity in the laboratory environment. Image from [116].

a reduced contamination of ^{210}Pb. The 33 metric tons of lead block the external γ radiation. An additional layer of polyethylene follows—20 cm thick and 1.6 t in weight—providing additional neutron shielding. Finally, 2 t of copper comprise the innermost shield, with a 5 cm layer surrounding the XENON100 detector. The copper wall absorbs the γ radiation from outer shield layers. Figure 3.2 shows a picture of XENON100 and the cavity in which it is installed. The different layers of shielding, previously described, can be observed.

As a consequence of the effective neutron shielding of XENON100, the main contribution to the NR background are radiogenic neutrons from isotopes in the decay chains of ^{238}U, ^{235}U and ^{232}Th present in the detector materials. Neutrons in the MeV range are produced by spontaneous fission (mainly from ^{238}U) as well as (α, n) reactions induced by α particles emitted along the decay chains.

Neutrinos also contribute to the NR background through coherent neutrino-nucleus scattering (CNNS). Astrophysical neutrinos, mainly those from ^{8}B decay in the Sun, are an irreducible background in detectors without the possibility to measure the recoil direction. Since they produce single scatter NRs uniformly distributed in the active volume of the TPC, they define the ultimate limit for WIMP direct detection experiments [119]. For the next generation experiments, CNNS will become a major contributor to the NR background. In XENON1T, although the NR rate from CNNS in the (4,50) keV NR energy region is very low—estimated to be $(1.8\pm0.3)\cdot10^{-2}$ (t·y)$^{-1}$—the contribution becomes more relevant once the response of the detector and its energy resolution are taken into account (see section 6 in [102]).

Some upgrades against the NR background have been included in XENON1T, such as the muon veto [117], which consists of a water tank 10 m in height and 9.6 m in diameter. While shielding the detector from external neutrons and γ rays, the tank is also equipped with PMTs that allow to identify muons through the Cherenkov light they produce in the water. Considering both the active and passive shielding of the muon veto, the resulting neutron background is

$< 0.01\,\mathrm{y}^{-1}$ in a 1 t FV, rendering this background negligible compared to other NR sources in XENON1T. The contribution of radiogenic neutrons from the detector materials—with a rate of $(0.6\pm0.1)\,(\mathrm{t{\cdot}y})^{-1}$—has been estimated through simulations and the contaminations of the detector materials [102].

In the following studies, the focus will be on the ER background, which constitutes a major source of events in dark matter experiments and must be adequately understood and characterized to be taken into account in the sensitivity of detectors to WIMP interactions.

3.2 The Electronic Recoil Background

In XENON100—as well as in XENON1T—ERs are distinguished from NRs by the ratio S2/S1. The rejection efficiency achieved in XENON100 is around 99.5 % at 50 % signal acceptance [94]. Even then, ER events can potentially leak into the NR region and emulate a WIMP signal. Because of this, it is crucial to understand the ER background of the detector.

As described in the previous section, the γ and β radiations from external sources are blocked by the shields surrounding XENON100. Nevertheless, ERs may still be produced by electromagnetic radiation from the experiment itself. The sources of radiation include the materials used in the construction of the detector, as well as the intrinsic radiation from the LXe. The details of these electromagnetic backgrounds are briefly discussed.

3.2.1 Radiation from the Detector Materials

The materials used to construct the XENON100 detector and its surrounding shields have been carefully selected according to their radioactive contamination. All of the components were screened with low-background Ge detectors, with which their intrinsic radioactivities have been determined. The screening facilities used by the XENON collaboration include some of the most sensitive germanium detectors in the world—such as the Gator detector, operated by the University of Zurich [120]; GeMPI-I and GeMPI-II, operated by MPIK [121]; as well as inductively coupled plasma mass-spectrometers (ICP-MS). Gator consists of a high purity coaxial Ge detector with a sensitive mass of 2.2 kg, an energy resolution of ∼3 keV FWHM at 1332 keV, and a sample cavity with a volume of 19 liters.

The main radioactive contaminants in the detector materials that contribute to the electromagnetic background are ^{238}U, ^{232}Th, ^{40}K and ^{60}Co. Table 3.1 shows the measured radioactivity values implemented in the Monte Carlo simulations that are used in this work. The uncertainties have been disregarded for the MC and all upper limits have been implemented as fixed values. The data is taken from the published XENON100 screening results [122] and, in particular, from the concise list presented in [123].

Material	Unit	^{238}U	^{232}Th	^{60}Co	^{40}K
Stainless steel	mBq/kg	1.65	2.0	5.5	9.0
PTFE	mBq/kg	0.06	0.10	0.03	0.75
PMTs	mBq/piece	0.25	0.5	0.75	8.1
PMT bases (Cirlex)	mBq/piece	0.16	0.07	0.01	0.16
Support bars (steel)	mBq/kg	1.3	2.9	1.4	7.1
Copper (inside)	mBq/kg	0.22	0.16	0.2	1.34
Resistor chain	μBq/piece	27	14	3	0.19
Cathode support ring	mBq/kg	3.6	1.8	7.3	4.92
Top grids support rings	mBq/kg	2.7	1.5	13	12
PMT signal cables	mBq/kg	1.6	3.7	0.69	35
Copper shield	μBq/kg	83	12	39	3.2
Polyethylene shield	mBq/kg	0.23	0.094	–	0.7
Lead shield (inner layer)	mBq/kg	0.66	0.55	0.11	1.46
Lead shield (outer layer)	mBq/kg	0.92	0.72	0.12	14

Table 3.1: Main radioactive contaminants in the detector and shield materials that contribute to the XENON100 electromagnetic background. The values shown are those implemented in the Monte Carlo simulations used in this work—without uncertainties, and all upper limits taken as fixed values. The data is taken from the screening results in [123]. The stainless steel is that used for the cryostat and the bell.

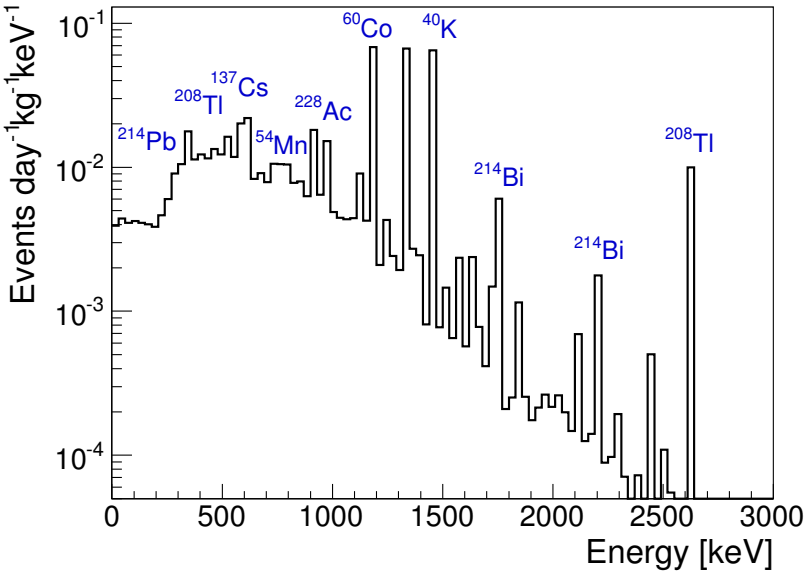

Figure 3.3: Simulated spectrum of the electromagnetic background from the XENON100 detector components. The input values for the Monte Carlo are those shown in table 3.1. Elements such as ^{214}Pb, ^{208}Tl, ^{214}Bi and ^{228}Ac are products in the decay chains of ^{238}U and ^{232}Th, shown in figure 3.4

For the prediction of the intrinsic and ambient electronic recoil backgrounds in XENON100—as well as the simulation of the detector response to various types of particles—a detailed GEANT4 model is used. A description of the model, along with its implementation in Monte Carlo (MC) simulations, is presented in [123]. The same model has been used in the analyses of this work (section 3.3), in order to compare the results from simulations to the measured XENON100 data from Run 12. Figure 3.3 shows the result of the MC simulations of the activity in the XENON100 detector materials.

3.2.2 Radon intrinsic background

Radioactive radon and krypton isotopes are one of the most relevant sources of radiation in noble liquids, such as LXe. Being noble elements themselves, they are difficult to isolate by chemical or physical processes. They are dispersed within the whole liquid volume and thus cannot be reduced through the self-shielding property of noble liquids, as can be done for external or surface radiations. Because of this, the understanding of these intrinsic contaminants is crucial not only for XENON100, but is of even greater relevance for the ton-scale detector generation, including XENON1T, where the surface effects become almost negligible.

The main intrinsic background comes from the decays of ^{222}Rn. As part of the ^{238}U chain—see figure 3.4 (left)—it can emanate from the detector materials and the gas system, or diffuse through the vacuum seals, spreading homogeneously in the LXe volume due to its relatively long half life of 3.8 days. The highest contributor of the ^{222}Rn daughters is the β decay of ^{214}Pb to the ground state of ^{214}Bi. With an endpoint energy of 1019 keV, its branching ratio is 10.9 % according to GEANT4 v10.0 [102].

Decays to other energy levels have an increased contribution with larger fiducial volumes, since, if the decay occurs at the border of the active region, the accompanying γ can exit the detector unidentified. This causes a higher background rate from ^{222}Rn at larger fiducial masses [123]. In XENON1T, given the increased target mass with respect to XENON100, this effect is less relevant.

The only other β emitter in the ^{238}U chain is ^{214}Bi. Being also a potential background source, it can be rejected in the analysis phase by correlating its emission with the α decay of its daughter ^{214}Po, occurring with a 164 μs half-life.

The other important radon isotope, ^{220}Rn, has its origin in the ^{232}Th chain—figure 3.4 (right). In contrast to ^{222}Rn, its half-life is very short, only 55.6 s. It also decays by α emission. The α radiations along the ^{238}U and ^{232}Th chains will deposit energies two orders of magnitude above the region of interest for WIMP interactions, thus will not be a relevant background contribution. The β decays, however, can be a source of background. Amongst these, the decays of ^{214}Bi and ^{212}Bi can be identified through their coincidence with the prompt α emission of their respective daughters, ^{214}Po and ^{212}Po, leading to so-called BiPo analyses. It is then the β decays of ^{214}Pb and ^{212}Pb that will be the

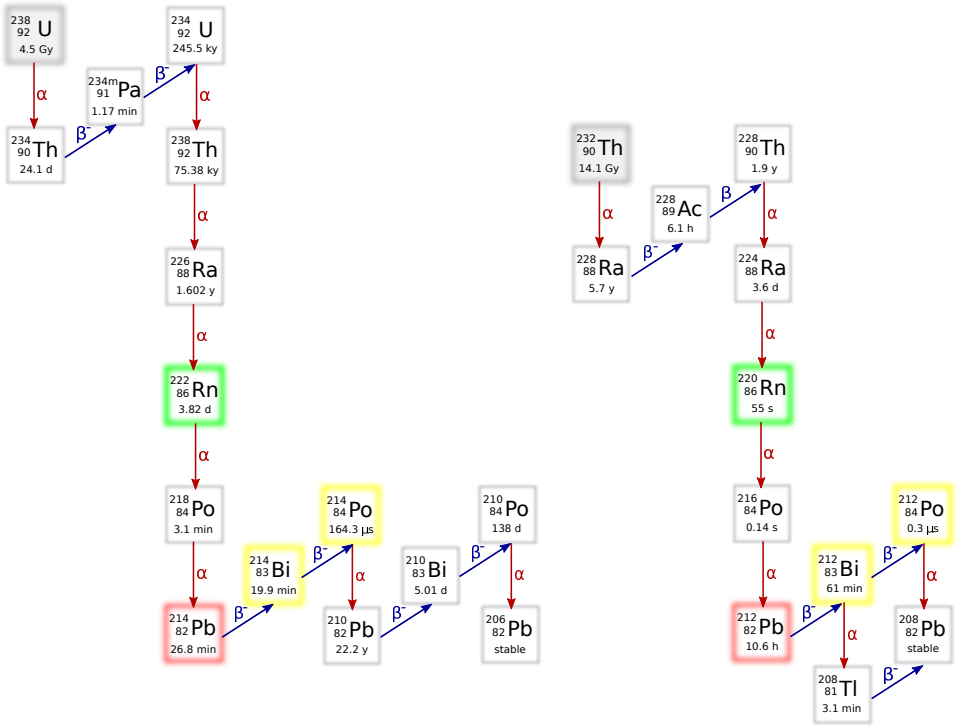

Figure 3.4: Decay chains of ^{238}U and ^{232}Th. The time constants correspond to half-lives. Decays with branching ratios below 0.1 % are neglected. Along the chains, the radon isotopes ^{222}Rn and ^{220}Rn (green) are produced. The short-lived decays of ^{214}Po and ^{212}Po (yellow) are used for BiPo coincidence analyses. Data collected from [124].

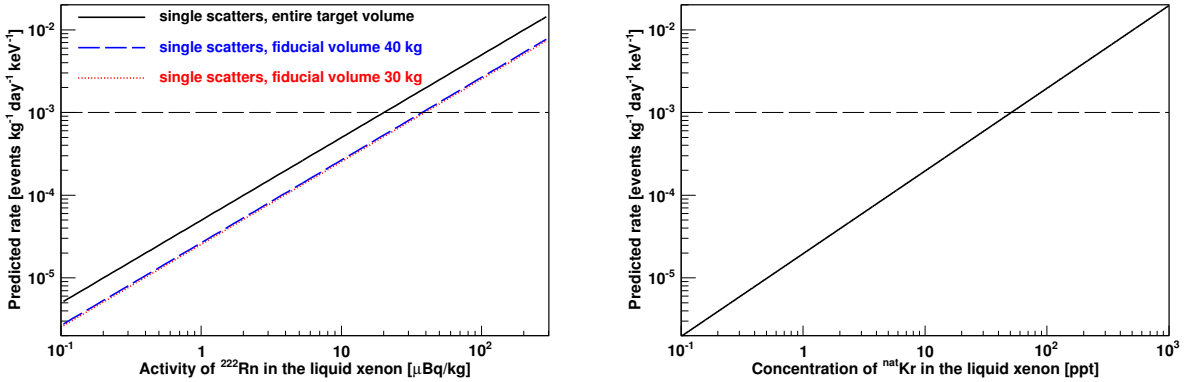

Figure 3.5: (Left) Predicted background rate as a function of ^{222}Rn concentration in XENON100. (Right) Predicted rate of single electronic recoils from ^{85}Kr as a function of the concentration of natural Kr in LXe. Both plots consider recoils in the energy region below 100 keV. The horizontal dashed lines indicate a reference value of 10^{-3} events·kg^{-1}·day^{-1}·keV^{-1}. Figures taken from [123].

greater contributors to the background. With endpoint energies of 1019 keV and 570 keV, respectively, the continuity of the spectrum down to zero kinetic energy causes overlap with the WIMP recoil energy range. In most cases, prompt γ ray emission will occur alongside the β radiation. Whether the emitted photon will produce a second scatter resolvable by the detector will depend on the Compton and photo-absorption scattering lengths in LXe as a function of energy. The energy overlap with the dark matter region in XENON100 has been previously calculated with Monte-Carlo simulations to estimate the number of expected background events [123]. The published radon induced background expectation is shown in figure 3.5 (left), where ^{222}Rn and all subsequent decays were simulated in GEANT4 down to the long-lived ^{210}Pb. The radon was assumed homogeneously distributed within the xenon volume. Only events with a deposited energy below 100 keV (region of interest) are taken into account. The rate prediction corresponds to single scatters, considering an S2 peak separation resolution of 3 mm along the z-axis to distinguish single from multiple interactions. The expected rate depends slightly on the fiducial volume, as photons emitted in outer layers of the TPC have a better chance to escape undetected. leading to an event identified as a single-scatter.

3.2.3 Krypton radioactive contamination

Xenon is obtained commercially as a by-product of the separation of oxygen and nitrogen in air, generally performed by distillation. A concentration of natural krypton is present in commercial xenon at the ppm level. Natural krypton contains a fraction of radioactive ^{85}Kr, mainly produced by nuclear fission and released into the atmosphere by nuclear weapons and power plants. The relative abundance of ^{85}Kr in Europe is 2×10^{-11} [125]. It undergoes β^- decay with a half-life of 10.756 years and an endpoint energy of 687.1 keV.

The krypton concentration in XENON100 has been reduced to < 10 ppb by processing the xenon gas at a commercial distillation plant. To further remove Kr impurities, additional gas purification has been performed in XENON100 with cryogenic distillation. A Kr concentration as low as (0.95 ± 0.16) ppt has been achieved with the use of a distillation column, obtaining the purest xenon ever for a LXe detector [126]. The Kr level in XENON100 varies over the different stages of the experiment—as it depends on the purification processes—thus, the background rate is predicted for different concentrations of ^{nat}Kr in LXe, as shown in figure 3.5 (right). The goal in XENON1T is to further reduce the ^{nat}Kr concentration to 0.2 ppt by using a new high separation cryogenic distillation column [127].

3.2.4 ^{136}Xe Double Beta Decay and Solar Neutrinos

Naturally occurring xenon is composed of eight stable isotopes and one very long-lived isotope: ^{136}Xe. With an abundance of 8.9 % in ^{nat}Xe, and a half life extend-

ing up to 2.17×10^{21} y [108], ^{136}Xe undergoes two-neutrino double beta decay with a Q-value of 2.46 MeV. The predicted average background rate below 100 keV for $2\nu\beta\beta$ decay of ^{136}Xe is in the order of 10^{-6} events·kg^{-1}·day^{-1}·keV^{-1} [123]. In XENON100, this rate is around three orders of magnitude below other background components. In the case of XENON1T the contribution of ^{136}Xe is more relevant but still predicted to be less than 2 % of the total ER background [102].

Solar neutrinos can also produce ERs in the low energy region by scattering elastically off the electrons in LXe. These will constitute the ultimate background source for dark matter searches since there is no way to shield the neutrino flux. In XENON1T, solar neutrino interactions—92 % of which come from *pp*-neutrinos—will contribute close to 5 % of the total ER background [102]. For the future multi-ton detector, DARWIN, the contribution to the electronic recoil background via neutrino-electron scattering is estimated at the level of ~ 26 events $\cdot$ t^{-1}y^{-1} in the low-energy region for dark matter signals [128].

3.3 XENON100 EM Background in Run 12

In this section, a detailed study of the electromagnetic background in XENON100 is presented. The focus is on the data acquired during the period between April 2013 and January 2014, which corresponds to the so-called Run 12. Similar analyses have been performed for previous runs of the XENON100 experiment and reported in [123] [129] and [130]. The background conditions of the XENON100 experiment change over time. Some radioactive contaminants in the detector materials decay, such as ^{60}Co. The level of purification of the LXe also changes and, hence, the concentration of radioactive ^{85}Kr. In addition, the amount of ^{222}Rn varies with time, affecting the expected background. Because of this, it is important to perform a study of the electromagnetic background in each of the XENON100 runs.

3.3.1 Run 12 Data and Cuts

The data acquired during Run 12 for dark matter search is divided into 165 datasets, taken between April 22nd 2013 and January 8th 2014. The full set of data amounts to a total of 110 live days. These datasets—labeled as "dark matter data"—correspond to the operation of the detector at nominal conditions, with the anode voltage set to 4.4 kV and the cathode voltage at 15 kV.

Additional "background data" has also been taken in periods during which the detector has not been in optimal conditions for a dark matter search, such as the electrodes being at different voltages or after AmBe calibration. During the acquisition of "dark matter data", several measurements with calibration sources have also been taken. These are described in detailed in the following section.

Once acquired, the raw data is processed through the XENON Raw Data Processor. The so-called `xerawdp` constitutes a software framework written in

Cut	Description
`Xsignalnoise5`	`_corrected`. Rejects events with a large amount of noise, missed peaks or shifted baselines.
`Xs1coin2`	Increases coincidence threshold according to the amount of noisy PMTs.
`Xs2peaks2`	Requires the largest S2 peak to be larger than the trigger threshold (150 PE).
`Xs1width0`	Rejects noisy events with a small width.
`Xentropy1`	Rejects noisy events based on the entropy (a measure of the inhomogeneity) of the PMT signals.
`Xs1single5`	Restricts the number of coincident S1s in a waveform to avoid misidentification of signals.
`Xs2single3`	Restricts the size of secondary S2 signals below a threshold.
`Xs2width_er_3`	Removes noise populations with unphysical S2 widths, used for ER studies.

Table 3.2: General list of cuts used in the EM background studies presented here. The names are those used in XENON100 analyses.

C++ and based on ROOT. It has been developed specifically for the data analysis of XENON100, but its modular design has allowed for some of its elements to be used for data processing in other experimental setups, such as those described in section 4.2.2.

The first step in `xerawdp` is the pre-processing of the acquired waveforms, during which the baselines are computed and peak candidates are identified. In the second step, the waveforms of all PMT channels are added into a total waveform that is used to search for S1 and S2 signal candidates. All relevant properties of the S1 and S2 signals are stored in ROOT files which are then used to perform further physics analyses.

The following step in data handling is the application of cuts that select the relevant data to be used in a specific analysis. For the background analysis presented here, the set of cuts that have been applied are summarized in table 3.2. In general, these cuts have been defined such that events with unphysical signals (noise) are rejected and the quality of S1 and S2 signals is ensured, with which the analysis can best be performed.

An additional cut that is used throughout these studies is that of the *fiducial volume*. As mentioned before, the LXe acts as a shield for electromagnetic radiation. Thus, the selection of different target volumes will impact the background spectrum. Figure 3.6 shows the fiducial volumes defined for this work. A total of five different volumes will be used, ranging from 5 kg in the central region of the TPC, up to 30 kg. The vertical coordinates of all volumes are kept the same and only the radius has been varied. This is chosen in order to study the radial dependence of the background rate.

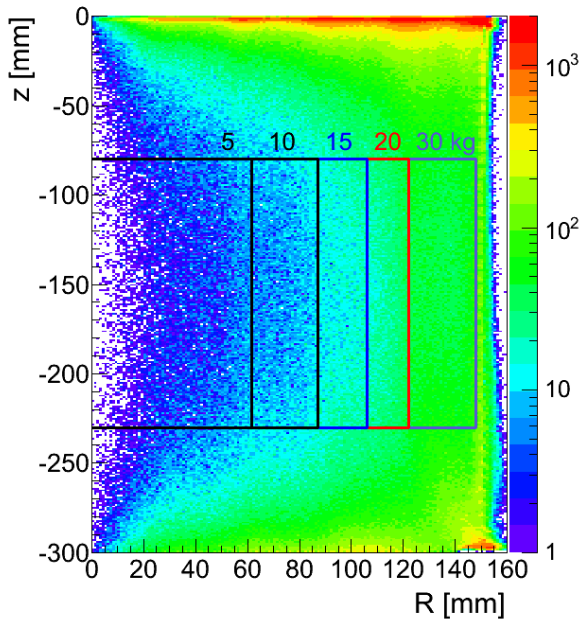

Figure 3.6: Position distribution of events in the XENON100 TPC. The fiducial volumes defined for the EM background studies are overlaid. The radial coordinate changes for each volume as listed below:

Volume	Radius
5 kg	61.5 mm
10 kg	87 mm
15 kg	106 mm
20 kg	122 mm
30 kg	148 mm

The vertical range is fixed to: $-230\,\text{mm} < z < -80\,\text{mm}$.

3.3.2 Calibration Data

Several radiation sources are used during each XENON100 run in order to calibrate the detector. The different sources are useful for calibration at various energy ranges. The following section describes the main sources used in this analysis and their characteristics.

AmBe

The oxide of americium-241 pressed with beryllium (AmBe) is an efficient neutron source. Neutrons are produced when the alpha particles emitted by the ^{241}Am impinge upon the low-atomic-weight atoms Be, owing to the large cross-section of Be to the (α,n) nuclear reaction. The neutrons from the AmBe source can produce the metastable states ^{129m}Xe and ^{131m}Xe when interacting with the xenon atoms in the LXe—either through thermal-neutron capture on ^{128}Xe and ^{130}Xe, or by fast neutron inelastic scattering on ^{129}Xe and ^{131}Xe.

Both ^{129m}Xe and ^{131m}Xe subsequently emit gammas which are useful for calibration of LXe detectors. The decay of ^{129m}Xe produces gammas at 40 keV, 236 keV and 320 keV—being the 236 keV channel the longest lived, with a half life of 8.9 days. In turn, the gammas from ^{131m}Xe have energies of 80 keV and 164 keV, the latter having a half-life of 11.8 days. Figure 3.7 (left) shows the activated Xe lines in the S2–S1 parameter space. The boxes indicate the selection cut for each energy line, used in subsequent analyses.

Since NRs are also present in the AmBe data, a cut on S2 is applied, below which the NRs are excluded (`cS2sTot[0]` > 8000). A total of 66 AmBe datafiles, between May 16th – 21st 2013, have been considered. The total live

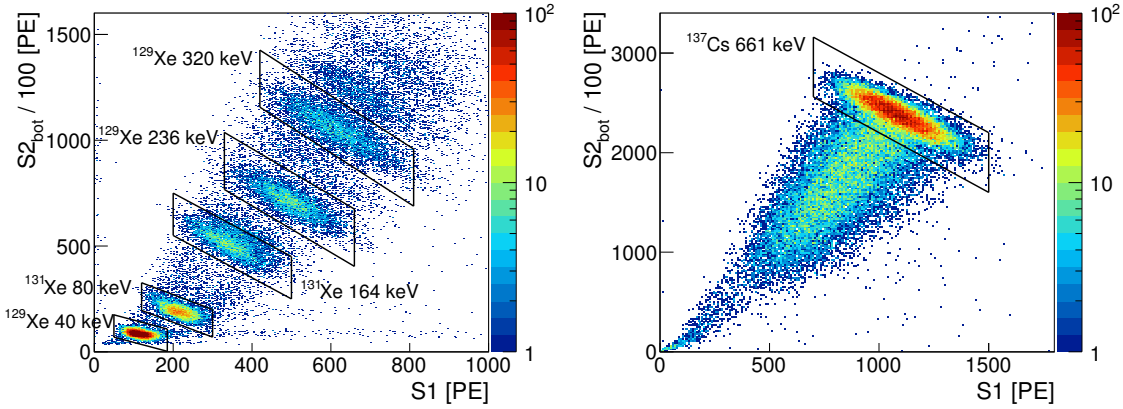

Figure 3.7: (Left) AmBe calibration events in the S2 – S1 parameter space. The corresponding variables in `xedaq` are `cS2sTotBottom[0]` and `cxS1sTot[0]`. The activated Xe lines are indicated in the boxes, which correspond to the cuts for each energy line used in subsequent analyses. (Right) Events from ^{137}Cs calibration. The S2 signal has been corrected for the electron life-time via equation 3.1.

time corresponds to 4.8 days.

Caesium-137

Caesium-137 is a radioactive isotope of caesium formed as a product of nuclear fission of ^{235}U and other fissionable isotopes. It is commonly used to calibrate radiation-detection equipment and is also an important calibration source for XENON100. With a half-life of about 30.17 years, ^{137}Cs decays around 95 % of the time to ^{137m}Ba by β emission, which, in turn, has a half-life of 153 s and emits γ radiation. The main photon peak of ^{137m}Ba is 661.7 keV.

Since ^{137}Cs data is used to estimate the electron life-time in the TPC, the S2 signal is not corrected by this factor (as it is for all other processed datasets). The S2 signal has thus been manually corrected as follows:

$$\texttt{eltcS2sTotBottom} = \texttt{cS2sTotBottom[0]}\ \frac{\mathrm{dt}}{\mathrm{elt}}, \tag{3.1}$$

where elt is the electron life-time and dt is the drift time (the time difference between the S1 and S2 signals: `S2sPeak[0] - S1sPeak[0]`). The S2 signal in the bottom PMT array (`cS2sTotBottom[0]`) is preferred over the top array signal for the energy reconstruction. This is because of the lower saturation of the bottom PMTs from high energy signals—an effect which is discussed in detail in section 3.3.7.

Events from the ^{137}Cs calibration are shown in figure 3.7 (right) using the S2 – S1 parameter space. The S2 signal has been corrected according to equation 3.1. The datafiles selected are those after AmBe calibration, in the period between

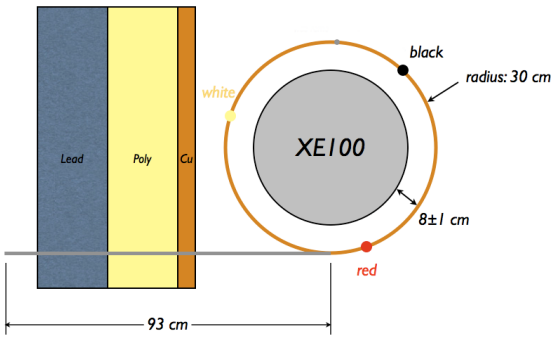

Figure 3.8: Positions around the XENON100 detector at which the ^{137}Cs and ^{60}Co sources are located during calibration. For consistency throughout the analyses presented here, the data at the red location has been selected for when the interaction vertices of the events are involved.

July 8th 2013 and January 6th 2014.

Three positions around the XENON100 detector have been established for the location of the ^{137}Cs source during calibrations. The positions—labeled as red, black and white—are shown in figure 3.8. For consistency throughout the following analyses, where the event position is relevant, only the data taken at the red location has been used in this work.

Cobalt-60

Cobalt-60 is a synthetic radioactive isotope of cobalt produced artificially in nuclear reactors. With a half-life of 5.27 years, ^{60}Co decays via β emission to the stable isotope ^{60}Ni. The activated Ni nucleus emits two gamma rays with energies of 1.17 and 1.33 MeV. The main advantage of ^{60}Co, compared to other gamma ray sources of similar intensity, is that it emits high intensity gammas with a relatively long half-life. The β-decay energy is low and easily shielded, while the γ-rays are highly penetrating.

The ^{60}Co source is also used in XENON100 for calibrations, during which it is located at the positions shown in figure 3.8. The datafiles selected for analysis are those between July 18th and December 6th 2013, at the red source position. Figure 3.9 (left) shows the ^{60}Co data in the S2 – S1 parameter space. The boxes indicate the cuts used to select the event from each of its two gamma lines.

Thorium-232

Thorium-232 is the only primordial isotope of thorium and makes up effectively all of natural thorium. It decays by α emission with a half-life of 1.405×10^{10} years. Its decay chain is shown in figure 3.4 (right), which includes the isotope ^{208}Tl. The gamma rays following the decay of ^{208}Tl have an energy of 2614 keV, which is also useful for calibrations. Figure 3.9 (right) shows the events from ^{232}Th in the S2 – S1 parameter space, indicating the ^{208}Tl gamma line. The selected files are those from August 27th to November 28th 2013.

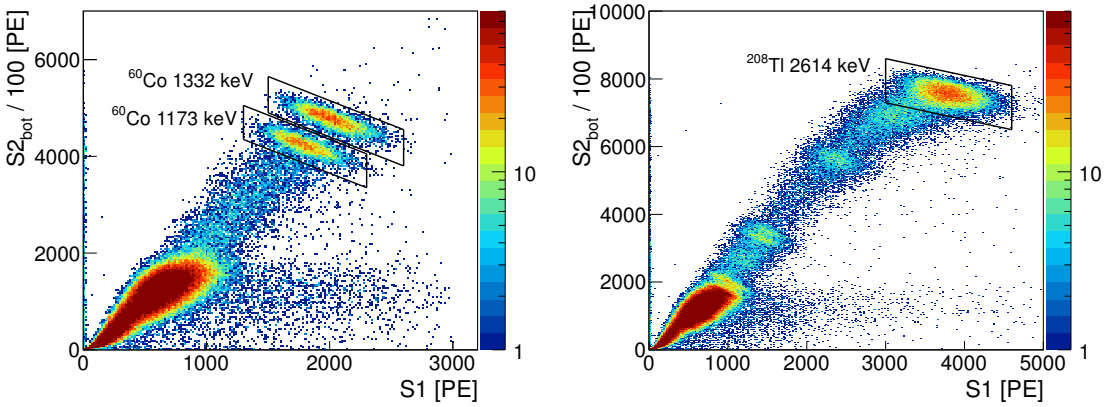

Figure 3.9: (Left) ^{60}Co calibration events in the S2 – S1 parameter space. The corresponding `xedaq` variables are `cS2sTotBottom[0]` and `cxS1sTot[0]`. The boxes indicate the cuts used to select each energy line, as used in subsequent analyses. (Right) Calibration events from a ^{232}Th source. The box indicates the ^{208}Tl line used for calibrations.

3.3.3 Combined Energy Scale

The detection of both the S1 and S2 signals performed by dual-phase TPCs, along with the anti-correlation between the two signals, can be exploited to improve the energy resolution of the detector. The resolution of the combined scale is higher than that of the independent S1s or S2s since its fluctuations are smaller than those of the individual signals. The combination of the scintillation and ionization signals into a new energy scale yields a result independent of the drift field and, to a certain extent, particle energy—as will be seen next.

The aim is to construct a combined energy scale (CES) of the form:

$$\mathrm{CES} = a\,\mathrm{S1} + b\,\mathrm{S2}, \tag{3.2}$$

where a and b are scaling factors for S1 and S2 which take into account the anti-correlation and energy normalization of both signals.

In order to construct the CES, the data from several calibration sources has been used. The de-excitation energy-lines of each source, when represented in the S2 – S1 parameter space, result in ellipses that are rotated at a certain angle. The CES can be estimated by determining the rotation angle of the main axis of the ellipse through a 2D Gaussian fit.

An un-rotated 2D Gaussian fit is of the form:

$$f(x,y) = A\exp\left(-\left(\frac{(x-\mu_x)^2}{2\sigma_x^2} + \frac{(y-\mu_y)^2}{2\sigma_y^2}\right)\right), \tag{3.3}$$

which corresponds to an ellipse with an amplitude A and center at (μ_x, μ_y). The

major and minor axes of the ellipse, σ_x and σ_y, correspond to the x and y spreads of the 2D distribution.

A counterclockwise rotation of the ellipse by an angle ϕ can be obtained by using the following rotated system:

$$x' - \mu'_x = (x - \mu_x)\cos\phi - (y - \mu_y)\sin\phi \tag{3.4}$$

$$y' - \mu'_y = (x - \mu_x)\sin\phi + (y - \mu_y)\cos\phi \tag{3.5}$$

The combination of equations 3.4 and 3.5 with equation 3.3 results in the following rotated ellipse, representing the general 2D Gaussian fit:

$$\begin{aligned} f(x,y) = A\exp\Bigg(- \Bigg(& \frac{\left((x-\mu_x)\cos\phi - (y-\mu_y)\sin\phi\right)^2}{2\sigma_x^2} + \\ & + \frac{\left((x-\mu_x)\sin\phi + (y-\mu_y)\cos\phi\right)^2}{2\sigma_y^2} \Bigg) \Bigg). \end{aligned} \tag{3.6}$$

Several energy lines from different calibration sources in the S2 – S1 parameter space are shown in figure 3.10. The data has been fitted with the function from equation 3.6, where $x = \mathrm{S1}$ and $y = \mathrm{S2}_{bot}$. From the fit it is possible to extract the rotation angle ϕ, as well as μ_x and μ_y. From the anti-correlation of S2 and S1, the main axis of each ellipse—or the tangent of ϕ—represents a line of constant energy (i.e. the full absorption energy of that particular gamma peak). The linear equation representing the main axis is:

$$y = -\mathrm{m}\,(x - \mu_x) + \mu_y, \tag{3.7}$$

where the slope is $\mathrm{m} = \tan\phi$ and (μ_x, μ_y) is a point on the line. Since all points on the line correspond to the same energy, equation 3.7 can be rewritten as:

$$y + \mathrm{m}x = \mu_y + \mathrm{m}\mu_x \equiv k \cdot \mathrm{Energy}, \tag{3.8}$$

where k is a proportionality constant that can be determined from the measured m, μ_x and μ_y from the elliptical fit.

Finally, the CES can be written as:

$$\mathrm{CES} = \frac{1}{k}\,(\mathrm{S2} + \mathrm{m}\,\mathrm{S1}), \tag{3.9}$$

with $k = (\mu_y + \mathrm{m}\mu_x)/\mathrm{Energy}$ and $\mathrm{m} = \tan\phi$.

The results of the elliptical 2D Gaussian fits from figure 3.10 are shown in table 3.3. The CES parameters k and m have been calculated from the measured rotation angle ϕ, as well as the mean S2 and S1. The errors correspond to the systematic uncertainties that result from changing the initial fitting parameters, as well as the variation of the fiducial volume.

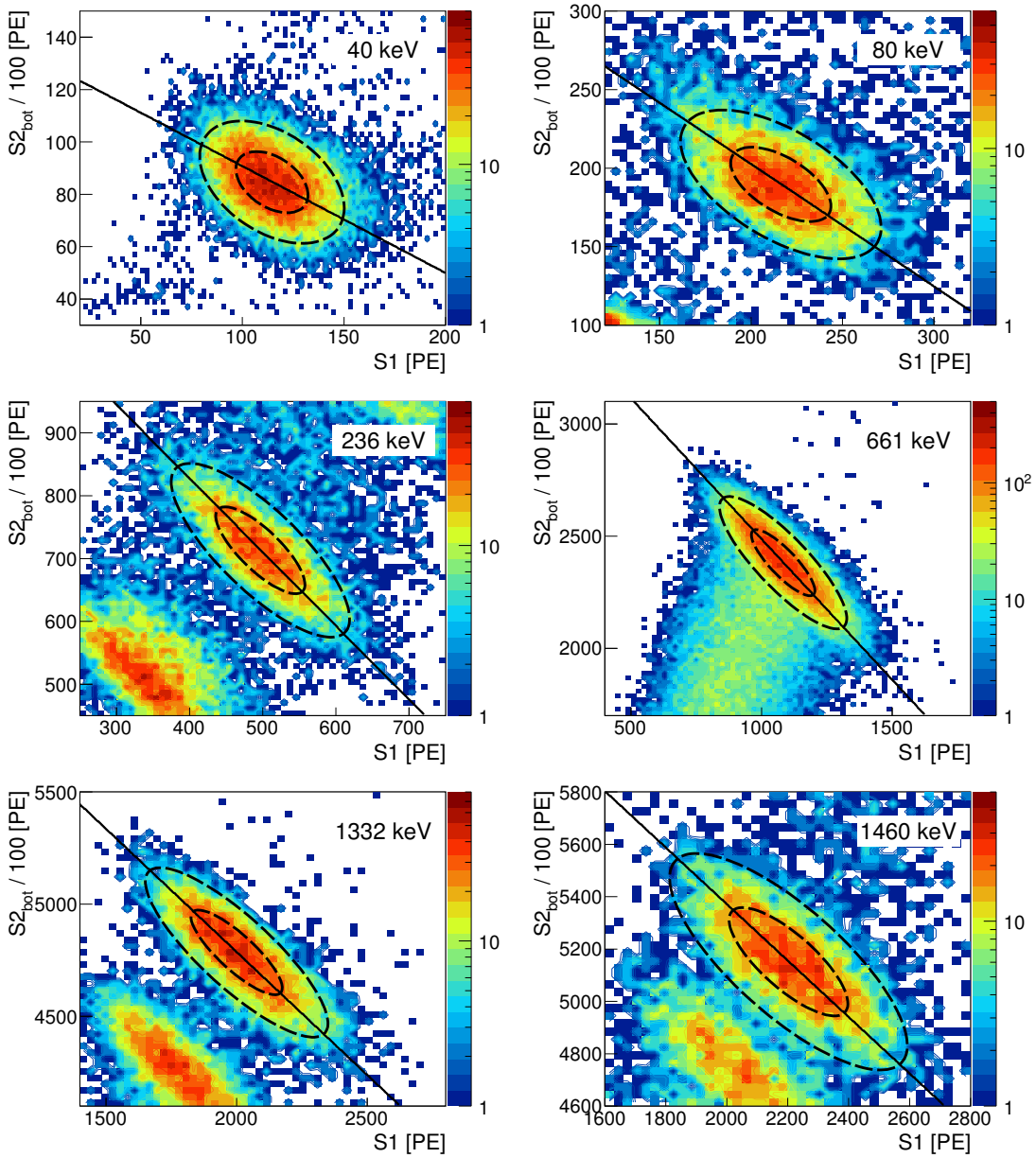

Figure 3.10: Full absorption lines for different calibration sources in the S2–S1 parameter space (corresponding to the `cS2sTotBottom[0]` and `cxS1sTot[0]` variables from `xerawdp`). $S2_{bot}$ has been divided by a factor 100 to have a similar scale as S1. In this way the data appear as rotated ellipses which can be fitted with the 2D Gaussian function from equation 3.6. The rotation angle and other parameters shown in table 3.3 are obtained from the fit and used to construct the CES.

Energy [keV]	μ_{S1} [PE]	$\mu_{S2}/100$ [PE]	ϕ [rad]	m [$\tan\phi$]	k
^{129}Xe: 40	114	84	0.39 ± 0.02	0.41 ± 0.02	3.30 ± 0.05
^{131}Xe: 80	215	189	0.65 ± 0.01	0.76 ± 0.02	4.42 ± 0.05
^{131}Xe: 164	343	515	0.88 ± 0.01	1.21 ± 0.03	5.68 ± 0.05
^{129}Xe: 236	495	714	0.87 ± 0.01	1.17 ± 0.01	5.50 ± 0.03
^{129}Xe: 320	607	1063	0.89 ± 0.02	1.24 ± 0.06	5.67 ± 0.11
^{137}Cs: 661	1082	2380	0.90 ± 0.01	1.25 ± 0.02	5.66 ± 0.04
^{60}Co: 1173	1779	4239	0.89 ± 0.03	1.23 ± 0.08	5.48 ± 0.09
^{60}Co: 1332	2002	4774	0.85 ± 0.01	1.14 ± 0.04	5.30 ± 0.03
^{40}K: 1460	2197	5149	0.83 ± 0.02	1.09 ± 0.04	5.17 ± 0.04
^{208}Tl: 2614	3798	7554	0.67 ± 0.02	0.80 ± 0.03	4.05 ± 0.05

Table 3.3: Results of the elliptical 2D Gaussian fits describing the distribution of events from calibration sources in the S2 – S1 parameter space. The activated Xe lines are obtained from the AmBe calibration data, while the ^{208}Tl line is obtained from the ^{232}Th calibration. The parameters $k = (\mu_y + \mathrm{m}\mu_x)/\mathrm{Energy}$ and $\mathrm{m} = \tan\phi$ have been computed from the measured rotation angle ϕ, as well as the mean S1 and S2 (μ_{S1}, μ_{S2}).

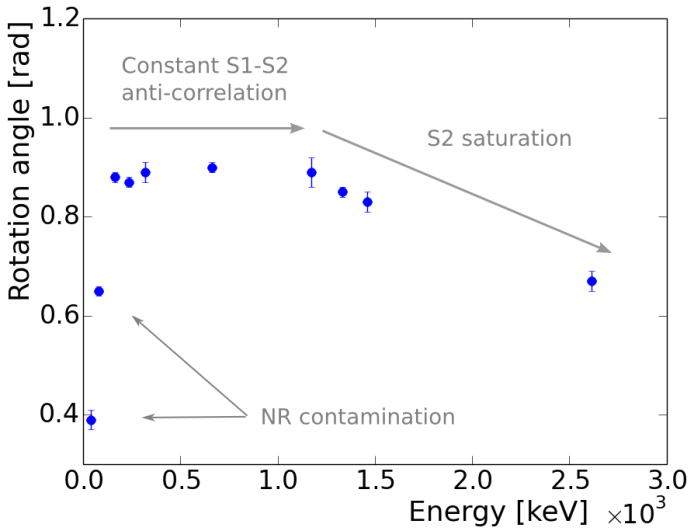

Figure 3.11: Rotation angle ϕ as a function of energy. The angle ϕ is a measure of the anti-correlation between the S1 and S2 signals, as seen in figure 3.10. The anti-correlation is expected to be constant, as shown in [131]. The decrease in rotation angle at energies above ∼1 MeV is caused by the saturation of the S2 signal at high energies. The measurements at 40 and 80 keV from AmBe calibration are affected by simultaneous NRs and are thus not pure ERs, which affects the light and charge yield.

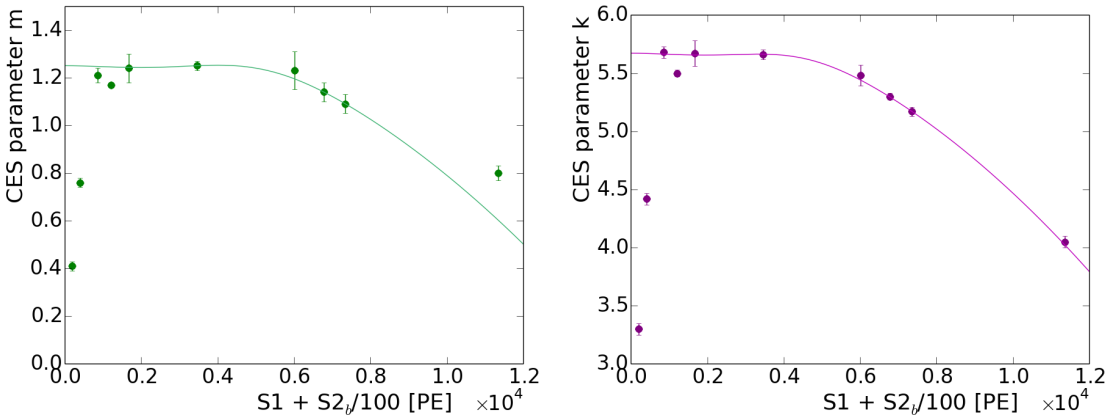

Figure 3.12: (Left) CES parameter m = $\tan\phi$ as a function of the energy estimator $S1 + S2_{bot}/100$. (Right) CES parameter $k = (\mu_y + m\mu_x)/\text{Energy}$, also as a function of the same energy estimator. In both cases, the fit curve is of the form $-A\exp(-Bx^3) - Cx^2 + D$. The lines from AmBe data have been excluded from the fit for reasons described in the text. The decline observed above the ^{137}Cs line is caused by saturation of the S2 signal. The effect is evident in the ^{60}Co, ^{40}K and ^{208}Tl data points, where the impact of the S2 saturation is highest.

The measured rotation angle ϕ as a function of energy is shown in figure 3.11. Since ϕ is a measure of the anti-correlation between S1 and S2, it is expected to be a constant with energy, as shown in [131]. It can be observed that ϕ is constant until about 1 MeV, above which it begins to decline. The deviation from the constant value is due to the saturation of the S2 signal at high energies. The value of ϕ at 40 keV and 80 keV is also far from the constant value. This is because the prompt gamma lines of ^{129}Xe and ^{131}Xe at these energies contain also contributions from the simultaneous nuclear recoils, altering the relation between the measured S1 and S2 signals.

As seen in equation 3.9, in order to construct the CES it is necessary to determine the parameters k and m. Since both parameters depend on ϕ, a CES which extends beyond 1 MeV requires parameters which are energy dependent. For this, k and m will be determined as a function of a simple energy estimator $S1 + S2_{bot}/100$, as shown in figure 3.12. In both cases, the function that best describes the energy dependence of these parameters was found to be of the form: $-A\exp(-Bx^3) - Cx^2 + D$. For the fit at low energies, some data points have been excluded. The 40 and 80 keV lines from the AmBe calibration are contaminated with simultaneous NRs. The 236 and 320 keV lines have contributions from multiple gamma decays and are thus not purely mono-energetic. Finally, the 164 keV line overlaps with the 197 keV line of ^{19}F, which is present in the PTFE and activated during AmBe calibration. Being present only in the PTFE walls, smaller fiducial volumes do minimize the effect of ^{19}F, but the effect can still

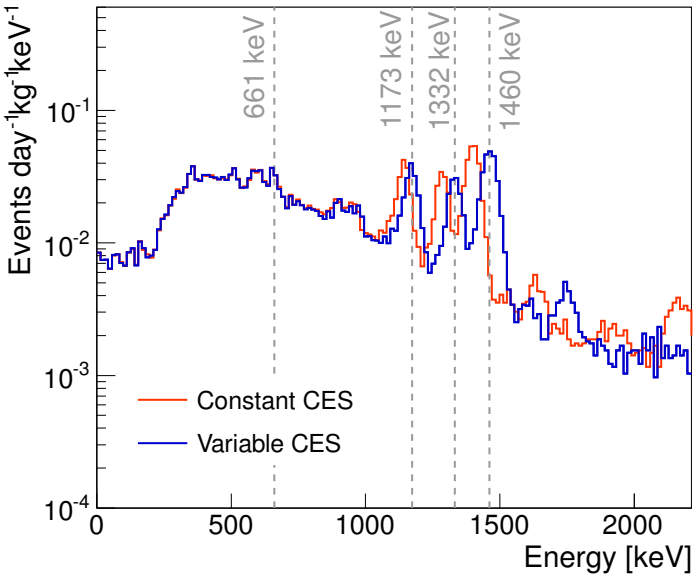

Figure 3.13: Spectrum of the EM background in run 12 of XENON100. The spectrum obtained with the variable CES derived in equation 3.12 (blue) is compared to the constant CES (orange), which uses constant k and m parameters obtained from the ^{137}Cs calibration only. It can be observed that only the variable CES matches correctly the energy lines above 1 MeV—which correspond to ^{60}Co and ^{40}K. The FV used in this plot is 15 kg.

reduce the accuracy of the Gaussian fit to the 164 keV line.

As a result of the fits in figure 3.12, the CES parameters have been defined as:

$$\mathrm{m}(x) = -0.19\, \mathrm{e}^{-(1.24\times10^{-11})x^3} - (0.65\times10^{-8})x^2 + 1.44 \tag{3.10}$$

$$k(x) = -0.33\, \mathrm{e}^{-(1.83\times10^{-11})x^3} - (1.53\times10^{-8})x^2 + 6.0 \tag{3.11}$$

where $x = \mathrm{S1} + \mathrm{S2_{bot}}/100$. The CES is thus defined as:

$$\mathrm{CES} = \frac{1}{k(x)}\left(\mathrm{S2_{bot}}/100 + \mathrm{m}(x)\,\mathrm{S1}\right), \tag{3.12}$$

where $\mathrm{S2_{bot}}$ and S1 correspond to the `xerawdp` variables `cS2sTotBottom[0]` and `cxS1sTot[0]`, respectively.

Figure 3.13 shows a comparison of the run 12 background spectrum with a CES of constant m and k, and the variable CES constructed in equation 3.12. In the case of the constant CES, the values of k and m have been chosen as the constants from the ^{137}Cs gamma line. This is because it is the cleanest measurement in terms of mono-energetic electronic recoils. As expected, at low

energies both spectra are similar, but above ∼1 MeV only the variable CES manages to match the energy lines of ^{60}Co and ^{40}K, while the CES with constant parameters fails to do so.

3.3.4 Energy Resolution

The energy resolution of the detector, $R = \frac{\sigma(E)}{E}$, depends on a series of different factors, such as the resolution of the scintillation and ionization processes in LXe, as well as the geometrical effects on the collection of photons. Some properties of the PMTs also play a role, such as the statistical fluctuations in the production of photoelectrons from incident photons, the light collection and the variations in the gain (see chapter 4 for a detailed description of the PMT characteristics).

The energy resolution improves with increased signal energy. This derives from the fact that a larger number of measured photoelectrons minimizes the effect of the statistical fluctuations mentioned earlier. Hence, a better resolution is also achieved by considering the proportional scintillation signal S2, since it is two orders of magnitude larger than S1. For this reason, in the following analysis the energy resolution will be determined from the CES derived in the previous section.

Source energy [keV]	Fit mean [keV]	σ_E [keV]	σ_E/E [%]
^{129}Xe: 40	40	3.6 ± 0.1	9.0 ± 0.2
^{131}Xe: 80	81	5.2 ± 0.1	6.5 ± 0.2
^{131}Xe: 164	164	6.4 ± 0.2	3.9 ± 0.3
^{129}Xe: 236	236	8.3 ± 0.2	3.5 ± 0.3
^{129}Xe: 320	322	9.4 ± 0.3	2.9 ± 0.2
^{137}Cs: 661	661	13.9 ± 0.1	2.1 ± 0.2
^{60}Co: 1173	1166	23.8 ± 0.5	2.0 ± 0.3
^{60}Co: 1332	1340	26.3 ± 0.3	1.9 ± 0.3
^{208}Tl: 2614	2608	85.9 ± 0.7	3.3 ± 0.2

Table 3.4: Measurement of the energy resolution $\sigma(E)/E$ at different energies using calibration data. The results correspond to the gaussian fit to the different energy lines in CES, as shown in figure 3.14. The uncertainty on $\sigma(E)/E$ includes the systematic errors of changing the fit range. The agreement within 1 % between the theoretical energy of the calibration source and the mean value of the Gaussian fit indicates a good performance of the CES. The activated Xe lines are obtained from the AmBe calibration data, while the ^{208}Tl line is obtained from the ^{232}Th calibration.

The energy resolution for the XENON100 run 12 has been measured at multiple energies from several calibration sources. This has been done by fitting a Gaussian curve to each of the known energy lines and recording the mean and standard deviation of the distribution. Figure 3.14 shows the spectra of the

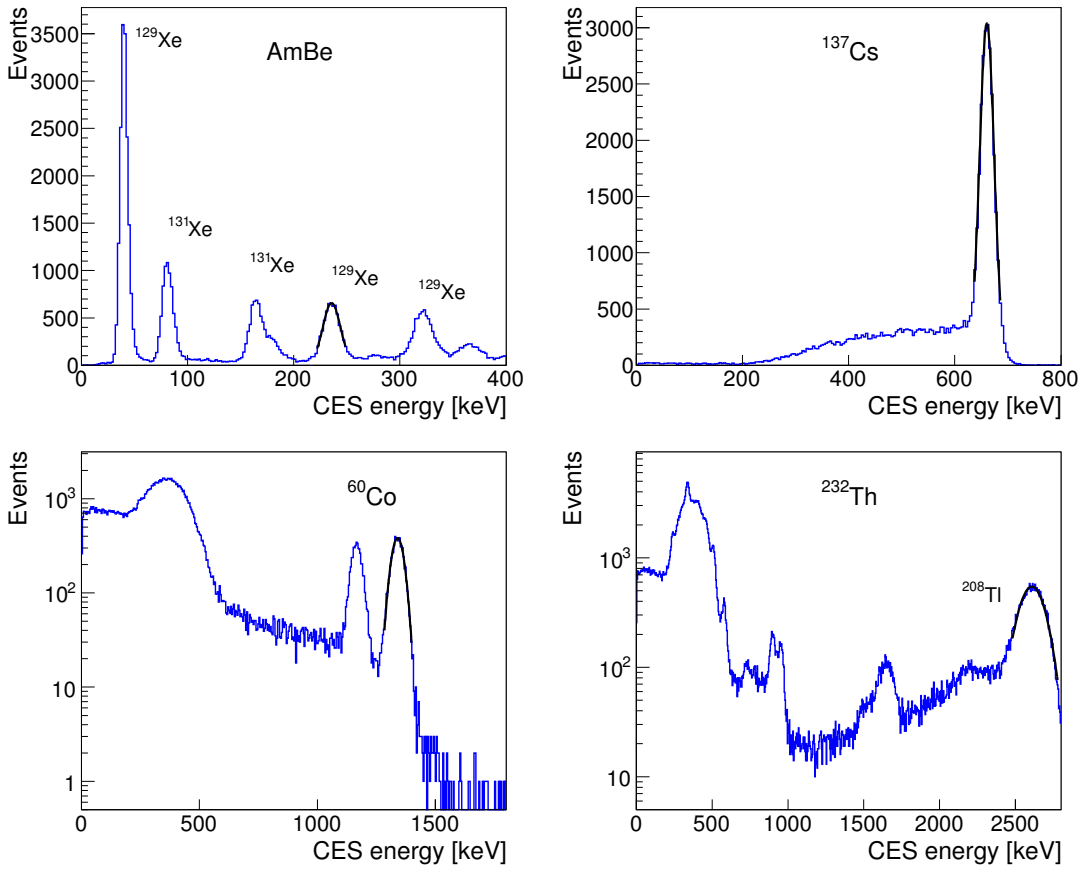

Figure 3.14: Spectra of the different calibration sources using the CES. A gaussian fit to each of the known energy lines is used to determine the energy resolution of the XENON100 detector. The results are summarized in table 3.4.

calibrations with AmBe, ^{137}Cs, ^{60}Co and ^{232}Th. In each case, an example Gaussian curve is shown, which is used to fit a known energy line to determine its resolution. A summary of the results for all energy lines is presented in table 3.4.

The energy resolution as a function of energy using the data from table 3.4 is shown in figure 3.15. The datapoints have been fitted with a function of the form:

$$f(E) = a + \frac{b}{\sqrt{E}}, \tag{3.13}$$

where a and b are constants and E is the energy in keV. The points for 40 and 80 keV have been excluded from the fit due to the NR contributions, as mentioned earlier. The result of the fit—and thus the energy resolution as a function of energy—is the following:

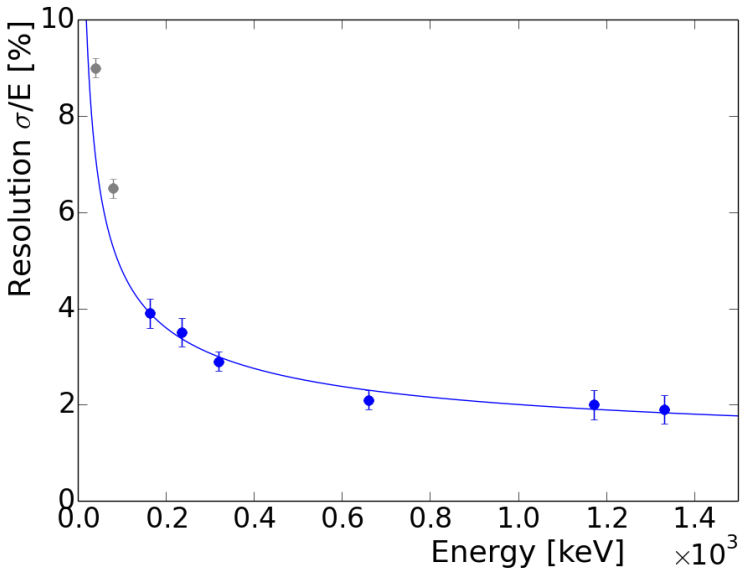

Figure 3.15: Energy resolution as a function of energy in XENON100. The datapoints correspond to the spread of the Gaussian fit to several energy lines from calibration data. The 40 and 80 keV points are excluded from the fit due to the NR contamination which contributes to the spread.

$$\frac{\sigma(E)}{E}[\%] = 0.7 + \frac{40.9}{\sqrt{E\ [\mathrm{keV}]}}. \tag{3.14}$$

3.3.5 Analysis of Run 12 Subsets

As shown in section 3.3.3, the resolution and precision of the XENON100 energy spectrum depends on the CES used. In turn, the CES varies according to the saturation of the S2 signal. From this it can be expected that a certain CES will not fit the full period of a given run if certain conditions change over time—especially those conditions affecting the S2 signal.

A selection of different subsets of run 12 are compared in figure 3.16. It can be seen that the spectra agree at energies below ∼1 MeV. But for the higher energy lines, such as those of ^{60}Co and ^{40}K, not all spectra match the correct energy. In particular, the earlier datasets—before mid-May 2013—have the largest discrepancy at high energies. This can be attributed to the fact that the calibration data used to determine the CES corresponds to a later period. The AmBe calibration was performed between May 16th – 21st, while the ^{60}Co and ^{40}K data selected for the CES are from July onwards.

The main reason a variable CES becomes necessary is because of the saturation of the S2 signal. The S2 saturation is also responsible for the discrepancies

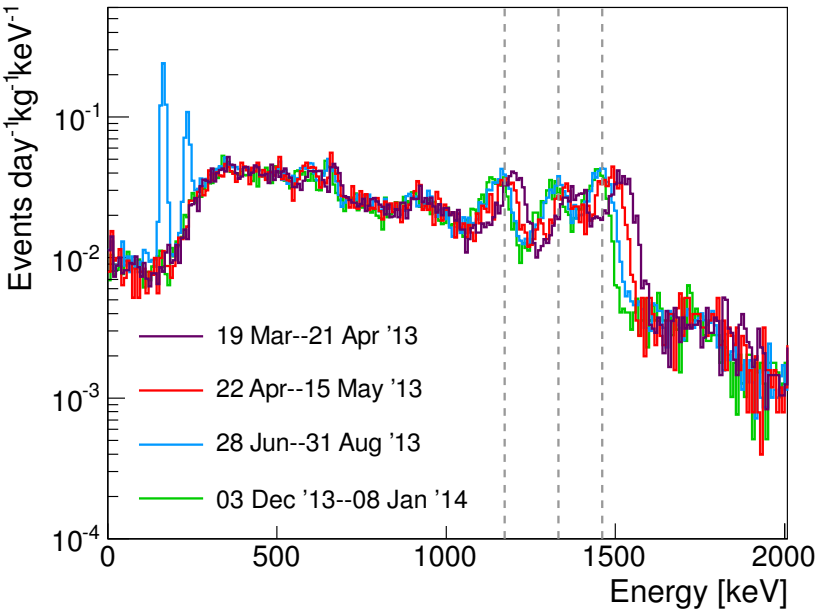

Figure 3.16: Comparison of the spectra in different periods of run 12. The CES used is the one derived in equation 3.12. The earlier subsets do not match the energy lines above 1 MeV—which correspond to ^{60}Co and ^{40}K. This is because the CES has been derived from data taken after the AmBe calibration on May 15th – 21st. The blue spectrum still shows the activated Xe lines, which remain several weeks after the AmBe calibration. The FV used here is 20 kg.

in the spectra of figure 3.16. If the size of the S2 signals changes over time, so will the energy at which saturation of the signals occurs. This, in turn, will cause the observed shift in the energy spectrum of the CES.

One factor that changes over the course of a XENON100 run is the electron life-time (ELT). The ELT is defined as the average time it takes an electron to recombine in the LXe. The longer the ELT, the more electrons are extracted into the gaseous phase and contribute to the S2 signal. During a run, the purity of the LXe is improved through the recirculation of xenon through a heated getter for gas purification. Figure 3.17 shows the evolution of the ELT in run 12. As can be seen, the ELT starts at a value around 380 μs and increases up to ~900 μs over the course of 9 months. The shorter ELT at the beginning of the run results in smaller S2 signals for larger recoil energies, allowing saturation to occur at higher recoil energies. In later periods of the run, where the ELT is longer, the S2 signals are larger and, hence, saturation occurs at lower recoil energies.

The data chosen to determine the CES and energy resolution in the previous section, as well as for the analyses in the following sections, corresponds to the run 12 period after July 2013. There are two main reasons by which this choice

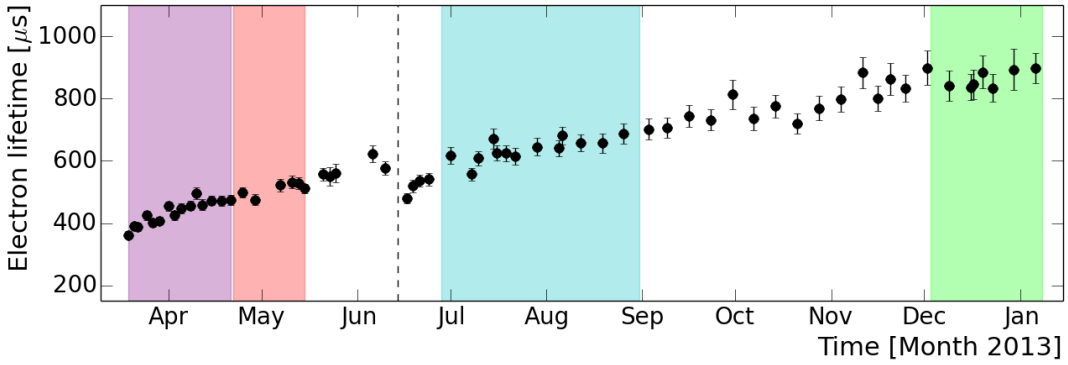

Figure 3.17: Evolution of the electron lifetime (ELT) in run 12. The shaded color areas correspond to the periods in figure 3.16. A higher ELT allows for larger S2 signals at a given recoil energy—which, in turn, saturates the S2 signals at lower energies. The increase of the ELT causes the observed shift in the background spectra when using the same CES. The dotted line indicates the malfunction of a valve that caused a decrease in the LXe purity—directly affecting the ELT.

was made. The first is that, as already mentioned, working with a large period in time reduces the energy resolution and precision of the spectrum, because one CES is not effective over a full run with changing conditions. The second reason is to avoid the activated Xe lines after AmBe calibration, which remain for up to several weeks. This is mostly relevant when comparing to the Monte Carlo simulations in the following sections.

Another factor that can change during a run is the radon concentration in the LXe. Figure 3.19 shows the evolution of the radon activity during run 12. These values are a result of the alpha and BiPo analyses described in [132]. The Rn concentration is estimated from the measurement of α decays and BiPo tagging in the uranium chain (shown in figure 3.4). A value of $\sim$44 μBq/kg has been determined as a mean of the periods before May 15th and after December 5th 2013. In between, the Rn activity concentration increased to $\sim$73 μBq/kg due to an air leak which was eventually solved by bagging the vacuum pump at which the leak was identified.

A comparison between two spectra taken during periods with different Rn concentrations is shown in figure 3.18. The spectrum with 73 μBq/kg corresponds to the period between August 27th and December 1st 2013, while the spectrum with 44 μBq/kg combines the periods before May 15th and after December 20th 2013. The ratio plot shows that there is about a 10 % higher event rate in the latter spectrum at energies below $\sim$600 keV, where the Rn contribution is most significant. In the following studies, in which the data is compared to the simulations, the Rn level will be of relevance. The data selected for comparison is that with the 73 μBq/kg activity concentration, shown in figure 3.18.

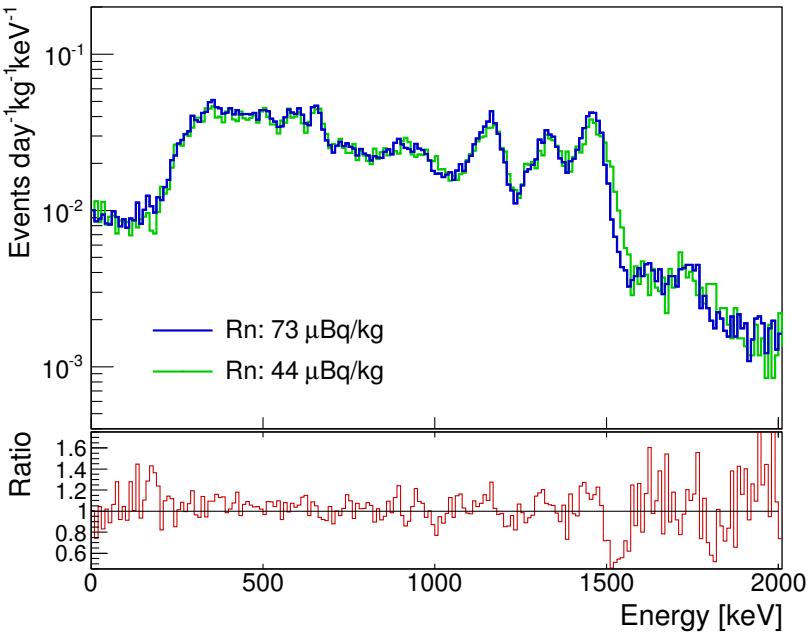

Figure 3.18: Comparison between two spectra of run 12 with different Rn levels. The spectrum with 73 μBq/kg corresponds to the period between August 27th and December 1st 2013, while the spectrum with 44 μBq/kg combines the periods before May 15th and after December 20th 2013 (see figure 3.19). The ratio plot shows a higher event rate in the latter spectrum of about 10 % at energies below ~600 keV—where the Rn contribution is most significant. The FV used is 20 kg.

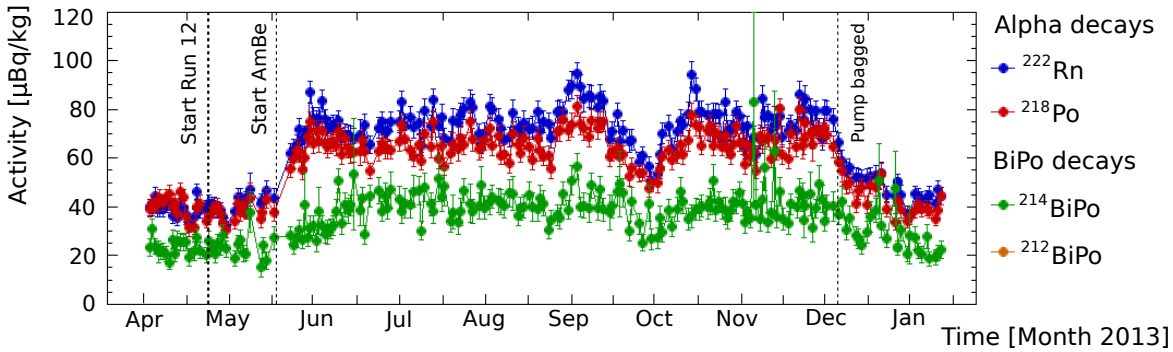

Figure 3.19: Evolution of the Rn levels in run 12. The Rn concentration is estimated from the measurement of α decays and BiPo tagging in the uranium chain shown in figure 3.4. This data is a result from an analysis performed by Marc Weber [132]. The Rn level shows an increase after May 15th due to an air leak which was eventually solved on December 3rd by bagging the vacuum pump where the leak was identified.

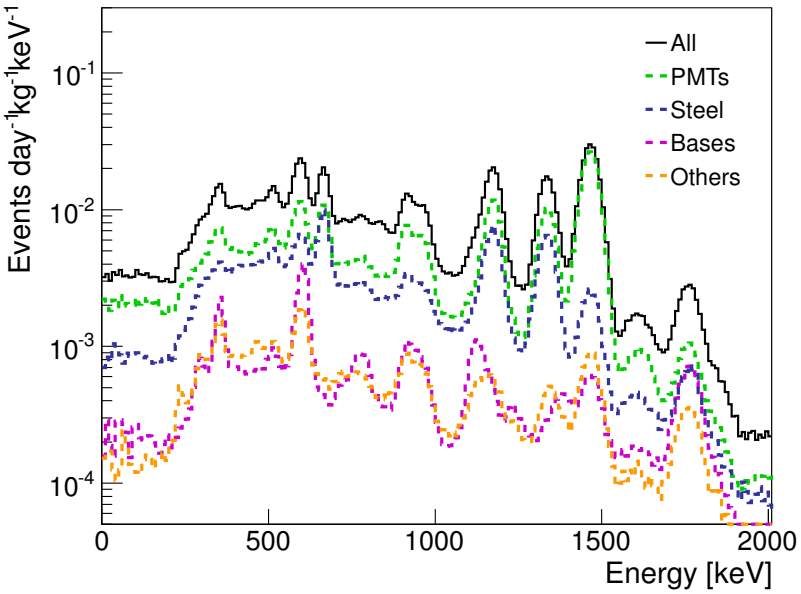

Figure 3.20: Monte Carlo spectrum from the radioactivity in the XENON100 materials. The energy resolution of the detector (equation 3.14) has been applied to the simulation data. The main contribution to the background comes from the PMTs (green dotted line)—followed by the stainless steel (blue dotted line), which includes components such as the cryostat vessel and the bell. The bases for the PMTs (magenta) have a contribution which is about an order of magnitude lower, at the same level as the sum of the remaining components—cables, PTFE, polyethylene, copper, etc.

3.3.6 Matching the XENON100 data to the Monte Carlo

Understanding the detector and its backgrounds is crucial for the interpretation of the measurements and results obtained with XENON100. A detailed model of the detector has been previously developed in GEANT4 and described in [123]. Along with the radioactivity of its various components (see section 3.2.1), the background event rate has been simulated for comparison with the measured data, scaling the MC with the screening results from table 3.1. Upper limits in the screening results have been implemented as fixed values for the scaling.

The simulated spectrum of recoil events produced by the radioactivity of the materials of the detector is shown in figure 3.20. The spectrum has been smeared with the Gaussian function in equation 3.14, using the energy resolution determined from calibration sources in section 3.3.4. The individual contributions of some elements—such as the PMTs, the stainless steel components and the PMT bases—are also shown. The largest contributors to the background are the PMTs, including both the top and bottom arrays. A high radio-purity of the materials used in these devices is difficult to obtain. In addition, the PMT arrays are

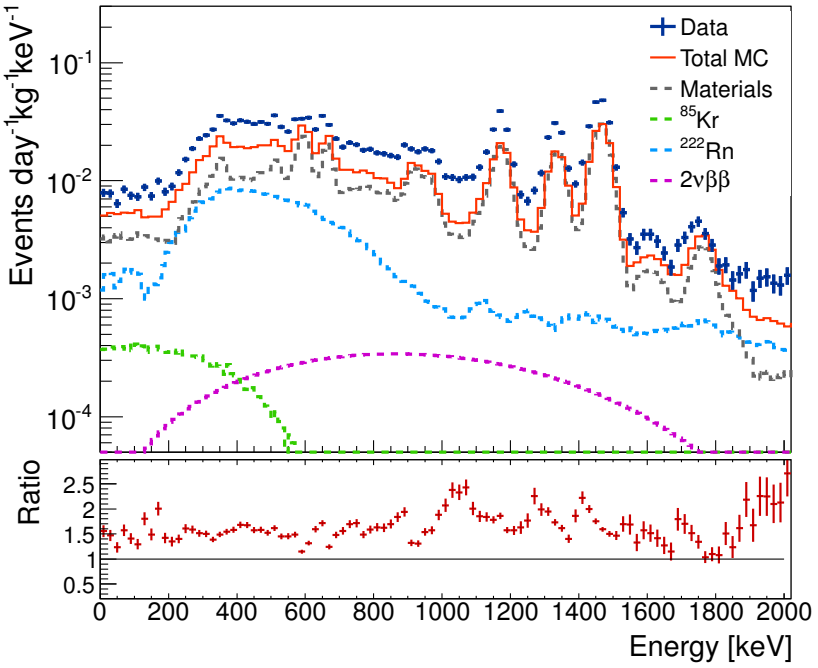

Figure 3.21: Comparison between the measured event rate in run 12 (blue data) and the total Monte Carlo spectrum for a 15 kg FV (orange). The MC includes the radioactivity from the detector materials (gray), a ^{222}Rn activity concentration of 73 μBq/kg (cyan), the ^{85}Kr contribution at the level of 10 ppt (green) and the $2\nu\beta\beta$ background (magenta) from the decay of ^{136}Xe, with a half-life of 2.17×10^{21} y.

in close proximity to the detection volume. In particular, the PMTs contribute the majority of the ^{40}K and ^{137}Cs. Following in activity are the stainless steel components, including the cryostat vessel and the diving bell structure. With a considerably lower activity—but still at a relevant level—comes the contribution of the PMT bases (PCBs of the voltage divider circuit used to bias the PMTs and extract the signal) in account of the resistors and capacitors assembled on them. The remaining contribution encompasses the rest of the detector components, including the cables and the PTFE, polyethylene and copper shields.

In order to compare the simulations with the measured data, the backgrounds from sources intrinsic to the LXe, such as ^{222}Rn and ^{85}Kr, have been added to the MC. Figure 3.21 shows the total MC event rate compared to the run 12 data in a 15 kg FV. The ^{222}Rn level included in the MC corresponds to an activity concentration of 73 μBq/kg. This is equivalent to the mean value estimated from figure 3.19 for the period under study. The mean ^{85}Kr level, over the same time period, is around 10 ppt and has also been included. Although having a very small contribution, the background from the $2\nu\beta\beta$ decay of ^{136}Xe has also been taken into consideration. The half-life for the decay has been taken as 2.17×10^{21} y,

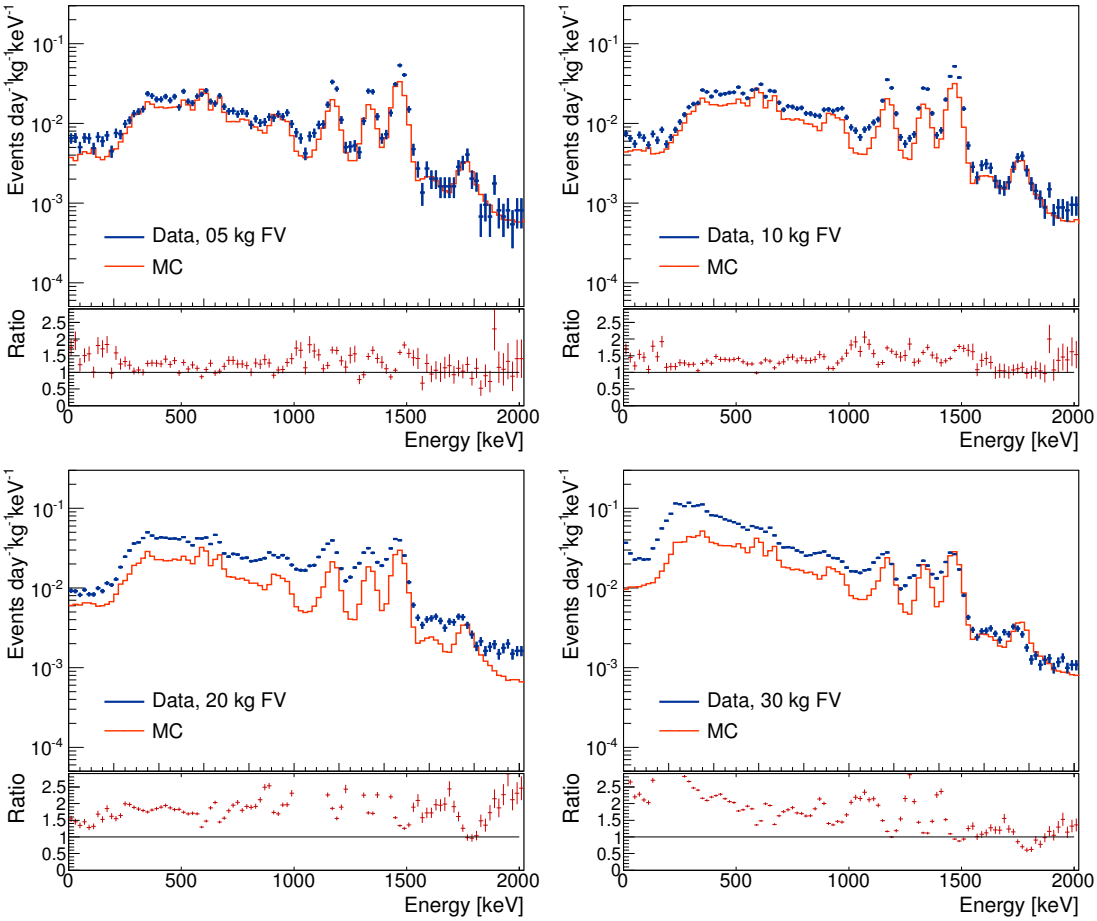

Figure 3.22: Comparison between the measured event rate (blue data) and the MC background spectrum (orange) for different FVs. Defined in figure 3.6, the FVs share the same z coordinates and differ only in radius. The volumes shown correspond to 5, 10, 20 and 30 kg. The 15 kg FV is shown in figure 3.21.

according to [108]. The ratio plot in the bottom panel of figure 3.21 shows the difference between the total MC and the measured data.

The MC and data comparison has also been studied for several FVs, as shown in figure 3.22. The cylindrical volumes have been previously defined in figure 3.6. they share the same z coordinate, but differ in radius. For the smallest volume (5 kg) the ratio is close to 1, indicating a good agreement. For the 10 and 20 kg volumes, the mismatch increases over the whole spectrum. For 30 kg, however, the peaks above 1 MeV show an adequate match, but the rate difference below 500 keV has increased to a factor of 3. These discrepancies may be attributed to different reasons. First of all, it can be that the scaling factors used for the ^{222}Rn, ^{85}Kr and/or material activities must be modified. In addition, the estimation of the ^{222}Rn activity does not have a 100 % efficiency, which allows

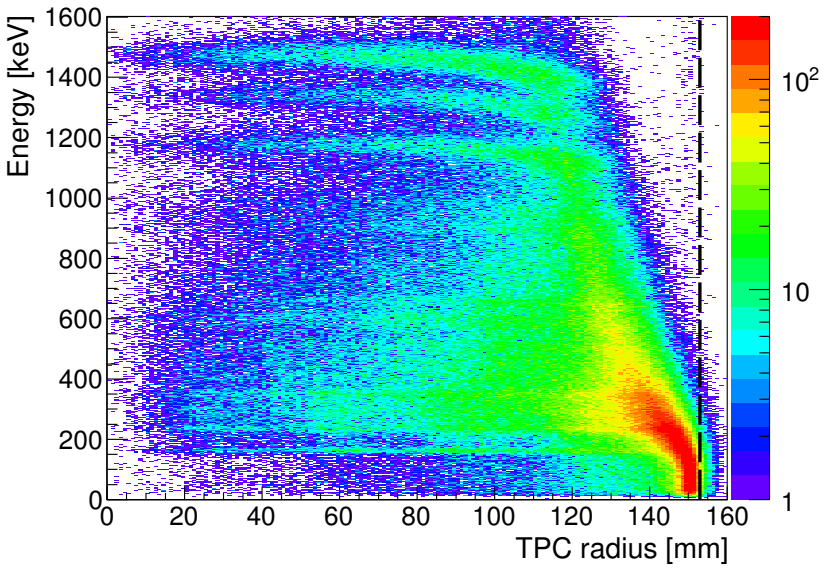

Figure 3.23: Background spectrum displaying the events of run 12 as a function of their energy on the vertical axis (using the CES) and the reconstructed radial position on the horizontal axis. The vertical dashed line indicates the border of the TPC. It can be observed that as the energy of the events increases, so does their shift towards the inside of the TPC. This effect is caused by the event position reconstruction being affected by the saturation of the top PMTs.

for the possibility that the actual radon contribution is higher. There is also an uncertainty in the material screening results, especially for the PMTs, since not 100 % of them were screened. Another factor, affecting mostly the event rates at higher energies, is the error in the event position reconstruction due to saturation of the PMT signal. The shifting of events, due to a mis-reconstruction of the interaction vertex, will change the population within a certain radius and, hence, the measured rate (see figure 3.23). This effect is studied in the following section, before considering a modification of the MC scaling factors.

3.3.7 Effect of the PMT Saturation on the Event Position Reconstruction

Saturation of the S2 signal on the top PMTs—which are used to determine the (x, y) coordinates of an event—contributes to a mis-reconstruction of the event position. If the reconstructed events are shifted in the radial direction, the event rate measured for a given fiducial volume will change with respect to the simulated rate. The following analysis explores the effect of the event position reconstruction on the background rate in a given FV. The result is shown to be an influencing factor in the observed mismatch between the measured data and

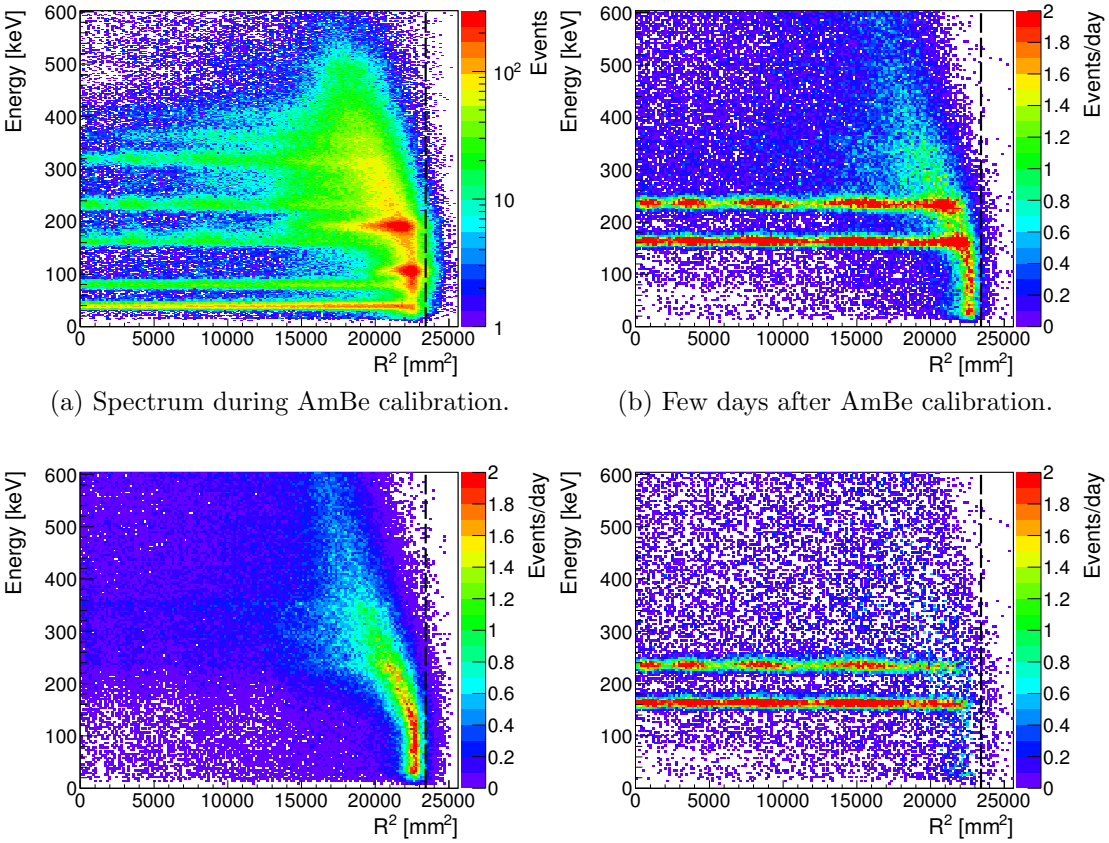

(a) Spectrum during AmBe calibration.

(b) Few days after AmBe calibration.

(c) Spectrum at a later period, in which the activated Xe lines have disappeared.

(d) Subtraction of figures (b) and (c).

Figure 3.24: Isolation of the 164 and 236 keV ^{Act}Xe lines after AmBe calibration, where the events have distributed homogeneously throughout the TPC volume.

the simulated data (for which no PMT saturation occurs). The rate variation will be studied at different energies and FV radii. With this, a correction factor will be determined—as a function of energy and radius—to be implemented on the simulated data to account for the mis-reconstruction observed experimentally.

The background events of run 12 are shown in figure 3.23 as a function of their energy (in CES) and reconstructed radial position in the TPC. It can be observed that, at higher energies, the reconstructed position of the events is shifted towards the center of the TPC. This suggests that for a FV with a given radius, more events are being reconstructed towards the inside of the volume than in the case of the simulated data. This observation is in agreement with the results presented in the previous section.

In order to construct a correction factor as a function of energy and radius, the measured event rate will be studied for different calibration sources and FVs. The first analysis will be performed with the activated Xe lines from the AmBe calibration. Figure 3.24 (a) shows the AmBe spectrum—with its 40, 80, 164, 236

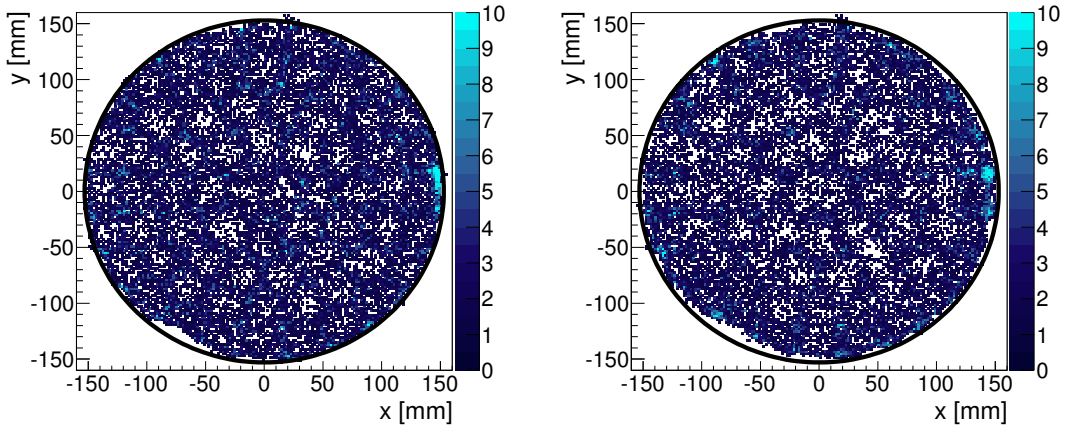

Figure 3.25: Reconstructed event positions for the energy lines at 164 keV (left) and 236 keV (right). The reconstruction algorithm has agglomerated events between the PMTs of the top array.

and 320 keV lines—as well as the additional lines from ^{19}F. The inwards event shift will be quantified by comparing the measured rate to the expected rate of a homogeneous distribution throughout the whole TPC. For this, only the 164 and 236 keV lines can be used since they have relatively high half-lives—around 12 and 9 days, respectively—giving enough time for the events to have distributed evenly throughout the volume of the TPC. Figure 3.24 (b) shows the background data in the days following the AmBe calibration, where only the two activated Xe lines remain. In order to isolate these events from the rest of the background, the spectrum in figure 3.24 (c)—corresponding to a later period in which the activated Xe lines are no longer present—is subtracted bin-by-bin, resulting in the isolated lines shown in figure 3.24 (d).

Over the course of several days, the decay events of the 164 and 236 keV lines of ^{act}Xe are expected to be distributed homogeneously throughout the volume of the TPC. Figure 3.25 shows the (x, y) distribution of the reconstructed event positions, where it can be seen that their distribution is, in fact, not completely homogeneous. The events have been mostly reconstructed in the spaces between the PMTs. This is a feature of the neural network reconstruction algorithm, which weighs the contribution of each PMT and will place the event vertex between them if the weights are comparable (see reference [129]).The question now is whether there is also a substantial shift of these events in the radial direction. To answer this, the events in the 164 and 236 keV energy lines have been plotted as a function of the radius squared (R^2) in the left plots of figure 3.26. The agglomeration between the PMT rings shows up as bumps in an otherwise flat distribution. There is also a slight inwards shift of the events, most noticeably at the border of the TPC. The right plots in figure 3.26 show the integrated events as a function of R^2.

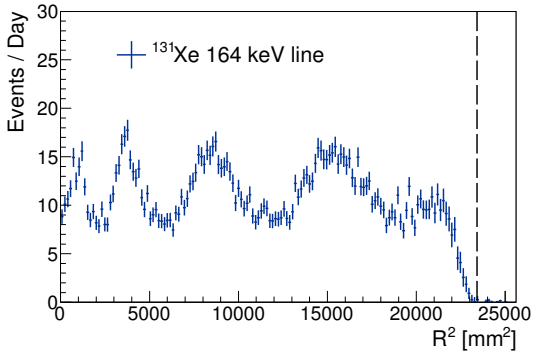

(a) Radial distribution of the reconstructed event positions for the 164 keV line.

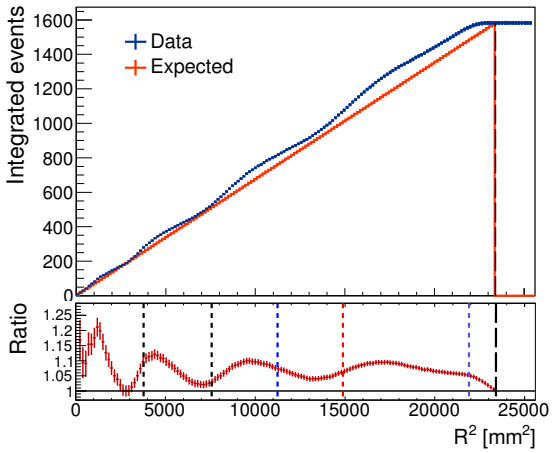

(b) Integrated events as a function of R^2 in the TPC for the 164 keV line.

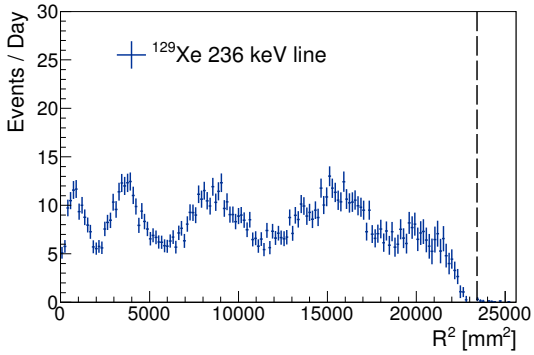

(c) Radial distribution of the reconstructed event positions for the 236 keV line.

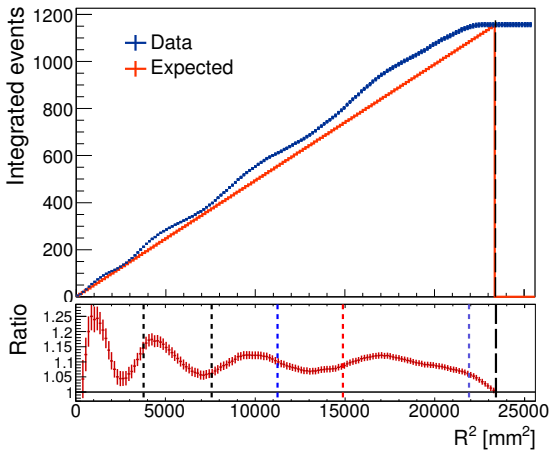

(d) Integrated events as a function of R^2 in the TPC for the 236 keV line.

Figure 3.26: A homogeneous event distribution throughout the TPC is expected for the decays of ^{act}Xe after AmBe calibration. The left plots show, however, that there is a position reconstruction bias between the top PMT rings, as well as a slight shift towards the inside of the TPC. The right plots show the integrated events as a function of R^2. A comparison is made with the expected behavior of a homogeneous distribution. The ratio indicates the factor by which the experimental data differs from the expected result. The vertical dotted lines indicate the radii of the FVs in figure 3.6.

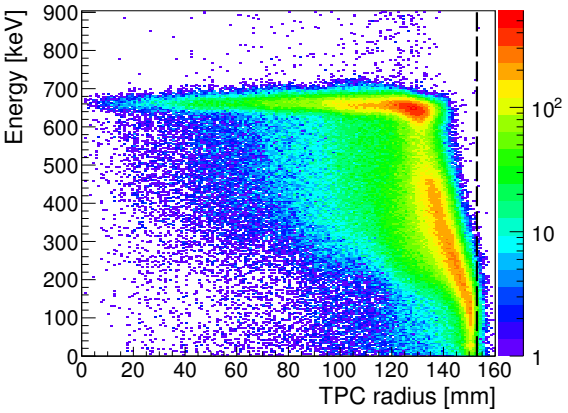

(a) Spectrum of ^{137}Cs data as a function of energy and reconstructed event radius.

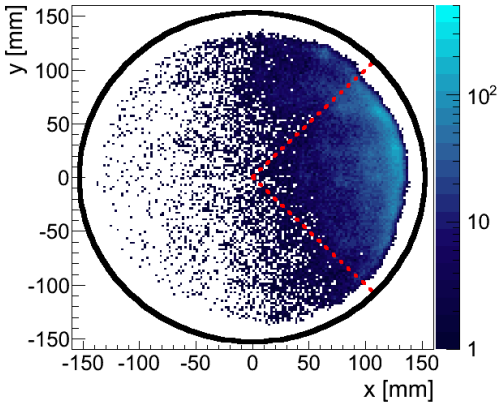

(b) Reconstructed position of events in the 661 keV line of ^{137}Cs at the red location.

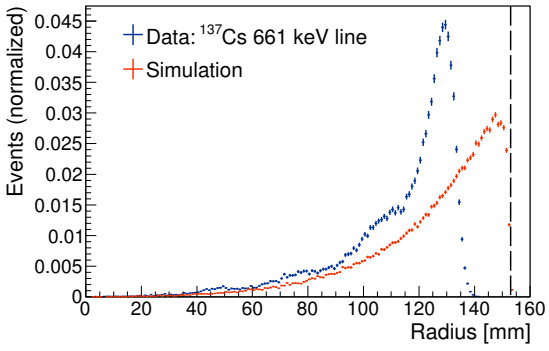

(c) Radial distribution of the reconstructed event position for the 661 keV line.

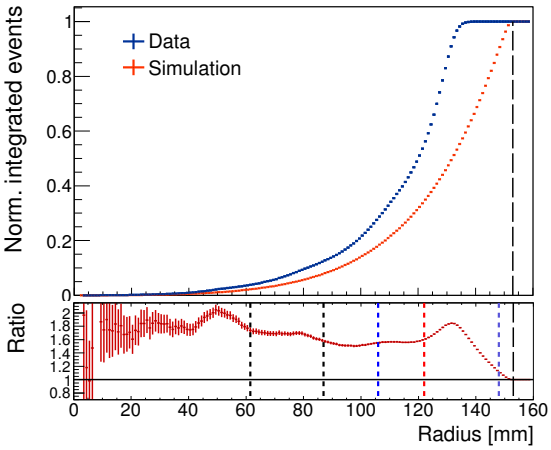

(d) Integrated events as a function of R^2 in the TPC for the 661 keV line.

Figure 3.27: Comparison between the measured and simulated event rates as a function of radius from ^{137}Cs data. Figure (c) shows an inwards radial shift of the reconstructed event positions for the 661 keV line. The ratio of the measured and simulated integrated events in figure (d) indicates the factor by which the simulated rates can be corrected to compare with the experimental results.

If the events were homogeneously distributed, a steady rise would be expected as the events are integrated with increasing radius. As seen in the ratio plots in figure 3.26, this is not the case for the reconstructed event positions. The ratio between the measured and expected integrated rates indicates the fraction by which the outer events are being reconstructed into the volume delimited by a given radius.

A different approach has been adopted for the calibration data at higher energies. The decay events of ^{137}Cs are not expected to be homogeneous within

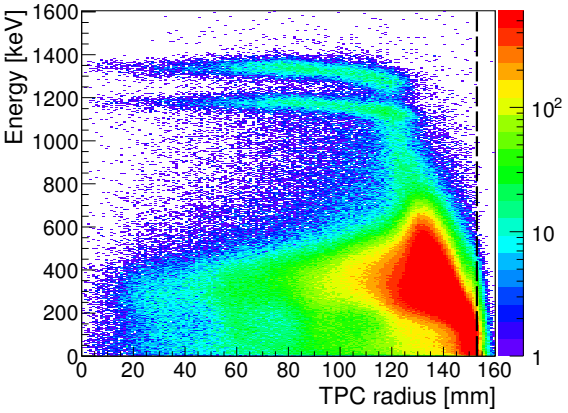

(a) Spectrum from ^{60}Co data.

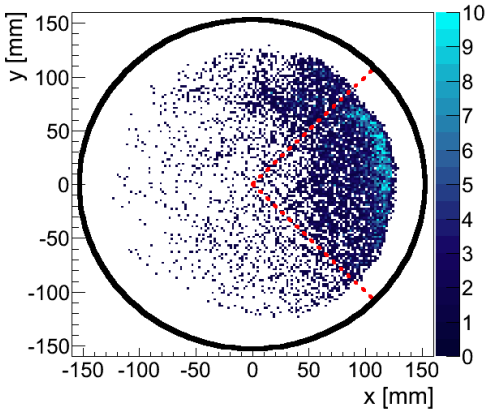

(b) 1173 keV line event positions.

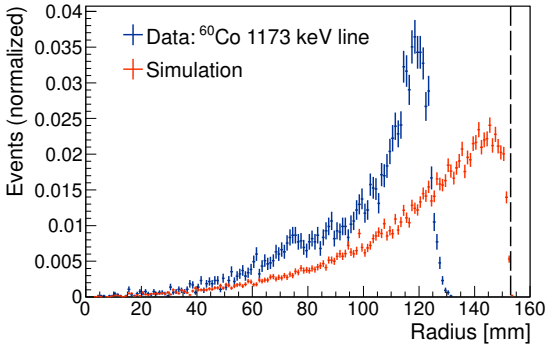

(c) Radial distribution of the reconstructed event positions for the 1173 keV line.

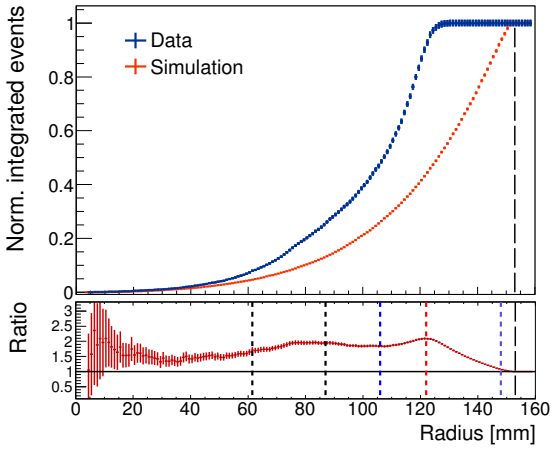

(d) Integrated events as a function of R^2 in the TPC for the 1173 keV line.

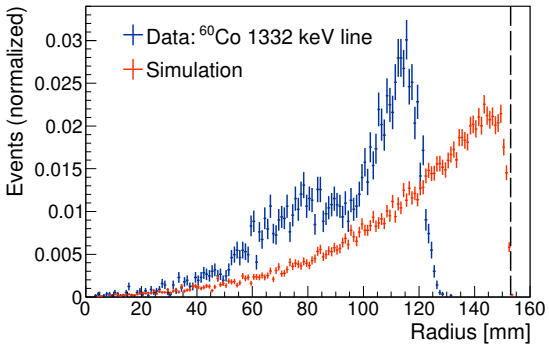

(e) Radial distribution of the reconstructed event positions for the 1332 keV line.

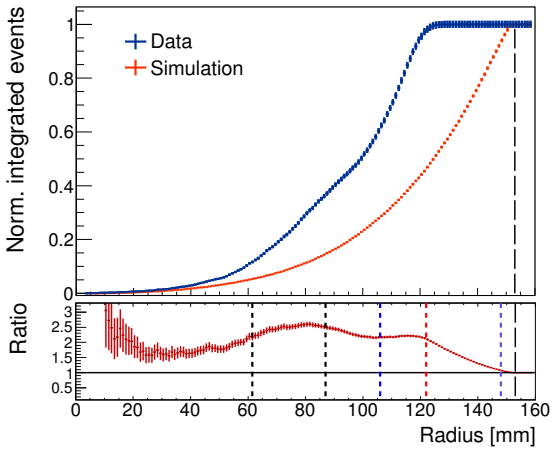

(f) Integrated events as a function of R^2 in the TPC for the 1332 keV line.

Figure 3.28: Event rate as a function of radius for ^{60}Co data compared with the results from simulation. An inwards radial shift of the reconstructed event positions can be observed on the left figures. The right figures show the ratio between the measured and simulated integrated events as a function of radius.

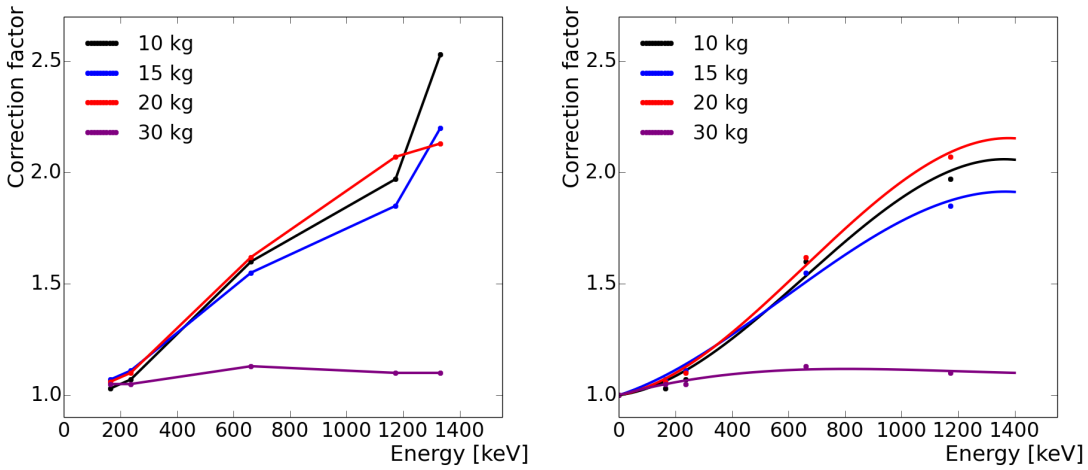

Figure 3.29: (Left) Correction factors as a function of energy for different fiducial volumes. (Right) Polynomial fit to the data which best describes the expected behavior. The last datapoints have been excluded and the $(0, 0)$ datapoint has been included, according to empirical considerations.

the active volume since the source is located on the outside of the TPC and the event rate decays exponentially with the distance from the source. In this case, the measured data is compared with the results from simulations. Figure 3.27 (b) shows the reconstructed position of events from ^{137}Cs data at the red source position (see figure 3.8). The radial coordinate of these events is compared with those from a simulated source at the same location, as shown in figure 3.27 (c). There is a clear shift towards inner radii for the position of the measured events compared to the simulated ones. Figure 3.27 (d) shows the integrated events as a function of radius, along with the ratio between data and simulation. Once again, the ratio indicates the factor by which the simulated rate measured for a volume with a given radius can be corrected to match the results of the experiment, in this way accounting for the reconstruction error caused by PMT saturation.

The same approach is taken for the ^{60}Co energy lines. Once again, the calibration data at the red source position is used. Figure 3.28 shows the results for the 1173 and 1332 keV lines. With this, a total of 5 energy lines have been used for the study. Figure 3.29 (left) summarizes the resulting data points for the correction factors as a function of energy for the different FVs under consideration.

These results can be used to construct a correction function that can be applied to the MC to attempt a better matching with the XENON100 data. Such a function has been determined from the data points, along with some empirical assumptions—such as a null correction at zero energy, and a flat correction at energies above 1 MeV. The results for different FVs are shown in figure 3.29 (right), where the fit functions are of the form: $Ax^3 + Bx^2 + Cx + D$.

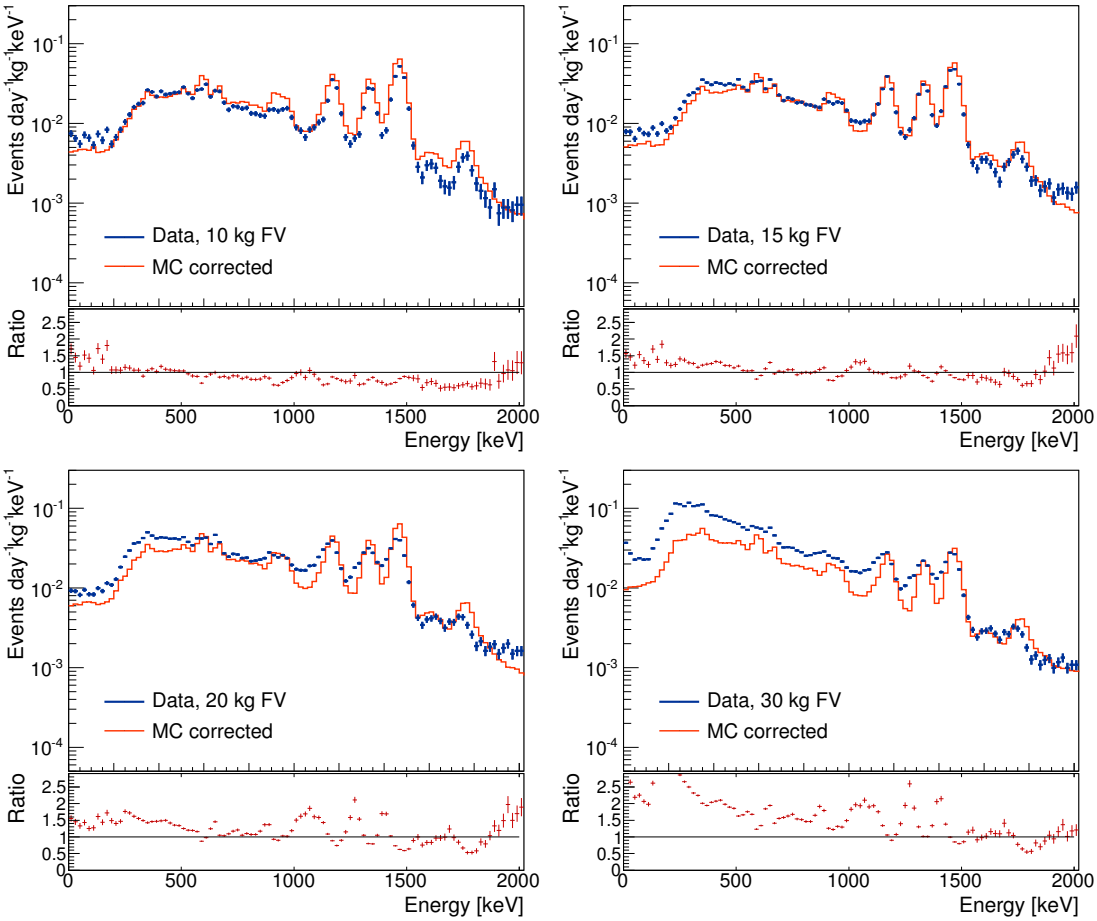

Figure 3.30: Comparison between the measured event rate (blue data) and the MC background spectrum (orange) for different FVs. A correction has been made to the MC in order to take into account the shift in the reconstructed event positions from PMT saturation in the XENON100 data. The correction function for each volume is shown in figure 3.29 (right).

3.3.8 Improving the Agreement between the Measured and Simulated Background Spectra

The implementation of the correction functions from figure 3.29 (right) to the MC data yields the results shown in figure 3.30. From the comparison to the measured data, it can be seen that the agreement between both spectra in the different FVs has been improved at energies above 1 MeV with respect to the results with the uncorrected MC in figure 3.22.

For energies below ∼600 keV, the measured event rate is still higher than the results from the MC, especially at larger radii. A possible explanation is that the contribution from the emanation of ^{222}Rn is larger than estimated by the BiPo analysis and α rates. In order to investigate this possibility, the ^{222}Rn activity

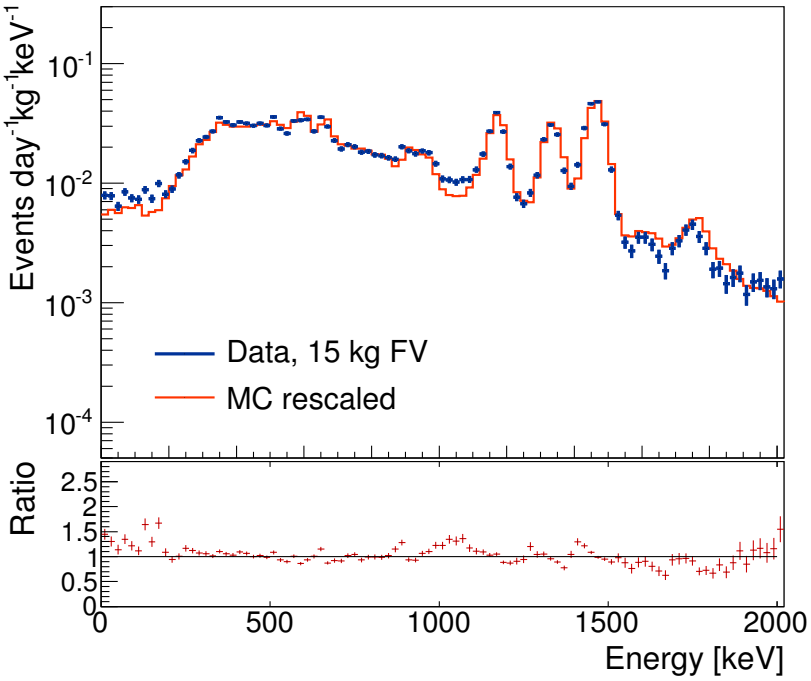

Figure 3.31: Comparison between the measured event rate in run 12 (blue data) and the total Monte Carlo spectrum for a 15 kg FV (orange). The correction from figure 3.29 (right) has been applied to the MC. The ^{222}Rn activity concentration in the MC has been scaled from of 73 to 146 μBq/kg. The ^{232}Th activity from the PMTs has also been rescaled by a factor of 0.6, through which the ^{228}Ac peak around 900 keV has been adjusted to match the data.

concentration in the MC has been scaled from 73 to 146 μBq/kg, with which the matching is improved considerably for the 15 kg FV spectrum, as seen in figure 3.31. Unfortunately, this scaling is still insufficient for the larger FVs (20 and 30 kg). It is thus plausible that an additional radioactive component close to the TPC walls remains to be taken into account in the MC. A possible candidate is ^{220}Rn. Its short life-time (55.8 s) prevents it from spreading homogeneously within the LXe volume and thus has a considerable effect near the TPC walls. The spatial distribution of α decays from radon studied in [132] shows a higher density of events at $r > 140$ mm. These α decays are most likely to be initiated by the emanation of ^{220}Rn from the PTFE surfaces. Since it is short-lived (and so is its decay product ^{216}Po), ^{220}Rn does not have enough time to move away from the TPC walls before decaying.

Other considerations for the optimization of the data and simulation matching have been explored. The contributions from the radioactivity of individual components of the detector, specifically from the PMTs, have been rescaled in the attempt to better fit specific energy lines. Since only 56 % of the top PMTs

and 89 % of the bottom PMTs were screened, the result of tuning their activities was investigated. The discrepancy in the ^{228}Ac peak (around 900 keV) has been adjusted by rescaling the ^{232}Th contribution of the PMTs by 0.6 (implemented in figure 3.31). The excess observed at 164 keV corresponds to events from activated ^{131}Xe that are still present in the selected data after the AmBe calibration. The peak can be further reduced by excluding a longer period of data, but in the current analysis the small excess has been tolerated in favor of a larger statistics for the spectra studied here.

In conclusion, the comparison between the MC simulations and the measured data has allowed to better understand the background sources in XENON100 during run 12. The saturation of the PMT signals has been shown to influence the measured event rate in a given FV. The effect has been studied and quantified, obtaining an energy and radius dependent correction factor. By implementing this correction to the MC data, a better matching with the experimental results has been obtained. The persistent mismatch at lower energies for the larger FVs indicates that a radial dependent contribution to the simulated event rate must be considered—possibly from ^{220}Rn. The background study and combined-energy-scale constructed from calibration data have been useful for the general analysis of run 12.

The full 153.6 live-days of run 12 (also known as science run III) were combined with the previous two science runs to provide a total exposure of 477 live-days. The XENON100 dark matter search results published in 2016 improved the previously reported exclusion limits by setting a maximum spin-independent WIMP-mucleus cross-section at $1.1 \times 10^{-45}\,\mathrm{cm}^2$ for a 50 GeV WIMP mass [96].

Chapter 4

Characterization and Performance of the XENON1T Photomultipliers

Photomultiplier tubes (PMTs) are extremely sensitive light detectors that can multiply the current produced by incident light by a factor of millions. This very high *gain* enables to measure the dimmest of light sources, all the way down to individual photons.

PMTs rely on two fundamental phenomena in order to function: the photoelectric effect and secondary emission. The former corresponds to the emission of electrons when light shines upon the PMT window. Electrons emitted in this manner are called *photoelectrons*. The latter corresponds to the ability of such photoelectrons to produce the emission of secondary electrons by striking an electrode in the vacuum tube. An avalanche is created as further multiplication occurs along various stages at increasing potential throughout the PMT.

Photomultiplier tubes have been around since the 1930s [133] [134] and, unlike most other vacuum tube technologies, are not obsolete. On the contrary, PMTs continue to play an essential role in a variety of fields—from science (astronomy, nuclear and particle physics), to medical diagnostics and imaging, to industry (high-end image scanning, radio jamming, oil well logging, etc). They owe their great success to a combination of high gain, low noise, ultra-fast response, and large collection area.

While semiconductor devices—such as avalanche photodiodes (APDs) and silicon photomultipliers (SiPMs)—are alternatives to PMTs, the latter still excel in low-noise applications, detection of imperfectly collimated light and large area detectors.

The Hamamatsu R11410-21 is the photomultiplier tube of choice for the XENON1T detector—being the latest in the R11410 series. A total of 248 tubes comprise the two PMT arrays of the TPC. With a 3-inch (76 mm) diameter window it provides the large area coverage required by the experiment (compared to the 1-inch R8520 used in XENON100). It has been designed for low-temperature

operation, down to -110°C, working stably in the cryogenic conditions of a LXe detector.

Being one of its major features, the R11410-21 counts with a greatly reduced intrinsic radioactivity level which is very important for rare-event detection, such as in dark matter searches. Of great importance is its high quantum efficiency (QE) at the xenon scintillation wavelength of 178 nm, with a mean value of 35% for the tubes installed in the XENON1T TPC [135]. Its 90% electron collection efficiency [136] ensures a high capability to detect VUV scintillation photons from particle interactions in xenon.

4.1 The Hamamatsu R11410 PMT

Figure 4.1 shows an illustration of the R11410 photomultiplier produced by Hamamatsu Photonics. The right diagram illustrates the various components of the tube, which are assembled according to the following general procedure of PMT production:

1. The individual parts are cleaned. The electrodes and window are treated prior to the following evaporation stage.

2. Antimony (Sb) is evaporated onto the electrodes and window, which will become the dynodes and photocathode of the PMT, respectively.

3. The electrodes are assembled to form the dynode chain and fixed with an insulator. The rest of the elements are put together inside the PMT body.

4. The window on the front of the PMT, as well as the stem at the back, are sealed by heating.

5. Through an opening at the back, the alkali materials are inserted in the PMT, guided magnetically and deposited on the heated surfaces of the dynodes and photocathode. This process is called *activation*.

6. Once all the components are in place and the PMT is completely sealed, *aging* is done by biasing the tube through the pins with a high voltage for several hours. This process stabilizes the output current of the photomultiplier before being operated for the first time [137].

7. The PMT is finally inspected to test its functionality and determine its performance.

In the following sections the main components of the phototube will be described along with the relevant parameters that characterize them.

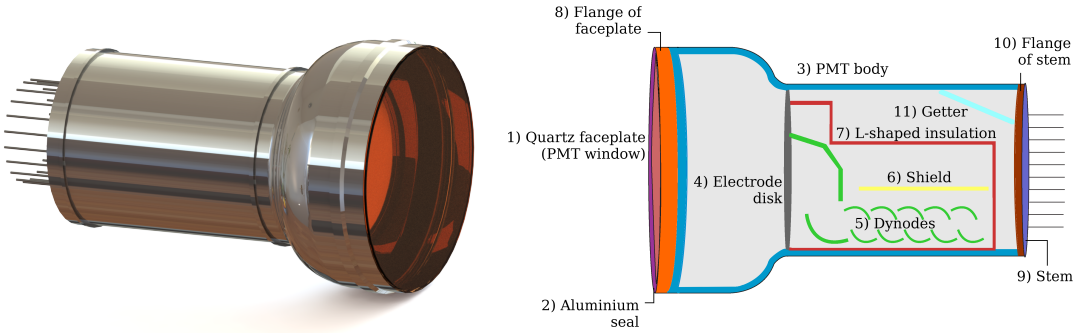

Figure 4.1: The Hamamatsu R11410 PMT and a schematic illustration of its various components.

4.1.1 The Photocathode and PMT Window

The PMT photocathode and window materials are selected based on their capability to induce the photoelectric effect and to transmit photons according to the wavelength to be detected.

Most photocathodes are made of compound semiconductors consisting of alkali metals with a low work function (energy required to remove an electron from a solid). There are above ten types of photocathodes currently employed in practical applications [138], available as a transmission (semitransparent) or a reflection (opaque) type, each with different characteristics in terms of spectral response and radiant sensitivity.

The R11410 models have a transmission photocathode of the *bialkali* type, meaning that two alkali metals are employed, along with antimony (typically Sb-Rb-Cs and Sb-K-Cs). That of the R11410 is denominated *low-temperature bialkali* and has been designed specifically for LXe operation, with an enhanced sensitivity at short wavelengths and maximum response at 175 nm. From the measurements of the PMT radioactivity reported in [139], it is speculated that K may be one of its components.

Even though most photocathodes have high sensitivity down to the ultraviolet region, the short wavelength limit is determined by the transmittance of the PMT window. VUV photons tend to be absorbed by most materials, such as borosilicate glass, which is the most commonly used window material but does not transmit radiation shorter than 300 nm. The R11410 PMT itself features a quartz (synthetic silica) window that transmits ultraviolet radiation down to 160 nm with low levels of absorption.

4.1.2 The Dynode Chain

There are also a variety of dynode types that provide a different gain, time response, uniformity and collection efficiency for secondary electrons [140]. These

features depend on the dynode structure and number of stages. The optimal type will depend on the application.

The R11410 is a head-on photomultiplier tube featuring a *linear-focused* dynode structure consisting of 12 amplification stages. The main features of this type of dynodes include fast time response, good time resolution, good collection efficiency and excellent pulse linearity.

The dynode chain is designed considering the trajectory of the electrons such that they may be efficiently collected and multiplied. Some electrons will, however, deviate from the optimal path and not contribute to the subsequent avalanche. The *collection efficiency* of a phototube is the probability with which photoelectrons will impinge on the surface of the first dynode. Although there is a probability that a few secondary electrons are not collected by the subsequent dynode stages, the effect on the total multiplication is very small—it is the collection on the first dynode which plays the greatest role in the formation of the electron cascade. These considerations are evident in the design of the R11410, as shown in figure 4.1, where the surface of the first dynode is largest, followed in size by the second dynode and then the rest of the stages.

4.1.3 Other Components and Development History

The material selection for the R11410 components was done with consideration of the low radioactivity levels needed in dark matter experiments and the requirement to maintain a tight sealing between the different elements after large temperature changes. Regarding the latter, the PMT window is made out of quartz while the stem pins (leads) are made of a Kovar alloy. Unfortunately, quartz has a greatly different thermal expansion coefficient than that of Kovar. For this reason other materials are needed to complete the stages in between. In the first R11410 version, borosilicate glass was used for the stem, while a standard Kovar alloy was used for the body. Both materials have very close thermal expansion coefficients, which is crucial for maintaining the PMT structure uncompromised when cooling down. As a dynode insulator, ceramic was used. The seal between the body and the quartz window was made with aluminium of standard purity.

Component	R11410	R11410-10	R11410-20	R11410-21
Stem	Glass	Ceramic	Ceramic	Ceramic
Body	Kovar alloy	Kovar alloy	Co-free Kovar	Co-free Kovar
Insulator	Ceramic	Quartz	Quartz	Quartz
Al seal	Std. purity	Std. purity	High purity	High purity

Table 4.1: Materials used for the main components across the different versions of the R11410 PMT. The -20 and -21 versions feature the same overall design, but the latter employs low-background materials selected specifically for use in the XENON1T experiment.

Further versions of the R11410 PMT have been developed in a joint campaign between the XENON collaboration and Hamamatsu, with the objective of minimizing the overall radioactivity of the final product [139]. The R11410-10 (originally delivered as R11410-MOD) featured a ceramic stem instead of borosilicate glass and a quartz insulator for the dynodes instead of ceramic. The next version, R11410-20, featured a Co-free Kovar alloy for the body and a high-purity aluminium seal at the window.

The final R11410-21 version has been assembled from low-background materials selected specifically for XENON1T, according to the results from their individual radioactivity measurements (see section 4.1 in [139]). Table 4.1 shows the evolution of the R11410 photomultiplier in its various stages towards a reduced radioactivity level.

4.1.4 The Voltage Divider Base

A voltage divider circuit is required to operate the PMTs, setting the potential difference between the photocathode, dynodes and anode for an optimal performance. The scheme with a grounded anode and a negative potential on the photocathode has been adopted. This allows to eliminate the voltage difference between the PMT anode and external components, which facilitates the connection of elements such as operational amplifiers, analog-to-digital converters (ADC), etc. In addition, if the faceplate or bulb near the photocathode were to be grounded, the slight conductivity of the glass material would generate a small current between the photocathode and ground, possibly causing damage to the photocathode. In the anode grounding scheme, however, proper insulation of the PMT window and body (at photocathode potential) is required to isolate them from external metallic components.

The resistor ratios between dynode stages suggested by Hamamatsu, along with the diagram of the voltage divider designed for the XENON1T PMTs are shown in figure 4.2. While the ratio between resistors for the different dynode stages optimizes the total gain of the PMT, the actual values are adapted to fulfill the heat dissipation and signal linearity requirements for XENON1T.

Linearity is the degree of proportionality between the output signal and the photoelectrons emitted at the photocathode of the PMT. A large dynamic range in terms of linearity allows to avoid saturation of large signals—an effect that impacts the data analysis, as has been discussed in section 3.3.7 for the case of XENON100. In addition to the resistor values, which limit the dynode current, capacitors are required in the final stages to avoid saturation and improve linearity. The final divider design includes 5 capacitors of 10 nF each—taking into account the capacitance reduction during operation at low temperatures.

The final resistor chain has been chosen with a 5 MΩ resistance as the basic unit, providing a compromise between good linearity and low heat dissipation. With a total resistance of $R_{tot} = 92.5 M\Omega$, the current at 1500 V is $I = 16.2 \mu A$. The power is thus $P = VI = 0.024\,W$ per base. For 248 PMTs, the total power

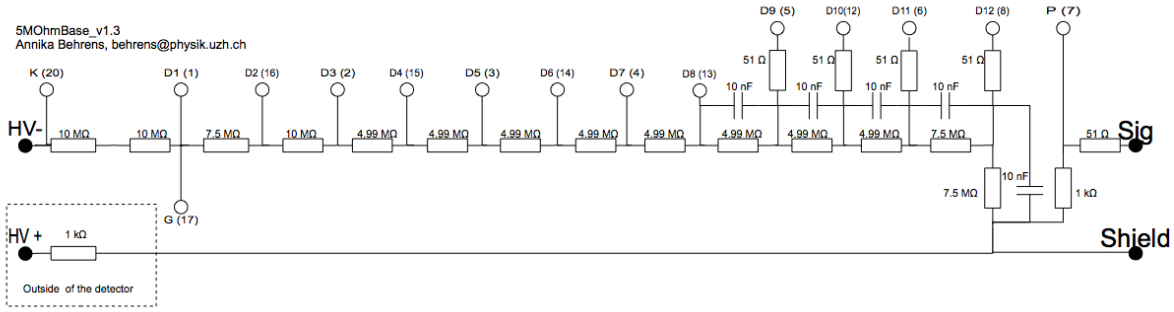

K/G-D1	D1-D2	D2-D3	D3-D4	D4-D5	D5-D6	D6-D7	D7-D8	D8-D9	D9-D10	D10-D11	D11-D12	D12-P
4	1.5	2	1	1	1	1	1	1	1	1	1.5	1.5

Figure 4.2: Design of the XENON1T voltage divider base with the values of the resistors and capacitors for each dynode stage. The table indicates the optimized ratios between stages given by Hamamatsu.

from the bases is around 6 W.

The base itself has shown good linearity up to the point where it is the analog-to-digital converter (ADC) which saturates first and not the base (see [130] for a detailed study of the base linearity). It is thus the ADC which ultimately limits the signal linearity.

The CAEN V1724 ADC used in XENON1T has an input voltage range of 0 - 2.25 V. Signals larger than 2.25 V will thus saturate. The current from such a signal is:

$$I_{max} = \frac{V_{max}}{R} = \frac{2.25\,\mathrm{V}}{50\,\Omega} = 45\,\mathrm{mA}$$

In order to have an idea of what this means for XENON1T—in terms of photoelectrons—a pulse of 1 μs will be considered (which is similar to the length of an S2 signal). Such a pulse can thus carry a maximum charge of:

$$C_{max} = I_{max} \cdot t = 45\,\mathrm{mA} \cdot 1\,\mu\mathrm{s} = 45\,\mathrm{pC} = 2.81 \times 10^{11} e^{-}$$

Dividing by the gain of the PMT and amplifier (assuming a combined gain of 2×10^7), the number of photoelectrons generating such a signal will be:

$$PE_{max} = \frac{2.81 \times 10^{11}}{2 \times 10^7} = 14050\,\mathrm{PE}.$$

The substrate of the voltage divider base and its components have been selected according to their radioactivity and cryogenic performance. Cirlex®, a polyamide material developed by DuPont, has been selected as the printed circuit board (PCB) material. The standard material commonly used for PCB production cannot be used due to its intrinsic radioactivity contamination, since

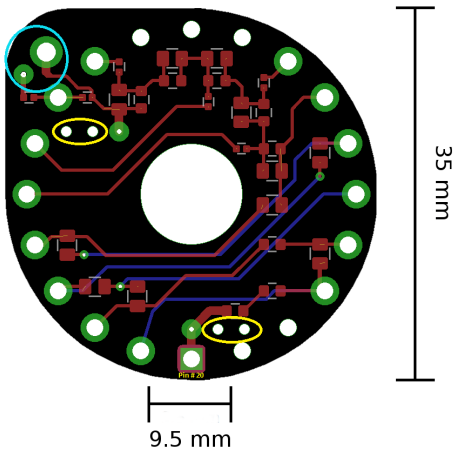

Figure 4.3: Layout of the voltage divider base for the XENON1T PMTs. The red and blue paths correspond to the circuits on the front and back side, respectively. The green contours indicate the location of the sockets for the PMT pins and the soldering points for the HV and signal cables. The holes within the yellow markers are the strain reliefs for the HV cables, while the cyan circle indicates the strain relief for the signal cable.

it is made of glass reinforced epoxy laminate sheets. Cirlex has similar physical, chemical, and electrical properties as Kapton®, but is available in thicker sheets (1.55 mm in the case of the XENON1T bases) and has an overall operating temperature range from -269°C to 351°C [141]. It has been used successfully in the XENON100 bases and has proven to perform adequately in LXe.

The resistors have been selected with a temperature coefficient of 100 ppm/°C and 1% tolerance to minimize the change in resistance during cryogenic operation. Ceramic capacitors have been preferred over PEN film capacitors. The former present a large loss of capacitance at low temperature, but the latter can be damaged during soldering due to a lower heat tolerance.

Each R11410-21 PMT has 15 pins to be connected to the voltage divider base. Two options have been considered for their assembly: soldering the pins directly to the base or having sockets on the base into which the pins can be inserted. The soldering option would reduce the total amount of radioactivity, since the sockets are the largest radioactive contribution of the base. But at the same time it introduces the risk of damaging the PMT with heat transfer during the soldering process, as well as reducing the flexibility to remove and exchange PMTs once installed in the XENON1T TPC. The choice was made to use lead free spring-loaded sockets, ensuring a high mechanical stability and a more practical coupling of the divider circuit to the PMT.

Figure 4.3 shows the final base design. The asymmetrical shape and the square pad, corresponding to pin 20 (cathode), serve as indicators to the correct coupling of the base to the PMT. The holes indicated with the yellow contours are strain reliefs. The HV cables pass through them, releasing the tension from the soldering points. This feature proved to be of utmost importance during the assembly and installation of the PMT arrays for XENON1T. A similar solution was implemented for the signal cable, in which the ground pad is used as strain relief (indicated in light blue).

A total of 336 bases were ordered and produced at the company Fralock in

2015. The circuits were printed on snap-out frames containing 21 bases each. The PCBs were then shipped to the Swiss company Elfab for the assembly of the components. Back at UZH, the resistance and capacitance of each base was tested, as well as the the current through the voltage divider. The bases were then sent again to Elfab, where the HV, ground and signal cables were manually soldered onto the circuits.

The PMT tests and measurements presented in section 4.3 also reflect the extensive evaluation of the XENON1T base, as several prototypes were tested for their performance, stability and durability in LXe. The final assembly of the bases onto the PMTs in the TPC arrays is described in chapter 5.

4.2 Testing Procedure and Experimental Setups

As mentioned before, the XENON1T TPC houses a total of 248 R11410-21 PMTs. Each tube has undergone a rigorous process of evaluation and the final selection constitutes the best performers out of 321 tested devices. The general testing procedure will be discussed next, followed by a description of the experimental setups. Detailed studies and their results are presented in section 4.3.

The PMTs have been produced at the Hamamatsu Factory in Japan. Once the PMTs have been shipped and received by the XENON collaboration, each tube is screened for its intrinsic radioactivity. The screening procedure is performed with high-purity germanium detectors at LNGS [139]. The average levels measured per PMT are lower than 0.4 mBq/cm^2 for ^{238}U and 0.012(3) mBq/cm^2 for ^{228}Th [139]. The impact of the PMT radioactivity on the XENON1T dark matter search is discussed in [102].

After screening, every PMT has been tested at room temperature and in a nitrogen atmosphere at around -100°C (temperature which will also be referred to as "cold"). The testing facilities at MPIK Heidelberg, which were used to measure the complete set of PMTs, are described in the following section 4.2.1. The general tests at MPIK served to verify the agreement of the PMT parameters with the production specifications. Such measurements include the gain, transit time, dark count and afterpulse rates. A characterization of the PMTs has also been performed, including the dependency of the gain to the applied voltage, the signal resolution and the afterpulse spectrum. A cryogenic test is also performed by cooling the PMTs down in cold nitrogen gas.

A selection of the tubes has been further tested in GXe and LXe at UZH. In the setups described in section 4.2.2, the PMTs have been operated over extended periods of time (from a couple of weeks to several months) and the dark count rate and gain evolution have been studied. Detailed afterpulse measurements have been performed to analyze the changes in the spectra after each cool down. The results have proven useful for vacuum quality diagnosis and a general understanding of the phototubes. These studies are discussed in section 4.4.

4.2.1 General Testing Facility

The experimental setup for room temperature measurements at MPIK is designed to test 12 PMTs simultaneously in a large Faraday cage. Each PMT is installed in a compartment equipped with an optic fiber connected to an LED emitting UV light at 380 nm. In this setup, several measurements are performed on the PMTs, such as a high voltage scan, evaluation of the response to single photoelectrons, spectrum of afterpulses and determination of the transit time. Further details regarding this setup can be found in [142].

Figure 4.4 shows a schematic of the setup for cryogenic tests. It consists of a cooling tank designed to operate the tubes at temperatures around -100°C. The volume is filled with nitrogen vapor and cooled by means of a copper coil carrying liquid nitrogen. Two arrays of PMTs—six on each one—are placed parallel inside the tank with the PMT windows facing each other. PT100 sensors are used to measure the temperature at several positions within the volume. These are used to monitor the conditions during the cool-down tests, which last up to several hours. Further details can be found in references [143] and [144].

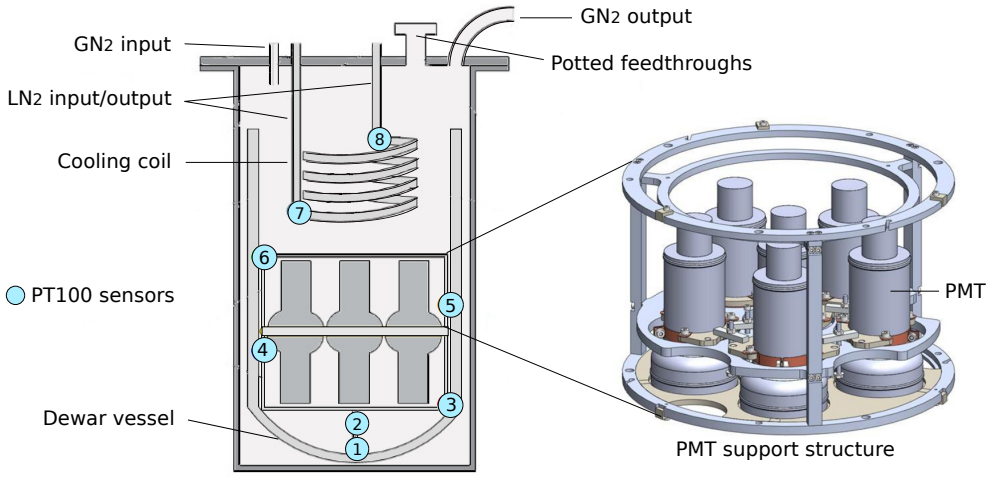

Figure 4.4: Illustration of the cryogenic setup for PMT testing at MPIK. The temperature of the nitrogen gas is stabilized at around -100 °C. A total of 12 PMTs can be operated simultaneaously, divided into two arrays. The PT100 sensors, of which the positions are indicated with numbers, monitor the temperature during cool down.

The data acquisition system used by both setups is described in [142] and briefly summarized here. The signals from a PMT are magnified by a ×10 amplifier and sent to a fan out. The signal is then split and read out by a charge-to-digital converter (QDC) with a resolution of $\Delta q = 97.6\,\mathrm{nC}$. After a second amplification by a factor 10, the signal is subsequently sent to a discriminator, after which it is processed by either a scaler or a time-to-digital converter (TDC).

The TDC has a maximal time span of $1.2\,\mu s$ with a time resolution of 0.3 ns. The outputs of the QDC, TDC and scaler are then read out and stored in a computer for analysis.

4.2.2 Xenon Testing Facility

Around 15 % of the PMTs have been tested at UZH in GXe and LXe for periods ranging from a couple of weeks up to several months. These tests have been performed to characterize the PMTs and test their stability under operational conditions similar to those in XENON1T. A small chamber called MarmotXS, capable of fitting a single PMT, was used to test the early versions of the R11410 tubes. A larger setup, denominated MarmotXL (figure 4.5), has been used to test the R11410-21 tubes for XENON1T, allowing to operate 5 PMTs simultaneously [1].

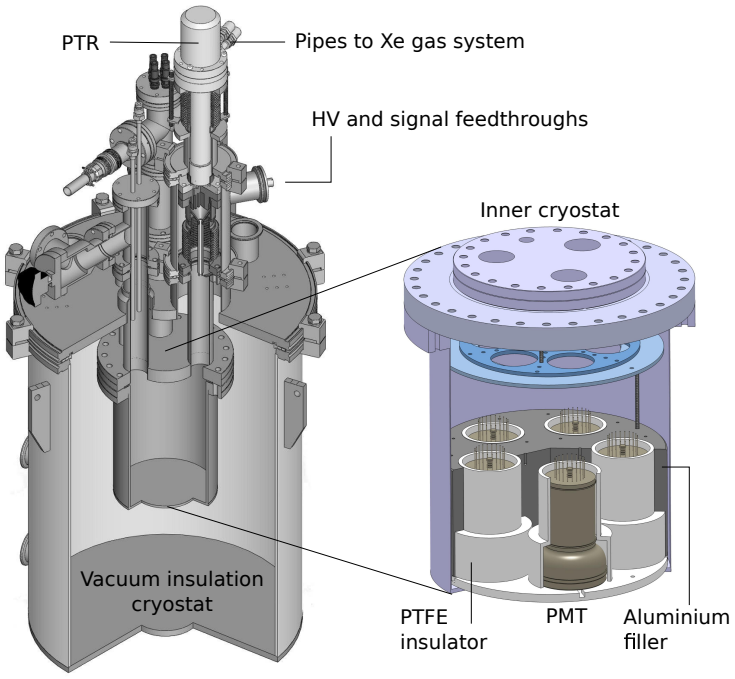

Figure 4.5: Illustration of the MarmotXL testing facility for PMTs in gaseous and liquid xenon. The inner chamber is vacuum insulated by a larger outer vessel. The cooling power for xenon liquefaction is provided by a pulse tube refrigerator. Up to 5 PMTs can be operated simultaneaously. An aluminium filler reduces the amount of LXe required to cover the PMTs, while the PTFE sleeves insulate the metallic bodies.

[1] The MarmotXL facility has since been upgraded to a larger version which can operate 10 tubes simultaneously, divided into two arrays. This setup is currently used to test replacements for XENON1T and the PMTs for XENONnT.

The MarmotXL Chamber

The MarmotXL testing facility consists of a double-walled vacuum-insulated cryostat capable of housing up to 5 PMTs simultaneously. The inner cryostat contains the 3-inch PMTs facing downwards onto a polytetrafluoroethylene (PTFE) reflector. A circular cut-out in the PTFE below is provided to optically couple the PMTs. The tubes are surrounded by PTFE insulators to separate them from an aluminium filler (see figures 4.6 A-B), which is used to minimize the amount of LXe required to cover the PMTs (∼2.5 kg). Two temperature sensors have been installed, one at the bottom of the chamber next to the PMT windows and another above the aluminium filler at the height of the PMT pins. A blue LED is installed in the common volume of the PTFE reflector between the PMTs. In addition, up to 4 optical fibers are placed close to that same location, coupled to a blue LED located outside of the cryogenic system. The inner chamber is vacuum-insulated with a larger cryostat, evacuated with a Pfeiffer HiCube 80 pumping station. The cooling power for xenon liquefaction is provided by a pulse tube refrigerator (PTR) Iwatani PDC08 (18 W at 77 K).

Xenon is filled into the inner chamber through the dedicated gas system shown in figure 4.6 (right). It is equipped with a PS3-MT3 MonoTorr heated getter to remove impurities. The gas flow is circulated with a built in pump, controlled with a flow meter and monitored on the displays.

Potted feedthroughs link the high voltage and signal cables from the PMTs inside the vessel to the external electronics for data acquisition. The voltage dividers used for the PMTs are those described in section 4.1.4, with the same design and components as those used in XENON1T. In addition, both the signal and HV cables in MarmotXL are the same 1.83 mm PTFE coaxial cables and AWG 30 single wire Kapton cables used in the PMT arrays of XENON1T (see figure 4.6 C). Custom connectors designed specifically for XENON1T have also been used and tested in this setup [145].

The MarmotXS Setup

The MarmotXS chamber (originally known simply as MarmotX) was designed to test one PMT at a time in LXe. A PTFE structure around the tube doubles as an insulator and a filler, reducing the amount of xenon required to fill the vessel. The PMT window is placed downwards into the xenon volume, resting on a PTFE ring over a PTFE reflector at the bottom of the chamber. The vessel is filled with ∼300 g of xenon, covering the PMT body in liquid while the pins and base remain in xenon gas.

For cooling, the MarmotXS chamber is placed a few centimeters above liquid nitrogen inside a dewar. The liquid level does not touch the chamber and only nitrogen vapor does the cooling. The temperature and pressure are monitored by PT100 sensors at the bottom, at the PMT photocathode, at the top and outside the chamber. An automatic system consisting of a solenoid valve on a large

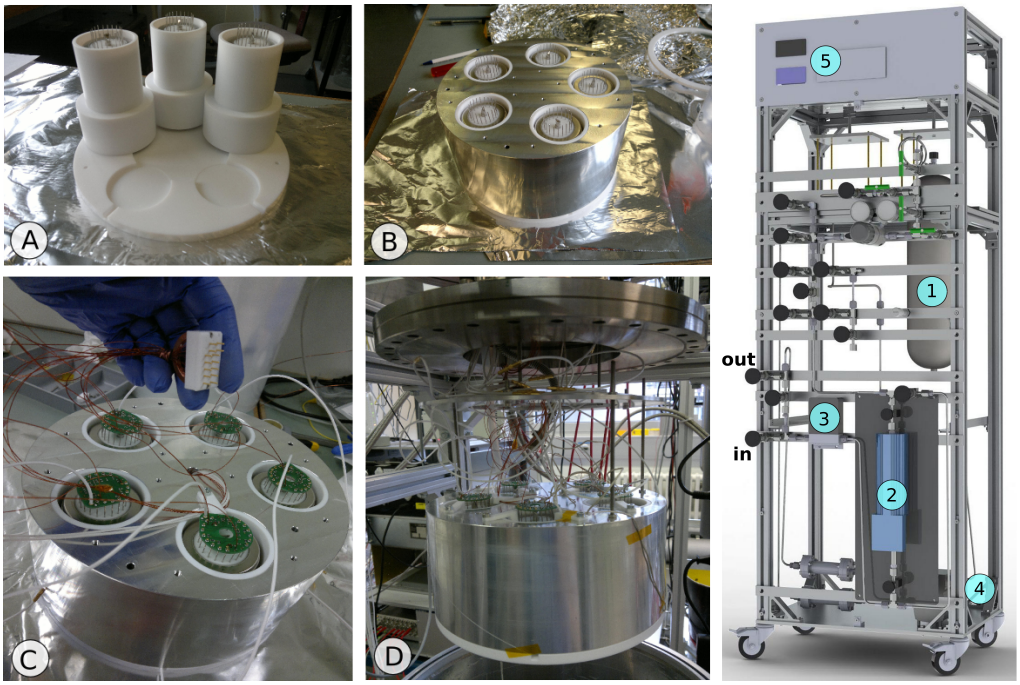

Figure 4.6: (Left) PMTs in MarmotXL. (A) PTFE reflector and insulators. (B) Aluminium filler. (C) PMT bases, cables and connector. (D) Inside MarmotXL. (Right) Xenon gas system. (1) Xenon bottles. (2) Getter. (3) Flow meter. (4) Circulation pump. (5) Displays.

nitrogen dewar refills the nitrogen level according to slow control parameters. The temperature is further stabilized by a 3 mm thick copper conductor providing a maximum of 25 W heating power.

This chamber was eventually replaced by the larger and more stable setup of MarmotXL. Nonetheless, relevant long-term stability measurements on R11410-10 phototubes have been performed with this system and are described in section 4.3.2.

4.2.3 Data Acquisition System

The PMT signal cables inside MarmotXL are connected to double-shielded cables outside the chamber that minimize the noise pickup. The signal amplitude for single photoelectrons from the R11410-21 is in the order of 5-10 mA, depending on the PMT gain and operating voltage. The typical rise time is around 5 ns with a fall time of 10 ns (figure 4.7). The PMT signal goes through various stages before acquisition depending on the measurement to be performed. The flow chart in figure 4.8 shows the signal acquisition process, with the colored lines indicating the different acquisition modes:

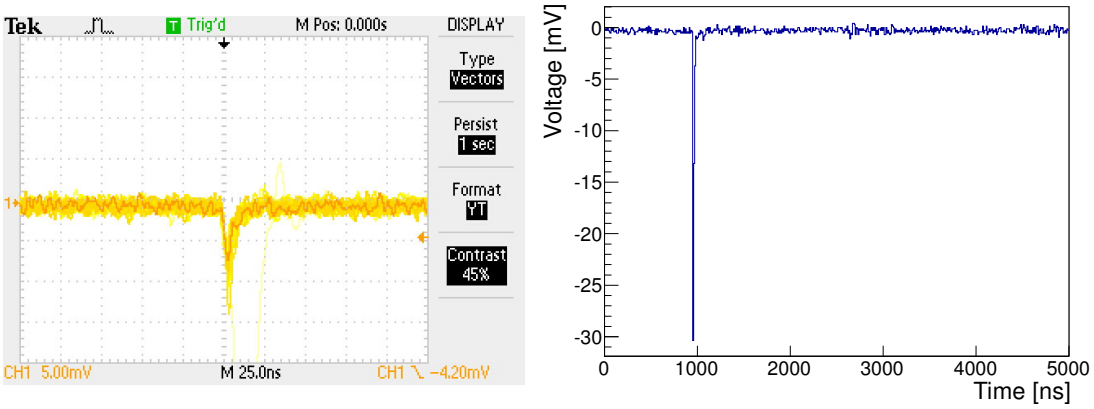

Figure 4.7: (Left) Single photoelectron signals as seen on the oscilloscope—in persistency mode—without amplification. (Right) Digitized waveform acquired with the ADC and a ×10 amplification.

Measurements with an LED light source (Blue path). The LED is driven by a BNC 505-4C pulse generator (pulser). In MarmotXL, the LED light is guided via PMMA (acrylic) optical fibers. The same system is implemented in XENON1T for PMT calibrations (see section 5.2). The PMT signal is amplified with a Phillips 776 ×10 linear amplifier (as in XENON100 and XENON1T). The output signal is digitized with a CAEN V1724 flash ADC: 8 Channels, 14 bits, 100 MHz sampling rate. The ADC is triggered via the LED pulser.

Self trigger measurements (Green path). The acquisition of PMT dark pulses is done with a ×50 signal amplification (Phillips 777 variable gain amplifier). This is done in order to trigger on the pulses themselves, since the LeCroy discriminator used to generate the trigger requires a minimum input of 30 mA. The dark pulse signal is then acquired via the ADC, as before, with the discriminator providing the trigger. Counting measurements **(red path)** are performed with a CAEN V260 scaler commanded via a CAEN V2718 crate controller.

The data acquisition software for the ADC board is called `miniDAX` and has been adapted for this work from the original version developed by Dr. Marc Schumann—itself based on the Wave Dump program by C. Tintori (CAEN). Data is stored as digitized waveforms of a given time window, as seen in right sample of figure 4.7. The raw data is processed via a program based on the `miniProcess` script developed by Annika Behrens (see [130]). For each waveform, the baseline value is estimated by averaging over the first 50 samples of the waveforms before the trigger. The baseline level is stored along with the standard deviation. A simple peak finder algorithm determines the presence of signals. This is done by means of a *high* and a *low* threshold set in a configuration script. When an excursion of the waveform above the high threshold occurs, it is

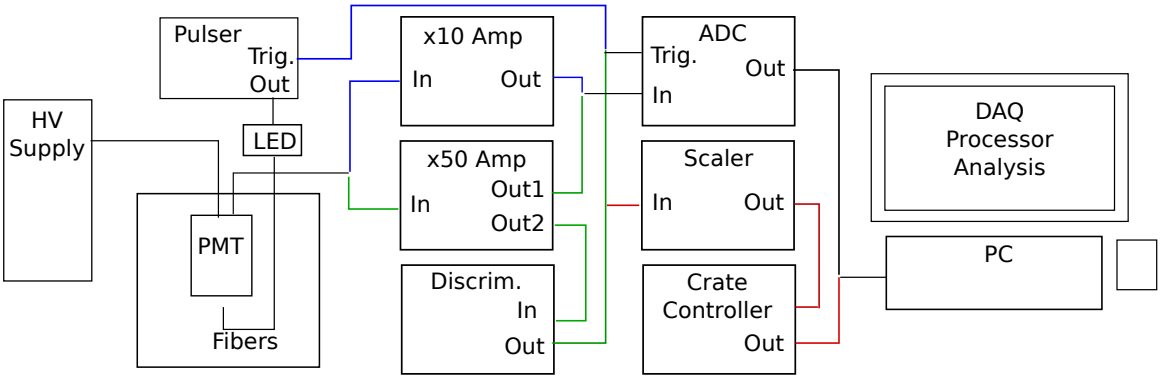

Figure 4.8: Diagram of the PMT signal processing and acquisition. The colored lines indicate different acquisition modes, according to the performed measurement.

labeled as a signal pulse. The beginning and ending of the signal are determined by the points at which the lower threshold is crossed in each case. The main properties saved by the processor for each signal include: time stamp (position), width, height and area. The processed data is stored in a `ROOT` file which is then accessed by dedicated analysis scripts in `C++` and `Python` for the various studies presented in the following sections.

4.3 Measurement of PMT Properties and Cryogenic Performance

4.3.1 Dark Count Rates and Stability

Even in the absence of a light source, a biased PMT produces output signals in the range of single PEs, called *dark counts* (DC). These signals are produced by thermionic emission of electrons, which occurs when the electron thermal energy overcomes the work function of the photocathode material. At cryogenic temperatures, a non-thermal DC remnant is still present due to electron field emission—an effect consisting of electrons emitted from a solid surface into a vacuum through quantum tunneling in the presence of an electrostatic field. For dark matter and neutrino searches, a low dark count rate is important to reduce the accidental coincidences between PMTs. These random coincidences may interfere with the measurement of scintillation events in such experiments and, hence, contribute to the background in the search of rare events.

The dark count rate of a PMT is the number of signals per second above a given threshold in the absence of light. The left plot in figure 4.9 shows an example of a typical DC rate measurement during a cooling cycle in the nitrogen cryogenic setup described in section 4.2.1. For these measurements, a threshold

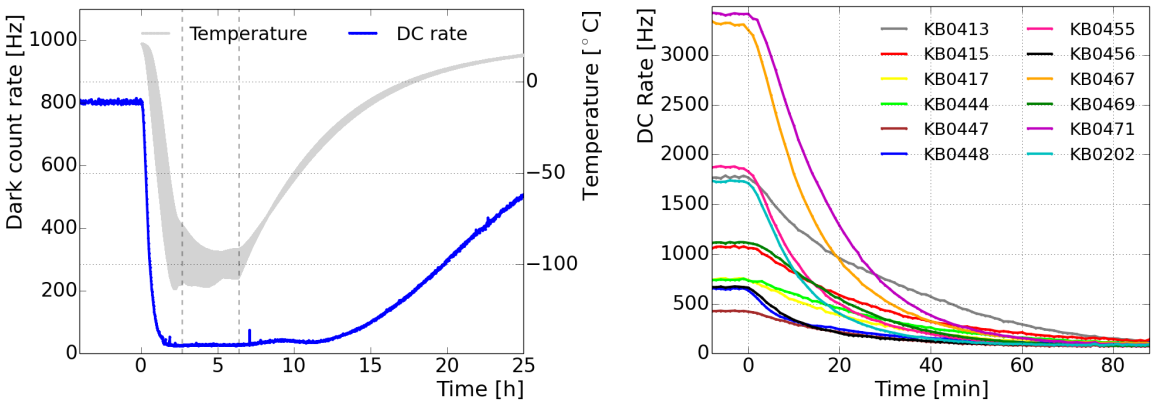

Figure 4.9: (Right) Evolution of the dark count rate over time (blue line) during a cool down in the MPIK cryogenic nitrogen setup. The gray shaded area indicates the temperature range between the top and bottom PMT arrays (Left) Dark count rates of 12 PMTs during a cool down in the MPIK setup. The steeper curves correspond to the top PMTs, which are closer to the cooling coil, while the bottom PMTs take longer to cool and display a slower decrease in DC rate.

of around $\frac{1}{4}$ PE has been used. The time evolution of the dark count rate is shown by the blue curve. The shaded gray area represents the temperature in the chamber, with the lower limit being the temperature at the bottom of the PMT arrays (sensor furthest to the cooling coil at position 3 in fig. 4.4) and the upper limit being the temperature at the top of the PMTs (closest to the cooling coil at position 6). At room temperature, the DC rates are in the order of several 100 Hz to a few kHz. The variation can be large between PMTs, as seen in figure 4.9 (right), where all 12 PMTs of a cool down are shown. The measurements begin at room temperature, with the DC rate starting to decrease at T = 0, indicating the beginning of the cool down at an average rate of 1.5 K/min. The decrease of the DC rate by thermionic emission follows an exponential decay according to Richardson's law [146]:

$$DC(T) \propto T^2 e^{\frac{-W}{kT}}, \tag{4.1}$$

where T is the temperature of the photocathode, W is its work function and k is the Boltzmann constant. The proportionality factor corresponds to a material-specific correction [147]. Due to the exponential behavior, already at around -30 °C the DC rate reaches values close to its minimum, dominated by non-thermal processes. After approximately 2.5 hours, the temperature has decreased and stabilized at around −100 °C—first dotted vertical line in figure 4.9 (left)—from where the DC rate remains at an approximately constant value. The performance of the tubes is evaluated in this period of stable temperature and DC rate, until the cooling of the chamber is stopped (indicated by the second dotted vertical line). As the system heats up, the DC rate of the PMTs also rises to

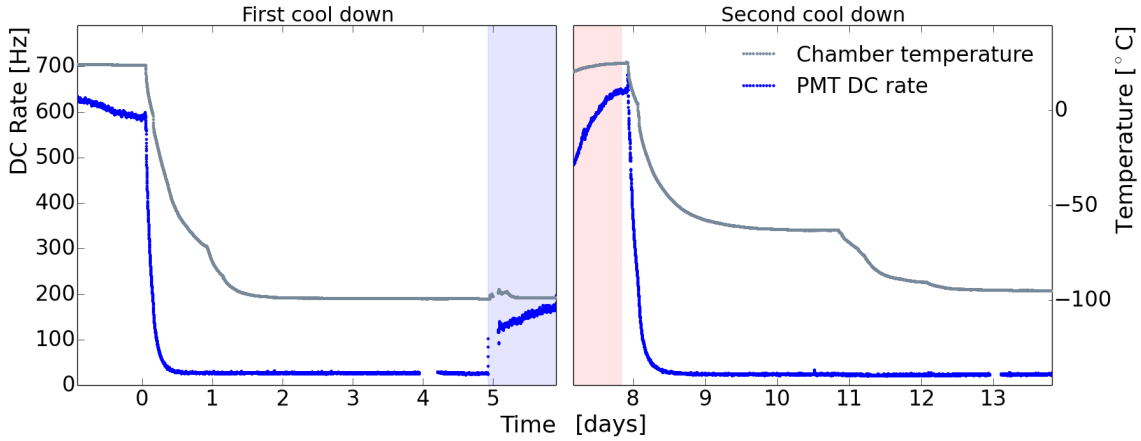

Figure 4.10: Evolution of the dark count rate of a PMT during operation in gaseous and liquid xenon in MarmotXL. The rate decreases from a few hundred Hz to an average of 28 Hz when operated in the gas phase, at around −100 °C, remaining stable within 2 Hz. The blue shaded area indicates the filling of LXe, after which the rate increases to a couple hundred Hz due to scintillation light in the liquid phase. A second cooling cycle is also performed on the PMT. The dark count rises during warm up to ambient temperature (red shaded area) and returns to its low point during cool down.

its previous value at room temperature. Typically, two to three cool downs are performed, with different settings for the PMT voltage: 1500 V, 1680 V and the corresponding voltages for an equalized gain of 3×10^6.

The average dark count rate at room temperature for all 321 tested PMTs is 1348 Hz, with a standard deviation of around 988 Hz. For the 248 PMTs in XENON the value is 1400 ± 1025 Hz. However, after cooling the tubes to −100 °C the mean DC rate reduces to only 40 ± 13 Hz [135]. A larger distance between the PMT arrays in this setup has been observed to increase the measured values and spread of the DC rates. This is due an increased solid angle to observe photons produced by external sources of ionizing radiation, such as radioactive components and Cherenkov light from cosmic rays. These contributions depend on the shielding of the experiment and the radioactive levels of the materials, it is thus reasonable to assume that the external contributions to the measured DC rate will be lower in a stronger shielded detector, such as XENON1T.

Dark Count Rate Stability and LXe Tests

Figure 4.10 shows an example of the testing cycle for a PMT in gaseous and liquid xenon in the MarmotXL setup (described in section 4.2.2). The gray line indicates the temperature of the inner chamber during cool down. The temperature for the cold tests is set to around −100 °C. This is achieved by filling GXe in several steps. In the first step, after reaching a vacuum pressure below

2×10^{-5} mbar, around 0.1 kg of xenon gas is introduced in the chamber, raising the absolute pressure to 1.8 bar. As the PTR cools the system and the pressure decreases close to 1.4 bar, more xenon is filled to increase the cooling rate. These steps can be observed as a change of slope in the temperature curve. The cooling of the chamber down to −100 °C is achieved in approximately 24 hours, corresponding to an average cooling rate below 0.1 °C/min. For measurements in LXe, 2.8 kg are filled to cover the PMT body. This period is represented by the blue shaded area in figure 4.10. Several cool downs are performed for each PMT to test the stability and resistance to thermal cycling. A second such cycle is also shown, with the red shaded area indicating the warm up of the chamber before the cool down is restarted. Between cool downs, the xenon is extracted from the chamber and recuperated into the bottles through the gas system. This process is performed through cryogenic pumping, in which the storage bottle is frozen with liquid nitrogen. Xenon gas will then flow from the MarmotXL chamber—where the pressure is higher—into the storage vessel, where it condenses. A vacuum around 0.01 bar can be achieved in the PMT chamber with this process. During this operation, the PMTs are turned off due to the fact that at low pressure (below 1 bar) but not a good enough vacuum (higher than 10^{-3} mbar) the mean free path of electrons in the medium allows for discharges to occur at the PMT pins.

The MarmotXL facility is suitable for long term measurements of PMT properties given that it operates in very stable conditions for long periods of time. With the set point at −100 °C, the temperature in the cryostat is kept stable within 0.2 °C in a day. The changes over a month of operation are no larger than 2 °C. The pressure, in turn, varies between 0.03 bar in a day and up to 0.07 bar within a month. The blue curve in figure 4.10 corresponds to the dark count rate of an R11410-21 PMT at -1500 V during cool down. In cold GXe, the average dark count rate is 28 Hz with a spread of only 2 Hz over several days (with the rate being measured in 1 minute intervals). The average dark count rate of 30 PMTs tested in similar conditions was measured to be 46 Hz, with an average spread of 4 Hz over several weeks. This represents a stability of around 10 % for the dark count rate of the XENON1T PMTs at cryogenic temperatures. The average DC rate in cold GXe is in agreement with the cold test results in the cryogenic nitrogen setup, in which the mean rate was 40 ± 13 Hz. When filling the chamber with LXe, the PMT dark count rate increases from tens of hertz to a few hundred hertz (blue shaded area). This is due to scintillation light produced in the liquid phase. During warm up, the DC rate returns to its previous value at room temperature.

During some cool downs, as the one shown in figure 4.11, large instabilities in the DC rate are observed at the beginning of the cool down. These spikes in the dark counts occur generally at temperatures between −60 and −90 °C, but once the temperature stabilizes at −100 °C, so does the DC rate. The low temperatures discard thermionic emission as a source of the instabilities, which

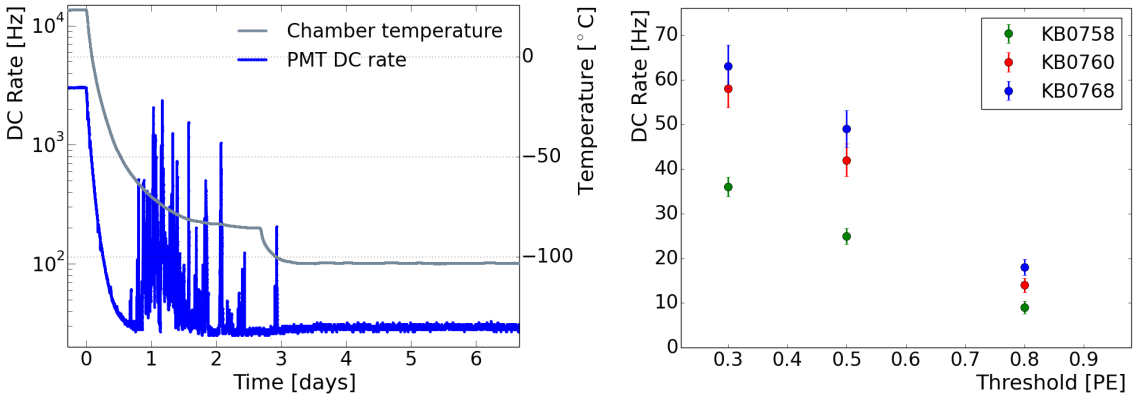

Figure 4.11: (Left) Example cool down in which instabilities in the PMT DC rate have been observed. Such spikes in the rate occur in some cool downs and mainly in the temperature transition phase between -60 and -90 °C. (Right) DC rate as a function of trigger threshold. The PMTs are operated at 1350 V, corresponding to a gain of roughly 2×10^6. The rates have been measured at thresholds of 0.3, 0.5 and 0.8 PE.

must be caused by other processes triggered by the decreasing temperature, such as metastable molecular excitations in the photocathode and other parts of the tube which may cause scintillation.

The measurement of the DC rate is threshold dependent. The results presented in this section correspond to a threshold around $\frac{1}{3}$ PE. Figure 4.11 (right) shows the dependency of DC rate to threshold. The PMTs are operated at 1350 V, corresponding to a gain of roughly 2×10^6, as is the objective operating gain in XENON1T. On average, the DC rate at 0.3 PE is around 50 Hz. Increasing the threshold to 0.5 PE gives an average rate of 38 Hz, corresponding to 3/4 of the value at 0.3 PE. Increasing further to 0.8 PE gives an average of 13 Hz, corresponding to about 1/4 of the value at 0.3 PE.

Light Emission

During the tests in the cryogenic nitrogen facility, some PMTs have been observed to emit light. The quantification of such light emission depends strongly on the setup and ambient conditions, as will be discussed. A qualitative study has been done by measuring the change in the dark count rates of the light emitting PMT or the one opposite to it.

The light emission has been categorized in two types. The first type consists of "flashes", by which a PMT emits a large amount of light in a short time. It is observed in the tube itself and the PMTs operated on the opposite array of the setup. Afterwards, the dark count rates may take from several minutes up to a few hours to decrease to the previous levels. Given their rare occurrence, most

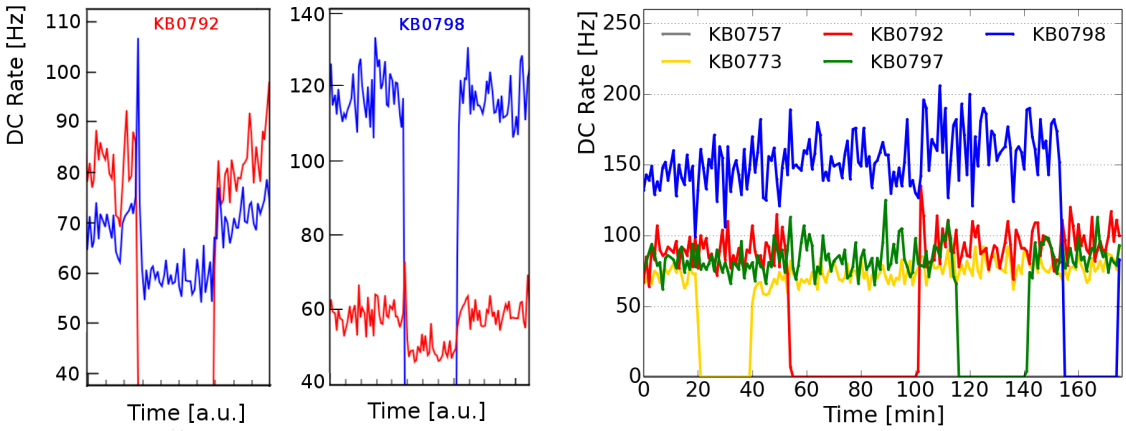

Figure 4.12: (Left) Examples of the detection of micro light emission in the cryogenic nitrogen setup. When a PMT is switched off, the PMT facing it in the opposite array displays a decrease in DC rate, indicating light emission from the PMT that was switched off. (Right) PMTs for which micro light emission has been detected in the nitrogen setup have been tested in the xenon testing facility. Since there are no face-to-face PMTs in the latter setup, no light emission is detected when the PMTs are switched off, one at a time.

tubes identified with such an event have not been rejected or replaced.

The second type is denominated "micro light emission". Its effect is more subtle, producing a small change of the dark count rate on the opposing PMT. Figure 4.12 (left) shows the time evolution of the dark count rates in cold for two opposing PMTs. When the light-emitting PMT is switched off, a clear decrease in the rate of the opposing PMT is observed. The decrease is larger at 1680 V (around 25 Hz) but often present at lower voltages (with an effect of about 10 Hz), indicating a voltage correlation of micro light emission. A detailed study is presented in [135].

A similar light-emission test to the one performed in the MPIK setup has been attempted in MarmotXL. Figure 4.12 (right) shows several PMTs—which had been previously identified with light emission—operating in MarmotXL at 1680 V. As can be seen, no effect on the rates of the other PMTs is observed when turning the PMTs off, one at a time. This stems from the fact that in this setup[2] the tubes are not facing each other. Although the geometry of the common reflecting surface was redesigned to improve the optical coupling between PMTs, no effect could be observed. This indicates, as mentioned earlier, that the observation of such micro light emission is setup dependent and difficult to determine without face-to-face PMTs.

Other studies of the R11410 PMT have also shown light emission due to

[2]As of 2016, MarmotXL has been upgraded to a double array setup and light emission measurements are currently being performed.

processes within the tube [148]. It goes without saying that this behavior is problematic for any search of rare events, such as dark matter, since it may trigger uncorrelated signal coincidences in the detector. For this reason, the PMTs in which micro light emission has been detected have been rejected and replaced for XENON1T.

4.3.2 Gain: Calibration and Evolution

One of the main features of photomultiplier tubes is the amplification of one photoelectron into a measurable electric current in the output. This is called the *gain* and is obtained by secondary emission of electrons through the dynode chain. The secondary emission ratio of a given dynode stage δ_i is given by:

$$\delta_i = a\Delta V_i^k, \tag{4.2}$$

where ΔV_i is the interstage voltage of the ith dynode, a is a constant and k is determined by the dynode structure and material with typical values from 0.7 to 0.8 [149].

Secondary emission on the first dynode is determined by the ratio between the secondary electron current I_{d1} and the incident photoelectron current I_k emitted from the photocathode:

$$\delta_1 = \frac{I_{d1}}{I_k}. \tag{4.3}$$

The secondary emission on the n-th dynode will be given by:

$$\delta_n = \frac{I_{dn}}{I_{d(n-1)}}. \tag{4.4}$$

The ouput anode current will thus be:

$$I_p = I_k \cdot \alpha \prod_{i=1}^{n} \delta_i, \tag{4.5}$$

where α is the collection efficiency.

As defined before, the gain g is equal to the ratio I_p/I_k, thus:

$$g = \alpha \prod_{i=1}^{n} \delta_i. \tag{4.6}$$

In the example case of a PMT with $\alpha = 1$ and n dynode stages operated at an equal differential potential ΔV, the gain as a function of the total supplied voltage V_s will be given by:

$$g = \left(a\Delta V^k\right)^n = a^n \left(\frac{V_s}{n+1}\right)^{kn} = A \cdot V_s^{kn}, \tag{4.7}$$

with $A = a^n/(n+1)^{kn}$. From this equation it can be seen that the gain is proportional to the kn power of the PMT bias voltage.

Spectrum Fit and Gain Estimation

Experimentally, the gain of the PMTs is obtained here from the so called single photoelectron spectrum. The SPE spectrum is a histogram of the areas of PMT pulses acquired with the ADC. It is obtained with an LED light source set to a single photon intensity, such that a photon signal is measured in about 5% of the waveforms. This results in a spectrum in which the Gaussian distribution from single photons is discernible, as shown in figure 4.13. The other features of the spectrum include a pedestal from electronic noise in the waveform, as well as contributions from double and triple PE signals. The gain of the PMT corresponds to the mean value of the SPE Gaussian. The Gaussian is obtained by fitting the spectrum according to the model described in the following paragraphs.

The pulse area of PMT signals in the ADC is equivalent to the measured charge. The histograms of figure 4.13, are displayed in units of signal electrons, obtained by converting the ADC units. An ADC sample in time is equivalent to 10 ns (given its 1 MHz sampling rate). Meanwhile, its 2.25 V range is covered by 16,384 channels. Thus, 1 ADC channel = 0.137 mV. Using a 50 Ω impedance, the equivalent charge in number of electrons is obtained from a pulse of area A in ADC units by:

$$Q\,[\text{electrons}] = \frac{V \cdot t}{R \cdot e} = \frac{A \cdot 0.137\,\text{mV} \cdot 10\,\text{ns}}{50\,\Omega \cdot 1.602 \times 10^{-19}\,\text{C}} = 171,428 \cdot A. \tag{4.8}$$

The basic model for the SPE spectrum is shown by the fit in figure 4.13 (b). For the noise pedestal, a Gaussian fit is implemented (gray curve):

$$A_0 \exp\left(-\frac{(x-\mu_0)^2}{2\,\sigma_0^2}\right) \tag{4.9}$$

The SPE contribution (blue curve) as well as the double and triple PE contributions (green and magenta) also show a Gaussian behavior. The amplitudes and spreads of the higher-order PE contributions are correlated to those of the SPE Gaussian, given that—due to the very low light intensity—the photons arriving at the PMTs can be assumed to follow Poissonian statistics. Thus, the n-th PE contribution is given by:

$$\frac{\mu^n e^{-\mu}}{n!} \exp\left(-\frac{(x-n\mu_1)^2}{2n\sigma_1^2}\right) \tag{4.10}$$

with the amplitude modulated by the Poissonian statistics of the light source, being $\frac{\mu^n e^{-\mu}}{n!}$ the probability that n photoelectrons are observed by the PMT, with $\mu = mq$ the mean number of photons collected by the first dynode and depends on the number of photons hitting the photocathode (m) and the PMT QE (q).

The total fit function (red curve) is thus:

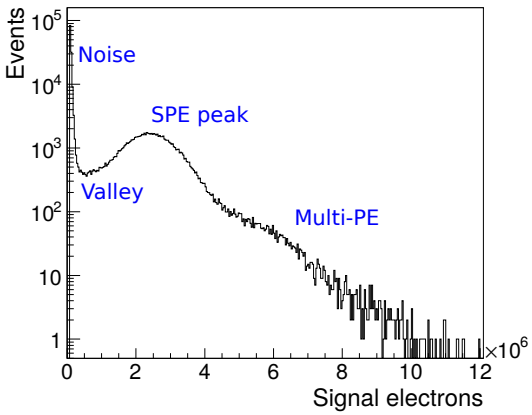

(a) PMT spectrum with a low intensity (single photon) light source. Its main features include the pedestal (noise), a valley before the SPE peak from single photons and higher order PE contributions.

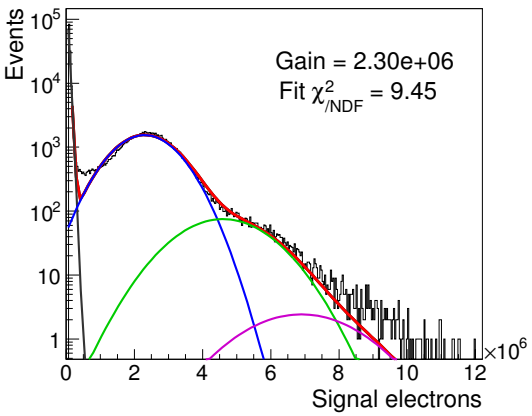

(b) Spectrum fit (red) including the pedestal (gray), SPE (blue), double PE (green) and triple PE (magenta) components. The fit fails to describe the valley and multi-PE regions accurately.

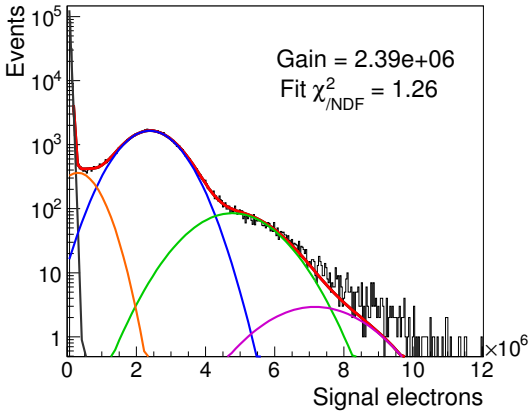

(c) An additional gaussian (orange) is implemented to describe the valley. In addition to improving the fit, it is motivated as a description of underamplified photon signals.

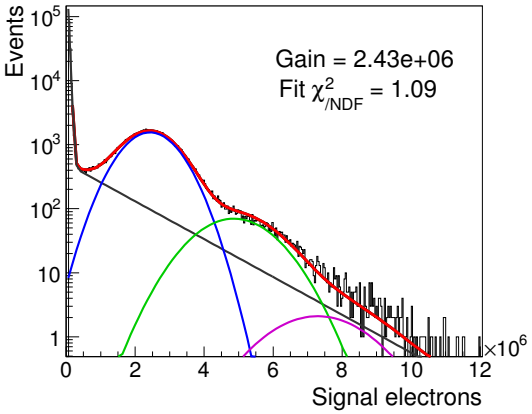

(d) In this case, an exponential is included to fit the valley, which also improves the fit at the higher PE levels. It describes underamplified photons and other background processes.

Figure 4.13: PMT spectrum with a light intensity at the single photon level. On the x axis, the PMT pulse area (charge) has been converted to electrons, from which the gain can be derived as the mean of the SPE Gaussian (blue). The overall fit (red) includes a Gaussian describing the pedestal (gray) and Gaussians for the SPE and multi-PE components. Different fits are shown, varying the function that describes the valley: an additional Gaussian (orange) or an exponential (dark gray). The global fit is improved as indicated by the $\chi^2/_{\mathrm{NDF}}$. The variation in the gain value between models (c) and (d) is below 2%, as estimated from fits of several PMT spectra.

$$A_0 \exp\left(-\frac{(x-\mu_0)^2}{2\,\sigma_0^2}\right) + A_1 \sum_{n=1}^{N} \frac{\mu^n e^{-\mu}}{n!} \exp\left(-\frac{(x-n\mu_1)^2}{2n\sigma_1^2}\right), \tag{4.11}$$

where A_1 is the amplitude of the SPE gaussian.

It is clear from figure 4.13 (b) and its goodness of fit ($\chi^2/_{\mathrm{NDF}}$) that this basic model fails to properly match the valley between the noise and the SPE peak. Figure 4.13 (c) shows the implementation of an additional Gaussian curve (orange) to better fit the spectrum at the valley. Although the goodness of fit is improved, the matching at larger signals around the 3PE domain is still lacking. Following [150], figure 4.13 (d) includes instead an exponential (gray curve) which improves the overall fit. The total function becomes:

$$A_0 \exp\left(-\frac{(x-\mu_0)^2}{2\,\sigma_0^2}\right) + w\,\alpha\,\exp(-\alpha\,x) + A_1 \sum_{n=1}^{N} \frac{\mu^n e^{-\mu}}{n!} \exp\left(-\frac{(x-n\mu_1)^2}{2n\sigma_1^2}\right), \tag{4.12}$$

where α is the coefficient of the exponential decrease and w is the probability to have such background events.

The variation in the estimated gain (mean of the SPE Gaussian) between the models describing the valley with a Gaussian and an exponential is below 2%, as measured from several PMT spectra. The motivation for such additional functions and the possible origin and nature of the events they describe are discussed in the following section.

Under-amplified signals in the SPE spectrum

A proper fit of the full SPE spectrum requires a description of the underlying events present in the valley region of the spectrum.

The first question is whether the signals in the valley are caused by electronic noise as in the pedestal, or if they are related to the presence of light. Figure 4.14 shows the spectrum of a PMT with a gain of $5.5{\times}10^6$ on the x axis and the timestamp of each event on the y axis. Noise pulses from the pedestal are distributed homogeneously in time from T = 50 ns (when the trigger starts) until the end of the acquired waveform. On the other hand, photon signals are present only between T = 70 ns and 170 ns, when the LED is on. The pulses in the valley region appear only in the presence of light. This suggests their origin to be under-amplified photoelectrons and/or photon feedback from dynode photoemission.

Under-amplification of photoelectrons may be caused by inefficient collection of the electron avalanche in the dynode chain, as well as photons missing the PMT window and striking the first dynode directly. The latter would result in a signal amplified by 11 dynode stages instead of 12, as depicted in figure 4.15

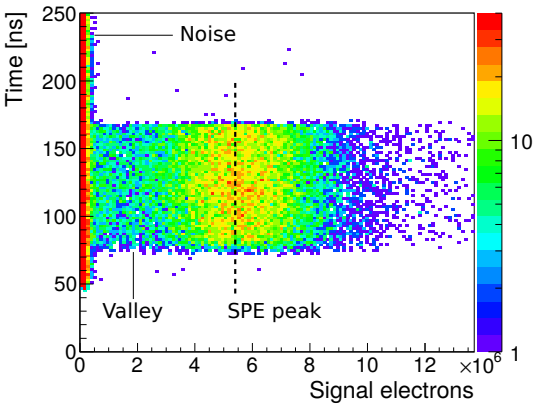

Figure 4.14: SPE spectrum of a PMT with a gain of 5.5×10^6 (dotted line) on the x axis and the timestamp of events on y. Pulses are registered starting at T = 50 s. The LED is active between T = 70 ns and 170 ns. While the electronic noise is present over the whole acquisition window, events in the spectrum valley appear only in the presence of light.

(right). This is the original motivation behind the addition of a Gaussian to fit the valley as in figure 4.13 (c), with the Gaussian mean indicating the gain with 11 stages. In order to study such signals, an analysis has been performed on spectra generated from a focused light source on different points of the PMT window. For this, the SandBox experimental setup, presented in reference [151], has been used. It consists of a black box in which the PMT is illuminated with a collimated light source fixed on a two-axis scanner. The light source is a blue LED ($\lambda = 470$ nm) encapsulated in a box with two aligned orifices (0.5 mm diameter) separated by a small gap, acting as a collimator. The typical distance to the PMT window is 1 mm, resulting in an illuminated area of 0.7 mm on the photocathode.

Figure 4.15 (left) shows a sample of positions on the PMT window for which an SPE spectrum has been acquired. The numbered locations correspond to the spectra presented in figure 4.16. Position 3 is located in the center of the PMT, directly above the focusing grid and the aperture towards the first dynode. Positions 2 and 4 are at the edges of the apperture, while 1 and 5 are in locations away from the first dynode. Figures 4.16 (a) and (b) show a comparison of the SPE spectra from the horizontal and vertical scans, respectively. An excess of events is observed in the region between noise peak and valley for the spectrum at position 3. This component corresponds to photons penetrating through the PMT window and impinging on the first dynode.

Figure 4.16 (c) shows the subtraction of spectra 3 and 5. The difference corresponds to the signals from photons striking the first dynode. The fit corresponds to a Poisson function, given that the distribution is generated by a discrete and low number of photoelectrons. The expected value (λ) indicates the average number of photoelectrons generated on the first dynode. The value of λ, measured for several spectra, varies between 3 and 4. The average gain for an 11-stage amplification is then around 0.3×10^6 (taken at the peak of the distribution), compared to the 5.5×10^6 gain of the fully amplified signal.

The results show that part of the valley events in the SPE spectrum are in fact from first dynode photoelectrons, but they account for a small fraction

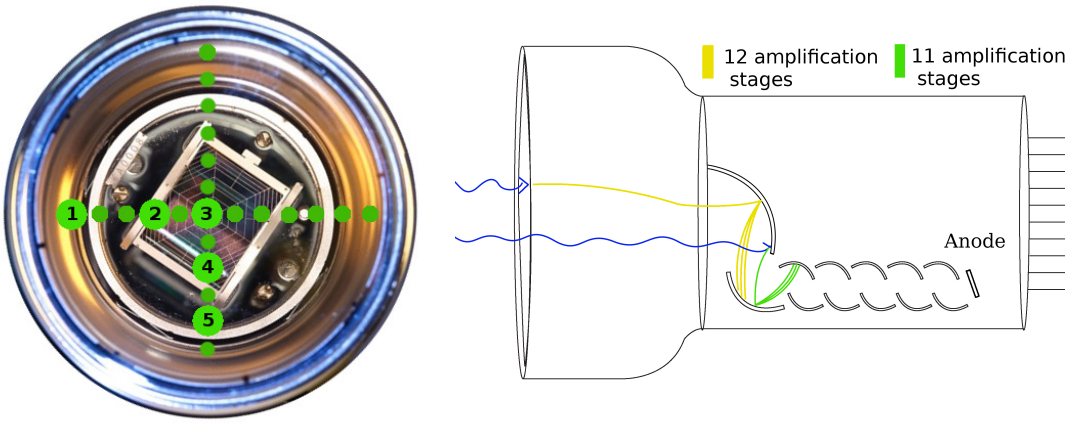

Figure 4.15: (Left) Front view of an R11410 PMT. The focusing grid can be seen in the center, located accross the rectangular aperture that leads to the first dynode. The PMT has been scanned in the horizontal and vertical directions indicated by the green markers, generating the spectra presented in figure 4.16 for the numbered locations. (Right) Photoelectrons generated at the PMT window (yellow) will undergo full amplification through the 12 dynode stages. Photons penetrating the window and striking the first dynode will generate a photoelectron to be amplified through 11 stages only (green).

of the total events and only at the lower end of the spectrum. Figure 4.16 (d) shows that the spectrum in position 5 still requires an additional component to fit the valley. The remaining underlying events are most likely comprised of photons from photoemission at the dynodes. The production of such photons can be expected to increase exponentially towards the final stages of the dynode chain. Such photons will produce photoelectrons of their own by interacting with the electrodes. The amplification will be lower the later the photoelectron is produced in the dynode chain. It can then be expected that the population of such underlying events is highest at lower amplifications, with an exponential decrease along the spectrum. This motivates the inclusion of the exponential function to the overall description of the spectrum—along with the empirical fact that it provides the best fit to the data.

Gain and Peak-to-Valley Ratio

Figure 4.17 (left) shows the gain as a function of HV for PMTs in LXe. The gain at each voltage has been estimated, as described earlier, by fitting the PMT spectra with the function in equation 4.11. The HV scan allows to determine the bias voltage required to equalize the gains of all PMTs. In XENON100, the PMTs are operated at the same gain in order to accurately determine the amplitude of the measured signals in the detector, which is translated into the

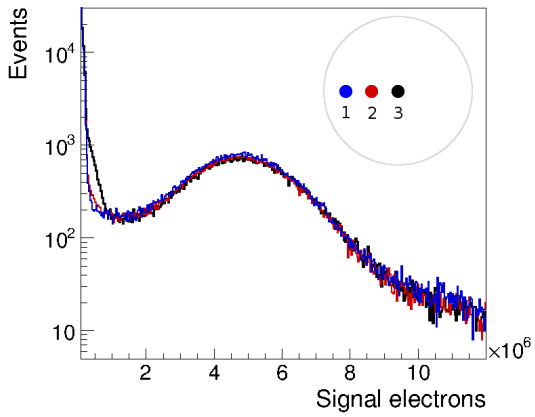

(a) Horizontal PMT scan. Position 3 is directly above the first dynode. The excess in the lower end of the spectrum is caused by photons striking the first dynode.

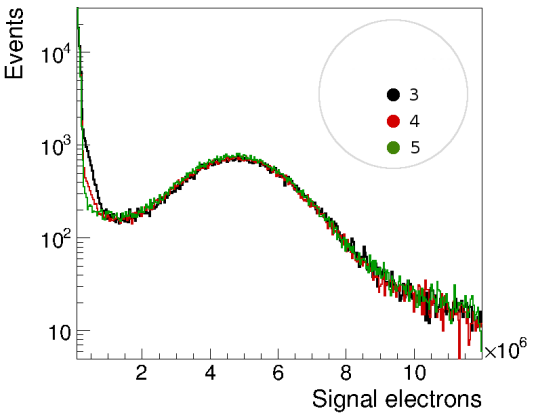

(b) Vertical PMT scan. Position 4 is at the edge of the first dynode and position 5 is away from it. The lower end excess in the spectrum decreases accordingly.

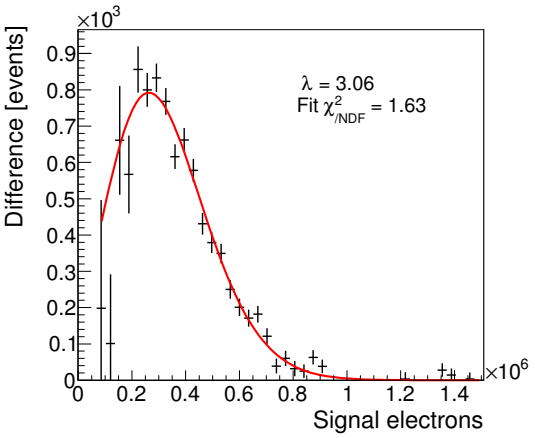

(c) Difference between spectrum 3 and spectrum 5. The population of first dynode PEs follows a Poisson distribution, with λ being the expected value.

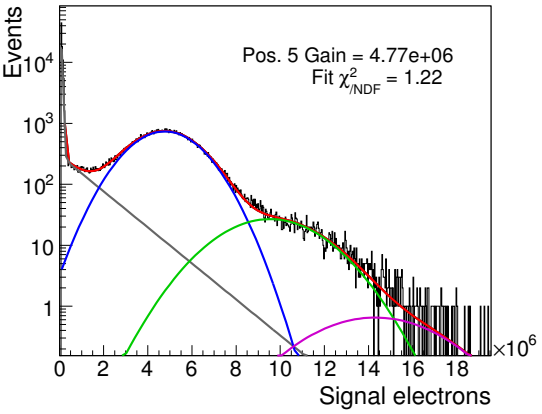

(d) Spectrum at position 5. An exponential function (gray) is included to describe the valley. The mean of the SPE Gaussian (blue) is the PMT gain.

Figure 4.16: Study of the under-amplified components in the SPE spectrum. An illumination scan has been performed at different positions of the PMT window. The spectra obtained in the central position show an excess at lower PE amplifications from photons impinging on the first dynode. Other phenomena, such as photon feedback, produce under-amplified signals in all spectra that fill the valley between the noise and fully amplified SPE signals. An exponential distribution best describes such underlying events.

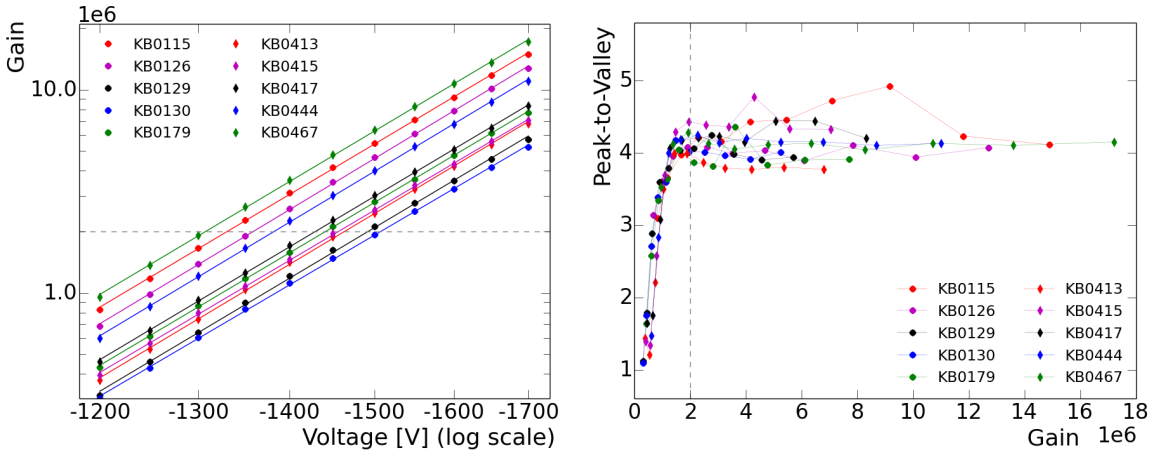

Figure 4.17: (Left) Gain as a function of HV for 10 PMTs in LXe. The fit is obtained with equation 4.13, which is linear in a log-log plot. The dotted line indicates the suggested equalization gain for PMT operation. (Right) Peak-to-valley ratio as a function of gain in LXe. The dotted line at 2×10^6 indicates the equalization value, below which the P/V decreases sharply, meaning a lower resolution between noise and SPE signals.

recoil energies in LXe. In XENON1T, however, gain-equalization is one option, while optimizing the gain in each individual channel according to the signal-to-noise separation is also considered.

In a log-log diagram, the gain g as a function of the supplied voltage V_s will show a linear trend, as seen by rewriting equation 4.7 as:

$$\log(g) = kn \cdot \log(V_s) + \log(A), \tag{4.13}$$

where, as before, k is a constant dependent on the dynode structure and material, n is the number of dynodes and A is a constant related to k and n.

A low bias voltage minimizes the stress on a PMT operated over long periods of time. It also reduces the saturation of high amplitude pulses, which affects the position resolution and energy reconstruction of signals in a dark matter detector. The aim in XENON1T is to operate the PMTs at the lowest voltages possible without compromising the power to resolve single photons. A useful parameter to quantify the resolution of the SPE peak from the noise background is the peak-to-valley ratio (P/V). It is derived from the spectrum fit as the ratio between the maximum value at the SPE peak and the minimum value at the valley.

A good separation of the SPE peak from the noise pedestal corresponds to a P/V ≈ 4, while an overlap with the noise causes P/V $\rightarrow 1$, as seen in figure 4.17 (right). The P/V is approximately constant at gains above 1.6×10^6 and decreases sharply below this value. From these measurements in LXe, a

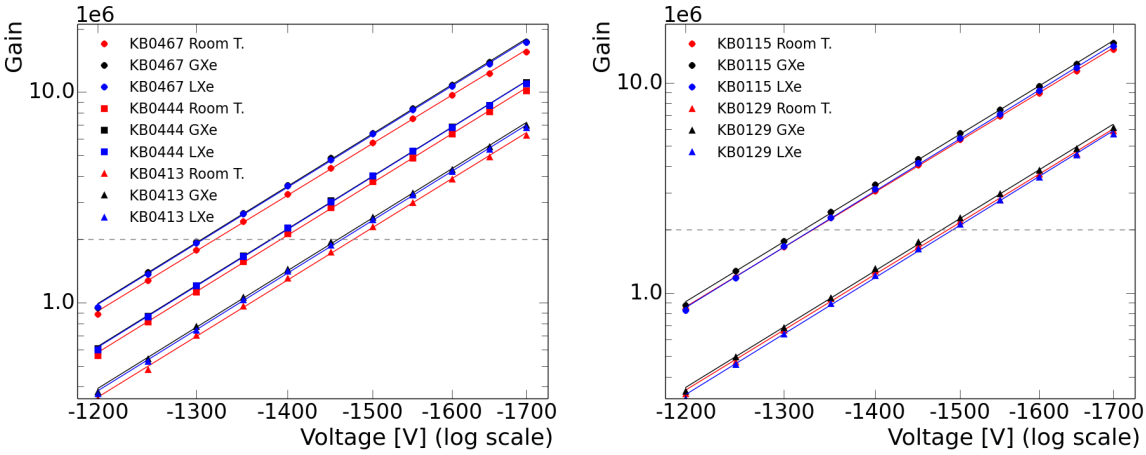

Figure 4.18: Comparison of the gain as a function of HV for PMTs at room temperature (red), GXe at −100 °C (black) and LXe (blue). On average, the gains in GXe at −100 °C increased by 7 % with respect to the value at room temperature. Whereas, when operated in LXe, the PMT gain decreased with respect to the GXe conditions. For some PMTs, like KB0444 and KB0467 (right plot) the decrease is less than 1 %, but for others like KB0115 and KB0129 (right plot) the decrease was as much as 5 % and 7 % respectively.

gain equalization at 2×10^6 is suggested. It is important to mention that the P/V depends strongly on the level of electronic noise in the acquisition system. The noise levels in MarmotXL are considerably low, allowing for a good SPE separation even at low gains. In the case of the MPIK setup, the noise pedestal is somewhat broader, leading to a suggested P/V threshold of 3×10^6 (see [135]).

Gain Evolution

Given that the PMTs are often operated at different temperatures, a study has been made comparing the PMT gains under different conditions. Figure 4.18 shows a comparison of the gain as a function of HV for different PMTs. The measurements at room temperature are shown in red, while the values at −100 °C in GXe are shown in black and in blue for the case of LXe. On average, the gains in GXe at −100 °C increased by 7 % with respect to its value at room temperature. This effect is explained by the decrease in electric resistance of the PMT components, voltage divider and signal cables, which results in a higher charge output. The same effect has been measured in the nitrogen cooling setup at MPIK. When operated in LXe, another effect occurs by which the gain decreases with respect to the value in GXe. For some PMTs the decrease is less than 1 %, but for others it is as much as 7 %, with an average around 3 %.

Figure 4.19 shows a comparison of SPE spectra under different conditions for KB0179 at 1500 V. The solid lines correspond to the global fits and the gain

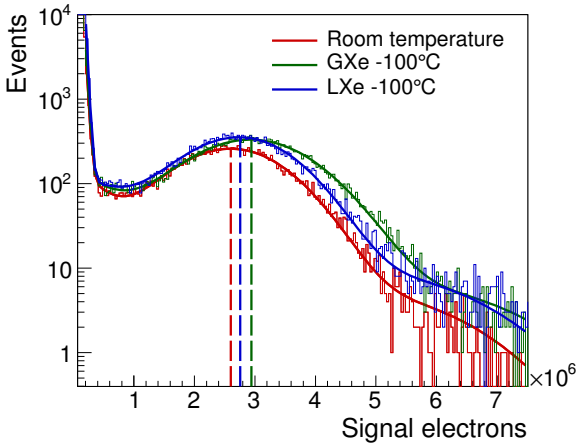

Figure 4.19: Comparison of the SPE spectra at room temperature (red), GXe at −100 °C (green) and in LXe (blue) for KB0179 at 1500 V. The gain is indicated by the dashed vertical lines. The gain in GXe is 13 % higher than the value at room temperature (2.6×10^6). In LXe, the gain decreased 6 % with respect to the value in GXe.

is indicated by the dashed vertical lines. The gain in GXe is 13 % higher with respect to the value at room temperature (2.6×10^6). In LXe, the gain decreased 6 % with respect to the value in GXe. The plot illustrates clearly the shift of the SPE spectra in the different environments.

The gain evolution of KB0179, KB0115 and KB0129 has been studied in a period of 4 weeks, during which the phototubes were operated in GXe and LXe. The results are shown in figure 4.20. Measurements were taken at intervals between 30 minutes and 2 hours at different stages of the study. Starting at room temperature, the cool down in GXe takes a day to reach −100 °C, during which the gains increase abruptly. After a few days of stabilization, the gains remain constant for around 2 weeks with variations below 1 %. On days 20 and 21, the chamber was filled with liquid xenon (depicted with blue shaded areas in the plot), covering the PMTs. Upon this, the gains decreased asymptotically during the remaining week to a lower value than in GXe. These results confirm the measurements in figure 4.18 and show in more detail how the gain evolves in time and in different conditions.

Long Term Stability and Cooling Cycles

Tests of the PMT stability were also performed in the MarmotXS setup described in section 4.2.2. These measurements took place in the early stages of the testing campaign during the evaluation of the R11410-10 version [152].

Figure 4.21 (a) shows the gain measurements over a period of 4 months for a PMT at 1600 V in LXe. The gain was measured automatically every 4 hours, with the exception of a few periods where the automatic system failed. The pressure and temperature of the xenon inside the chamber were constantly monitored. The solid blue line indicates the mean value. The gain was stable within ± 2 %, indicated by the dashed lines. The variation in the gain estimation is higher in these measurements than in MarmotXL (figure 4.20), mostly due to higher noise levels. MarmotXL was improved with respect to MarmotXS with the implementation of double shielded cables and better grounding of the cham-

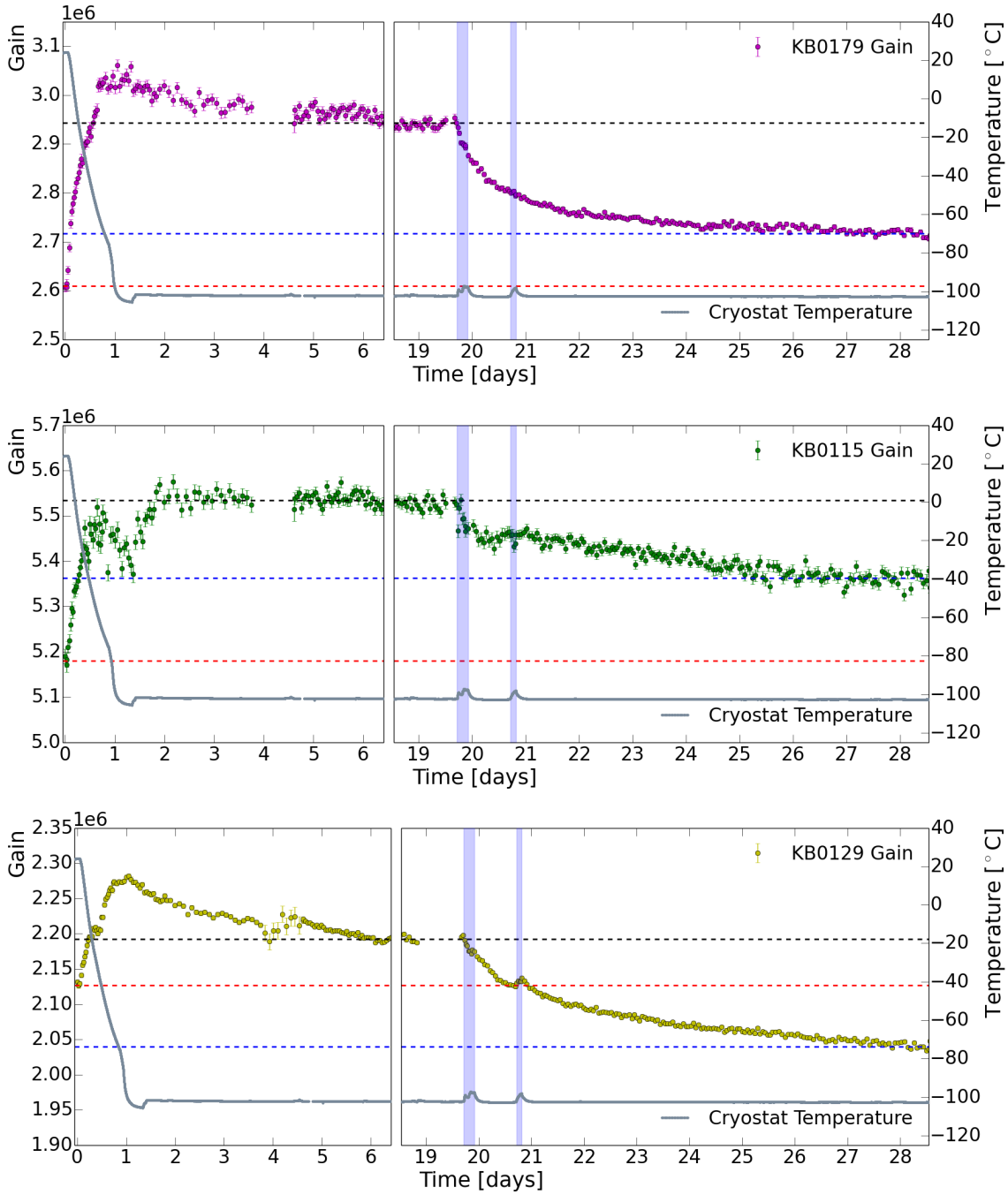

Figure 4.20: Gain evolution of KB0179, KB0115 and KB0129 over a period of 4 weeks during a cool down in Xe. The temperature in the MarmotXL chamber is shown in gray. The gains at room temperature are indicated by the red dashed line. The cool down in GXe to −100 °C takes around 1 day, during which the gains increase abruptly. During the next weeks in GXe the gains stabilize at values indicated by the black dashed lines, with variations below 1 %. The blue shaded areas at days 20 and 21 indicate the filling of the chamber with LXe, covering the PMTs. The gains then decrease asymptotically to the levels indicated by the blue dashed lines.

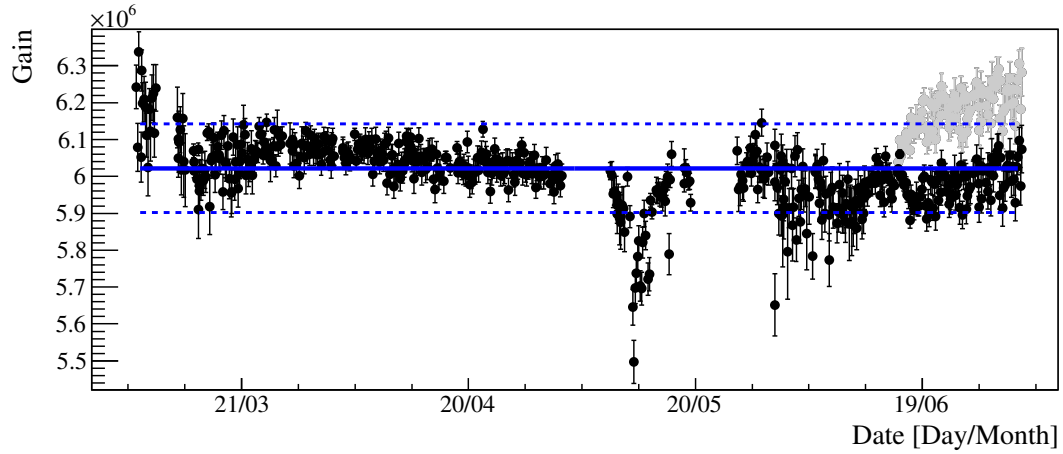

(a) Gain stability over a 4 month period in LXe. The blue solid line indicates the mean gain value, while the dashed lines correspond to ± 2 %.

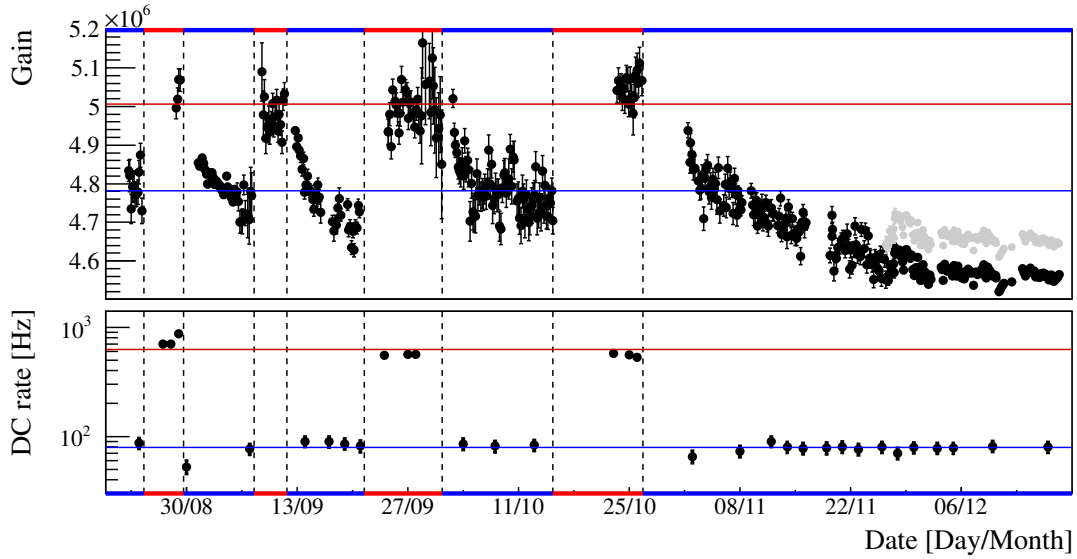

(b) Thermal cycling of a PMT for over 3 months. The top panel shows the gain evolution. The red and blue horizontal bars indicate operation at room temperature and in LXe, respectively. The bottom panel shows the changes in the DC rate.

Figure 4.21: Long term stability and thermal cycling tests of R11410-10 phototubes in MarmotXS. The gray data points have been corrected to account for temperature and pressure changes in the MarmotXS chamber. (Published in [152]).

ber and electronics. Nonetheless, a variation of 2 % is within the uncertainty of the fitting method, as shown in figure 4.13.

In some periods the gain deviates from the ± 2 % range. In every case it is related to a change in the experimental conditions: At the beginning of the test the gain is still decreasing from its value at room temperature, taking several days to reach a stable condition. The two deviations to lower gains are not caused by a real gain change, but by changes in the noise conditions which affect the gain estimation. In the first case, the voltage of the LED was set too high and too much light illuminated the PMT for a few hours. In the second case, a malfunction in the cooling system lead to a sudden temperature decrease followed by an increased noise level. In both cases the system returned to a stable gain. The increase in gain observed at the end of the measurement (gray data points) is directly correlated to an increase in the temperature (+1 K) and pressure (+100 mbar) inside the chamber. The corresponding black points have been corrected for this effect by subtracting the difference of the average gains before and after the temperature/pressure increase.

In XENON100, around 1-2% of the PMTs were not functional after the first cool-down of the detector [116]. For this reason the XENON1T PMTs have been tested during several cool downs in nitrogen and in LXe, as described before. Before these tests, some R11410-10 PMTs were also stress tested with cooling cycles in LXe using the MarmotXS setup. During each cooling cycle, the temperature was kept at $(-99 \pm 1)^{\circ}$C for a typical period of 5 days and then raised to $(21 \pm 3)^{\circ}$C for another 5 days, before filling the chamber again with LXe.

Figure 4.21 (b) shows an R11410-10 PMT operated during 5 consecutive cooling cycles in MarmotXS. The top panel shows the gain evolution during thermal cycling for over 3 months. The PMT was biased at −1600 V. The red and blue horizontal bars indicate operation at room temperature and in LXe, respectively. The average gain at room temperature (red line) was about 5% higher than at LXe temperature (blue line). The gain in LXe stabilized only after several weeks. In the last cool down it took up to 4 weeks to reach a stable level at a value ∼10% lower than at room temperature. These observations have been qualitatively reproduced in the case of the R11410-21 version, as seen in figure 4.20.

The bottom panel in figure 4.21 (b) shows the dark count rate of the PMT. It was measured after turning off the LED for gain calibration for about an hour. For the DC rate estimation the PMT signal was amplified and triggered by a discriminator. An SPE spectrum was recorded with a multi-channel analyzer and the Gaussian describing the SPE peak was integrated above 0.3 PE. The average dark count rate at room temperature was 630 ± 110 Hz and 79 ± 8 Hz at LXe temperature. The uncertainties are given by the standard deviation of all measurements. The measured DC rate in LXe is affected by scintillation light. To measure the scintillation contribution in the MarmotXS setup, the dark count rate was also measured in vacuum immediately after LXe recuperation, when the

temperature inside the chamber was still −73 °C. Under such conditions the DC rate was measured at (40 ± 8) Hz, a factor 2 lower than in LXe. This result is in agreement with the results in section 4.3.1.

As a conclusion, none of the tested R11410-10 PMTs showed any malfunctioning or worsened performance concerning the gain during the long term stability and thermal cycling tests.

4.3.3 Quantum Efficiency

The quantum efficiency (QE) of a photocathode is the percentage of photoelectrons emitted from the photocathode with respect to the number of incident photons. Incident photons transfer their energy to electrons in the valence band of the photocathode. However, not all electrons are successfully emitted as photoelectrons, making photoemission a probabilistic process.

The measurement of QE, as performed at Hamamatsu, relies on the concept of *radiant sensitivity* [153]. Radiant sensitivity is defined as the ratio between the photoelectric current generated by the photocathode and the incident radiant flux at a given wavelength. It is expressed in units of amperes per watt (A/W). This quantity can be more easily measured in the lab and the QE derived from it. The measuring process is the following: a light beam is made to shine through a spectroscopic filter and produce photons of a specific wavelength. This beam is then split into two paths. The first beam is detected with a known and precisely calibrated photodiode with which the incident radiant flux (L_p) is measured. Meanwhile, the second beam is detected with the PMT under study and its photocurrent at the first dynode (I_k) is measured. The radiant sensitivity S_k of the PMT is then calculated from the following equation:

$$S_k = \frac{I_k}{L_p} [\mathrm{A/W}] \tag{4.14}$$

The QE can be obtained from S_k using the following equation:

$$\mathrm{QE}\,[\%] = \frac{h \cdot c}{\lambda \cdot e} S_k = \frac{1240}{\lambda} S_k \times 100\,\% \tag{4.15}$$

where h is Planck constant, λ is the wavelength of the incident light in nanometers, c is the velocity of light in vacuum and e is the electron charge.

Figure 4.22 shows the measurements of S_k and the derived QE for four different PMT samples with quartz windows, each with a different photocathode [3]. On the right plot it can be observed that the maximum quantum efficiency of a PMT occurs at a wavelength slightly shorter than that of its maximum radiant sensitivity. This is because photons of shorter wavelengths carry higher energy compared to those at longer wavelengths and contribute to an increase in the photoemission probability. The left plot corresponds to measurements for

[3] These measurements were performed during an internship at Hamamatsu Photonics.

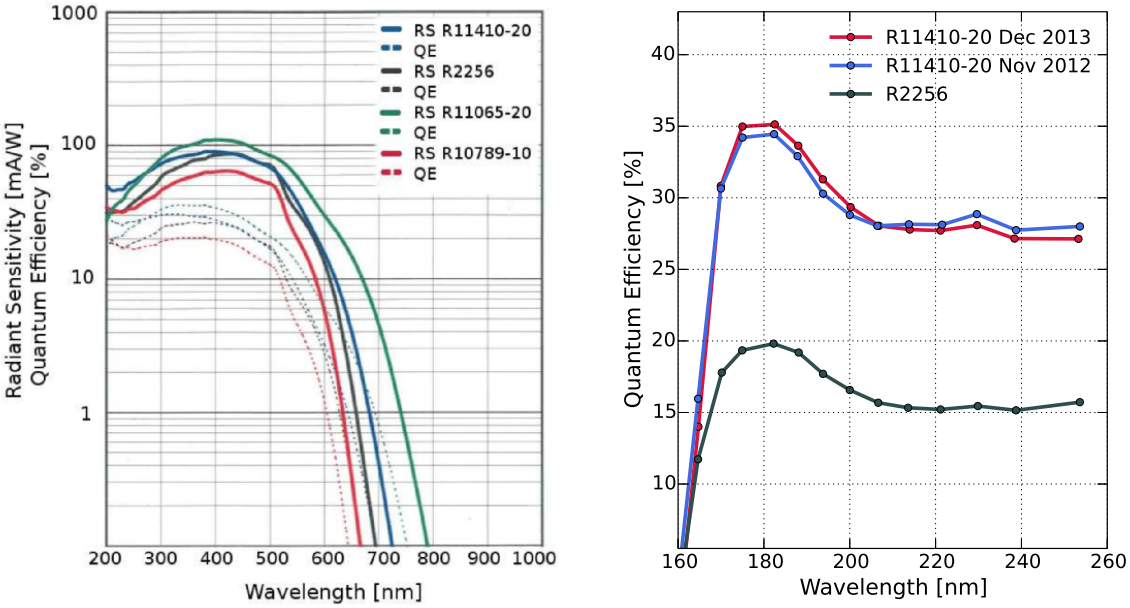

Figure 4.22: (Right) Radiant sensitivity (solid lines) and quantum efficiency (dotted lines) as a function of wavelength for various PMT samples with different photocathode materials. (Left) Quantum efficiency measurement for wavelengths in the VUV band. The R11410-20 sample has been measured twice, with a 1 year period in between.

ultraviolet light. The setup is similar to that previously described but with all elements in a vacuum to avoid absorption of the VUV photons.

The standard bialkali photocathode in the R2256 displays a noticeable decrease in QE for wavelengths in the ultraviolet, indicating its unsuitability for LXe detectors. Meanwhile, the R11410-20 features a photocathode designed specifically for LXe operation. Even though its QE at 400 nm is similar to that of the standard bialkali version, it is in the VUV region where it excels, displaying a maximum QE of $\sim 35\,\%$ at 175 nm. The R11065-20 is a PMT designed for LAr experiments (such as GERDA [154] and DarkSide [155]). Its peak QE is around 380 nm since such experiments use wavelength shifters to detect the LAr scintillation photons of 128 nm. The R10789-10 is also used in LXe by the XMASS experiment [156]. Its design is focused on low radioactivity and a hexagonal window shape to maximize the surface coverage around the spherical detector.

The R11410-20 measurements in vacuum were performed on the PMT with serial number KB0058. The results on the right plot of figure 4.22 show that after 1 year the QE remains unchanged, within the measurement uncertainty. The error is mostly due to the fact that the QE is measured in a small area of the photocathode surface. An estimation of this error was made by changing the area

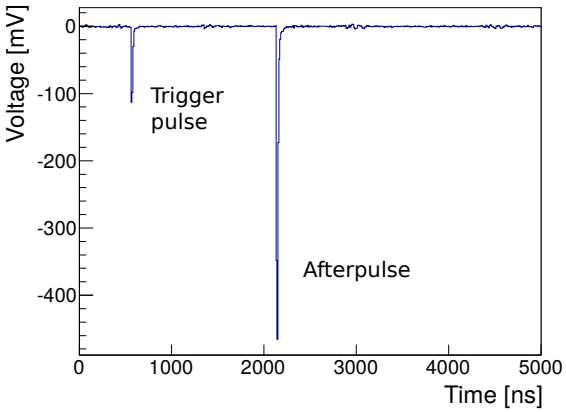

Figure 4.23: Example PMT waveform triggered by a dark pulse at 0.5 μs. An afterpulse with a time delay of around 1.6 μs is observed.

covered by the incident light beam. Three different surfaces were considered and a fluctuation of around 1 % was measured—meaning a change in QE of ± 0.3 % at a QE of around 30 %.

The temperature dependence of the QE for the R11410-10 has been measured by UCLA members of the XENON collaboration [157]. It has been shown that during the cooldown from room temperature to $-110\,^{\circ}$C the absolute QE of the PMTs increases by a factor of 1.1 - 1.15 at 175 nm. Thus, it can be expected that during XENON1T operations in LXe the actual QE of the tubes will be about 10 % larger than the values provided by Hamamatsu.

4.4 Study of Afterpulses

One of the main sources of background noise in a PMT are spurious signals generated within the tube after a photon interaction. These are called *afterpulses*. These pulses can affect the accurate measurement of low level signals after a large pulse in experiments focusing on small amplitude and low-rate events, such as dark matter and neutrino detectors. It is thus important to use PMTs with the lowest afterpulse rate as possible and to have a proper understanding of the nature and origin of such signals.

Figure 4.23 shows an example waveform with the main pulse that triggers the acquisition at 0.5 μs and an afterpulse with a time delay around 1.6 μs. The following study of afterpulses has been performed mostly with dark pulses as trigger signals (described in section 4.3.1). Afterpulse measurements with an LED trigger at single photon intensity have also been performed, as well as measurements with a multi-photon intensity at a mean of 8 and a maximum around 20 photons. Unless otherwise stated, the measurements and analysis described are on dark pulse data. Triggering on such signals allows for an accurate study of the afterpulse production by single photoelectrons without the requirement of tuning the LED source to single photon intensity or normalization of the data according to a mean value from multi-photon illumination.

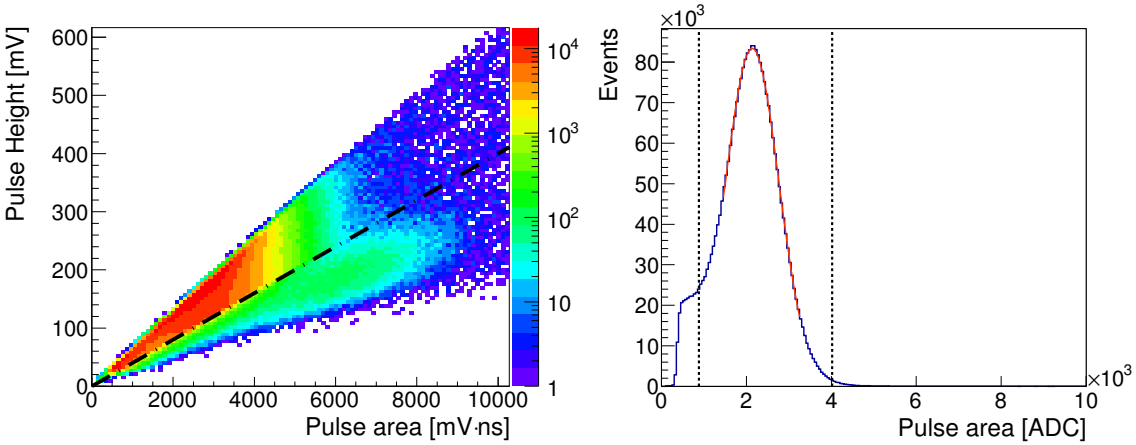

Figure 4.24: (Left) Pulse area and pulse width of trigger signals in an afterpulse measurement. A cut below the dashed line is made to exclude the population comprised mostly of noise and pile-up signals. (Right) Single photoelectron peak with a Gaussian fit to determine the mean value and implement further cuts at -2 σ and +3 σ for the selection of single PE triggers.

Further selection cuts have been implemented on the pulses to ensure single photoelectron triggers. Figure 4.24 (left) shows a histogram of the pulse width and pulse area. The population below the dashed line includes noise and pile-up signals, for which the ratio of width to area is higher. The right histogram of the figure shows the pulse area spectrum after implementation of the previous cut. The empty bins in the low range are a result of the threshold required by the discriminator for the self-trigger of dark count signals. The single photoelectron peak is fit with a Gaussian in order to determine its mean value. Additional cuts are made at -2 σ and +3 σ to further reject noise and multiphotoelectron pulses. Each afterpulse measurement has been done with a total of 3×10^6 triggers, of which around 90% pass the cuts.

Figure 4.25 (left) shows a 2D histogram of an afterpulse measurement with the time delay on the x axis and the afterpulse size (pulse area)—normalized to that of a single photoelectron—on the y axis. The afterpulses have been classified into three distinct groups:

- **A1:** Pulses with a very short time delay (several tens of nanoseconds) and amplitudes around 1 pe. These signals are likely generated by electrons scattering off the first dynode. While most secondary emission electrons are collected through the dynode chain and read out as the primary signal, some may scatter backwards and return onto the first dynode, generating a secondary signal a few nanoseconds later.

- **A2:** Pulses with a time delay of up to several microseconds and amplitudes around 1 pe. Part of this population corresponds to dark pulses with a

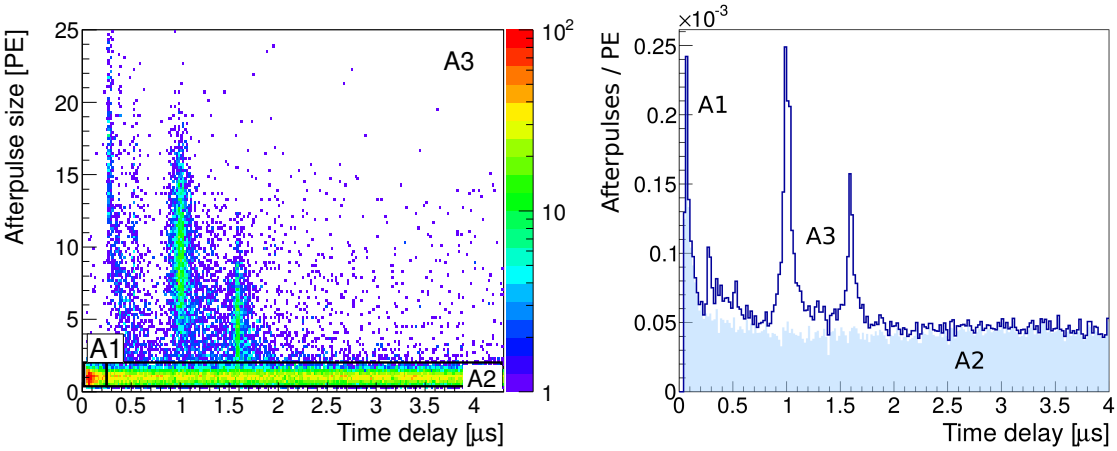

Figure 4.25: (Left) Histogram of afterpulses according to size and time delay. The afterpulses are classified by origin and properties into the groups A1, A2 and A3. The group A3 corresponds to afterpulses generated by ions of residual gas molecules in the PMT vacuum. (Right) Afterpulse spectrum with the contribution from single PE afterpulses (A1 and A2) highlighted in the blue shaded area.

heterogeneous time distribution. Other afterpulses are also present and can extend over 5 μs, where the population starts to fall.

- **A3:** Pulses with amplitudes equivalent to several photoelectrons and appearing at distinct times. These signals are caused by positive ions from gas molecules within the PMT. Although the volume of the tube should ideally be vacuum, residual contaminants are inevitably present. Along its trajectory, a photoelectron may ionize one of these molecules, causing it to travel back towards the photocathode due to its positive charge. When hitting the photocathode, the ion liberates further electrons which in turn produce an afterpulse. The time delay of this signal will be defined by the mass and charge of the ion that produced it.

The right plot in figure 4.25 shows the afterpulse spectrum with the contribution from single PE afterpulses highlighted by the blue shaded area—with a high number of A1 afterpulses at short time delays and A2 afterpulses extended for several microseconds. The identification of the ions generating the A3 afterpulses is described next.

4.4.1 Timing of afterpulses from residual gas molecules within a PMT

The travel time of an ion located at position s_0 between the focusing grid (located at a distance L) and the PMT photocathode (located at 0) can be calculated from

the general equation:

$$t = \int_{s_0}^{0} \frac{1}{v(s)} ds. \tag{4.16}$$

The velocity *v(s)* as a function of position in the electric field can be determined using the Lorentz equation $F = q(E + v \times B)$. Given no magnetic field:

$$F = qE \longrightarrow ma = qE \longrightarrow a = \frac{q}{m} E. \tag{4.17}$$

Given that

$$a = \frac{dv}{dt} = \frac{dv}{dx}\frac{dx}{dt} = v\frac{dv}{dx}, \tag{4.18}$$

then, it follows that:

$$v\, dv = \frac{q}{m} E\, dx. \tag{4.19}$$

Integrating both sides:

$$\frac{v^2}{2} = \frac{q}{m}\int_{s_0}^{s} E dx = \frac{q}{m}[V(s_0) - V(s)]. \tag{4.20}$$

So:

$$\frac{1}{v} = \sqrt{\frac{m}{2q}}[V(s_0) - V(s)]^{-1/2} \tag{4.21}$$

and the time integral is finally:

$$t = \int_{s_0}^{0} \frac{1}{v} ds = \sqrt{\frac{m}{2q}} \int_{s_0}^{0} [V(s_0) - V(s)]^{-1/2} ds, \tag{4.22}$$

where m and q are the mass and charge of the ion, s_0 is the position of ionization, and $V(s)$ is the electric potential as a function of position. The trajectory of the ion ends at the photocathode, located at $s = 0$.

In order to solve this integral, the electric potential must be known. The actual potential in the PMT is complex, but a few constraints must be fulfilled. Boundary conditions require $V(0) = 0$ at the photocathode and $V(s) \neq 0$ elsewhere. At the focusing grid, $V(L) = V_0$ (same potential as the first dynode).

At first approximation, the field between photocathode and grid could be considered that of a parallel plate capacitor. In such a case the field would be constant and the potential would be $V(s) = V_0 \left(\frac{s}{L}\right)$. While this may be a good model for a 1 inch PMT, for example, in which the cathode window and grid have a similar size, it does not make a good approximation for PMTs with a larger window, such as the 3 inch R11410, where the photocathode is larger and

field lines converge into the focusing grid. In such cases, a quadratic potential is a more adequate solution [158]:

$$V(s) = V_0 \left(\frac{s}{L}\right)^2. \tag{4.23}$$

Equation 4.22 can then be written as:

$$t = \int_{s_0}^{0} \frac{1}{v} ds = \sqrt{\frac{m}{2q}} \int_{s_0}^{0} \left[V_0 \left(\frac{s_0}{L}\right)^2 - V_0 \left(\frac{s}{L}\right)^2 \right]^{-1/2} ds, \tag{4.24}$$

This integral can be simplified and solved as follows:

$$\int_{s_0}^{0} \frac{L}{s_0\sqrt{V_0}} \frac{1}{\sqrt{1-\left(\frac{s}{s_0}\right)^2}} ds = \frac{L}{s_0\sqrt{V_0}} s_0 \arcsin\left(\frac{s}{s_0}\right)\Big|_{s_0}^{0} = \frac{\pi}{2}\frac{L}{\sqrt{V_0}} \tag{4.25}$$

The arrival time calculated from the integral and eq. 4.24 is then:

$$t = \frac{\pi}{4}\sqrt{\frac{2m}{qV_0}} L, \tag{4.26}$$

which is independent of the position of ionization.

In the case of a parallel plate model, the timing would be $t = \sqrt{\frac{2mL(L-s_0)}{qV_0}}$, which depends on s_0 and differs from eq. 4.26 additionally by the factor $\pi/4$.

The values of the proton mass $m_p = 1.672 \times 10^{-27}$ kg and charge $q_p = 1.602 \times 10^{-19}$ C can now be substituted into equation 4.26:

$$t = \frac{3.1416 \times 1.4142}{4} \sqrt{\frac{1.672 \times 10^{-27}\text{kg} \cdot M}{1.602 \times 10^{-19}\text{C} \cdot Q} \frac{L^2}{V_0}}, \tag{4.27}$$

where M is the number of nucleons and Q is units of charge. This equation simplifies to:

$$t = 1.11\sqrt{1.043 \times 10^{-8} \frac{\text{kg}}{\text{C}} \frac{M}{Q} \frac{L^2}{V_0}} \tag{4.28}$$

Using $1\text{C} = (\text{kg}\,\text{m}^2)/(\text{V}\,\text{s}^2)$, equation 4.28 can be rewritten in units of cm and μs:

$$t = \left(1.134 \frac{\text{V}^{1/2}\mu\text{s}}{\text{cm}}\right) \sqrt{\frac{L^2}{V_0}\frac{M}{Q}} \tag{4.29}$$

with V_0 in volts, L in cm and t in μs. M and Q are dimensionless.

4.4.2 Identification of residual gas molecules in the R11410 tubes

The timing of an afterpulse produced by an ion with a given mass-to-charge ratio will depend on the distance (L) and voltage (V_0) between photocathode and grid. The former is a property of the PMT, with L = 4.1 cm in the case of the R11410. The latter depends on the overall voltage applied (V_{tot}) and the divider circuit used. From the design of the XENON1T PMT base (see section 4.1.4), the voltage at the first dynode and grid (V_{D1}) is given by:

$$V_{D1} = \frac{R_2}{R_1 + R_2} V_{tot}, \tag{4.30}$$

where R_1 is the resistance between the photocathode and grid/first-dynode, while R_2 is the resistance between the grid/first-dynode and ground. For the XENON1T base $R_1 = 20$ MΩ and $R_2 = 72.5$ MΩ.

At a total voltage of −1500 V, the voltage at the grid/first-dynode is then $V_{D1} = -1175.7$ V. Thus, the potential difference is $V_0 = 324.3$ V.

Equation 4.29 can be simplified to:

$$t = 0.258\sqrt{\frac{M}{Q}} \tag{4.31}$$

Table 4.2 shows the identified ions from afterpulses in the R11410-21 tubes, comparing the measured times from experiment, the calculated times from equation 4.29 and the times obtained from the simulations described in the following section. The experimental errors correspond to the spread of each peak of afterpulses. The calculated errors are propagated from the measurement uncertainty of the distance between photocathode and first dynode (± 0.1 cm), as well as the value of the voltage divider resistors (± 2 %). The simulation uncertainty corresponds to the spread of each simulated ion distribution.

4.4.3 Afterpulse Simulations

The transport of electrons and ions in the R11410 PMT has been simulated with the COMSOL Multiphysics® software. The phototube has been replicated in detail (model generated by Peter Barrow), with the dimensions taken from direct measurement of the elements in an open PMT sample. Special attention was given to the reproduction of the focusing grid and dynodes, as can be appreciated in figure 4.26. The electric field is generated by setting the potential on each surface in accordance to the applied input voltage and the divider specifications.

The simulation of 10,000 electrons drifting from the photocathode to the first dynode results in an average transit time of (45.4 ± 1.8) ns. This value is in agreement with the reported value of (46 ± 9) ns by Hamamatsu for this particular PMT model.

Ion	M/Q	Afterpulse Time [μs]		
		Measured	Calculated	Simulated
H^+	1	0.28 ± 0.02	0.26 ± 0.01	0.27 ± 0.01
H_2^+	2	0.39 ± 0.02	0.37 ± 0.01	0.38 ± 0.01
He^+	4	0.52 ± 0.02	0.52 ± 0.01	0.52 ± 0.01
CH_4^+	16	1.01 ± 0.03	1.03 ± 0.02	1.02 ± 0.02
Ne^+	20	1.13 ± 0.03	1.16 ± 0.03	1.14 ± 0.02
N_2^+	28	1.33 ± 0.03	1.37 ± 0.03	1.33 ± 0.03
Ar^+	40	1.58 ± 0.04	1.63 ± 0.04	1.57 ± 0.03
Xe^{++}	65	2.02 ± 0.05	2.08 ± 0.05	2.02 ± 0.04
Xe^+	131	2.85 ± 0.07	2.96 ± 0.07	2.80 ± 0.06

Table 4.2: Several residual molecules in the PMT have been identified as generators of afterpulses. M/Q corresponds to the mass-to-charge ratio in nucleons over units of charge. The time delay measured by experiment is compared to the calculated value from equation 4.29 and the result from simulations. The experimental errors correspond to the spread of each peak. The calculated errors are propagated from the measurement uncertainty of the distance between photocathode and first dynode, as well as the value of the voltage divider resistors. To quantify the uncertainty in the simulations, the grid-to-dynode distance and resistor values have been varied, and the distribution spread for each simulated ion has been taken into account.

In order to simulate the drift time of afterpulses, several ions are generated in the region around the focusing grid (where the probability of ionization is highest, as previously discussed) and allowed to drift in the electric field. The results are presented in table 4.2.

The afterpulse timing values from the experimental, calculated and simulated results differ on average by about 3 %, being in good agreement when taking into account the uncertainties. The experimental errors correspond to the spread of each peak. The calculated errors are propagated from the measurement uncertainty of the distance between photocathode and first dynode, as well as the value of the voltage divider resistors. To quantify the uncertainty in the simulations, these have also been made varying the distance and resistor values mentioned before and considering the spread of the distribution for each simulated ion. The comparison is also shown in figure 4.27 (right). It suggests a high accuracy in the identification of ions. The slight deviation between the calculated drift times for Xe ions with respect to the simulated and experimental values indicates that the quadratic potential implemented in section 4.4.1 is a good approximation but not an exact description of the complex electric field in the PMT, shown in figure 4.26 (left).

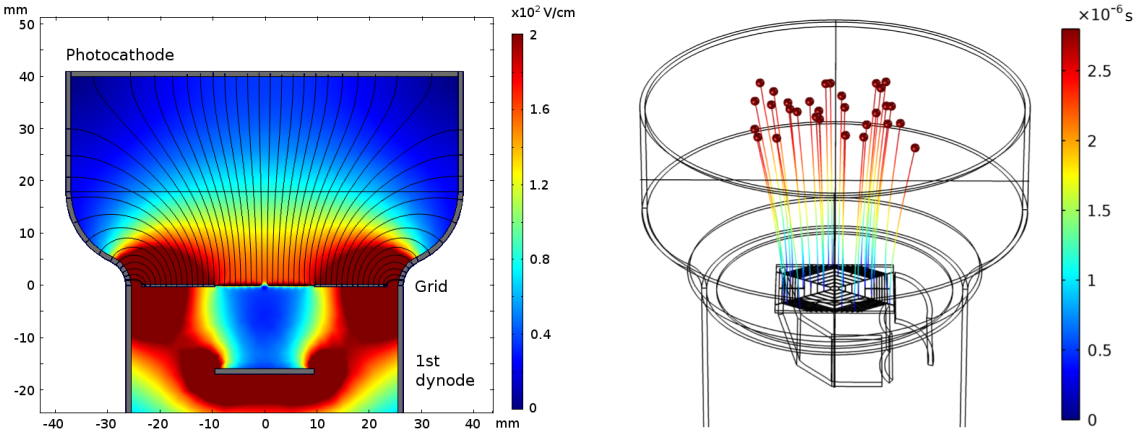

Figure 4.26: (Left) Simulation of the PMT electric field using COMSOL Multiphysics® (model developed by Peter Barrow). The color scale indicates the field strength in V/cm. (Right) Ion transport simulation in the R11410 PMT. Xe ions are generated at the focusing grid and drifted through the simulated electric field. The color scale indicates the ion drift time.

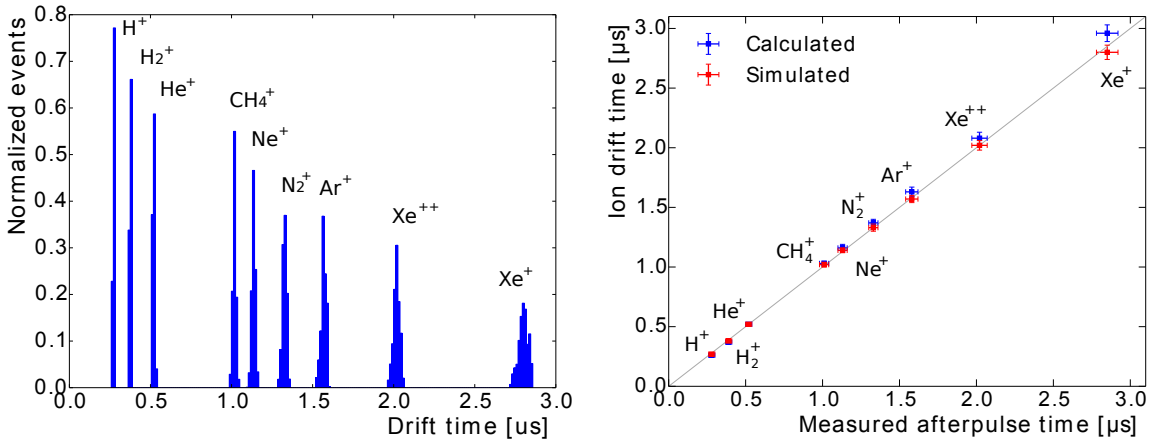

Figure 4.27: (Left) Histograms of the simulated drift times for different ions. The means indicate the expected delay of afterpulses generated by each ion. (Right) Comparison between the calculated (blue) and simulated (red) ion drift times with the measured afterpulse times from experiment. The values are taken from table 4.2. The results agree well within their uncertainties and differ on average by around 3 %, suggesting an accurate ion identification. The diagonal line indicates a one-to-one relation, for reference.

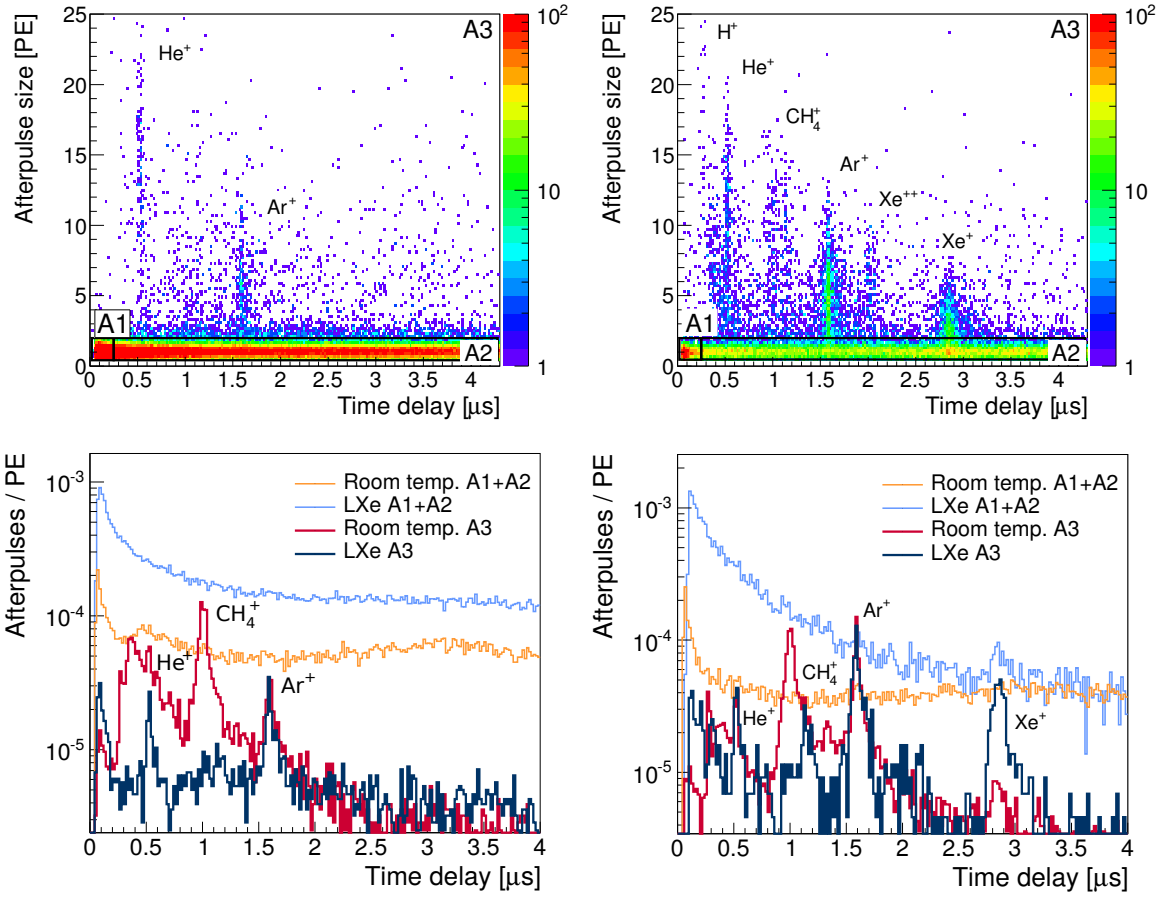

Figure 4.28: (Top) Afterpulse populations for PMT KB0413 in LXe on the left and KB0415 at room temperature after cool down on the right. The ions generating the A3 afterpulses have been identified and labeled. (Bottom) Comparison of the afterpulse spectra in LXe and at room temperature for KB0413 on the left and KB0415 on the right. The populations have been separated in A1+A2 (single PE) and A3 (multi-PE) for a clearer comparison of the He^+, CH_4^+, Ar^+ and Xe^+ peaks.

4.4.4 Afterpulse Analysis and Leak Diagnosis

Afterpulse measurements have been performed for the PMTs at room temperature and in LXe. The top plots in figure 4.28 show the A1, A2 and A3 populations of afterpulses defined earlier for PMT KB0413 in LXe (left) and for KB0415 at room temperature after cool down (right). The ions generating the A3 afterpulses have been identified. The bottom plots in figure 4.28 show a comparison of the afterpulse spectra in LXe and at room temperature for both PMTs (KB0413 on the left and KB0415 on the right). It can be observed that the A2 afterpulse rates increase drastically during operation in LXe and, while the He^+ and Ar^+

Afterpulses [%]:	Total	A1	A2	He^+	CH_4^+	Ar^+
Room temp.	1.4 ± 1.2	0.11 ± 0.05	0.9 ± 1.1	0.02 ± 0.01	0.07 ± 0.03	0.08 ± 0.07
LXe	8.6 ± 2.2	1.8 ± 0.5	6.4 ± 1.7	0.02 ± 0.01	0.02 ± 0.01	0.08 ± 0.02

Table 4.3: Afterpulse rates given as a percentage of the total SPE trigger pulses. A comparison is made between the measurements at room temperature and in LXe. The errors are computed statistically as mean absolute deviations. The rate increase in LXe is due to the A2 afterpulses from single photoelectrons distributed homogeneously in time, whereas the afterpulses from identified ions remain on average the same or decrease. Ions not shown in the table have an average rate below 0.02 % of the total triggers.

afterpulse rates remain unchanged, the H_2^+ and CH_4^+ afterpulses are suppressed considerably.

A quantification of the afterpulse rates has been performed on 44 PMTs measured in the xenon testing facility. The afterpulse rate is given as a percentage of the total SPE trigger signals. At room temperature, the mean total afterpulse rate is (1.4 ± 1.2) %. The ions with most afterpulsing are He^+ (0.02 ± 0.01) %, CH_4^+ (0.07 ± 0.03) % and Ar^+ (0.08 ± 0.07) %. All other ions show rates below 0.02 % of the total trigger signals. The same measurements were performed with 11 PMTs in LXe. The results are compared in table 4.3. In cold, the mean afterpulse rate has increased to (8.6 ± 2.2) %. The major increase is in the A2 afterpulsing, consisting of single photoelectrons spread out homogeneously over several microseconds. Part of this population may be comprised by photons from the micro light emission described in section 4.3.1. On the other hand, the average contributions of He^+ and Ar^+ remain unchanged, whereas the mean CH_4^+ rate decreased to (0.02 ± 0.01) %. The bottom-left plot in figure 4.28 also shows the H_2^+ afterpulse contribution being suppressed during cool down. These observations suggest that the lower temperatures do not alter the presence of noble gases in the PMT vacuum, while compounds of electronegative elements are effectively reduced. The latter may be more susceptible to adhesion on the PMT surfaces and no longer contribute to the afterpulsing.

From figure 4.28 (top right) it can be observed that the mean size of the afterpulses decreases with the mass of the ion that produced them. Figure 4.29 shows the afterpulse size distribution for selected ions. Heavier ions like Xe^+ produce afterpulses with a mean around 2 PE, while lighter ions like H^+ produce larger afterpulses of around 18 PE with a larger spread. From equation 4.20, it follows that the velocity of the ion is related to its mass by:

$$v = \sqrt{\frac{2q}{m}\Delta V}, \tag{4.32}$$

where ΔV is the potential difference; m and q being the mass and charge of the ion, respectively. Lighter ions will thus obtain higher velocities and be able to scatter more electrons uppon interaction with the photocathode. Heavier ions,

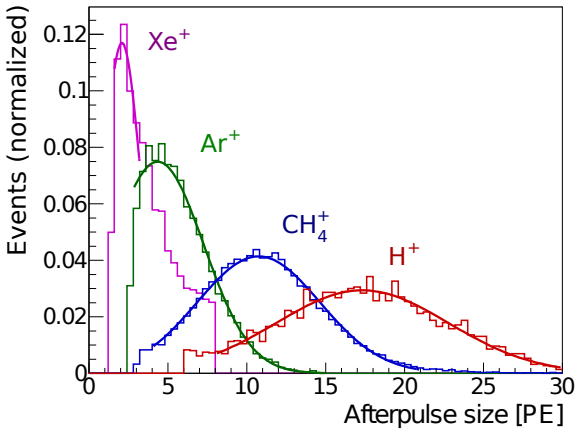

Figure 4.29: Distribution of the afterpulse size in PE produced by different ions. Heavier ions, like Xe^+, generate smaller afterpulses, while lighter ions, like H^+, produce larger afterpulses.

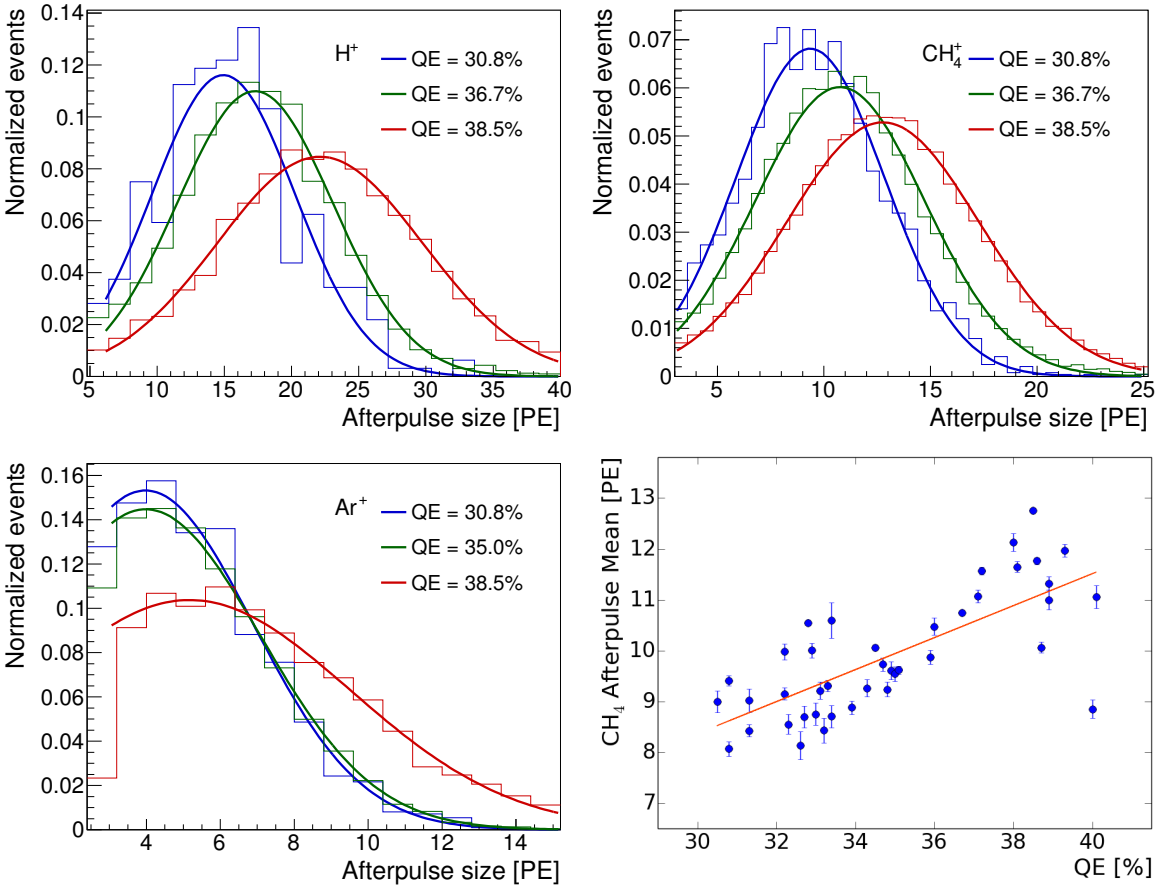

Figure 4.30: Comparison of the afterpulse size distributions for PMTs with different QE. Plots for the main observed ions are shown (H^+, CH_4^+ and Ar^+). The mean afterpulse size increases with increasing QE. The bottom right plot shows the distribution of the mean CH_4^+ afterpulse size compared to QE for 41 PMTs. A linear correlation is observed, meaning that the QE of the PMT also plays a role in the electron production from incident ions on the photocathode.

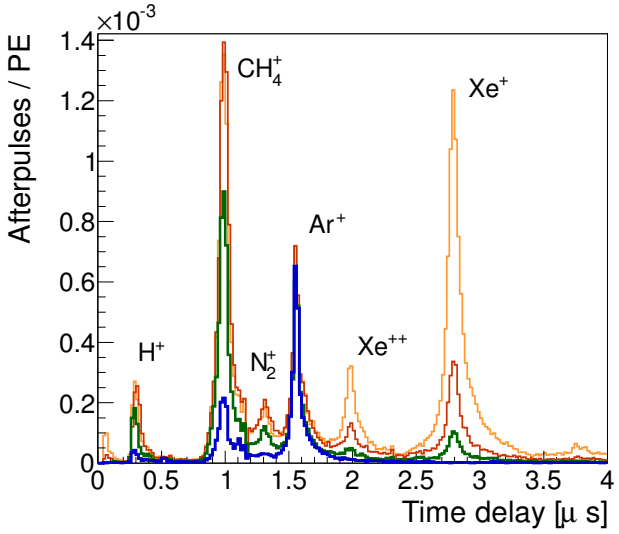

Figure 4.31: Afterpulse spectrum for KB0056 at room temperature before operation in LXe (blue curve) and its evolution after each one of a total of 3 cool downs in LXe. The Xe^+ peak appears after the first cool down (green curve) and increases after each successive cool down.

on the other hand, will produce fewer electrons and, hence, smaller afterpulses.

The afterpulse size has also been observed to be affected by the QE of the PMT. Figure 4.30 (bottom right) shows the distribution of the mean CH_4^+ afterpulse size compared to the QE of each PMT. A linear correlation is observed bewteen the two parameters. This shows that a photocathode with a higher electrons yield from photons also generates electrons more efficiently from impinging ions. As a result, the measurements of afterpulse size in PE can give an insight into the quantum efficiency of a PMT.

The appearance of a Xe^+ peak in the afterpulse spectrum has been observed for a few PMTs after operation in LXe (as in the case of KB0415 in figure 4.28). Another example is presented in figure 4.31, which shows the spectra of the A3 afterpulses for KB0056 (R11410-20 model) before any cool down in LXe (blue curve) and after each one of a total of 3 cool downs. A clear rise of afterpulses around 2.8 μs is observed, increasing after every cycle. After having been returned to Hamamatsu, a gas analysis was performed on this particular PMT and the presence of Ar^+ and Xe^+ was confirmed. Out of the 44 R11410-21 PMTs tested in LXe, 8 of them developed Xe^+ afterpulses. From a rate below 0.01%, the afterpulsing at 2.8 μs for these faulty PMTs increased to values between 0.04% and up to 1.0%. Such PMTs have been returned and replaced by Hamamatsu.

It is important to remark that many of the PMTs tested in Xe were preselected from the observation of an N_2^+ afterpulse increase after their first cryogenic tests or other issues such as unstable DC rates or sparking. Such an example

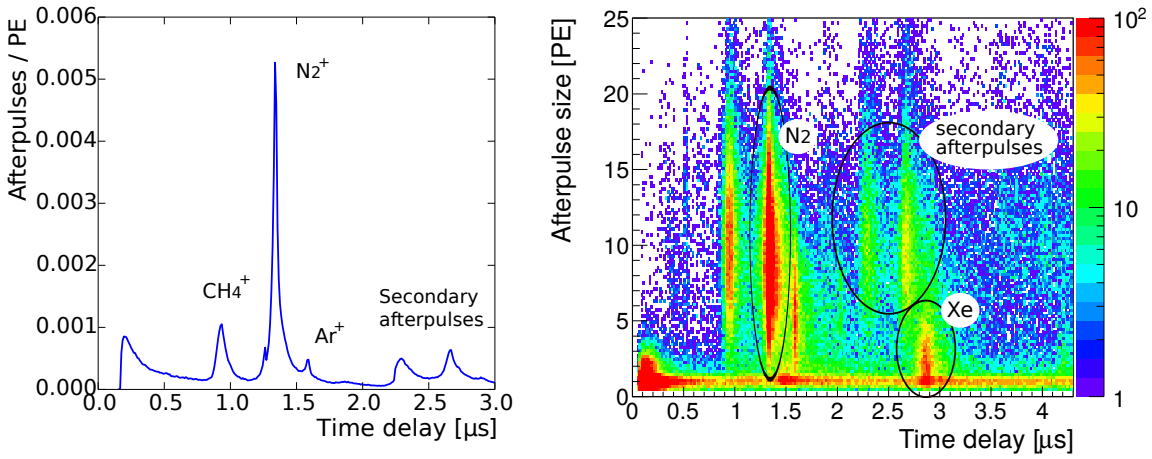

Figure 4.32: (Left) Afterpulse spectrum of KB0624 measured at the MPIK facility before any cool down. The large N_2^+ peak is a clear indicator of an air leak. The peaks above 2 μs correspond to secondary afterpulses generated from the N_2^+ afterpulses, as shown on the right plot. (Right) Afterpulses in KB0624 after operation in LXe. The appearance of Xe^+ afterpulses is clear at 2.8 μs. The population above 2 μs and larger than 5 PE is comprised from N_2^+ and Ar^+ secondary afterpulses.

is shown in figure 4.32, where the afterpulse spectrum of KB0624 measured in the MPIK setup showed a large peak for N_2^+, indicating a possible air leak. This diagnosis was confirmed by measurements in LXe, after which the appearance of Xe^+ afterpulses was evident. Due to the pre-selection of possible faulty PMTs, the statistics for the appearance of Xe^+ leaks was not expected to be representative of the full set of PMTs installed in XENON1T, of which the majority showed no issues during the tests described here. Results from measurements in XENON1T are presented in chapter 5.

4.5 Summary of the Evaluation Tests and Final PMT Selection

The testing campaign of the R11410-21 PMTs comprised a total of 321 units, out of which 248 were selected for operation in XENON1T. The evaluation of the tubes was based on their performance in terms of dark count rate, SPE response, transit time, quantum efficiency and level of light emission. Measurements in gaseous and liquid xenon were performed on a subset of PMTs, studying their DC rate, gain and afterpulse evolution. The results have been published in [135], where the parameter distributions for all PMTs are shown and discussed.

Out of all the PMTs tested, a total of 73 tubes were rejected and, thus, ex-

cluded for use in XENON1T—this corresponds to a rejection of 22 %. Out of these, 12 tubes were excluded due to an elevated or unstable dark count rate, either at cryogenic or room temperatures. The main problem encountered with the PMTs was light emission. A total of 53 units presented this undesired behavior and were returned to Hamamatsu, with replacements given in return. An additional 8 PMTs—out of the 44 tested in LXe—developed leaks after operation in LXe. These have also been rejected.

As presented in [135], the 248 PMTs selected for XENON1T have an average quantum efficiency of (34 ± 3) %. Their average dark count rate at $-100\,^{\circ}\mathrm{C}$ is (40 ± 13) Hz. At a gain between $(2 - 3) \times 10^6$, the peak-to-valley ratio ranges between 2.5 and 4.5, indicating a good signal to noise separation.

In XENON1T, the evolution of the gains, DC rates and afterpulsing are constantly monitored for all PMTs. Special attention is given to the detection of light emission and Xe leaks, since these can strongly affect the performance of the detector. The methods presented here are useful tools that are also used for the analysis of the PMTs in XENON1T, as will be discussed in chapter 5.

Chapter 5

The PMT Arrays in XENON1T

For the detection of light from interactions in the LXe, XENON1T relies on two arrays of R11410-21 PMTs. Located on opposite sides of the TPC, the top and bottom arrays are comprised of 127 and 121 PMTs, respectively. In this chapter, the assembly of the PMT arrays and their installation in the XENON1T TPC are described. The results from the first PMT operations and calibrations are also discussed. In addition, several tools have been developed for shifters and users within the XENON collaboration. These tools—such as the PMT database and software for gain calibration, along with their user interfaces—are described.

5.1 Assembly and Installation of the Arrays

After the PMT tests presented in chapter 4, the tubes that fulfilled all requirements were stored in a clean room—later to be included in the PMT arrays of XENON1T. The clean room—located at MPIK—has a total size of 26 m^2 and is a class 1000. The operations regarding the assembly of the PMT arrays, before shipment to LNGS, were performed in this room—as shown in figure 5.1.

Figure 5.1: (Left) PMT storage in the clean room. (Right) Clean room operations and assembly of the PMT arrays.

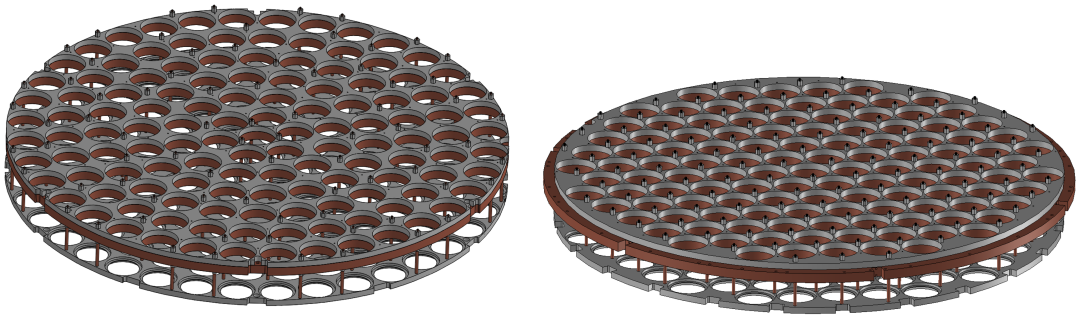

Figure 5.2: (Left) Top array structure. (Right) Bottom array structure. Each stack consists of three elements: (from top to bottom) PTFE support plate, copper support plate and PTFE reflector. Design by the UCLA group.

The design of the structures for the PMT arrays, as well as their production, was carried out at UCLA. Figure 5.2 shows a schematic of both the top and bottom arrays. The PMT positions in the top array are distributed in concentric rings for improved event position reconstruction. The more compact 'honeycomb' layout of the bottom array allows for an optimal light collection. In both cases, the structure consists of three layers stacked over one another. The first element of the stack is a PTFE reflector, the purpose of which is to maximize the light collection on the PMTs by reflecting the photons towards the PMT windows. The second element is a copper support plate, which gives rigidity to the whole structure. The third element is a PTFE support plate, to which the PMT holders are attached.

After production at UCLA, the array structures were shipped to MPIK, where they were degreased and cleaned with a dedicated procedure, described briefly. The PTFE plates were immersed in a nitric acid solution and rinsed several times in de-ionized water. The copper plates were etched and passivated with acid solutions, being rinsed after each solution with de-ionized water. All the small components, such as the nuts and screws used to hold the plates together, were also thoroughly cleaned. The PMTs were cleaned by wiping the body with alcohol.

Once all the individual parts were cleaned and chemically treated, the PTFE and copper plates were stacked and fixed with copper screws—acting also as spacers—according to the layouts depicted in figure 5.2. Each structure was then installed within a large multi-purpose black box. Said box served as a mounting station and testing facility, being used as well for storage and transportation of the arrays. Once inside the box, the PMTs were introduced into their corresponding positions in each array and held in place with locking caps.

The following step consisted in mounting the voltage divider bases (see in section 4.1.4) onto the pins of each PMT. Prior to this step, the HV and signal cables had already been soldered to the bases and the electrical continuity and

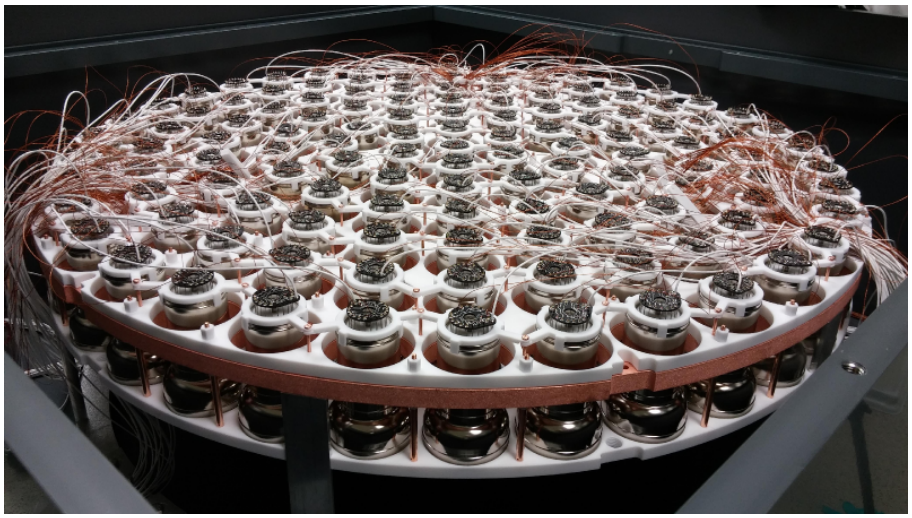

(a) Top PMT array.

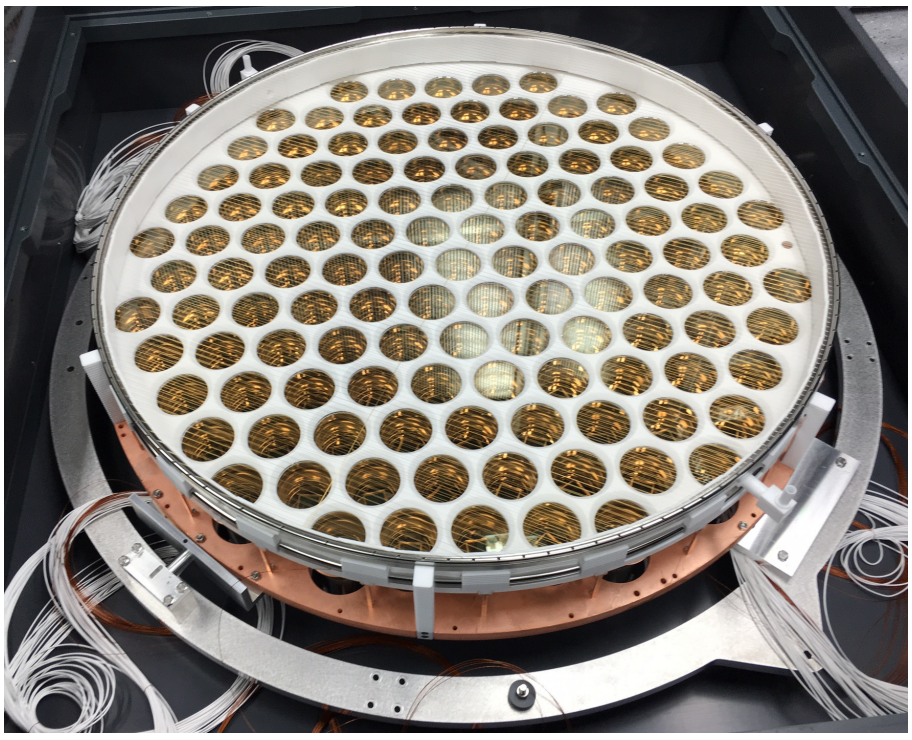

(b) Bottom PMT array.

Figure 5.3: Fully assembled PMT arrays. The top array, with the PMTs facing downwards, shows the voltage divider bases and the cabling for all PMTs. The bottom array—also assembled with the PMTs facing downwards—was rotated to the position shown in the image prior to its installation in the TPC.

Figure 5.4: (Left) Bottom view of the fully assembled TPC held in place within the XENON1T water tank. The cryostat vessel is being lifted to cover and enclose the TPC. (Right) An inside view of the XENON1T TPC, showing the top PMT array surrounded by the PTFE reflector pannels.

resistivity of each element was thoroughly tested at UZH (see [145] for details). The bases were grouped into 11 modules—6 for the top array and 5 for the bottom—according to the layout of the PMT read-out electronics. Figure 5.3 shows the fully assembled PMT arrays, with bases and cabling in place. Once again the electrical continuity and resistivity of the bases was confirmed. The functionality of each PMT was checked by observing signals from dark pulses in an oscilloscope.

The fully equipped arrays were then shipped to LNGS for their installation in XENON1T. Upon arrival and prior to their installation in the TPC, the bottom array was rotated to have the PMTs facing upwards—as seen in figure 5.3 (b). The cathode and screening meshes were stacked over the bottom array and the reflector panels were mounted around its perimeter. Figure 5.4 (right) shows the top array installed inside the bell and surrounded by the PTFE panels of the TPC. Figure 5.4 (left) shows a bottom view of the fully assembled TPC, while the cryostat vessel is being lifted to cover and house it for the first run of XENON1T.

The XENON1T detector was inaugurated in November 2015. An intensive commissioning phase took place during the first half of 2016, during which each subsystem was thoroughly checked and put into operation. At this time, the

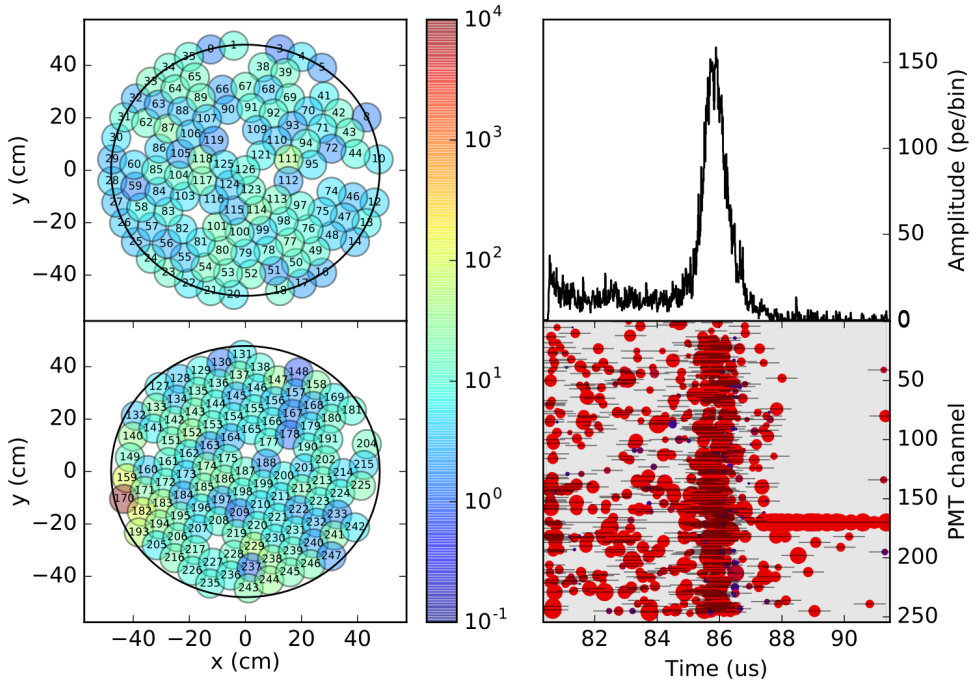

Figure 5.5: First S2-like signal observed in XENON1T. The left panels show the hit pattern on the top and bottom PMT arrays. The top-right panel is the summed waveform, while the bottom-right panel shows the individual hits on each PMT channel.

PMTs were connected to the HV modules and the DAQ electronics. Their functionality was checked and confirmed by successfully observing signals in every channel. Figure 5.5 shows the first S2-like signal observed with the PMTs on March 17th 2016. With the detector filled with GXe, although no drift field was applied, the scintillation signal was produced between the screening mesh and the PMTs—operated at –1500 V.

The following section presents the first measurements of LED light with the PMT arrays, as well as an analysis of the afterpulse spectra—which is then used to diagnose Xe leaks and the correlation with the PMT performance.

5.2 LED Data and Afterpulsing

The data in XENON1T is analyzed via the Processor for Analyzing XENON1T, a.k.a PAX. The fundamental data structures in PAX are the so-called *hits*. A hit is a fluctuation above threshold in the signal of a PMT, which can be caused by a photoelectron detection or noise. If hits are measured simultaneously over several channels, these are clustered into *peaks*. According to their properties, peaks are classified into possible S1s, S2s or noise. Peaks classified as S1s and S2s

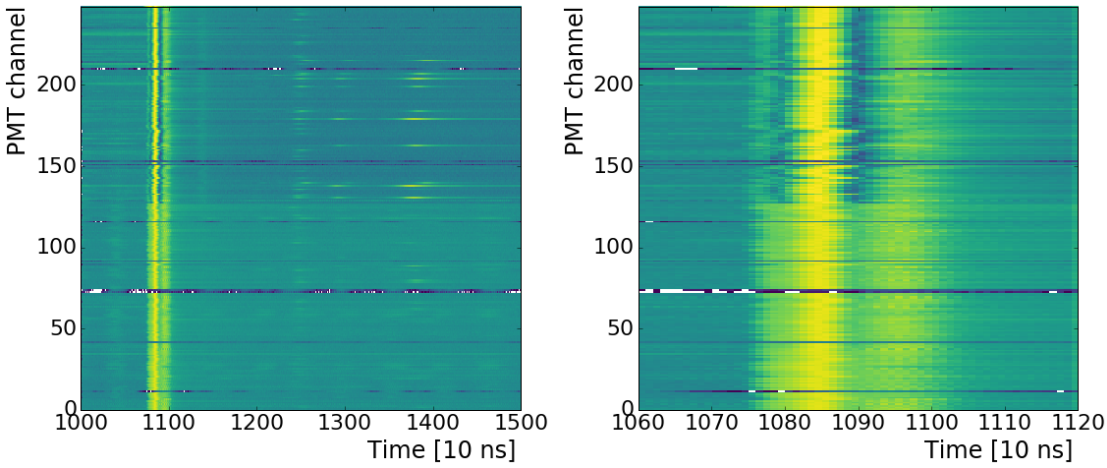

Figure 5.6: (Left) Hit distribution over time for all PMT channels in LED run 1334 (date and time: 160708_1340). (Right) Zoom into the period around LED ON. Empty channels correspond to PMTs that were OFF.

are paired into *interactions*. Finally, an *event* is constructed with one or more interactions. For the following study of LED data, the analysis is performed at the level of hits from individual PMTs. The results shown here correspond to run 1334 (date and time: 160708_1340). All PMT gains have been equalized to 2.5×10^6.

The data acquisition in LED mode is initialized by the LED trigger. Figure 5.6 shows the hits recorded on all PMT channels over a period of 4 μs. The LED is ON for around 100 ns, so the hits after this time correspond mostly to PMT dark counts and afterpulses. A zoom into the period around LED ON—seen in figure 5.6 (right)—shows a structure of three distinct vertical lines. The central line corresponds to the primary photons from the LED. The left and right lines are identified as pre-pulses and late pulses, respectively. Pre-pulses are caused by photons that pass through the PMT window and interact directly with the first dynode of the PMT. The resulting signal is faster than that of photoelectrons produced at the window by a factor equivalent to the transit time of the photoelectron towards the first dynode. The late pulses, in turn, can be produced by secondary electrons back-scattering off the first dynode and impinging a second time, producing a signal several tens of nanoseconds later. A detailed discussion of these populations is found in [159] [135]. Figure 5.7 (left) shows a histogram of the transit times relative to the primary LED photons, centered at zero, where the pre and late pulses can be observed.

As can be seen in figure 5.7 (right), a larger number of hits are measured by the PMTs of the top array (channels 0–126), than by the PMTs on the bottom array (channels 127–247). This is explained by the fact that light from the LED is diffused when traversing the liquid-gas interface of LXe, where the photons

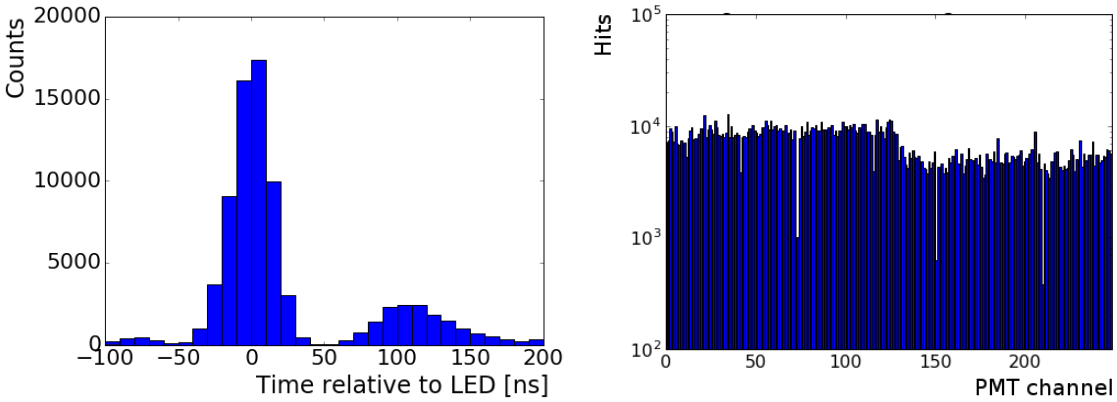

Figure 5.7: (Left) Transit time of the PMT hits. The primary photon signals from the LED are centered at zero. Late and pre-pulse populations are observed. (Right) Hit rates per channel. The top PMTs register a larger number of hits than the bottom PMTs.

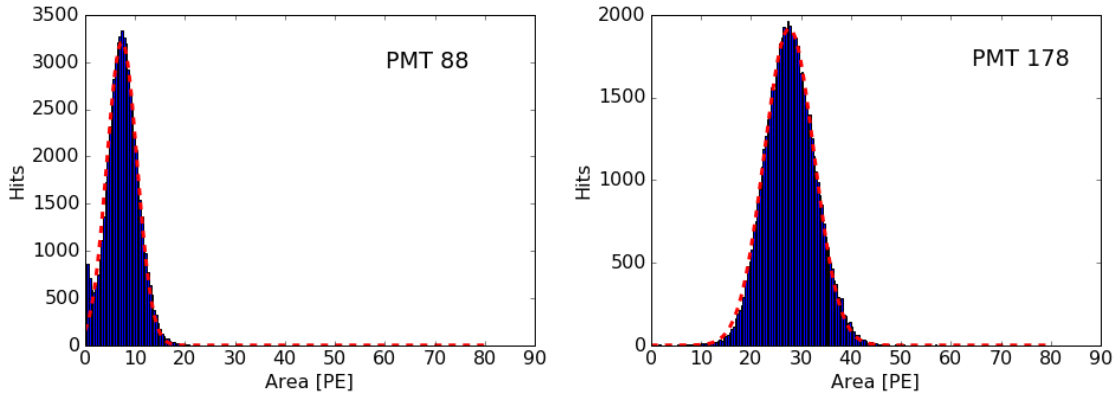

Figure 5.8: (Left) Distribution of the hit size (area) for a PMT in the top array. (Right) Hit size distribution for a bottom PMT. The total reflection of photons at the liquid-gas interface contributes to a higher illumination on the bottom array.

are scattered. This results in more hits in the top array with a smaller PE size—while the bottom array registers fewer hits, but with a larger average size in PE. Figure 5.8 shows that, in fact, the mean hit size of the bottom array (right) is larger than for the top (array), which is also influenced by a higher photon collection on the bottom array due to total light reflection on the liquid-gas interface.

A study of the afterpulses in each PMT has been performed by analyzing the timing of the measured hits relative to the LED trigger. In figure 5.9 (left), the number of afterpulses normalized to number of PEs (hits/PE) are shown as a

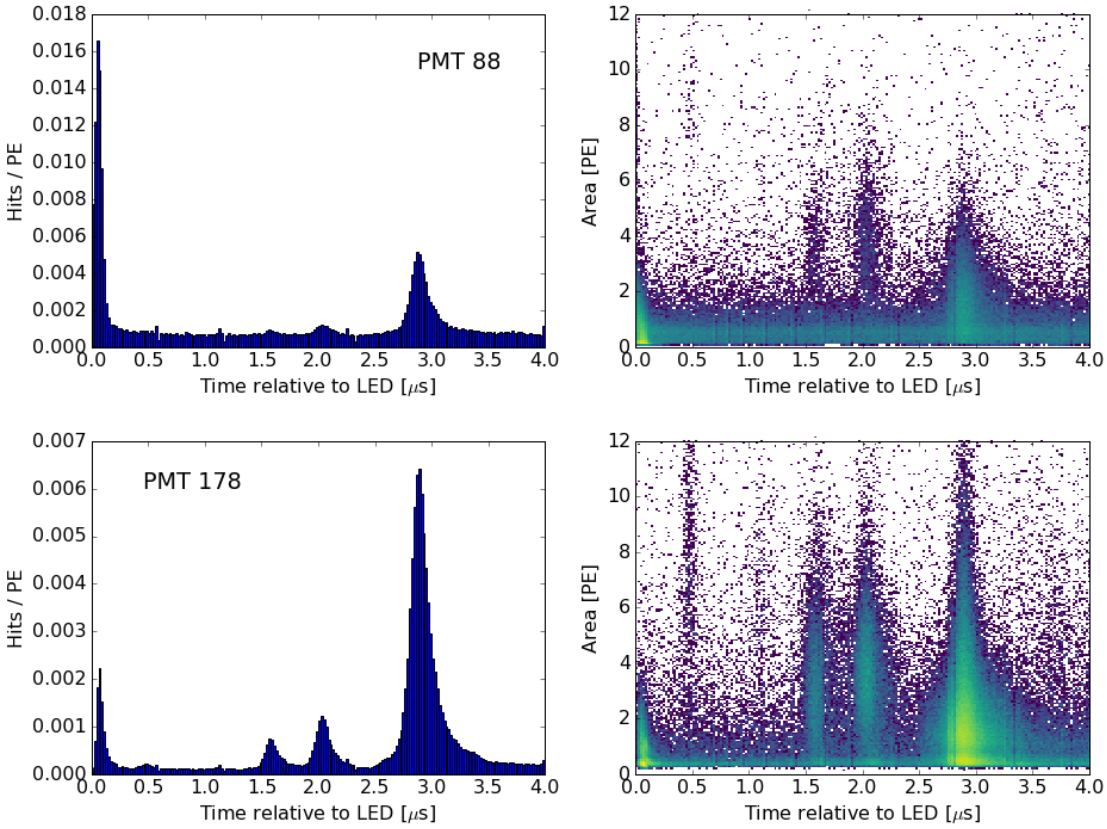

Figure 5.9: Example PMTs with detected Xe leaks. The afterpulse spectra indicate a large rate of Xe^+ afterpulses at around 2.8 μs (see analysis in section 4.4).

function of time. Two examples are presented here, for one PMT in each array. Following the analysis in section 4.4, the presence of a Xe^+ leak is identified by the large population of afterpulses at around 2.8 μs. Figure 5.9 (right) shows the distribution of the afterpulse hit size and time delay. Other ions identified in the afterpulse spectrum include Xe^{++}, at around 2 μs, and Ar^+ at 1.6 μs.

The Xe^+ afterpulse rate has been determined by integrating the number of hits in the range (2.7 – 3.2) μs and dividing by the total number of primary PEs. Dark count and noise events are rejected by subtracting the hits in an equal time period free of ion afterpulses. Table 5.1 lists the PMTs which show the presence of a Xe leak. As of July 8th 2016, a total of 24 PMTs have an observable peak of Xe^+ afterpulses, with varying rates, from 0.02 % up to 11.24 %. Of the PMTs for which a Xe leak has been identified, only PMTs 71 and 139 were measured in LXe at UZH—neither of which presented any signs of a Xe leak after 2 cool downs in LXe.

The afterpulse measurements for leak diagnosis are relevant since it is known that a PMT with a vacuum breach will eventually fail. During the operation

Table 5.1: List of PMTs that, as of July 8th 2016, presented signs of a Xe leak according to their measured Xe^+ afterpulse rates:

PMT	**137**	**178**	**214**	**130**	**88**	**162**	**203**	**139**	**79**	**206**	**78**	**1**
Xe^+ [%]	11.24	6.6	6.49	4.9	4.45	4.09	4.02	2.39	2.29	1.43	1.34	0.81

PMT	**198**	**85**	**183**	**65**	**61**	**102**	**66**	**119**	**135**	**71**	**2**	**217**
Xe^+ [%]	0.7	0.67	0.6	0.6	0.43	0.31	0.29	0.19	0.11	0.08	0.02	0.02

of XENON1T, a correlation between tripping PMTs and those with a Xe leak has been observed. As of August 2016, the top 8 PMTs with highest Xe afterpulsing had already tripped and shown unstable operation. It is clear that a low quality vacuum increases the chances of a PMT to trip. Stemming from the analyses presented here, dedicated afterpulse measurements are taken frequently by shifters in XENON1T in order to monitor the development of Xe leaks.

5.3 Tools for users

Several tools have been developed for shifters and other users of the PMTs in XENON1T. These include a calibration framework and GUI for generating the SPE spectra and estimating the PMT gains and other parameters. A database containing the results of PMT measurements includes a web interface to visualize and interact with its information. Results from the LED calibrations are also added to the database.

5.3.1 Gain Calibration Framework

A graphical user interface (GUI) has been developed to aid shifters in performing the weekly gain calibrations from LED data. The GUI has been built with Tkinter—the standard GUI development package for Python. Figure 5.10 shows the GUI window which is launched with the `calib_GUI_v2-0.py` script. The calibration run is then selected by entering its `date_time` string in the uppermost text box—such as 160510_1409, in this example.

The first step in the process is the creation of the SPE spectra for all PMTs. This is performed via the `Process` button, which runs `make_spe_spectra_v1.py`. This script reads the processed root files from a calibration run, goes through all events and applies a cut on the amount of hits that are added to the PMT spectrum. This acts as a software light-equalization, providing an SPE spectrum with the adequate amount of single PE for the fitting procedure to be accurate. A hardware light-equalization is not viable given the large amount of PMTs, divided in two separate arrays which receive different amounts of light.

Once the SPE spectra for all PMTs have been created, the fitting routine is activated with the `Run All` button. This launches the `spe_gain_calib_v1.py`

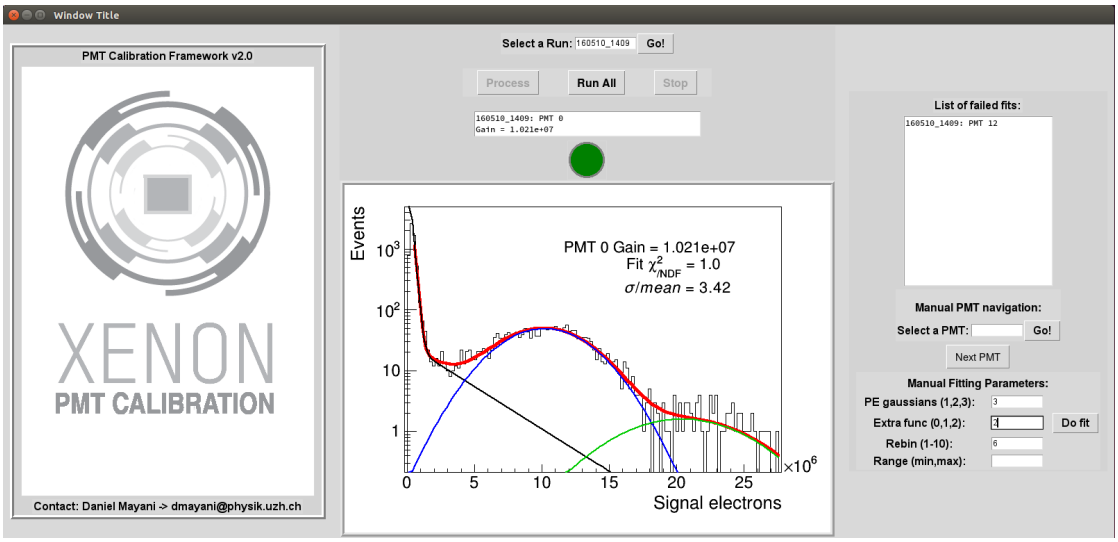

Figure 5.10: Graphical user interface for the PMT gain estimation from LED calibrations. Via the GUI, the shifter can produce and fit the SPE spectra—from which the gains are estimated—as well as modify the fit parameters.

script, which reads-in the spectra and performs the fit for gain estimation (see section 4.3.2 for details). The process is divided in several steps: first, the minima and maxima of the spectra are determined via `minmax_finder_v1.py`; second, the fit is calculated with `spe_fitter_v44.py`; third, the results—including the PMT gain and resolution, the peak-to-valley ratio of the spectrum and the $\chi^2_{/NDF}$ of the fit—are written into a text file; fourth and final, the fit results—together with the PMT spectrum—are drawn onto a canvas with `draw_myfit.py` and displayed on the GUI.

The GUI allows the shifter to also modify the parameters for the fit—such as number of Gaussians, additional exponential, number of bins and fit range—in order to improve the fit when necessary. A panel displays the list of spectra for which the fit has failed, to which the shifter can then navigate manually and investigate.

Some example spectra from run 160510_1409 are shown in figure 5.11. During the commissioning phase of the experiment, the noise conditions in the PMT electronics chain were not optimal and the fitting method for gain estimation encountered some difficulties. The bottom plots in figure 5.11 show some examples of failed fits due to large amounts of noise on the PMT channel. Because of this, another gain estimation method has also been adopted, consisting of a statistical estimation which is independent of the SPE spectrum model [160]. Once the noise conditions in the detector are improved, the fitting method can be used more effectively. At the moment, even with sub-optimal noise conditions, the gains estimated from the SPE fit agree within 5 % with other estimation methods, such as the Gaussian mean of the hits in 'small' S1 signals (less than 100

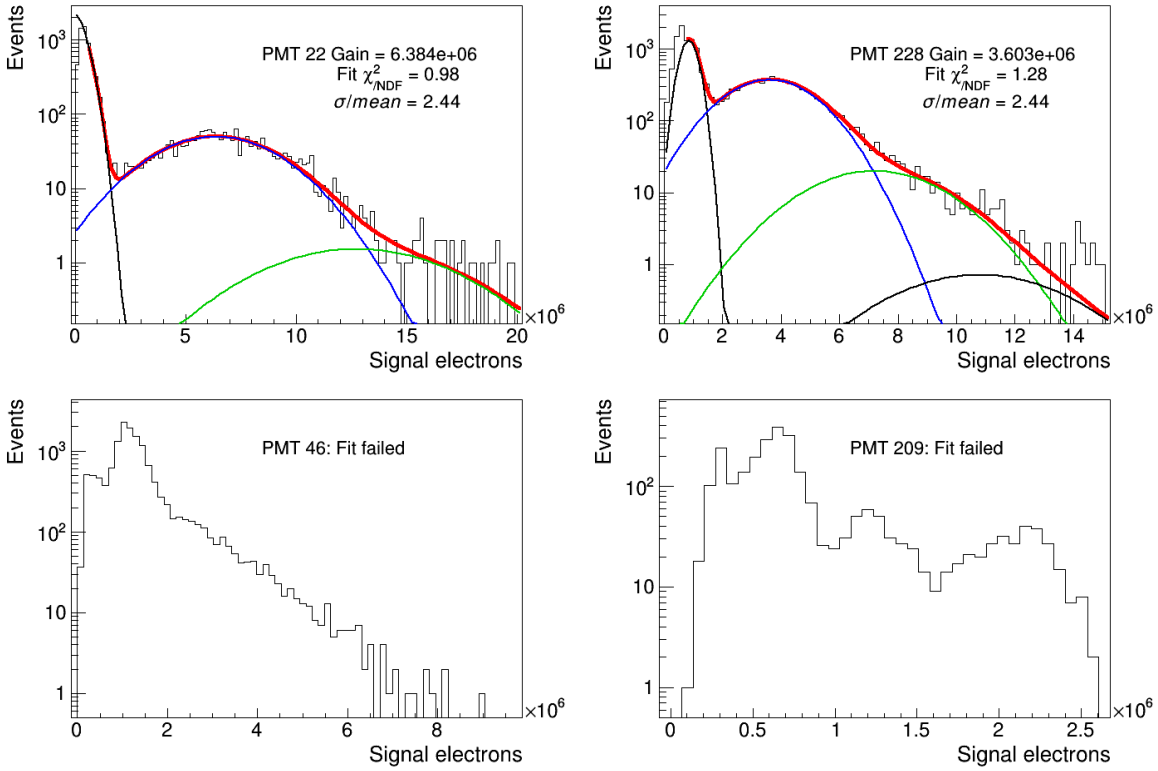

Figure 5.11: Sample spectra from the LED calibration run 160510_1409. The top plots show successful fits with which the gain of the PMTs has been estimated. The bottom plots show failed fits due to excessive noise from the electronics.

hits)—an analysis performed by Richard Saldanha. See figure 5.12.

5.3.2 PMT database

In order to keep track of all present and future information of the XENON1T PMTs, a database has been developed. It has been written in the structured query language MySQL, designed specifically for managing data in a relational database. Hosted on `xecluster`, the database is called `xenon1tpmts` and is accessed via the following command:

```
$ mysql -u xenon1tpmts_user -p
```

It must be noted that access is password protected. The user may now switch to the PMT database by typing:

```
mysql> use xenon1tpmts;
```

In order to see the list of tables, the following command is used:

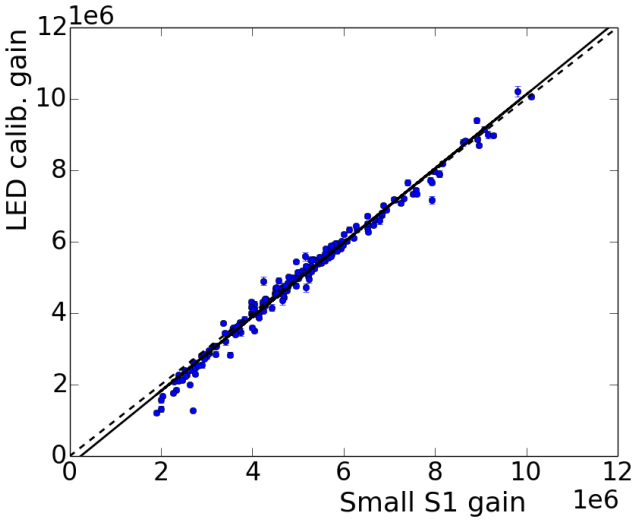

Figure 5.12: Comparison between the gains obtained by fitting the LED calibration spectra and the 'small' S1 Gaussian mean method. The latter calculates the mean from a Gaussian fit to the hits in 'small' S1 signals (analysis by Richard Saldanha). The solid line indicates the best fit to the data. Both methods agree within 5 %, according to the standard deviation of their residuals.

```
mysql> show tables;
```

This will display a list of tables for both the muon veto (identified with the prefix '`mv_`') and the TPC PMTs (identified with the prefix '`tpc_`'). The following list shows the relevant tables concerning the PMTs from the TPC:

Table	Description
tpc_arrays	Positions, cabling and modules of the PMTs in each array.
tpc_batches	List of PMTs in each screening batch.
tpc_calibs_run_0	Information on the LED calibrations during Run 0.
tpc_click_map_top	PMT image coordinates for online click map.
tpc_click_map_bottom	PMT image coordinates for online click map.
tpc_datasheets	PMT information from the Hamamatsu datasheets.
tpc_history	Status and history for each PMT (such as trips).
tpc_locations	PMT locations and owners (ZH, HD, BO).
tpc_mpik_measurements	Results from the PMT tests at MPIK.
tpc_radioactivity	Screening results per batch.
tpc_uzh_afterpulses	PMT afterpulse measurements at UZH.

Details on each of the tables can be consulted via the `describe` command. A brief description is presented next for the most relevant tables, detailing the fields and data types that they include:

```
mysql> describe tpc_arrays;
```

Field	Type	Description
pmt_pos	int(5)	PMT position in the TPC (0–247)
pmt_sn	varchar(10)	PMT serial number (KB0XXX)
array	enum('top','bottom')	TPC array (top or bottom)
adc_crate	int(1)	ADC crate (0 or 1)
adc	float(5,2)	ADC channel
adc_id	int(10)	ADC ID
sig_con	float(5,2)	Signal connector (0–10)
sig_ft	int(5)	Signal feedthrough (0–3)
amp	float(5,2)	Amplifier (0–15)
hv	float(5,2)	HV module (0–10)
hv_con	float(5,2)	HV connector (0–10)
hv_ret	int(10)	HV return (0–10)
hv_ft	int(5)	HV feedthrough (0–2)

```
mysql> describe tpc_batches;
```

Field	Type	Description
pmt_sn	varchar(10)	PMT serial number (KB0XXX)
batch_id	int(5)	Screening batch number

```
mysql> describe tpc_calibs_run_0;
```

Field	Type	Description
date_time	varchar(11)	Date and time of calibration
type	varchar(30)	'LED', "HV scan' or 'LED tuning'
pmt_settings	varchar(30)	HV values
led_settings	varchar(50)	Voltage on T1, T2 and T3 LEDs
comments	varchar(50)	Additional comments

```
mysql> describe tpc_datasheets;
```

Field	Type	Description
pmt_sn	varchar(10)	PMT serial number (KB0XXX)
sk	float	Cathode Luminous Sens [uA/lm]
skb	float	Cathode Luminous Sens. Blue [uA/lm]
sp	float	Anode Luminous Sens. at 1500V [A/lm]
anodedc	float	Anode Dark Current at 1500V [nA]
gain	float	Gain at 1500V
ebbv	float	Supply Voltage at 5e6 gain [V]
ebbi	float	Current at 5e6 gain [nA]
qe	float	QE at 175nm [%]
owner	varchar(2)	PMT owner (ZH, HD, BO)
filedate	int(8)	Filename date

`mysql> describe tpc_history;`

Field	Type	Description
id	int(6) unsigned	Event ID / auto increment
pmt_pos	int(5)	PMT position (0-247)
date	datetime	Date and time of event
operator	varchar(30)	Shifter or operator
event	varchar(20)	'Trip", 'Ramp up/down'
comments	varchar(90)	Additional comments
new_status	varchar(20)	'ON', 'OFF', 'Low voltage'

`mysql> describe tpc_mpik_measurements;`

Field	Type	Description
pmt_sn	varchar(6)	PMT serial number (KB0XXX)
run	int(3)	Run number
dcwarm	float	Dark count at room temperature [Hz]
dcwspread	float	Dark count spread at room temperature
dccold	float	Dark count during cool down [Hz]
dccspread	float	Dark count spread during cool down
tt	float	Transit time [ns]
tts	float	Transit time spread [ns]
apbc	float	Afterpulse rate before cool down
apac	float	Afterpulse rate after cool down
hv0X	float	HV for gain: 00 = 3e6, 01 = 2e6
sigma0X	float	PMT SPE spread at HV0X
pv0X	float	SPE P/V ratio at HV0X
gain0X	float	Gain at HV0X*
sigma0X	float	PMT SPE spread at HV0X
pv0X	float	SPE P/V ratio at HV0X

* HV0 2: 1320 V, 3: 1380 V, 4: 1440 V, 5: 1500 V, 6: 1540 V, 7: 1580 V, 8: 1640 V, 9: 1680 V

`mysql> describe tpc_radioactivity;`

Field	Type	Description
batch_id	int(2)	Batch number
detector	varchar(10)	Gator, GeMPI
pieces	int(2)	Number of PMTs in batch
mass	float	Total mass sampled [kg]
livetime	float	Days of screening
date	date	Starting date of screening
isotope*	float	Isotope activity [mBq/PMT]
err_isotope	float	Measurement uncertainty

* Isotopes: ^{238}U, ^{226}Ra, ^{228}Ra, ^{228}Th, ^{235}U, ^{40}K, ^{60}Co, ^{137}Cs, ^{54}Mn, ^{110}Mg

```
mysql> describe tpc_uzh_afterpulses;
```

Field	Type	Description
id	int(4)	Measurement ID / Auto increment
pmt_sn	varchar(6)	PMT serial number (KB0XXX)
date_time	varchar(11)	Date an time of measurement
cooldowns	int(2)	Number of cool downs
temp	varchar(12)	Temperature
dcrate	int(6)	Dark Count rate [Hz]
triggers	int(7)	Number of trigger pulses
totalaps	float	Total number of afterpulses
A1	float	Afterpulses in A1 [%] (see fig. 4.25)
A2	float	Afterpulses in A2 [%]
A3	float	Afterpulses in A3 [%]
Ion*	float	Afterpulses from ion X [%]

* Ion = H^+, H_2^+, He^+, CH_4^+, Ne^+, N_2^+, Ar^+, Xe^{++}, Xe^+

The information in the database can be used, for example, to compare the gains reported by Hamamatsu with the calibrations in XENON1T—or with the measurements at MPIK—as shown in figure 5.13. The measured gains at −100°C in XENON1T are, on average, lower than the values reported by Hamamatsu at room temperature. This is expected according to the temperature dependence studies of the PMT gain in section 4.3.2. The standard deviation of the residuals between these two measurements is around 9 %. On the other hand, the σ of the MPIK and Hamamatsu residuals—with both measurements performed at room temperature—is around 6 %, neglecting the far outlying datapoints.

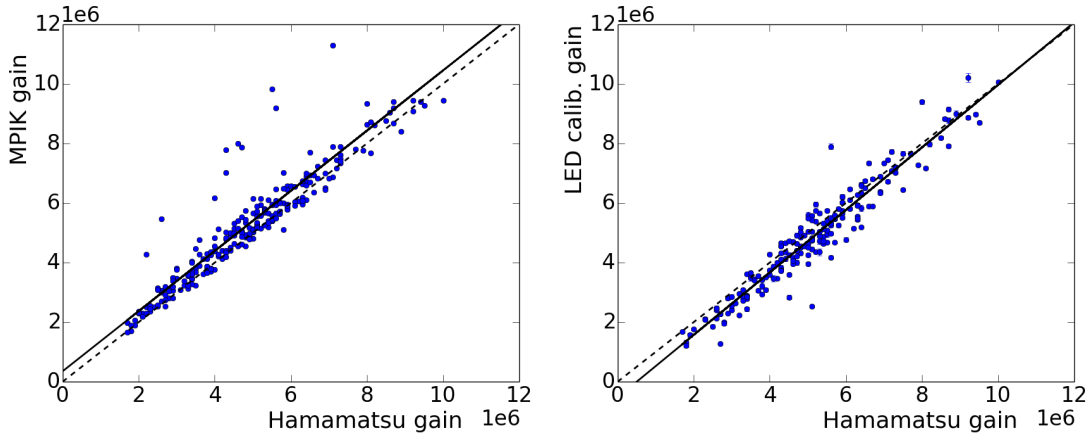

Figure 5.13: (Left) Comparison between the MPIK and Hamamatsu PMT gains—both at room temperature. (Right) Hamamatsu gains compared with the XENON1T calibration results in LXe (run 160510_1409). The dotted line indicates a one-to-one correlation, while the solid line indicates the linear fit.

5.3.3 Web Interface

A web interface has been developed for users to interact with the information in the PMT database and access the results from LED calibrations. The web page has been written in HTML and interaction with the database is coded in PHP. Figure 5.14 shows a screenshot of the web page.

The site is divided into several sections, listed on the left panel. Under *Calibration and Monitoring*, the user has access to the information regarding the weekly LED calibrations, where the SPE spectrum of each PMT is monitored and the gain is determined. The shifter performing the weekly calibration may also load the new data onto the database through this interface. The *Status and History* displays relevant events that have occurred to the PMTs—such as trips—as well as a change in status—such as being turned ON or OFF. The PMT operator or current shifter may also add new events to the database.

The test information received from Hamamatsu for all PMTs is listed under

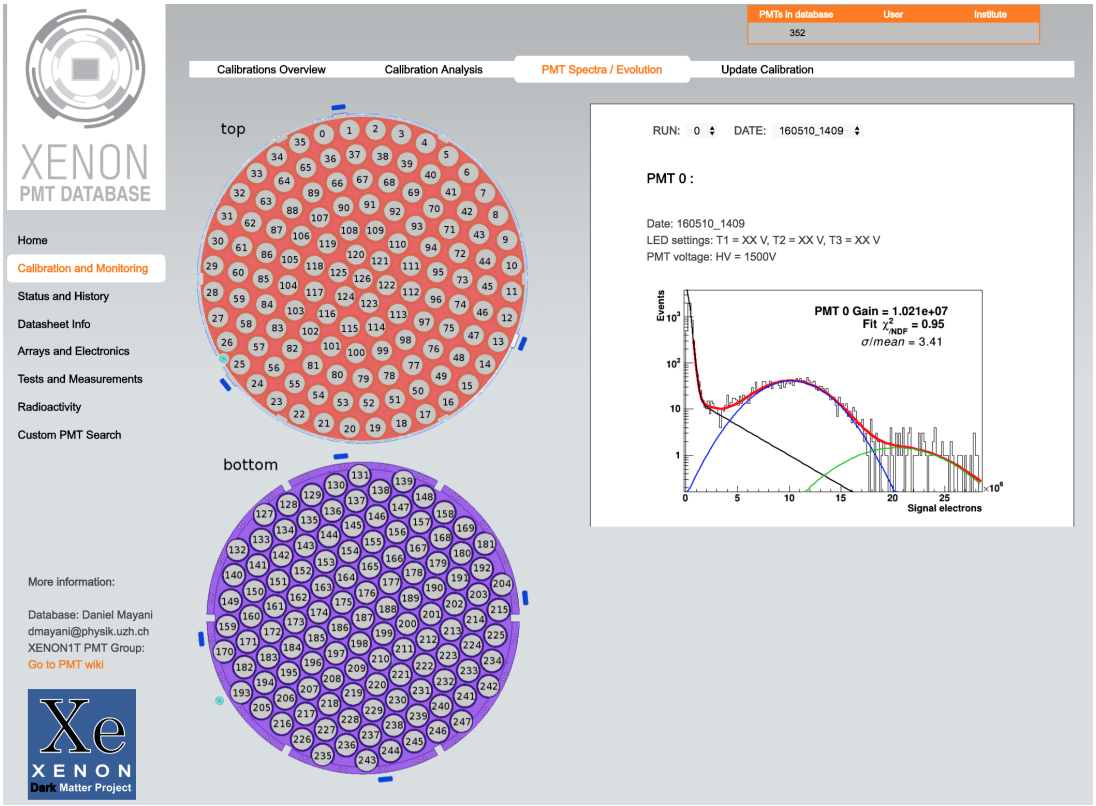

Figure 5.14: Web interface for the PMT database. This example screenshot shows the 'Calibration and Monitoring' section, where the results of gain calibrations can be consulted, along with the SPE spectra and fits. Interactive click-maps of both the top and bottom arrays allow for fast and intuitive navigation between the PMTs in the TPC.

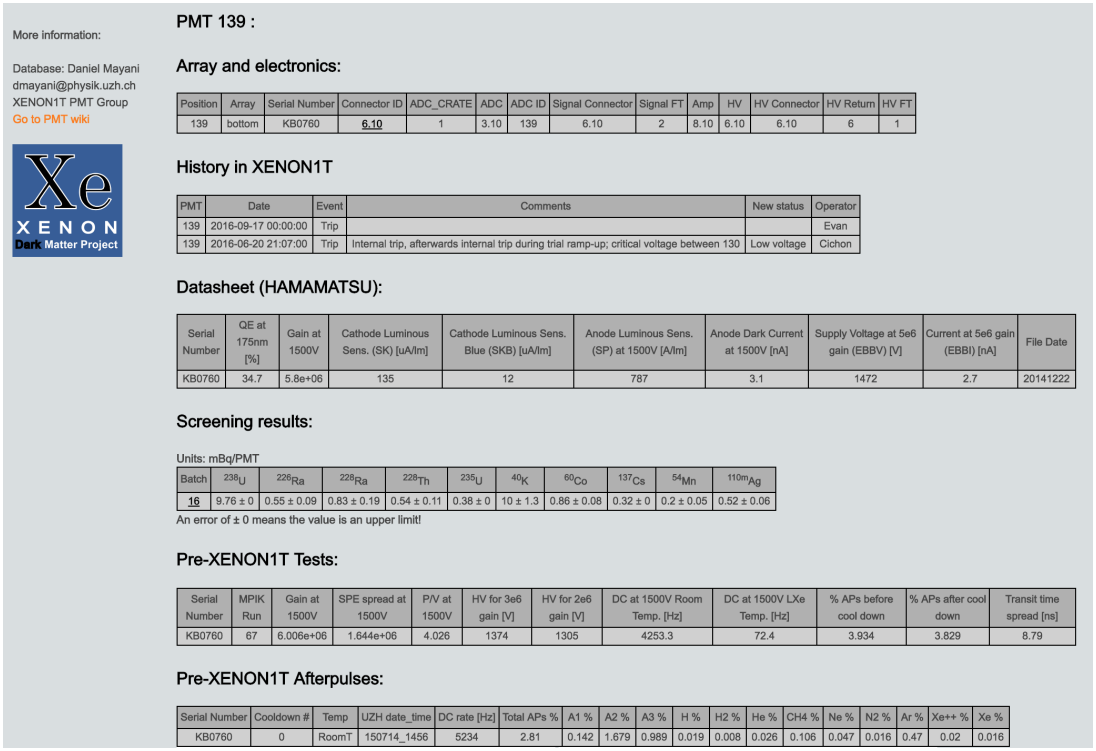

More information:

Database: Daniel Mayani
dmayani@physik.uzh.ch
XENON1T PMT Group
Go to PMT wiki

XENON Dark Matter Project

PMT 139 :

Array and electronics:

Position	Array	Serial Number	Connector ID	ADC_CRATE	ADC	ADC ID	Signal Connector	Signal FT	Amp	HV	HV Connector	HV Return	HV FT
139	bottom	KB0760	6.10	1	3.10	139	6.10	2	8.10	6.10	6.10	6	1

History in XENON1T

PMT	Date	Event	Comments	New status	Operator
139	2016-09-17 00:00:00	Trip			Evan
139	2016-06-20 21:07:00	Trip	Internal trip, afterwards internal trip during trial ramp-up; critical voltage between 130	Low voltage	Cichon

Datasheet (HAMAMATSU):

Serial Number	QE at 175nm [%]	Gain at 1500V	Cathode Luminous Sens. (SK) [uA/lm]	Cathode Luminous Sens. Blue (SKB) [uA/lm]	Anode Luminous Sens. (SP) at 1500V [A/lm]	Anode Dark Current at 1500V [nA]	Supply Voltage at 5e6 gain (EBBV) [V]	Current at 5e6 gain (EBBI) [nA]	File Date
KB0760	34.7	5.8e+06	135	12	787	3.1	1472	2.7	20141222

Screening results:

Units: mBq/PMT

Batch	^{238}U	^{226}Ra	^{228}Ra	^{228}Th	^{235}U	^{40}K	^{60}Co	^{137}Cs	^{54}Mn	^{110m}Ag
16	9.76 ± 0	0.55 ± 0.09	0.83 ± 0.19	0.54 ± 0.11	0.38 ± 0	10 ± 1.3	0.86 ± 0.08	0.32 ± 0	0.2 ± 0.05	0.52 ± 0.06

An error of ± 0 means the value is an upper limit!

Pre-XENON1T Tests:

Serial Number	MPIK Run	Gain at 1500V	SPE spread at 1500V	P/V at 1500V	HV for 3e6 gain [V]	HV for 2e6 gain [V]	DC at 1500V Room Temp. [Hz]	DC at 1500V LXe Temp. [Hz]	% APs before cool down	% APs after cool down	Transit time spread [ns]
KB0760	67	6.006e+06	1.644e+06	4.026	1374	1305	4253.3	72.4	3.934	3.829	8.79

Pre-XENON1T Afterpulses:

Serial Number	Cooldown #	Temp	UZH date_time	DC rate [Hz]	Total APs %	A1 %	A2 %	A3 %	H %	H2 %	He %	CH4 %	Ne %	N2 %	Ar %	Xe++ %	Xe %
KB0760	0	RoomT	150714_1456	5234	2.81	0.142	1.679	0.989	0.019	0.008	0.026	0.106	0.047	0.016	0.47	0.02	0.016

Figure 5.15: Example of the tables and data displayed for a PMT in the web interface, through which the user can interact with the PMT database.

Datasheet Info. This data is a useful benchmark with which to compare the performance of the PMTs, as shown in figure 5.13. The section *Arrays and Electronics* displays the locations and electronics modules—such as ADCs and amplifiers—for each PMT. Results from the testing phase of the PMTs at MPIK and UZH are summarized in *Tests and Measurements*. The screening results can be consulted under *Radioactivity*, where the information is available per PMT batch. Finally, a *Custom PMT Search* can be performed, where all relevant information for a specific PMT is displayed, as seen in figure 5.15.

Chapter 6

Conclusions

With XENON100 delivering its final results and ceasing operations in 2016, the baton has been passed on to XENON1T, continuing the race for the discovery of dark matter. The work presented here has been carried out during the overlapping period between the two experiments, comprising data analysis for the former and R&D for the latter.

A study of the electromagnetic background in XENON100 has been presented, focusing specifically on the data from run 12 (also known as science run III). This study has been necessary for the understanding of the background sources in the experiment, which change over time due to radioactive decay, purification of the LXe and changing environmental and hardware conditions. The main contributors to the measured background include the radioactivity of the detector materials, as well as the ^{222}Rn and ^{85}Kr isotopes found in the LXe.

The main goal of the analysis has been to match the measured XENON100 background with the predictions from Monte Carlo simulations, which have been fed with the radioactivity values for the detector materials, along with the estimated activities of ^{85}Kr and ^{222}Rn (section 3.3.6). The comparison between the MC and the measured data for different fiducial volumes (figure 3.22) shows that the measured event rate is higher than the one expected from the simulations. One of the reasons for this result is the mis-reconstruction of the event position due to PMT saturation, studied in section 3.3.7. An inward shift of the reconstructed positions has been found to increase the number of events within a given volume. The effect has been measured for several radii and energies, from which a correction function has been constructed (figure 3.29). The correction has been implemented on the MC data, consequently improving its agreement with the XENON100 data at energies above 1 MeV. For energies below ∼600 keV, the measured event rate is still higher than the one from the MC, especially for larger volumes. This result suggests the presence of a radioactive contribution with increased activity at larger radii which must be included in the MC. A possible candidate is ^{220}Rn, which can emanate from the TPC walls and, given its short life time (55.8 s), will decay before spreading into the central LXe volume.

The measured background spectrum has been constructed with a Combined

Energy Scale obtained from the composition of the S1 and S2 signals (section 3.3.3). The energy resolution of the detector as a function of energy has also been estimated and applied to the MC data (section 3.3.4). These results have also been useful for the general analysis of run 12.

The full live-time of run 12 (amounting to 153.6 days) has been combined with the previous two science runs to provide a total exposure of 477 live-days. The latest XENON100 dark matter search results have been published by the collaboration in 2016, improving the previously reported exclusion limits to WIMP-nucleus interactions, with a spin-independent cross-section of $1.1 \times 10^{-45}\,\mathrm{cm}^2$ at a 50 GeV WIMP mass [96].

XENON1T, the successor of XENON100, was inaugurated in November 2015 and during the following year its many subsystems have been commissioned and put into operation. The PMTs in the top and bottom arrays of the TPC are the "eyes" with which XENON1T looks for WIMP interactions in the LXe. An extensive testing campaign was performed in the facilities at UZH and MPIK, from which the final selection of 248 PMTs was made for XENON1T. The results provide a detailed characterization of the PMTs and evaluation of their performance, both at cryogenic and room temperatures. The properties studied include the dark count rate, the SPE response, the transit time, the quantum efficiency, the level of light emission and afterpulsing. These parameters were used to determine whether the PMTs were approved or rejected for long-term operation in XENON1T (section 4.3).

The quantum efficiency of the selected PMTs corresponds to an average value of $(34 \pm 3)\,\%$, with a minimum QE of 28 % requested to Hamamatsu. In terms of dark count rate, an average of $(40 \pm 13)\,\mathrm{Hz}$ has been measured at $-100\,^{\circ}\mathrm{C}$. A low DC rate is necessary in XENON1T since accidental coincidences of dark count pulses can lead to false S1 candidates. Various other parameters must fall into place for such a false signal to be confused with a WIMP-like event, such as a coincident S2, a correct light to charge ratio and an interaction depth within the fiducial volume. This reduces the problems that coincident dark counts may cause, but a low DC rate is still very important. With a DC rate of 40 Hz, an accidental rate of $\sim$1.5 Hz is expected from the 248 PMTs (assuming a time coincidence window of 30 ns). From this point of view, a low rate of the R11410-21 is a relevant feature. The long-term tests of these PMTs in LXe show their stability over several weeks of operation, with the DC rates remaining within 10 % of the mean value (section 4.3.1).

The gain and peak-to-valley ratio of the PMTs has also been studied (section 4.3.2). At a gain between $(2-3) \times 10^6$ the peak-to-valley ratio ranges from 2.5 to 4.5, proving a large signal-to-noise separation for this tube. The aim in XENON1T is to operate the PMTs at the lowest possible gains, while maintaining an adequate signal-to-noise separation. The main reason for this is to reduce the saturation of the PMT signals. As shown in the XENON100 analysis, the PMT saturation from S2s can lead to errors in the event position reconstruction.

The evolution of the gain has also been studied during operation in gaseous and liquid xenon (section 4.3.2). With a decrease of the temperature down to −100 °C in GXe, an average increase of 7 % in the gain has been measured with respect to the value at room temperature. The effect is explained by the decrease in electric resistance which results in a higher charge output. On the other hand, when operated in LXe, the measured gain decreases with respect to the value in GXe. For some PMTs the decrease is less than 1 %, but for others it is as much as 7 %—the average being around 3 %. These results must be taken into account when comparing the gains measured during XENON1T operations in LXe (figure 5.13).

An extensive study of the PMT afterpulsing has been performed (section 4.4). Through an analysis of the experimental data— along with analytical computations and the use of simulations—the ions producing afterpulses in the R11410-21 PMTs have been accurately identified according to their transit times. This allows to evaluate the quality of the PMT vacuum and determine the presence of leaks. This analysis is currently used in XENON1T to identify Xe leaks and diagnose the behavior of the PMTs and their performance in the experiment (see section 5.2).

XENON1T is ready to begin its search for dark matter. The sensitivity of the detector after a 2 year measurement in a 1 t fiducial volume is expected to reach a minimum cross section of $1.6 \times 10^{-47}\,\mathrm{cm}^2$ for a WIMP mass of 50 GeV [102] (see figure 6.1). An upgrade of the detector, known as XENONnT, has already been planned. The TPC will be increased by 20 – 30 % and the number of PMTs will amount to around 450. The projected sensitivity will surpass XENON1T by one order of magnitude. Figure 6.1 summarizes the current status of direct dark matter searches and the future prospects of the XENON collaboration.

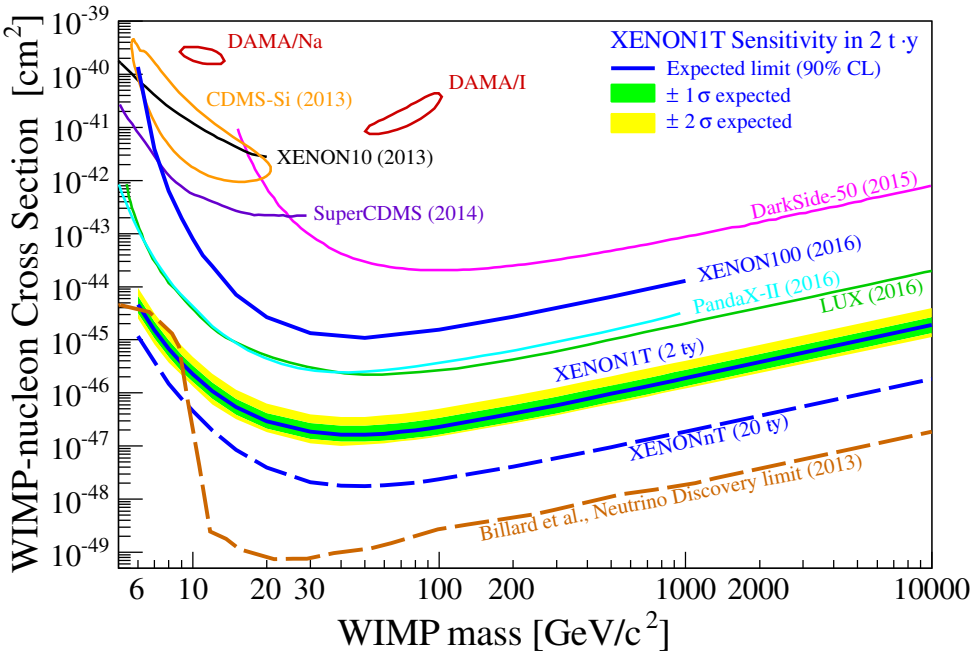

Figure 6.1: Comparison of the sensitivity to spin-independent WIMP-nucleus interactions from several dark matter experiments. The XENON1T and XENONnT limits are estimated in [102]. The dashed brown line indicates the "neutrino discovery limit" from [119]. Figure credit: XENON collaboration.

Bibliography

[1] C.C.W. Taylor (Translator). *The atomists, Leucippus and Democritus: Fragments*. University of Toronto Press Incorporated, 1999.

[2] René Descartes. *Principles of Philosophy II, 'On the Principles of Material Things', no. 4*. 1644.

[3] Isaac Newton. *PhilosophiæNaturalis Principia Mathematica*. 1687.

[4] J. J. Thomson. Cathode rays. *Phil. Mag.*, 44:293–316, 1897.

[5] E. Rutherford. The scattering of alpha and beta particles by matter and the structure of the atom. *Phil. Mag.*, 21:669–688, 1911.

[6] Georges Aad et al. Observation of a new particle in the search for the Standard Model Higgs boson with the ATLAS detector at the LHC. *Phys. Lett.*, B716:1–29, 2012.

[7] Serguei Chatrchyan et al. Observation of a new boson at a mass of 125 GeV with the CMS experiment at the LHC. *Phys. Lett.*, B716:30–61, 2012.

[8] J. C. Kapteyn. First Attempt at a Theory of the Arrangement and Motion of the Sidereal System. *Astrophys. J.*, 55:302–328, 1922.

[9] J. H. Oort. The force exerted by the stellar system in the direction perpendicular to the galactic plane and some related problems. *Bulletin of the Astronomical Institutes of the Netherlands*, 6:249–287, 1932.

[10] F. Zwicky. Die Rotverschiebung von extragalaktischen Nebeln. *Helv. Phys. Acta*, 6:110–127, 1933.

[11] H Babcock. The rotation of the Andromeda Nebula. *Lick Observatory bulletin*, 498, 1939.

[12] Vera C. Rubin and W. Kent Ford, Jr. Rotation of the Andromeda Nebula from a Spectroscopic Survey of Emission Regions. *Astrophys. J.*, 159:379–403, 1970.

[13] V. C. Rubin, N. Thonnard, and W. K. Ford, Jr. Rotational properties of 21 SC galaxies with a large range of luminosities and radii, from NGC 4605 /R = 4kpc/ to UGC 2885 /R = 122 kpc/. *Astrophys. J.*, 238:471, 1980.

[14] Edvige Corbelli and Paolo Salucci. The Extended Rotation Curve and the Dark Matter Halo of M33. *Mon. Not. Roy. Astron. Soc.*, 311:441–447, 2000.

[15] Galaxy Evolution Explorer (GALEX) Spitzer Space Telescope (NASA/JPL-Caltech). PIA12000. http://photojournal.jpl.nasa.gov/catalog/PIA12000, accessed August 2016.

[16] K. G. Begeman, A. H. Broeils, and R. H. Sanders. Extended rotation curves of spiral galaxies: Dark haloes and modified dynamics. *Mon. Not. Roy. Astron. Soc.*, 249:523, 1991.

[17] Gianfranco Bertone, Dan Hooper, and Joseph Silk. Particle dark matter: Evidence, candidates and constraints. *Phys. Rept.*, 405:279–390, 2005.

[18] J.I. Read. The Local Dark Matter Density. *J. Phys.*, G41:063101, 2014.

[19] Benoit Famaey. Dark Matter in the Milky Way. 2015.

[20] F. J. Kerr and Donald Lynden-Bell. Review of galactic constants. *Mon. Not. Roy. Astron. Soc.*, 221:1023, 1986.

[21] Martin C. Smith, G.R. Ruchti, A. Helmi, R.F.G. Wyse, J.P. Fulbright, et al. The RAVE Survey: Constraining the Local Galactic Escape Speed. *Mon. Not. Roy. Astron. Soc.*, 379:755, 2007.

[22] Ray Carlberg, H. K. C. Yee, E. Ellingson, R. Abraham, P. Gravel, S. Morris, and C. J. Pritchet. Galaxy cluster virial masses and Omega. *Astrophys. J.*, 462:32, 1996.

[23] Jeremy L. Tinker, David H. Weinberg, Zheng Zheng, and Idit Zehavi. On the mass-to-light ratio of large scale structure. *Astrophys. J.*, 631:41–58, 2005.

[24] Alexey Vikhlinin, A. Kravtsov, W. Forman, C. Jones, M. Markevitch, S. S. Murray, and L. Van Speybroeck. Chandra sample of nearby relaxed galaxy clusters: Mass, gas fraction, and mass-temperature relation. *Astrophys. J.*, 640:691–709, 2006.

[25] NASA Hubble Space Telescope. Galaxy Abell 1689's "Gravitational Lens" Magnifies Light of Distant Galaxies. http://hubblesite.org/newscenter/archive/releases/2003/01/image/a/, accessed August 2016.

[26] Chandra X-Ray Observatory. Images of 1E 0657-56. http://chandra.harvard.edu/photo/2006/1e0657/more.html, accessed August 2016.

[27] F. W. Dyson, A. S. Eddington, and C. Davidson. A Determination of the Deflection of Light by the Sun's Gravitational Field, from Observations Made at the Total Eclipse of May 29, 1919. *Phil. Trans. Roy. Soc. Lond.*, A220:291–333, 1920.

[28] F. Zwicky. Nebulae as gravitational lenses. *Phys. Rev.*, 51:290, 1937.

[29] D. Walsh, R. F. Carswell, and R. J. Weymann. 0957 + 561 A, B - Twin quasistellar objects or gravitational lens. *Nature*, 279:381–384, 1979.

[30] A. N. Taylor, S. Dye, Thomas J. Broadhurst, N. Benitez, and E. van Kampen. Gravitational lens magnification and the mass of abell 1689. *Astrophys. J.*, 501:539, 1998.

[31] M. Fukugita, C. J. Hogan, and P. J. E. Peebles. The Cosmic baryon budget. *Astrophys. J.*, 503:518, 1998.

[32] Douglas Clowe, Marusa Bradac, Anthony H. Gonzalez, Maxim Markevitch, Scott W. Randall, Christine Jones, and Dennis Zaritsky. A direct empirical proof of the existence of dark matter. *Astrophys. J.*, 648:L109–L113, 2006.

[33] Marusa Bradac, Steven W. Allen, Tommaso Treu, Harald Ebeling, Richard Massey, R. Glenn Morris, Anja von der Linden, and Douglas Applegate. Revealing the properties of dark matter in the merging cluster MACSJ0025.4-1222. *Astrophys. J.*, 687:959, 2008.

[34] Cheng-Jiun Ma, Harald Ebeling, and Ellizabeth Barrett. An X-ray/optical study of the complex dynamics of the core of the massive intermediate-redshift cluster MACSJ0717.5+3745. *Astrophys. J.*, 693:L56–L60, 2009.

[35] A. Mahdavi, H. y Hoekstra, A. y Babul, D. y Balam, and P. Capak. A Dark Core in Abell 520. *Astrophys. J.*, 668:806–814, 2007.

[36] D. J. Fixsen, E. S. Cheng, J. M. Gales, John C. Mather, R. A. Shafer, and E. L. Wright. The Cosmic Microwave Background spectrum from the full COBE FIRAS data set. *Astrophys. J.*, 473:576, 1996.

[37] G. Hinshaw et al. Nine-Year Wilkinson Microwave Anisotropy Probe (WMAP) Observations: Cosmological Parameter Results. *Astrophys. J. Suppl.*, 208:19, 2013.

[38] R. Adam et al. Planck 2015 results. I. Overview of products and scientific results. 2015.

[39] P. A. R. Ade et al. Planck 2015 results. XIII. Cosmological parameters. 2015.

[40] Adam G. Riess et al. Observational evidence from supernovae for an accelerating universe and a cosmological constant. *Astron. J.*, 116:1009, 1998.

[41] Volker Springel, Carlos S. Frenk, and Simon D.M. White. The large-scale structure of the Universe. *Nature*, 440:1137, 2006.

[42] Mark Vogelsberger et al. Introducing the Illustris Project: Simulating the coevolution of dark and visible matter in the Universe. *Mon. Not. Roy. Astron. Soc.*, 444(2):1518, 2014.

[43] Lauren Anderson et al. The clustering of galaxies in the SDSS-III Baryon Oscillation Spectroscopic Survey: baryon acoustic oscillations in the Data Releases 10 and 11 Galaxy samples. *Mon. Not. Roy. Astron. Soc.*, 441(1):24, 2014.

[44] M. Milgrom. A Modification of the Newtonian dynamics as a possible alternative to the hidden mass hypothesis. *Astrophys. J.*, 270:365, 1983.

[45] J.E. Felten. Milgrom's revision of Newton's laws - Dynamical and cosmological consequences. *ApJ*, 286:3, November 1984.

[46] Jacob D. Bekenstein. Relativistic gravitation theory for the MOND paradigm. *Phys. Rev.*, D70:083509, 2004.

[47] N. E. Mavromatos, M. Sakellariadou, and M. F. Yusaf. Can the relativistic field theory version of modified Newtonian dynamics avoid dark matter on galactic scales? *Phys. Rev. D*, 79(8):081301, April 2009.

[48] C. Alcock et al. The MACHO project: Microlensing results from 5.7 years of LMC observations. *Astrophys. J.*, 542:281, 2000.

[49] Fabio Iocco, Gianpiero Mangano, Gennaro Miele, Ofelia Pisanti, and Pasquale D. Serpico. Primordial Nucleosynthesis: from precision cosmology to fundamental physics. *Phys. Rept.*, 472:1, 2009.

[50] Simon D.M. White, C.S. Frenk, and M. Davis. Clustering in a Neutrino Dominated Universe. *Astrophys. J.*, 274:L1, 1983.

[51] Laura Baudis. Dark matter detection. *J. Phys.*, G43(4):044001, 2016.

[52] Gerard Jungman, Marc Kamionkowski, and Kim Griest. Supersymmetric dark matter. *Phys. Rept.*, 267:195, 1996.

[53] Jonathan L. Feng. Dark Matter Candidates from Particle Physics and Methods of Detection. *Ann. Rev. Astron. Astrophys.*, 48:495–545, 2010.

[54] Stephen P. Martin. A Supersymmetry primer. 1997. [Adv. Ser. Direct. High Energy Phys.18,1(1998)].

[55] Daniel J.H. Chung, Edward W. Kolb, and Antonio Riotto. Superheavy dark matter. *Phys. Rev.*, D59:023501, 1999.

[56] Vadim Kuzmin and Igor Tkachev. Ultrahigh-energy cosmic rays, superheavy long living particles, and matter creation after inflation. *JETP Lett.*, 68:271, 1998.

[57] R.D. Peccei and Helen R. Quinn. CP Conservation in the Presence of Instantons. *Phys. Rev. Lett.*, 38:1440, 1977.

[58] Luca Visinelli and Paolo Gondolo. Dark Matter Axions Revisited. *Phys. Rev.*, D80:035024, 2009.

[59] The ATLAS collaboration. Search for Dark Matter production associated with bottom quarks with 13.3 fb1 of pp collisions at s = 13 TeV with the ATLAS detector at the LHC. 2016.

[60] CMS Collaboration. Search for dark matter in final states with an energetic jet, or a hadronically decaying W or Z boson using 12.9 fb^{-1} of data at $\sqrt{s} = 13$ TeV. 2016.

[61] Louis E. Strigari. Galactic Searches for Dark Matter. *Phys. Rept.*, 531:1, 2013.

[62] Mark W. Goodman and Edward Witten. Detectability of Certain Dark Matter Candidates. *Phys. Rev.*, D31:3059, 1985.

[63] J.D. Lewin and P.F. Smith. Review of mathematics, numerical factors, and corrections for dark matter experiments based on elastic nuclear recoil. *Astropart. Phys.*, 6:87, 1996.

[64] Anne M. Green. Astrophysical uncertainties on direct detection experiments. *Mod. Phys. Lett.*, A27:1230004, 2012.

[65] P. Toivanen, M. Kortelainen, J. Suhonen, and J. Toivanen. Large-scale shell-model calculations of elastic and inelastic scattering rates of lightest supersymmetric particles (LSP) on I-127, Xe-129, Xe-131, and Cs-133 nuclei. *Phys. Rev.*, C79:044302, 2009.

[66] Richard H. Helm. Inelastic and Elastic Scattering of 187-MeV Electrons from Selected Even-Even Nuclei. *Phys. Rev.*, 104:1466, 1956.

[67] Teresa Marrodán Undagoitia and Ludwig Rauch. Dark matter direct-detection experiments. *J. Phys.*, G43(1):013001, 2016.

[68] David N. Spergel. The Motion of the Earth and the Detection of Weakly interacting massive particles. *Phys. Rev.*, D37:1353, 1988.

[69] S. Ahlen et al. The case for a directional dark matter detector and the status of current experimental efforts. *Int. J. Mod. Phys.*, A25:1, 2010.

[70] E. Behnke et al. Spin-Dependent WIMP Limits from a Bubble Chamber. *Science*, 319:933, 2008.

[71] S. Archambault et al. Constraints on Low-Mass WIMP Interactions on ^{19}F from PICASSO. *Phys. Lett.*, B711:153, 2012.

[72] C. Amole et al. Dark matter search results from the PICO-60 CF_3I bubble chamber. *Phys. Rev.*, D93(5):052014, 2016.

[73] C. Amole et al. Improved dark matter search results from PICO-2L Run 2. *Phys. Rev.*, D93(6):061101, 2016.

[74] F. Aubin et al. Discrimination of nuclear recoils from alpha particles with superheated liquids. *New J. Phys.*, 10:103017, 2008.

[75] Katsuki Hiraide et al. XMASS: Recent results and status. 2015.

[76] M.G. Boulay. DEAP-3600 Dark Matter Search at SNOLAB. *J. Phys. Conf. Ser.*, 375:012027, 2012.

[77] R. Bernabei et al. The DAMA/LIBRA apparatus. *Nucl. Instrum. Meth.*, A592:297, 2008.

[78] R. Bernabei et al. Final model independent result of DAMA/LIBRA-phase 1. *Eur. Phys. J.*, C73(12):2648, 2013.

[79] R.W. Schnee. Introduction to dark matter experiments. 2011.

[80] Emily Shields, Jingke Xu, and Frank Calaprice. SABRE: A New NaI(Tl) Dark Matter Direct Detection Experiment. *Phys .Procedia*, 61:169, 2015.

[81] J. Amar et al. Status of the ANAIS Dark Matter Project at the Canfranc Underground Laboratory. *J. Phys. Conf. Ser.*, 718(4):042052, 2016.

[82] Kyungwon Kim. Status of the KIMS-NaI experiment. In *Proceedings, Meeting of the APS Division of Particles and Fields (DPF 2015): Ann Arbor, Michigan, USA, 4-8 Aug 2015*, 2015.

[83] C.E. Aalseth et al. CoGeNT: A Search for Low-Mass Dark Matter using p-type Point Contact Germanium Detectors. *Phys. Rev.*, D88:012002, 2013.

[84] C.E. Aalseth et al. Search for An Annual Modulation in Three Years of CoGeNT Dark Matter Detector Data. 2014.

[85] Jonathan H. Davis, Christopher McCabe, and Celine Boehm. Quantifying the evidence for Dark Matter in CoGeNT data. *JCAP*, 1408:014, 2014.

[86] C.E. Aalseth et al. Maximum Likelihood Signal Extraction Method Applied to 3.4 years of CoGeNT Data. 2014.

[87] G. Angloher et al. Results on light dark matter particles with a low-threshold CRESST-II detector. 2015.

[88] Z. Ahmed et al. Search for Weakly Interacting Massive Particles with the First Five-Tower Data from the Cryogenic Dark Matter Search at the Soudan Underground Laboratory. *Phys. Rev. Lett.*, 102:011301, 2009.

[89] Z. Ahmed et al. Dark Matter Search Results from the CDMS II Experiment. *Science*, 327:1619, 2010.

[90] Z. Ahmed et al. Search for annual modulation in low-energy CDMS-II data. 2012.

[91] R. Agnese et al. Search for Low-Mass Weakly Interacting Massive Particles with SuperCDMS. *Phys. Rev. Lett.*, 112:241302, 2014.

[92] R. Agnese et al. WIMP-Search Results from the Second CDMSlite Run. *Submitted to: Phys. Rev. Lett.*, 2015.

[93] A.I. Bolozdynya. Two-phase emission detectors and their applications. *Nucl. Instrum. Meth. A*, 422(1):314, 1999.

[94] E. Aprile et al. Dark Matter Results from 225 Live Days of XENON100 Data. *Phys. Rev. Lett.*, 109:181301, 2012.

[95] D.S. Akerib et al. First results from the LUX dark matter experiment at the Sanford Underground Research Facility. 2013.

[96] E. Aprile et al. XENON100 Dark Matter Results from a Combination of 477 Live Days. 2016.

[97] Andi Tan et al. Dark Matter Results from First 98.7 Days of Data from the PandaX-II Experiment. *Phys. Rev. Lett.*, 117(12):121303, 2016.

[98] D. S. Akerib et al. Results from a search for dark matter in the complete LUX exposure. 2016.

[99] M. Bossa et al. DarkSide-50, a background free experiment for dark matter searches. *JINST*, 9:C01034, 2014.

[100] P. Agnes et al. Results from the first use of low radioactivity argon in a dark matter search. *Phys. Rev.*, D93(8):081101, 2016.

[101] J. Calvo et al. Status of ArDM-1t: First observations from operation with a full ton-scale liquid argon target. 2015.

[102] E. Aprile et al. Physics reach of the XENON1T dark matter experiment. *JCAP*, 1604(04):027, 2016.

[103] D.C. Malling et al. After LUX: The LZ Program. 2011.

[104] J. Aalbers et al. DARWIN: towards the ultimate dark matter detector. 2016.

[105] J. Angle et al. First Results from the XENON10 Dark Matter Experiment at the Gran Sasso National Laboratory. *Phys. Rev. Lett.*, 100:021303, 2008.

[106] W.H. Lippincott et al. Scintillation yield and time dependence from electronic and nuclear recoils in liquid neon. *Phys. Rev.*, C86:015807, 2012.

[107] E. Aprile et al. Limits on spin-dependent WIMP-nucleon cross sections from 225 live days of XENON100 data. *Phys. Rev. Lett.*, 111:021301, 2013.

[108] J. B. Albert et al. Improved measurement of the $2\nu\beta\beta$ half-life of ^{136}Xe with the EXO-200 detector. *Phys. Rev.*, C89(1):015502, 2014.

[109] M. Berger et al. XCOM: Photon Cross Section Database. http://physics.nist.gov/xcom, 2010.

[110] Guillaume Plante. *The XENON100 Dark Matter Experiment: Design, Construction, Calibration and 2010 Search Results with Improved Measurement of the Scintillation Response of Liquid Xenon to Low-Energy Nuclear Recoils*. PhD thesis, Columbia University, 2012.

[111] S. Kubota, A. Nakamoto, T. Takahashi, T. Hamada, E. Shibamura, M. Miyajima, K. Masuda, and T. Doke. Recombination luminescence in liquid argon and in liquid xenon. *Phys. Rev.*, B17:2762, 1978.

[112] A. Hitachi. Properties of liquid xenon scintillation for dark matter searches. *Astropart. Phys.*, 24:247–256, 2005.

[113] A. Manalaysay. Towards an improved understanding of the relative scintillation efficiency of nuclear recoils in liquid xenon. 2010.

[114] G. Plante et al. New Measurement of the Scintillation Efficiency of Low-Energy Nuclear Recoils in Liquid Xenon. *Phys. Rev.*, C84:045805, 2011.

[115] M Yamashita, T Doke, K Kawasaki, J Kikuchi, and S Suzuki. Scintillation response of liquid xe surrounded by ptfe reflector for gamma rays. *Nucl. Instr. Meth. Phys. Res. Sect. A*, 535(3):692–698, 2004.

[116] E. Aprile et al. The XENON100 Dark Matter Experiment. *Astropart. Phys.*, 35:573, 2012.

[117] E. Aprile et al. Conceptual design and simulation of a water Cherenkov muon veto for the XENON1T experiment. *JINST*, 9:11006, 2014.

[118] Dongming Mei and A. Hime. Muon-induced background study for underground laboratories. *Phys. Rev.*, D73:053004, 2006.

[119] J. Billard, L. Strigari, and E. Figueroa-Feliciano. Implication of neutrino backgrounds on the reach of next generation dark matter direct detection experiments. *Phys. Rev.*, D89(2):023524, 2014.

[120] L. Baudis et al. Gator: a low-background counting facility at the Gran Sasso Underground Laboratory. *JINST*, 6:P08010, 2011.

[121] N. Neder, G. Heusser, and M. Laubenstein. . *Proc. of Intern. Conf. Isotop. Environm.*, 53:19, 2000.

[122] E. Aprile et al. Material screening and selection for XENON100. *Astropart. Phys.*, 35:43, 2011.

[123] E. Aprile et al. Study of the electromagnetic background in the XENON100 experiment. *Phys. Rev.*, D83:082001, 2011.

[124] National Nuclear Data Center. Freely available decay chain database. http://www.nndc.bnl.gov/, accessed July 2016.

[125] X. Du, K. Bailey, Z. T. Lu, P. Mueller, T. P. O'Connor, and L. Young. An atom trap system for practical ^{81}Kr dating. *Rev. Sci. Instrum.*, 75:3224, 2004.

[126] Sebastian Lindemann and Hardy Simgen. Krypton assay in xenon at the ppq level using a gas chromatographic system combined with a mass spectrometer. *Eur. Phys. J. C*, 74(2):1, 2014.

[127] S. Rosendahl, E. Brown, I. Cristescu, A. Fieguth, C. Huhmann, M. Murra, and C. Weinheimer. A cryogenic distillation column for the XENON1T experiment. *J. Phys. Conf. Ser.*, 564(1):012006, 2014.

[128] L. Baudis, A. Ferella, A. Kish, A. Manalaysay, T. Marrodan Undagoitia, and M. Schumann. Neutrino physics with multi-ton scale liquid xenon detectors. *JCAP*, 1401:044, 2014.

[129] Alexander Kish. *Dark Matter Search with the XENON100 Experiment.* PhD thesis, University of Zurich, 2011.

[130] Annika Behrens. *Light Detectors for the XENON100 and XENON1T Dark Matter Search Experiments.* PhD thesis, University of Zurich, 2014.

[131] E. Conti et al. Correlated fluctuations between luminescence and ionization in liquid xenon. *Phys. Rev.*, B68:054201, 2003.

[132] Marc Weber. *Gentle neutron signals and noble background in the XENON100 dark matter experiment.* PhD thesis, University of Heidelberg, 2013.

[133] Harley Iams and Bernard Salzberg. The Secondary Emission Phototube. *Proc. Ire.*, 23:55, 1935.

[134] V.K. Zworykin, G.A. Morton, and L. Malter. The Secondary Emission Multiplier-A New Electronic Device. *Proc. Ire.*, 24:351, 1936.

[135] P. Barrow et al. Qualification Tests of the R11410-21 Photomultiplier Tubes for the XENON1T Detector. 2016.

[136] K. Lung et al. Characterization of the Hamamatsu R11410-10 3-Inch Photomultiplier Tube for Liquid Xenon Dark Matter Direct Detection Experiments. *Nucl. Instrum. Meth.*, A696:32, 2012.

[137] Hamamatsu Handbook. *Photomultiplier Tubes: Basics and Applications*, chapter 4, page 64. Hamamatsu Photonics, 3 edition, 2007.

[138] Hamamatsu Handbook. *Photomultiplier Tubes: Basics and Applications*, chapter 4, page 30. Hamamatsu Photonics, 3 edition, 2007.

[139] E. Aprile et al. Lowering the radioactivity of the photomultiplier tubes for the XENON1T dark matter experiment. *Eur. Phys. J.*, C75(11):546, 2015.

[140] Hamamatsu Handbook. *Photomultiplier Tubes: Basics and Applications*, chapter 4, page 43. Hamamatsu Photonics, 3 edition, 2007.

[141] Fralock. Cirlex technical information. http://www.cirlex.com/technical.asp, accessed June 2016.

[142] C. Bauer et al. Qualification Tests of 474 Photomultiplier Tubes for the Inner Detector of the Double Chooz Experiment. *JINST*, 6:P06008, 2011.

[143] Dominick Cichon. *Examining Hamamatsu R11410-21 photomultipliers for XENON1T at room and liquid xenon temperatures.* Bachelor thesis, Max-Planck-Institut für Kernphysik in Heidelberg, 2013.

[144] Meike Danisch. *Scintillation light detection in XENON1T: Photosensor tests and light collection simulation.* Master thesis, Max-Planck-Institut für Kernphysik in Heidelberg, 2014.

[145] Gaudenz Kessler. *Inelastic WIMP-Nucleus Interactions in XENON100 and Cables and Connectors for XENON1T.* PhD thesis, University of Zurich, 2016.

[146] H. O. Meyer. Dark Rate of a Photomultiplier at Cryogenic Temperatures. 2008.

[147] C. R. Crowell. The Richardson constant for thermionic emission in Schottky barrier diodes. *Solid State Electronics*, 8:395–399, April 1965.

[148] D. Yu. Akimov, A. I. Bolozdynya, Yu. V. Efremenko, V. A. Kaplin, A. V. Khromov, Yu. A. Melikyan, and V. V. Sosnovtsev. Observation of light emission from Hamamatsu R11410-20 photomultiplier tubes. *Nucl. Instrum. Meth.*, A794:1–2, 2015.

[149] Hamamatsu Handbook. *Photomultiplier Tubes: Basics and Applications*, chapter 4, page 46. Hamamatsu Photonics, 3 edition, 2007.

[150] E. H. Bellamy, G. Bellettini, F. Gervelli, M. Incagli, D. Lucchesi, C. Pagliarone, F. Zetti, Yu. Budagov, I. Chirikov-Zorin, and S. Tokar. Absolute calibration and monitoring of a spectrometric channel using a photomultiplier. *Nucl. Instrum. Meth.*, A339:468–476, 1994.

[151] L. Baudis, S. D'Amato, G. Kessler, A. Kish, and J. Wulf. Measurements of the position-dependent photo-detection sensitivity of the Hamamatsu R11410 and R8520 photomultiplier tubes. 2015.

[152] L. Baudis, A. Behrens, A. Ferella, A. Kish, T. Marrodán Undagoitia, et al. Performance of the Hamamatsu R11410 Photomultiplier Tube in cryogenic Xenon Environments. *JINST*, 8:P04026, 2013.

[153] Hamamatsu Handbook. *Photomultiplier Tubes: Basics and Applications*, chapter 4, page 37. Hamamatsu Photonics, 3 edition, 2007.

[154] Karl Tasso Knpfle. Upgrade of the GERDA experiment. *PoS*, TIPP2014:109, 2014.

[155] P. Agnes et al. First Results from the DarkSide-50 Dark Matter Experiment at Laboratori Nazionali del Gran Sasso. *Phys. Lett.*, B743:456, 2015.

[156] K. Abe et al. XMASS detector. *Nucl. Instrum. Meth.*, A716:78, 2013.

[157] A. Lyashenko, Tam Nguyen, Adam Snyder, Hanguo Wang, and Katsushi Arisaka. Measurement of the absolute Quantum Efficiency of Hamamatsu model R11410-10 photomultiplier tubes at low temperatures down to liquid xenon boiling point. *JINST*, 9(11):P11021, 2014.

[158] K. J. Ma et al. Time and Amplitude of Afterpulse Measured with a Large Size Photomultiplier Tube. *Nucl. Instrum. Meth.*, A629:93–100, 2011.

[159] Florian Kaether and Conradin Langbrandtner. Transit Time and Charge Correlations of Single Photoelectron Events in R7081 PMTs. *JINST*, 7:P09002, 2012.

[160] R. Saldanha, L. Grandi, Y. Guardincerri, and T. Wester. Model Independent Approach to the Single Photoelectron Calibration of Photomultiplier Tubes. 2016.